Design, Development, and Analysis of a Morphing Aircraft Model for Wind Tunnel Experimentation

by

David A. Neal III

Thesis submitted to the Faculty of the
Virginia Polytechnic Institute and State University
in partial fulfillment of the requirements for the degree of

Master of Science

in

Mechanical Engineering

Daniel J. Inman, Chair
Harry Robertshaw
William Mason
Craig Woolsey

April 18, 2006
Blacksburg, Virginia

Keywords: Morphing, Wind Tunnel Model, Aerodynamic Modeling, Variable Geometry

Design, Development, and Analysis of a Morphing Aircraft Model for Wind Tunnel Experimentation

David A. Neal III

Abstract

Morphing aircraft combine both radical and subtle wing shape changes to improve vehicle performance relative to a rigid airframe. An aircraft wind tunnel model with considerable wing-shape freedom can serve as a tool in learning to model, control, and fully exploit the potential of such vehicles. This work describes the design, development, and initial analysis of a wind tunnel model that combines large and small wing shape variations for fundamental research in modeling and control of morphing air vehicles. The vehicle is designed for five primary purposes: quasi-steady aerodynamic modeling of an aircraft with large planform changes, optimization studies in achieving efficient flight configurations, transient aerodynamic modeling of high-rate planform changes, evaluating planform maneuvering as an control effector, and gimbaled flight control simulation of a morphing aircraft. The knowledge gained from the wind tunnel evaluations will be used to develop general stabilization and optimal control strategies that can be applied to other vehicles with large scale planform changes and morphing flight models.

After a brief background on the development of the Morphing Aircraft Program, and previous research ventures, the first phase vehicle development is described. The vehicle function, subsystems, and control are all presented in addition to the results of first phase wind tunnel testing. Deficiencies in the phase one design motivated the phase two development which has led to the current vehicle model: MORPHEUS. The evolution towards the MORPHEUS configuration is presented in detail along with an elementary strength analysis. The new embedded control implementation to permit a rate controllable planform is included. A preliminary aerodynamic analysis is presented to contrast MORPHEUS against the phase one design and an industry morphing concept. In particular, it is shown how the redesigned model has enhanced performance

characteristics and the additional degrees of freedom enable greater flexibility in optimizing a configuration, especially with respect to trim characteristics. An expansion of traditional analysis techniques is applied to derive a new optimal twist algorithm for the MORPHEUS model at each planform configuration. The analysis concludes with a hybrid continuous modeling method that combines first-order computational aerodynamic modeling with classic stability expressions and DATCOM enhancements. The elementary aerodynamic coefficients are computed over the range of possible planform configurations and combined with the optimal twist results for preliminary trim analysis. This work precedes phase two wind tunnel testing and transient modeling. Future work involves expansion into the five purposes detailed for the MORPHEUS model.

Acknowledgements

I would like to thank my advisor, Dr. Daniel Inman, for his patience with me and with this project. It has been a trying and expensive task without much payback to this point. I appreciate his willingness to look to the future potential and provide support and guidance throughout my endeavors. I thank my other committee members, Dr. Harry Robertshaw, Dr. William Mason, and Dr. Craig Woolsey for their input and advice over the years, both related and unrelated to this work.

I would like to extend a special thanks to my fellow graduate student Justin Farmer. Justin worked tirelessly on the MORPHEUS redesign with me and was an enormous help. During most of the design phase I was located in Maryland and limited to once a month visits for marathon work schedules. Justin did an incredible amount of work in testing out concepts and assembling the plane on too many occasions. He was very patient with my design iterations, and constant emails. There is absolutely no way I could have completed the project without him.

I thank my parents, David and LaTannia Neal, for their continued support throughout my academic career. They have always been a driving influence in my life and I appreciate them so much for the path they have set me on. I was truly blessed to be born into such a wonderful family.

I thank my daughter Kayla for being so innocent and smiling and running to hug me whenever I walked through the door after everything had gone wrong in the lab. When things went wrong she made the project seem so insignificant….and I needed that.

Most importantly I would like to thank my wife, Helen. Helen has sacrificed a good deal as I have been completely engrossed in my studies while she was taking care of our daughter Kayla. For the long nights away and the continual state of stress in my life concerning completing the plane, she shouldered the burden and supported me in every way. I appreciate her patience, her support, and her love.

Contents

List of Tables **x**

List of Figures **xi**

Nomenclature **xviii**

Chapter 1: Morphing Research and the APVE Model **1**

1.1 Motivation…….1

1.2 The APVE Model……..2

1.3 Morphing Aircraft Research Programs…….3

1.3.1 Variable Geometry Aircraft in the Department of Defense……4

1.3.2 Morphing Aircraft Research Programs in the Depart of Defense……5

1.3.3 Morphing Research in Academia……8

1.3.4 Morphing Research at Virginia Tech……11

1.4 Justification for the APVE Model……14

1.4.1 The Aerodynamics of Morphing Aircraft……14

1.4.2 APVE Implementation……..16

1.5 Thesis Overview.…….....16

Chapter 2: Phase One Design and Testing **17**

2.1 Chapter Overview……....17

2.2 Synopsis of the Adaptive Aircraft Configuration……17

2.3 External Vehicle Design……..19

2.4 Internal Vehicle Design……...21

2.4.1 Internal Vehicle Design Overview……....21

2.4.2 Flow Control Devices……...23

2.4.3 Span Extension Unit…….25

2.4.4 Twist Actuation…….26

2.4.5 Sweep Actuation……...28
2.4.6 Wing Assembly……29
2.4.7 Tail Actuation……...30
2.4.8 Control Circuit……..30
2.5 Aerodynamic Performance……..32
2.5.1 Vortex Lattice Aerodynamics……...33
2.5.2 Wind Tunnel Test Setup……...37
2.5.3 Wind Tunnel Test Results……39
2.5.4 Experimental Data and Vortex Lattice Predictions……..42
2.6 Chapter Summary……45

Chapter 3: Phase Two Development: Design and Analysis 46
3.1 Chapter Overview……46
3.2 Morpheus Design Overview……47
3.3 Detailed Design and Elementary Strength Analysis……50
3.3.1 Composite Fuselage Base……52
3.3.2 Internal Layout and Function……55
3.3.3 Variable Geometry Tail Design……63
3.3.4 Compliant Twist Wings……66
3.3.5 EPC Circuit……...69
3.4 Embedded Vehicle Control……..72
3.4.1 Pneumatic Control Design……73
3.4.2 Electromechanical Control Methods……78
3.5 Chapter Summary……82

Chapter 4: Elementary Aerodynamic Analysis 84
4.1 Chapter Overview……84
4.2 Comparison of APVE and NMAS Configurations……..84
4.2.1 *Loiter-Dash* Geometry Comparisons……85
4.2.2 MORPHEUS Airfoil Analysis……..89
4.2.3 *Loiter-Dash* Drag Response……..91

4.2.4 *Loiter-Dash* Planform Characteristics……100
4.3 Chapter Summary……..106

Chapter 5: Continuous Aerodynamic Modeling 108
5.1 Chapter Overview……..108
5.2 A Note on Computational Tools……108
5.3 Washout Optimization for Continuous Planform States……109
5.3.1 Washout Optimization from Lifting-Line Theory……..111
5.3.2 Extension of Washout Optimization to Arbitrary Planforms…….115
5.4 Continuous Modeling of Aerodynamic Coefficients……...120
5.4.1 Aerodynamic Expansions for a Dynamic Planform……...121
5.4.2 Implementing the VLM Solution into DATCOM Stability Equations……..122
5.4.3 Minimum Drag Trim Analysis……128
5.4.4 VLM Surface Plot Solutions……...130
5.5 Chapter Summary……..137

Chapter 6: Conclusions 138
6.1 Contributions……138
6.2 Future Work Recommendations……140

Bibliography 142

Appendix A. Castigliano's solution for point load transfer to internal wing structure 147

Appendix B. Variable Geometry Tail time-varying transformations for vehicle coordination 151

Appendix C. Nonlinear equations of motion for pneumatic cylinder system 154

Appendix D: Custom Vortex Lattice Code 156

List of Tables

2-1. Comparison of Phase One APVE and N-MAS planform geometries……..19

2-2. Validation of Custom VLM Code……..35

2-3. Vortex-Lattice results for Aerodynamic Changes with Planform Shape…….37

2-4. Test condition and reference parameters…….38

2-5. Comparison of Vortex Lattice and Experimental Test Results……..43

4.1. Loiter-Dash geometry comparison of APVE Models and N-MAS prototype…….87

4.2. Skin Friction Drag Computations for Loiter Configuration…….93

4.3. Skin Friction Drag Computations for Dash Configuration……...93

4.4. Viscous Drag Computations for Loiter Configuration……..94

4.5. Viscous Drag Computations for Dash Configuration……96

4.6. Parasite Drag Computations for Loiter Configuration……..97

4.7. Parasite Drag Computations for Dash Configuration……97

4.8. Maximum Lift to Drag Ratio for all vehicles and configurations…….99

4.9. N-MAS Aerodynamic Coefficients and Stability Parameters…….104

4.10. P1-APVE Aerodynamic Coefficients and Stability Parameters……105

4.11. MORPHEUS Aerodynamic Coefficients and Stability Parameters……..105

4.12. Modified MORPHEUS Aerodynamic Coefficients and Stability Parameters……106

List of Figures

1-1. The APVE Model in loiter, dash and asymmetric maneuvering. The maneuvering profile also demonstrates wing twist. These are three of the many possible vehicle configurations…….3

1-2. The N-MAS planform in high lift, cruise, and dash configurations. The sweep varies from 15 to 45-degrees and the half-span decreases from 10 to 7 feet…….7

1-3. The Lockheed Martin folding-wing configuration. The extended position is for loiter, the wings fold 130-degrees into the fuselage to form a highly maneuverable dash configuration……...8

1-4. The Hyper-Elliptic Cambered Span wing configuration. Hyper-elliptical describes both the planform layout and the wing fold shape when morphed……13

2-1. Various configurations of the adaptive aircraft model, a) Δb=0, t=0, Λ=0 b) Δb=0, t=0, Λ=100% c) Δb=100%, t=0, Λ=0 d) Δb=100%, t=0%, Λ=100% e) Δb=100%, t=100%, Λ=0 f) Δb=100%, t=100%, Λ=100%.....18

2-2. Vehicle cross-section and planform views detailing interpolated airfoil sections. Airfoil thickness was increased and shifted aft to permit an internal twist mechanism..20

2-3. Overview of internal vehicle structure. The five primary subsystems in the Phase 1 design are the sweep system, the tail actuation, span extension unit, twist mechanism and flow control devices…….23

2-4. Five-port solenoid valve and flow path description. EA is the exhaust port for A, EB is the exhaust port for B and P is the source pressure. This demonstrates a closed-center valve that nominally seals chamber ports……24

2-5. Electro-pneumatic pressure regulator. Internal solenoids track a high frequency PWM signal to track a command pressure value……24

2-6. Linear span thruster formed from 3-bar segment. The sliding support rods are intended to support torque loads from wing twist and to assist the extending cylinder rod in supporting wing bending loads. ……...25

2-7. Span control circuit demonstrating the solenoid directional flow valve porting to the span actuator chambers. Bang-bang control was used for static positioning because there was no proportional control capability with the solenoid…….26

2-8. Internal and external view of twist mechanism. Significant torque output is produced by the series combination of the pneumatic rotary actuator and the planetary gear set. The gear friction helps the actuator to maintain static positioning……..27

2-9. Linear twist distribution due to internal actuation. The compliant wing profile was manually cut from a closed-cell polyethylene wing. In addition to a rough exterior surface, the structure was incapable of supporting adequate wing loading……..28

2-10. Direct-drive sweep geometry. The figure illustrates the actual vehicle system and the corresponding linkage model describing the nonlinear transcendental relationship between linear actuator contraction and wing sweep angle…….29

2-11. Wing assembly demonstrates load transfer to the turnbuckle. The turnbuckle/turntable combination permits low friction wing sweep under aerodynamic loading……...30

2-12. Integration of computer hardware into control circuit. The embedded computing stack permits onboard actuator control from a remote unit via a SIMULINK design interface…….31

2-13. Custom vortex lattice structure for Warren 12 planform. o-left vortex boundary, *-right vortex boundary, +-control point, +-vortex lift location……...35

2-14. Custom vortex lattice structures for two APVE configurations. 1) Fully-extended planform 2) Fully swept, tail and wings contracted……...36

2-15. Experimental model mounted in Stability Tunnel for 1st phase static configuration testing. The testing was constrained to angle of attack sweeps for nine different wing configurations……...37

2-16. Relevant planform parameters to identify iterated wing shape changes……..38

2-17. The influence of span extension (Δb) and wing sweep (Λ) on the aerodynamic center location. The trends followed expected results with larger aftward area shifts corresponding to larger increases in static margin and trim requirements……39

2-18. The influence of span extension (Δb) and sweep (Λ) on the lift curve slope (C_{L_α}). Span extension was seen to have little effect on the negative wing sweep gradient although it increased with the absolute lift curve slope…….40

2-19. Lift-curve for swept and unswept configurations at full span extension. Although the swept configuration had a slightly decreased lift-curve slope, the delayed stall allowed it to achieve a higher total lift value……...41

2-20. Pitching moment response for swept and unswept configurations. The moment response indicates that the unswept configuration is highly unstable about the wind tunnel mount point which can be countered by shifting the nominal c.g. forward……..42

2-21. Drag reduction for obtaining a given lift coefficient by implementing different planform configurations. The response validates the use of multiple wing configurations to optimize the drag performance during various mission segments…….42

2-22. Comparison of $C_{L\alpha}$ changes with configuration for VLM and experimental data. The trends are similar although the absolute values are significantly offset ……44

2-23. Comparison of aerodynamic center changes with configuration for VLM and experimental data. The trends are similar but the absolute values are offset……44

3-1. Overview of MORPHEUS internal design structure UPPER VIEW Isometric...……47

3-2. Overview of MORPHEUS internal design structure LOWER VIEW Isometric…….48

3-3. Process Diagram illustrating MORPHEUS system organization. Command signals are transmitted through the embedded computer through transducers and out to the pertinent drive systems and actuators. ……50

3-4. Body-axis load distributions……...51

3-5. Assumed elliptic load distribution for strength analysis and span-wise location of mean load value……...52

3-6. Hybrid Fuselage Structure and Assumed Load State for ANSYS analysis. The primary loads are forces and moments from the wing and tail surfaces. The wing bending moment is supported by auxiliary devices……...53

3-7. Deformation of Acrylic Base Structure. The tail loads are supported directly by the base in induce significant deflection in the acrylic fuselage base design……53

3-8. Acrlyic Base AnsysAnalysis. There is a maximum deflection of 2.4 inches which would likely cause brittle failure in the structure……...54

3-9. Hybrid Composite/Aluminum Base Load Analysis. The maximum deflection is reduced to 0.16 inches. There is a significant reduction in the stress distribution around the sweep paths……54

3-10. Top View of Fuselage Base Layout. The overall component layout is shifted forward to create a weight distribution that assists in stabilizing the vehicle about the mount point……..55

3-11. Antagonistic turnbuckle arrangement above and below the fuselage base. The turnbuckles support wing bending moments, relieving the base from supporting the additional loads. They also ensure that the wings remain level regardless of loading….57

3-12. Sliding Sweep Constraint. The aluminum bar is coated with a teflon sheet to slide smoothly along the bottom of the base. Pitch moments are transmitted to the base through the sliding block or sweep mechanism depending on the load direction……58

3-13. Load transfer points to internal structure. The effective point loading is determined from applying Castigliano's theorem to the elliptic load distribution in Figure 3-5…….59

3-14. Sliding support to maintain wing orientation and support wing bending loads during span extension. A titanium screw joins the load beam to the sliding support rod……..60

3-15. Static Response of fully-extended sliding twist constraint. The load condition includes the transmitted wing torque from applied twist and wing bending loads……..61

3-16. Underside of Fuselage Base Detailing Component Arrangement. The design illustrates an efficient use of space permit smooth functioning and integration of all systems……..62

3-17. Vehicle Planform Transition. The wings sweep back and contract as the tail performs lateral extension and longitudinal contraction. The loiter and dash configuration become completely separate vehicles……..63

3-18. Tail Lateral Extension Mechanism and contraction of 'false-front' into wing body. The false-front contraction rate is governed by a manual flow control valve at the input to the solenoid……..64

3-19. Compliant Wing Cross-Section View. The molded inset shape was designed specifically to slide over the internal wing structure during span extension…….....66

3-20. Deformation of compliant wing cross-section from pressure loading on the internal cavity. Internal pressure build-up is from flow into fuselage openings. Significant deformation occurs without accounting for the additional external loading……66

3-21. Compliant wing with custom aluminum inserts for normal load support. The inserts cause a weight penalty but are required for twist actuation in the wind tunnel..67

3-22. Structural analysis of 2D compliant airfoil section with both internal and external pressure loading. The analysis ignores the integral skin structure which increases structural stiffness……68

3-23. Twisting the Compliant Wings. A smooth contour is achieved by combining the internal twist mechanism and the complaint external structure……..69

3-24. EPC Unit One. The top board is a DC/DC converter to clean the source power. Picture B shows the output ports from the valve board connected to the proportional

flow valves. Picture C displays the actual valve board which protects and routes data to the valves……..70

3-25. EPC Unit Two: Motor Control Unit. Two independent units are combined to independently control each sweep actuator. The unit is designed to control motor velocity in response to an analog command signal……71

3-26. EPC Unit Three: Analog Feedback Unit. The appropriate signal conditioning is embedded on the board for all of the analog inputs……...71

3-27. System Power Schematic. Dashed lines indicate devices that require intermittent power draw. The continuous load is approximated by the duty cycle of the actuator….72

3-28. Pneumatic Actuation Schematic. The nonlinear dynamics corresponding to each subsystem is presented in Appendix C……73

3-29. Friction Response of pneumatic cylinder. Highlighted peaks correspond to initiation of motion and static friction value. A pressure differential has to generate approximately 1.4 lbs of force before the unloaded cylinder rod moves……74

3-30. Controlled pneumatic response to proportional gain. High gain values cause 'stair-step' position tracking with an oscillatory velocity response……...75

3-31. Controlled pneumatic response to proportional gain. Low gain values experience a smooth motion but a significant response delay……76

3-32. Illustration of stair-step position tracking. In between steps the cylinder velocity stops until enough pressure builds up to overcome the static friction. Note that the command signal still is not achieved so the control gain is not large enough……76

3-33. Position and velocity tracking with tuned control law. Feedforward control allows almost perfect tracking but is not robust. Note that the delay in the velocity response is due in part to lag produced by the applied noise filter…….77

3-34. Direct-drive sweep geometry. The figure illustrates the actual vehicle system and the corresponding linkage model describing the nonlinear transcendental relationship between linear actuator contraction and wing sweep angle…….79

3-35. Relation between linear velocity of extension actuator and resulting sweep rate. The minimum value indicates the maximum constant-rate input signal……...80

3-36. Resulting linear extension command signal for constant rate sweep increase. Precise tracking of the deceleration signal is required because of the sensitivity of the sweep response at significant orientation……80

3-37. Tracking of ramped sweep reference signal. The bounded integrator ensures precise tracking of the decelerating linear extension command……...81

4.1. The three morphing aircraft in loiter-dash transition illustrating the qualitative differences in the geometry variations……..86

4.2. Three-dimensional solid models for computing wetted area of P1 and P2 APVE models. The addition of the tail structure causes an wetted area penalty on MORPHEUS which will increase profile drag……88

4.3. N-MAS fuselage perimeter plot and polynomial-fit integrated to approximate the wetted area. The integrated value yields a lower result than the 2-D approximation presented by Raymer that only considers profile views……....88

4.4. Half-span and full planform views of a wing planform demonstrating geometric reference parameters for multi-segmented vehicles. Computing parameters for segmented planforms requires repeated application of the integrals in (4.2) and (4.3)…89

4.5. Two-dimensional Airfoil Drag Characteristics for APVE modified airfoil and conventional airfoil sections. The wing thickness modification reduced the lift curve slope but increased the stall angle to permit similar maximum lift values…….91

4.6. Interpolating APVE fuselage for equivalent airfoil parameters……94

4.7. Tip-aligned and Stream-aligned airfoil sections for MORPHEUS dash. Wing sweep causes in increase in the effective chord which decreases the thickness ratio, creating a more efficient wing profile for dash……..95

4.8. XFOIL output of Viscous Flow Characteristics of Dash airfoil section. The thinner effective wing profile has an improved drag characteristic……..95

4.9. Viscous Flow Characteristics of Dash airfoil section comparing lift and drag to a standard NACA 0012 airfoil, the NACA 0020-64 airfoil of MORPHEUS-loiter, and an equivalent NACA 0016-64 airfoil……...96

4.10. Induced Drag and 'drag-due-to-lift' factor computed with TORNADO for dash and loiter configurations. The reduced span of the MORPHEUS dash configuration causes a significant increase in the induced drag factor……99

4.11. Nominal reference geometries used to normalize aerodynamic forces and moments to a constant planform for various morphing conditions……101

5.1. Induced Drag and Aerodynamic Efficiency of APVE P1 loiter model for various washout values. With the optimal twist distribution the minimum drag is maintained over all flight conditions……...115

5.2. Boundary Condition Assignment for VLM Collocation Points when combining variable twist with wing pivot. The image on the right shows the reassignment from equations (5.17)-(5.18) applied to enforce the correct boundary slope……..117

5.3. Parameter definitions for the classic stability equations presented by Etkin. All parameters are globally referenced to the nominal wing apex and are nondimensionalized by the reference mean aerodynamic chord……...124

5.4. Fuselage segmentation for computing pitching moment parameters. The first segment consists of upwash from (5.45). The intermediate and final segments are a linear function of the VLM derived downwash value……128

5.5. Aircraft Lift Curve Slope Variation with Planform State…….132

5.6. Aircraft Aerodynamic Center Shift with Planform State…….132

5.7. Variation in Aircraft Lift Sensitivity to Twist with Planform State……133

5.8. Variation in Aircraft Pitch Sensitivity to Twist with Planform State.…….134

5.9. Variation in Optimal Twist Distribution with Planform State……135

5.10. Minimum Drag Angle-of-Attack Trim Response……136

5.11. Minimum Drag Trimming Tail Incidence……136

Nomenclature

Chapter 2

u_o – initial sweep actuator length

δu – linear displacement of sweep actuator

ϕ_o – initial reference angle for sweep drive linkage

$\delta\phi$ – change in reference angle equal to sweep displacement

$r_{ac\ (bc)}$ – long (short) linkage length for sweep unit

$\vec{dl}$ -- vortex filament

$\vec{dV}$ -- velocity vector induced by vortex filament at collocation point

$\vec{r}$ -- position vector from midpoint of vortex filament to collocation point

r – distance from vortex filament to collocation point

Γ -- vortex filament circulation strength

U_∞ -- freestream velcocity

α -- angle of attack

C_{ij} – aerodynamic influence coefficient

L – total lift of horseshoe vortex system

ρ_∞ -- freestream air density

Γ_i -- circulation strength of *ith* horseshoe vortex

Δy_i – width of bound vortex in horseshoe element

r_i – distance from bound vortex filament to moment reference point

M – total pitching moment of horseshoe vortex system about reference point

Δb – percentage of maximum span extension

$\Delta\Lambda$ – percentage of maximum sweep extension

Δt – percentage of maximum tail boom extension

Λ -- true wing sweep value

S_{ref} – reference area for normalizing aerodynamic coefficients

c_{ref} – reference chord length for normalizing aerodynamic coefficients

x_{ref} – distance of moment reference point behind fuselage apex

$C_{L\alpha}$ -- aircraft lift curve slope

$C_{M\alpha}$ -- aircraft pitch stiffness

$x_{a.c.}$ – aerodynamic center measured from fuselage apex

Chapter 3

C_L – lift coefficient

C_D – drag coefficient

C_c – body-axis force coefficient

C_N – normal load coefficient

b – wingspan

W – aircraft weight

x, $\dot{x}$, $\ddot{x}$ -- cylinder rod extension, velocity, and acceleration

m – cylinder drive load

$A_{a/b}$ – piston area in chamber A/B

$P_{a/b}$ – pressure in chamber A/B

F_f – columb pneumatic cylinder friction

b – viscous pneumatic cylinder friction

$u_s(t)$ – span trajectory command

$\Lambda(t)$ – sweep trajectory command

$u_{ta}(t)$ – tail trajectory command

$\left|u_s^*\right|$ -- span displacement magnitude

$\left|\Lambda^*\right|$ -- sweep displacement magnitude

$\left|u_{ta}^*\right|$ -- tail displacement magnitude

τ_f – commanded vehicle transition time

$\left|r^*\right|$ -- vehicle drive command magnitude

$\Phi(t-\tau)$ – Heaviside step function

Chapter 4

S_{wet} – aircraft wetted area

$\bar{c}$ -- mean aerodynamic chord of reference wing area (MAC)

x_{mac} – distance of mean aerodynamic chord aft of wing apex

C_{Do} – parasite drag

C_f – skin friction parasite drag contribution

l – characteristic component length

R – local Reynolds number

FF – form-factor parasite drag contribution

t/c – airfoil thickness ratio

x/c – location of maximum airfoil thickness from leading edge

f – fineness ratio

Λ_m – sweep line corresponding to maximum thickness

LP – leakage drag contribution

K – drag-due-to-lift factor

L/D –lift to drag ratio

h – nondimensional moment reference location aft of MAC

h_n – nondimensional mean aerodynamic center location aft of MAC

K_n – static margin relative to reference moment location

C_{lp} – roll damping parameter

Chapter 5

e – Oswalds efficiency factor

$\Gamma(\phi)$ – circulation distribution across wing

$c(\phi)$ – chord distribution across wing

$\theta(\phi)$ – total orientation of 2D section relative to freestream

$\varphi(\phi)$ – wing twist distribution

$a_o(\phi)$ – 2D lift curve slope distribution across wing

C_{Dv} – induced drag coefficient

δ -- drag addition

$\underline{\Theta}$– twist distribution vector across horseshoe lattice structure

Δp – instantaneous planform state

γ -- nondimensional circulation distribution

J_{aug} – drag addition system cost

$N\left(p(t), w(t)\right)$ –aerodynamic function of planform and aerodynamic state

$\tilde{p}(t)$ -- planform state deviation

$\tilde{w}(t)$ -- aerodynamic state deviation

$p_o(t)$ – nominal planform trajectory

C_M – pitching moment coefficient

C_{Mo} – pitching moment coefficient at zero angle-of-attack

C_{Mq} – damping-in-pitch

α_o – equilibrium angle of attack

S_T – tail reference area

$C_{L\varphi w/t}$ – sensitivity of wing/tail lift coefficient to wing twist

$C_{M\varphi w/t}$ – sensitivity of wing/tail pitching moment coefficient to wing twist

G_{ij} –component of influence coefficient matrix inverse

V_{ij} – induced velocity influence coefficient due to trailing vortices

$w_{w/t}$ – downwash on wing/tail

$\varepsilon_{\alpha/\varphi}$ --tail downwash angle due angle of attack/wing twist

α_{wb} – wing-body angle of attack

K_{wf} – fuselage interference factor on wing lift

η -- dynamic pressure ratio at horizontal tail

i_t – horizontal tail incidence angle

V_H – horizontal tail volume ratio

C_{Mof} – fuselage pitching moment at zero angle of attack

dh_{nf} – shift in aerodynamic center due to fuselage effects

$h_{nw/t}$ – nondimensional aerodynamic center of wing/tail relative to apex of MAC

$\bar{q}$ -- dynamic pressure

C_{Lit} – lift coefficient sensitivity to horizontal tail incidence

C_{Mit} – pitching moment coefficient sensitivity to horizontal tail incidence

$\Omega(\Delta p)$ -- optimal twist ratio as a function of wing shape changes

Chapter 1
Morphing Research and the APVE Model

1.1 Motivation

Morphing is a frequently used description for adaptive vehicle systems that change shape in some novel manner to improve performance. For aircraft, we associate the notion of a 'novel' shape change with some enhanced function beyond control surface hinges, extravagant wing flap systems, and swing-wing geometries which are standard configuration options. The goal of morphing is to emulate nature in our engineered vehicles, to enable highly adaptive and fluidic motions with maximum configuration freedom for optimal performance. The concept of morphing aircraft actually began with the Wright Brother's first powered aircraft flight. In order to control the vehicle, the pilot shifted his hips, which in turn actuated tendons that twisted the wings [Hallenberg, 2004]. This concept of 'wing-warping' was abandoned to make way for the conventional hinged control surfaces in use today. The Department of Defense has used swing-wing aircraft since the 1950's and extending flaps are employed on many commercial airlines to increase lift and reduce the required takeoff/landing speeds. Only in the past 10 yrs has there been a major push by researchers to develop true morphing aircraft that go beyond these conventional motions to create vehicles with bird-like configuration ability.

There are numerous challenges involved with designing vehicles that can deform readily in flight while supporting aerodynamic loads. In general, morphing vehicles require actuators with extremely high power density along with wing surfaces that can shift from high to low stiffness in addition to having substantial recoverable strain. The balance required is "stiff enough to carry the load, flexible enough to morph". Researchers are making advances in smart structures, material science, and novel mechanisms to achieve high rate responses useful for flight control [Bartley-Cho, 2002].

Morphing is a new realm of flight science and requires a new approach in terms of analysis and design to take full advantage of new capabilities. One can imagine the active changes in aerodynamic and geometric states and the difficulty this poses with regard to flight control design and stability analysis. Current design methods are defined for rigid airframes, or at most 'slowly-varying' structures. A generally accepted notion is to apply analysis and control methods for static aircraft structures to morphing vehicles. This limits the notion of morphing to a collection of individual planform shapes connected through some scheduling parameter. While this method simplifies stability analysis and control design, it limits the flexibility and potential that arise from viewing the aircraft as a continuous dynamic system. It will be necessary to adapt new stability analysis techniques which can evolve to asymptotic control methods to fully exploit the potential of wing morphing.

At Virginia Tech, we are exploring experimental methods to perform the appropriate modeling and gain insight into developing new aerodynamic representations and control methods. In addition to theoretical development, an experimental platform is a useful tool to verify results and expose issues that are not captured in physical modeling. A unique testbed capable of numerous morphing shapes, precise planform positioning and rate control, and high load testing has been developed for this experimentation. This document overviews the design, development, and preliminary aerodynamic analysis of this testbed: an experimental morphing vehicle intended for aerodynamic modeling and flight control experimentation.

1.2 The APVE Model

The adaptive planform vehicle experiment (APVE) is a wind-tunnel scale flight model designed for low-speed (Mach < 0.2) load testing in the Virginia Tech Stability Tunnel. The APVE serves as a testbed for developing static and dynamic functions of morphing aerodynamics. Static modeling is an application of the classical approach and entails measuring quasi-steady aerodynamic derivatives at various planform configurations. Dynamic modeling is an extension to involve transient aerodynamics during morphing motions, not limiting the analysis to a set of fixed configurations. The

APVE is also intended for simulated flight control in the wind tunnel to evaluate stabilizing control algorithms during planform transition and to involve active planform maneuvering. APVE is a general term that corresponds to the two experimental designs which will be discussed, the Phase One APVE design and the revamped Phase Two model: MORPHEUS.

MORPHEUS is capable of planform morphing for mission adaptation, and control morphing for vehicle maneuvering. Planform variations include major changes in wingspan, sweep, and tail configuration such that the aspect ratio, planform area, and static margin are significantly modified. Control morphing refers to smaller motions that alter lesser portions of the flowfield to maneuver without significantly affecting the aircraft dynamics. On the current APVE model this consists of independent wing twist, which replaces elevons on conventional vehicles. Combinations of planform and control morphing can be used to study advanced maneuvering capabilities, e.g. using a combination of wing twist and asymmetric wing extension for efficient roll control. The APVE is displayed in Figure 1 in loiter, dash, and asymmetric maneuvering profiles. Wing twist is displayed as an elevon-style control in the maneuvering profile.

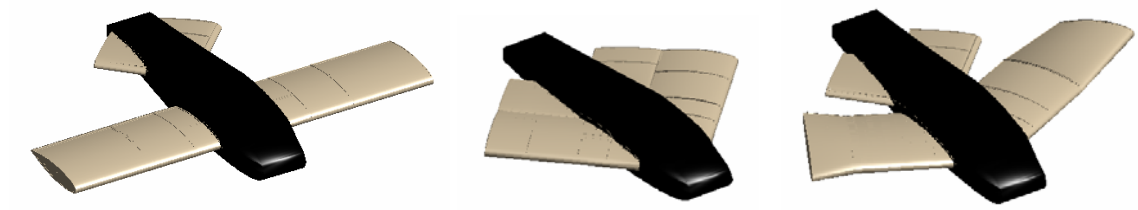

Figure 1-1. The APVE Model in loiter, dash and asymmetric maneuvering. The maneuvering profile also demonstrates wing twist. These are three of the many possible vehicle configurations.

1.3 Morphing Aircraft Research Programs

Specifically, morphing aircraft are vehicles that utilize adaptive geometry to enable enhanced flight capability over multiple mission profiles. Adaptive geometry is intended to create flight vehicles that behave similar to birds and are capable of efficient

performance over a global flight envelope. A common illustration is a hovering bird of prey at an efficient high-speed cruise that folds its wings in and dives for prey. This is the familiar 'loiter-attack' mission which set the background for developing the morphing program.

Configuration changes can be defined in terms of their effect on the vehicle performance. Varying the overall planform characteristic is termed mission morphing because it changes the base dynamics of the plant to optimize for different flight regimes. Mission, or planform, morphing can be further subdivided into in-plane and out-of-plane morphing. In-plane planform morphing might consist of some novel combination of variable sweep, wing span, and chord length. Out-of-plane planform morphing consists of motions that change the effective wing dihedral like wing folding.

Aircraft that utilize unique control effectors like variable twist or camber to replace traditional control surfaces, like elevons, are also classified as morphing vehicles. These aerodynamically efficient controls generate favorable pressure gradients that reduce drag and delay separation. The term 'control morphing' refers to smooth contour changes in the wing cross-section to enable efficient, high authority maneuvers. These continuous profile changes replace the geometric discontinuities of ailerons and elevators to approximate a more fluidic actuation like a bird or fish.

1.3.1 Variable Geometry Aircraft in the Department of Defense

The Department of Defense has used variable geometry vehicles in the past to enable performance at different flight regimes: the F-111 and the more maneuverable F-14. The F-111 was developed as a large, powerful, fighter/bomber that operated in combat with variable sweep capability. Take-off, landing, and loiter were done at sweep angles of less than 16 degrees. The decreased sweep angle also enabled low-speed landing on aircraft carriers. The moderate sweep angle of 35 degrees gave a high ratio of lift to drag for an efficient high-speed, subsonic, cruise. The extreme sweep angle of 70 plus degrees was used to delay transonic drag rise during a supersonic dash [Curry, 2004].

The bomber was adapted in the 1980's and fitted with a Mission Adaptive Wing designed by Boeing Aircraft Company [Thornborough, 1993]. The wing used internal

mechanisms that flexed the outer wing skin to produce variable camber for different flight regimes. Camber was used in subsonic speeds, a supercritical airfoil was formed for transonic speeds, and a symmetric section was produced for supersonic speeds. Unique contributions of the program included flexible wing skins and a digital control system to automatically adjust the camber for the different flight phases. Flight test data showed significant drag reduction at the designed cruise point and off-design conditions.

The F-14 was a lighter, more agile vehicle designed for air-to-air combat. Wing sweep was used to reduce the aspect ratio, which in turn increased maneuverability by reducing the inertia about the roll axis and decreasing the aerodynamic damping. By effectively shortening the wings, the vehicle could also withstand higher acceleration loads during maneuvering. The F-14 sweep schedule was automatically tuned to correspond to the flight condition. Both aircraft were multi-mission vehicles that consisted of slow deviations from the nominal state to accommodate a particular mission. They did not incorporate dynamic shape realignment to optimize maneuvering and mission performance. In addition, both of these vehicles demonstrated non-reactive configuration control that is programmed a priori. Biological systems would use inferences from sensor arrays to adjust the system which is a potential enhancement with morphing technology [Seigler, 2005].

1.3.2 Morphing Aircraft Research Programs in the Depart of Defense

The goal of the Active Aeroelastic Wing Program (AAW) was to develop and validate using wing twist roll-control by adapting the wings on a conventional fighter aircraft [Curry, 2005]. An F/A-18A was modified such that ailerons and leading edge flaps could manipulate the aerodynamic loads to twist the wings as opposed to developing actuators to overcome the combined structural and aerodynamic stiffness. The standard wing structure was also modified for increased compliance to assist the morphing. Flight tests demonstrated that the AAW vehicle was able to achieve roll rates within 15 to 20-percent of those achieved by a conventional F/A-18 at transonic and supersonic flight speeds. The modified vehicle achieved this performance without the addition of differential rolling horizontal tails which assist in roll maneuvering on the

standard F/A-18. The major problem with aeroelastic control is the dependence on the aerodynamic loads to achieve performance. Essentially, the system controllability is a direct function of the states being controlled which can ultimately limit performance.

The precursor to the current morphing initiative was the Smart Wing Program [Kudva, 1999]. The program was aimed at using intelligent actuators to enable hingeless, high rate control surfaces on the wing and compare the aerodynamic performance to conventional control surfaces. During Phase II of the Smart Wing Program, Northrop Gruman (NGC) developed a 30-percent scale, full-span model of the NGC Uninhabited Combat Air Vehicle for wind tunnel testing [Martin, 2004]. Opposing wings were fit with conventional elevons and smoothly contoured SMA-actuated leading and trailing edge control surfaces. In a second test researchers examined smoothly contoured surfaces powered by piezoelectric motors which enabled higher control surface rates. Testing showed a significant improvement in rolling moment authority with morphing control surfaces.

The Morphing Aircraft Structures (MAS) Program initiated by the Defense Advanced Research Projects Agency (DARPA) envisions a "*seamless, aerodynamically efficient, aerial vehicle capable of radical shape change*". Some general adaptive capabilities envisioned for a next generation morphing UAV include: (1) a 200 percent change in aspect ratio, (2) a 50 percent change in wing area, (3) a 5° change in wing twist, and (4) a 20° change in wing sweep [Wlezien, 1998]. There has been an evolution in the desired control capabilities of morphing wings to take advantage of large-scale planform changes for flight control. The short-term goal of the MAS program is a wind tunnel test of a flight traceable morphing model that exceeds the given specifications.

The current industrial competitors in the MAS program are NextGen Aeronautics and Lockheed Martin. NextGen Aeronautics has developed a 'bat-wing' concept that consists of in-plane wing folding to achieve specific planform geometries based on the instantaneous mission requirements (e.g. cruise, loiter, etc.). A single wing is capable of achieving of nearly optimum wing shapes for each mission segment. A half-wing of the vehicle can vary by over 50-percent in area, 38-percent in half-span, and 110-percent in aspect ratio. Distributed internal actuation of a 2-degree of freedom (DOF) kinematic mechanism is used to change the shape of the wing to generate each of

the configurations. Figure 1-2 details the Next-Generation Morphing Aircraft Structure (N-MAS) concept and three approximate design configurations.

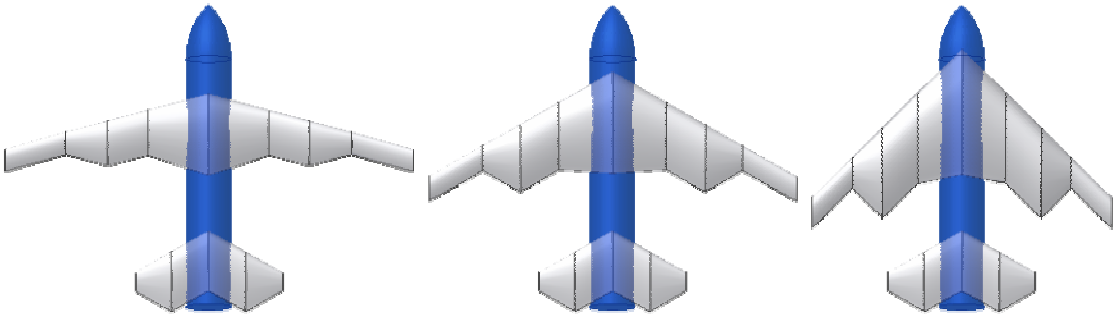

Figure 1-2. The N-MAS planform in high lift, cruise, and dash configurations. The sweep varies from 15 to 45-degrees and the half-span decreases from 10 to 7 feet.

Lockheed Martin (LM) has developed an out-of-plane folding wing concept that is primarily designed as a loiter-attack vehicle [Love, 2004]. This is a wing-adaptive version of the X-45A unmanned configuration that has the ability to maintain an efficient cruise followed by a defensive/offensive maneuvering state. As shown in Figure 1-3, there are two primary operation points and an intermediate configuration for control authority during landing. By folding the wings up against the fuselage, the aircraft is able to reduce its wing span by 100-percent and its planform area by 120-percent. This leads to a total aspect ratio change of approximately 100-percent. The wing folding is powered by a torque control device which introduces a geometric constraint to keep the outboard wing level, as the inboard wing folds up against the fuselage. It is also possible to use the airloads to assist in raising the wings to reduce system power requirements.

Both the N-MAS and LM-folding vehicles use conventional flaps for maneuvering and only take advantage of planform morphing. The LM vehicle and the F-14 Tomcat differ only in their plane of sweep. The challenges in terms of control effectiveness changes, center of gravity (c.g.) shifts, and gain-scheduling are similar. The N-MAS has five different operating configurations to allow the vehicle to meet performance specifications over a wider flight envelope and for different maneuvering situations. It is a unique concept that introduces totally new challenges for aircraft stability and control. Both vehicles have the potential to use asymmetric planform morphing for maneuvering.

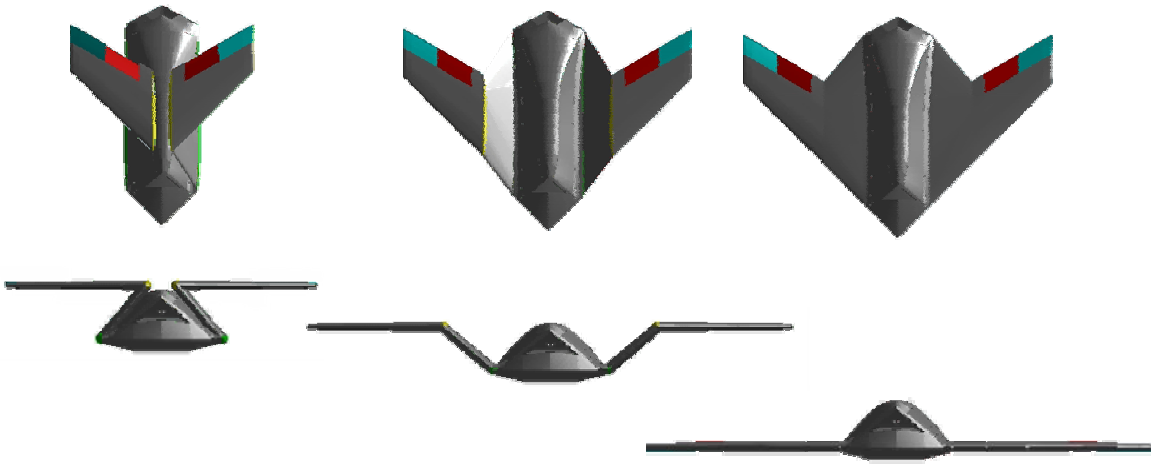

Figure 1-3. The Lockheed Martin folding-wing configuration. The extended position is for loiter, the wings fold 130-degrees into the fuselage to form a highly maneuverable dash configuration.

1.3.3 Morphing Research in Academia

Morphing research in academia began at only a few institutions connected with DARPA programs but has significantly expanded. Radically shape changing aircraft is a raw area of research with many mainstream tasks unanswered such as aerodynamic modeling, dynamic stabilization, and vehicle control.

Roth (2002) and Frommer (2005) have pursued theoretical optimization techniques to determine a desired set of wing planform shapes for a morphing aircraft. They applied Raymers 'big six' aircraft parameters: wing loading, thrust-to-weight ratio, thickness ratio, taper ratio, wing sweep, and aspect ratio [Raymer, 2001] and considered morphing as an independent variable in varying these design features. Holding the thrust-to-weight ratio constant, the other parameters were optimized for a various mission profiles to determine a desired set of achievable planform shapes for a morphing aircraft.

A major thrust of academic morphing research is design and test programs of small-scale models that incorporate some type of morphing variation. At the University of Maryland, Blondeau (2003, 2004) designed, built, and tested a morphing wing that changed aspect ratio using a pneumatic telescoping spar. The design incorporated sliding skins as the spar telescoped into three sections, increasing the total wing span

from 33-inches, to 54-inches, to 76-inches. The corresponding aspect ratios changed from 2.54 to 5.85. Wind-tunnel analysis verified large increases in the maximum lift to drag (L/D) ratios. The vehicle was limited in only having three possible configurations with no continuous control capability.

A variable sweep model was also tested at UMD by Marmier (2003). The model was capable of three sweep configurations (0, 30, and 45-degrees). Sweep was varied symmetrically by a pneumatic actuator/linkage device. Wind tunnel testing again confirmed theoretical expectations that the lift curve slope decreased with sweep but the swept wings also stalled later and could achieve a higher maximum lift. While the design of each of these vehicles demonstrates feasibility, neither is novel in it capabilities to extend the current knowledge of morphing aircraft or to develop new analysis techniques.

At the Univeristy of Manchester, analysis and testing has been done of changing the internal structure of the wing to enable aeroelastic tailoring for wing morphing [Amprikidis, 2005]. Specifically, by changing the flexural and torsional stiffness of internal structural elements, they are able to exploit aeroelastic effects to control wing twist and bending. The only difference from the AAW program is that the effective torsional stiffness is adapted as opposed to increasing the local external load with wing flaps. The two designs tested involved 1) rotating internal spars to change torsional stiffness and 2) shifting the chordwise location of internal spars to change flexural stiffness. Once the internal stiffness was changed the external aerodynamic loads were capable of twisting and bending the wing. The drawback of this approach is the lack of control in the direction and rate of morphing. For multi-mission control this could be feasible but bandwidth limitations could be significant when shifting the internal structure for the purpose of maneuvering.

At the Penn State, researchers are exploring compliant trusses actuated by tendons to permit large shape changes under load [Ramrkahyani, 2004]. The goal of the project is to present a mechanism for morphing the Hyper-Elliptic Cambered Span (HECS) aircraft. The concept uses octahedral unit cells supported by antagonistic cables to morph the vehicle. Skin design issues have not been solved and the models have not been tested under load.

Most recently, researchers at West Virginia University have wind-tunnel tested a swept, tailless UAV with twisting outer wing sections [Guiler, 2005]. Their final model consisted of a segmented outer wing section that was twisted by a torque rod connected to the tip rib. A latex sheet was used as a flexible skin over the segmented section to reduce the required actuator power to morph. Wind tunnel testing at cruise speeds identified an almost 15-percent increase in L/D for the twisting wing over an identical planform equipped with elevons. In generating control moments for maneuvering, the morphing wing sections generated less drag for a given moment although the absolute moment coefficients were less for the twisting wings.

Research in extending morphing to lightweight aircraft structures includes the micro-air-vehicle (MAV) program at the University of Florida and the inflatable wing program at ILC Dover and the University of Kentucky. The MAV program used rods and tendons to fold and twist the membrane wings [Abdulrahim, 2004]. The folding is out-of-plane and results in spanwise wing shapes similar to the HECS wing. Flight testing demonstrated that the combination of curling and twisting the wing produced high control authority for maneuvering. The inflatable wing program used piezoelectric actuators to deform the trailing edge of the inflatable wing structures but was not flight tested [Cadogan, 2004]. Both of these programs took advantage of having extremely compliant and lightweight wings that were easy to deform with relatively low force output. The morphing concepts developed in these two programs are not easily transferred to vehicles that have to perform under high-g loading but are useful for smaller reconnaissance vehicles.

Recently, control design methods accounting for quasi-steady morphing changes have been investigated. Valasek has implemented reinforcement learning with artificial intelligence to determine and achieve optimal wing shapes while pursuing a flight trajectory [Valasek, 2004]. The AI optimization was applied to an ideal surface that was simply a variable geometry block but demonstrated a method of learning control for morphing that is a step closer to what is accomplished in biological systems. Boothe modeled a morphing aircraft in several configurations accounting for the influence of planform inputs in the state dynamics [Boothe, 2005]. A linear input-varying framework is described in which the state matrix varies with the control input and can be stabilized

with the appropriate choice of planform input. The stability proofs assume an affine influence of planform variation on the state matrix which is an idealized assumption and cannot be extended to general morphing system.

1.3.4 Morphing Research at Virginia Tech

Morphing research at Virginia Tech began with aeroelastic modeling of Delta wing configurations with adaptive airfoil sections. Gern (2002a) used equivalent plate modeling to study the static performance of built up wing structures that included skins, spars, and ribs. Aerodynamic loads were computed using a three-dimensional Vortex Lattice code. The model was used to analyze the aeroelastic response of an aircraft comprised of morphing rib sections that changed camber and twisted. One of the contributions of the work was identifying the improved roll performance and roll reversal speed of hingeless control surfaces over conventional effectors. Gern (2002b) later used the model to determine power requirements of general distributed actuation against the wing structure and the aerodynamic loads.

Pettit (2001) produced Virginia Tech's first work on dynamic modeling and control of morphing aircraft. He created a novel combination of 2-dimensional conformal mapping with 3-dimensional VLM aerodynamics to generate real-time load information for a morphing wing as it changed camber and twist. He integrated this into a rigid-body dynamics model and was able to simulate flight path tracking using regulator control to determine the required morphing control inputs. He also computed the real-time work output required for morphing against the instantaneous loading. Pettit generated the first simulation of what a morphing wing might look like as it deformed to generate control moments for trajectory tracking.

Morphing research at VT was expanded to developing analytical energy functions to gain insight into the potential of using morphing to for partial energy recovery during flight [Johnston, 2003]. Neal defined a new NACA camber line that included an extra degree of freedom for reflex change. Johnston used the new camberline to develop analytical aerodynamic energy functions based on 3-dimensional VLM analysis. Lagrange multipliers were used to solve for minimum energy control deflections based on meeting predefined lift and moment constraints.

Johnston (2004) extended the energy studies to compute transient aerodynamic work requirements in changing camber to achieve a change in lift. He developed 2-dimensional unsteady analytical functions to compare the energy requirements for a conformal surface and a conventional surface while changing shape. He demonstrated that a conformal surface required less work than a conventional surface. He also showed that the relative energy of a variable camber wing was sensitive to actuator placement and could not be defined in a general manner.

Neal (2005) examined flight simulation and morphing control allocation based on intelligent control methods. He developed a morphing aerodynamic model using a three-dimensional Vortex Lattice code that used the new, 2-DOF camberlines. The time-cost for computing the solution to the full vortex lattice is prohibitive in real-time simulation so a neural network was developed as an input-output nonlinear map of the morphing aerodynamics. He then used the aerodynamic outputs from the network to drive Pettit's dynamic simulation model. Linear quadratic regulator control was used with rigid body dynamics to determine the required aerodynamic loading to track a given trajectory and orientation. A fuzzy-logic control allocation was developed with a rule set to use the highest control authority effector (twist, camber, or reflex) to meet the specific lift and moment requirements output from the regulator.

Current research investigates planform morphing for multi-mission flight roles. Researchers at NASA Langley developed the Hyper-Elliptic Cambered Span (HECS) wing as a morphing concept because testing demonstrated an L/D increase of 15-percent over other planar, elliptical wings [Davidson, 2003]. As demonstrated in Figure 1.4, the HECS wing develops a smoothly contoured dihedral increase toward the tip and is can be used as an effector for pitch, roll, and yaw control. At Virginia Tech, Wiggins (2004) developed an internal quaternary-binary link mechanism to meet specified wing shapes using a single degree of freedom. A complete design was performed that included considerations for the aerodynamic loading through a non-planar VLM code, and a finite element structural analysis.

Figure 1-4. The Hyper-Elliptic Cambered Span wing configuration. Hyper-elliptical describes both the planform layout and the wing fold shape when morphed.

In support of the Lockheed Martin MAS vehicle design, Neal (2004) performed Lagrangian-based dynamic modeling of the folding-wing and combined it with an aerodynamic model developed from Johnston's nonplanar VLM code. Changes in basic planform parameters, like the lift-curve slope and the pitch stiffness, along with changes in control effectiveness were fit to polynomial functions as they varied with the wing fold angle. Nonlinear sliding mode control and gain scheduled linear control were implemented to stabilize the aircraft through transition during trajectory tracking.

Bae and Seigler (2005) investigated a variable-span Tomahawk missile for roll maneuvering via asymmetric morphing in support of Raytheon Missle Systems. Bae developed an analytical function for the aerodynamic loading and stability derivative representation for asymmetric wing extensions. He performed a static aeroelastic analysis using MSC/Nastran and showed the decrease in divergence speed as the wingspan increased due to the increased wing flexibility. Seigler (2004) developed a control model by deriving the rigid-body dynamics and combining them with the analytical aerodynamic functions. He used sliding mode control to enable robust, flapless roll maneuvering through asymmetric wing extensions.

Seigler's work was expanded to develop novel dynamic architectures for general morphing aircraft structures [Seigler, 2006]. He used Gibb's equations to develop a time-varying model which treated an adaptive vehicle as separate elements of mass and

inertia with all momentum represented relative to a fixed coordinate system in the fuselage frame. Gibb's equations produced the same result as developing the equations using Lagrangian dynamics but in a much simpler derivation. Seigler also developed a time-invariant model with morphing as a feedback control. The model ignored inertia but was a simple method to produce tractable, analytical results for initial control design. Seigler (2005) also studied transition stability of a morphing planform with in-plane wing folding similar to the N-MAS design. An aerodynamic database was developed using DATCOM for two configurations and a gain-scheduled PI/lead-lag compensator was implemented to stabilize the vehicle for various transition rates. He determined that the controller was capable of stabilizing the vehicle, even at high transition rates, during trimmed flight. As the vehicle was commanded to maneuver while morphing, instabilities occurred from dynamic coupling between the aircraft modal response and the change in configuration parameters (mass distribution and aerodynamic loads). The work did not include effects from transient aerodynamics.

1.4 Justification for the APVE Model

In examining the previous research within the morphing community there are several key issues that lead to the need for a fully-adaptive aircraft configuration. In particular, most research programs are only examining single aspects of morphing. Their goals are to provide support in morphing aircraft development. The goal of the APVE model is the development of general stability analysis and control methodologies from considerations of the dynamic effects of morphing. Therefore a completely adaptive vehicle is required that incorporates smooth and extreme geometry changes quickly for aerodynamic modeling and control. The emphasis in the APVE design is not on using innovative materials or functions to morph, rather the goal is to enable high-rate wing shape changes under significant aerodynamic loading.

1.4.1 The Aerodynamics of Morphing Aircraft

The common thread in current morphing research is the absence of accurate aerodynamics. All of the aerodynamic modeling is based on linear theory applied in a

quasi-steady sense to a dynamic and possibly very nonlinear aerodynamic behavior. There have not been active investigations into the unsteady three-dimensional aerodynamics associated with morphing so there is no guide to determine the accuracy of the transitional aerodynamics. The primary computational aerodynamic tools for stability and control analysis are the Vortex Lattice method, and DATCOM.

Vortex Lattice is a numerical solution to a linear aerodynamic flow model [Bertin, 1998]. It involves breaking the wing into panels and applying Biot-Savart's law to determine the normal-velocity induced at a control point on each panel due to bound horseshoe vortices across the wing. Applying a boundary condition results in a square linear system that can be solved for the circulation strength of each of the bound vortices. Vortex Lattice has been shown to be accurate for determining general aerodynamic characteristics for discrete planform configurations at small aerodynamic angles. Morphing research at Tech has extended VLM to predict the aerodynamic loads at discrete configurations during planform morphing.

DATCOM is used in a similar manner to VLM. It is a compendium of data based on various wing geometries used to characterize the aerodynamics of rigid-aircraft [Hoak, 1978]. DATCOM is also limited in the configurations and control deflections it can consider to standard geometry changes. The Vortex Lattice Method and DATCOM both suffer in their inability to analyze time-varying systems in anything other than a quasi-steady state. Research has not been done to quantify the transition rates where the quasi-steady assumption becomes invalid.

Current assumptions are that in-flight morphing will be done 'slow-enough' so that transitional aerodynamics do not become an issue. In the future, morphing UCAV's will be high performance combat vehicles that will combine large-scale geometry changes with high-rate maneuvers. Assuming slow planform transition is not a long-term solution. It will be important to understand how the aerodynamic response changes for vehicles that undergo fast planform transitions with large-scale shape changes.

1.4.2 APVE Implementation

An optimal method to study the transitional aerodynamics of morphing aircraft during steady-state or slow maneuvers is wind-tunnel testing. The APVE permits aerodynamic characterization over a large range of aerodynamic angles for various static and dynamic configurations. Combining experimental results with computational tools, this vehicle will enable the development of general analytical models that account for transitional aerodynamics of morphing vehicles with differing geometries.

Another goal of the APVE research vehicle is to provide a testbed for morphing flight control experimentation. Flight control literature is bursting with articles on new control methodologies for better performance. There is rarely any justification of control methods outside of high-grade simulations. The APVE can be used for 'free-flight' testing in the wind tunnel to validate control law designs before application to flying models. The vehicle is capable of significant dynamic and aerodynamic changes which lends itself to control methods for time-varying plants such as nonlinear control, or adaptive and intelligent control.

Overall, the advancement of the APVE, specifically MORPHEUS, above all other academic morphing programs is 1) the combination of multiple morphing degrees of freedom, and 2) the ability to precisely control the morphing rate for transient aerodynamic experimentation and flight control testing.

1.5 Thesis Overview

This document will cover system design, development, and integration. First the Phase One design and wind tunnel test results will be described. The Phase One development formed the core of the vehicle design although significant enhancements were made in preparation for Phase Two testing. These modifications will be detailed in terms of external and internal design changes and in the actuation and control architecture. The theoretical aerodynamic performance of MORPHEUS is analyzed and compared to an industry morphing prototype and the Phase One APVE model. Finally an advanced modeling methodology is presented to obtain an improved model for control algorithm design.

Chapter 2
Phase One Design and Testing

2.1 Chapter Overview

The lack of experimental data for morphing aircraft structures motivated the design and construction of a variable geometry aircraft model for wind tunnel testing. Experimental analysis of a vehicle with an adaptive planform shape can provide the basis for new analytical developments in aerodynamic modeling. Significant to morphing aircraft is the issue of flight stability, specifically longitudinal stability changes while morphing. An experimental model provides the opportunity to investigate stabilizing an aircraft as it transitions through different planform configurations.

The development of the Phase One APVE model was an eight-month design and fabrication process that resulted in a wind-tunnel test of a morphing model. There were five independent planform changes along with independent twist control for each wing. Twist was not actually achieved during Phase One wind tunnel testing for lack of a sufficient compliant structure but the internal mechanism was designed and in place for future vehicle development. Wind tunnel testing was conducted in Virginia Tech's Stability tunnel to analyze the aerodynamic characteristics and evaluate the benefits of a UAV with multiple configuration capability. Lessons learned from the Phase One design served as the foundation for the MORPHEUS vehicle development.

2.2 Synopsis of the Adaptive Aircraft Configuration

Besides wind tunnel evaluation, a major effort of this work is in the design and construction of the adaptive aircraft model. The difficulty comes from coordinating and controlling a large number of actuators to obtain independent wing shape changes. Each

wing can increase span, vary sweep, and control positive or negative wing twist. In addition to these six shape changes, the tail boom can also contract and extend. This results in a 7-DOF experimental model.

The overall vehicle layout and configuration changes are pictured in Figure 2-1. Each wing can increase span from a nominal length of 17 inches to a maximum length of 24.5 inches, a 44-percent increase. The sweep of each wing can be varied between 0 and 40 degrees, while the internal wing twist actuator is controllable between ±20 degrees. Tail boom extension was intended as an independent mechanism to control the aerodynamic center location as the wing changes sweep and span. The nominal tail position is extended and can contract 6 inches which causes the overall fuselage chord length to decrease by 12%.

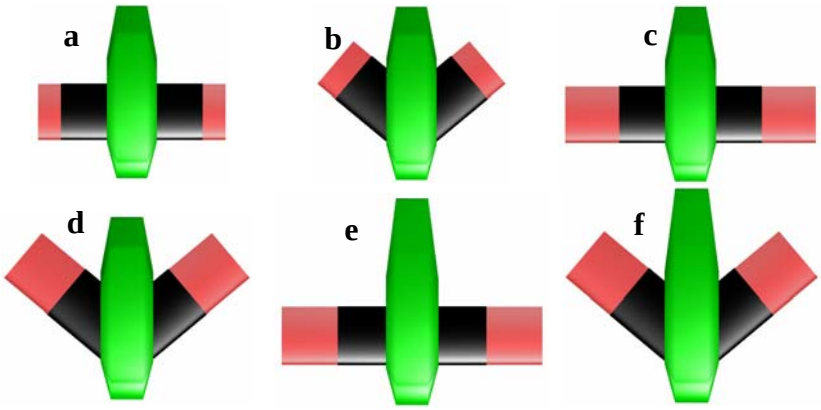

Figure 2-1. Various configurations of the adaptive aircraft model, a) Δb=0, t=0, Λ=0 b) Δb=0, t=0, Λ=100% c) Δb=100%, t=0, Λ=0 d) Δb=100%, t=0%, Λ=100% e) Δb=100%, t=100%, Λ=0 f) Δb=100%, t=100%, Λ=100%

The variables Δb, t, and Λ represent the respective span, tail, and sweep variations as a percentage of their maximum change. In combination, the wing shape changes cause large variations in the planform characteristic. Table 2-1 compares the geometry changes of the Phase One APVE model and the N-MAS design. It is evident that the percentage change in APVE parameters compares favorably with the N-MAS design. The drawback with the APVE model is that the large span changes are due to telescopic wing extension. Extending constant chord wings causes large planform area increase along with wing span increase which reduces the potential aspect ratio increase.

In the N-MAS design, the wing is able to increase span while decreasing wing area which causes much larger changes in the aspect ratio. Although the APVE model does not match up in terms of absolute performance metrics, Table 2-1 indicates that the percentage change in planform characteristics is enough to make the stability and control problems similar when morphing.

Table 2-1. Comparison of Phase One APVE and N-MAS planform geometries.

Parameters	Phase One APVE			N-MAS		
	Max	**Min**	**Δ (%)**	**Max**	**Min**	**Δ (%)**
One-Wing Area (sq. ft)	2.53	1.65	**53**	24.4	15.6	**56**
Half-Span (ft)	2.69	1.5	**79**	10	7.2	**38**
Aspect Ratio	3.44	1.28	**169**	11.8	4.3	**110**
Sweep	40	15	**166**	45	15	**200**

2.3 External Vehicle Design

Designing the external structure requires a compromise between aerodynamic function and creating space for internal actuators. The concept of morphing makes external design difficult because, in general, it is necessary to have a shell structure that supports the aerodynamic loads but is compliant enough for actuation. Because the goal of the APVE project is dynamic analysis, the external morphing design is simplified to rigid segments that move relative to one another. In its ultimate application, a morphing surface would be a continuous matrix that maintains an aerodynamically smooth shape with deformation.

The wing and fuselage cross-sections are both designed from modified NACA airfoil sections as seen in Figure 2-2. The wing airfoil sections are modified NACA 0020-64, and have a 14-inch chord. The 2-digit extension allows the leading edge radius (nominal value = 6) and maximum thickness location (nominal value = 3) to be modified in terms of percentage chord length. The modification shifts the maximum thickness closer to the center of the airfoil section to create space for internal twist actuators.

Twenty-percent is a relatively thick airfoil and would have significant drag consequences that increase for high-speed flight. For subsonic testing, airfoils up to twenty-percent thick have the potential to generate a higher maximum lift, so the relatively substantial thickness is actually beneficial for a wind tunnel model. The exact effect of the thicker airfoils on viscous drag is analyzed in the chapter on elementary aerodynamic analysis.

The fuselage design is an interpolation between two different airfoil sections. The mid-section of the fuselage is an extruded NACA 0017-64 with a chord length of 49 inches. On each end, the extruded section tapers down to a NACA 0020-65 with a 21 inch chord. The fuselage outboard airfoil shape creates enough space for the wings to sweep in without contacting the fuselage. This additional space is necessary because the wings sweep into the fuselage when they rotate about the pivots seen in Figure 2-2. Designing the fuselage as an airfoil (like a flying wing) streamlines the design, increasing the overall vehicle lift while decreasing drag. This too will be discussed in more detail in a subsequent aerodynamic analysis chapter.

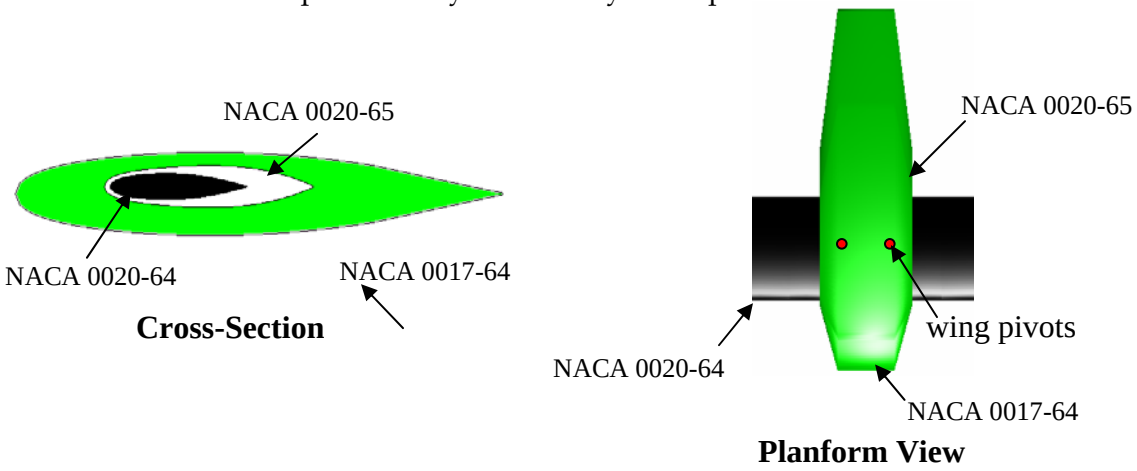

Figure 2-2. Vehicle cross-section and planform views detailing interpolated airfoil sections. Airfoil thickness was increased and shifted aft to permit an internal twist mechanism.

The fuselage and wings are constructed from fiberglass shells. Three-dimensional computer models are CNC-machined from foam and coated with fiberglass. The final parts are hollowed out and formed to rigidly attach to the internal structure.

The wing structure in Figure 2-1 is telescopic with a compliant semi-solid section (shown in red) that slides inside a rigid, hollow section (shown in black). Actuation mechanisms are placed inside the compliant section to twist the wing while the rigid-section acts as a zero-deflection boundary condition. The fiberglass shell for the hollow wings was therefore required to support not only the aerodynamic loads, but also to resist an internal torque from twisting the outer wing. The hollow wings were laid up with 1/8-inch thick fiberglass which was assumed rigid enough to resist the transmitted torque from the candidate complaint wing materials.

2.4 Internal Vehicle Design

The primary actuation system for the Phase One APVE vehicle is pneumatic. The span extension, tail boom extension, and wing twist are all driven by pneumatic actuators. The wing sweep is actuated with electromechanical lead-screw drives. Feedback control allows the model to operate at any point between the maximum and minimum ranges, permitting multiple symmetric configurations for static and dynamic testing. Because independent actuators are included for each morphing motion, the vehicle can achieve asymmetric planforms providing a limitless number of possible configurations. Controlling the vehicle requires embedded computing hardware, software, and interface methods to an external operator.

2.4.1 Internal Vehicle Design Overview

The model uses two rotational and five linear actuators to control the wing shape. Pneumatic actuators were chosen as the primary drive system because of its high power density which results in greater forces and velocities for a given weight. In addition, the weight benefit of pneumatics increases with stroke. Most of the initial weight penalty consists of flow valves and air supply units. As the stroke increases, these units are still applicable and the only weight increase is in actuator. An individual pneumatic cylinder consists of a solid rod and bearing sliding inside lightweight pressure vessels so that unit increases in cylinder stroke result in a small increase in total weight. For example, a 1.5-inch bore, 12-inch stroke pneumatic cylinder can be controlled at speeds as fast as 37.5 inches per second at a cylinder weight of 2-lbs and an

air pressure supply of 70-psi. The airflow control system normally consists of some type of solenoid valve resulting in a conservative estimate of 3-lbs for the entire system. At the same line pressure of 70-psi the static force output is approximately 120-lbs. Assuming an inverse correlation between velocity and load, the maximum power output is 3375 in-lbs/sec at half-load resulting in a power density of 1125 (in-lbs/sec)/lb with limitless duty cycle. A high end electromechanical of similar capability can produce speeds of up to 40 inches per second and a static load of 135 lbs resulting in a maximum power output of 4050 in-lbs/sec. The drawback is that to achieve this power output, the weight of the electromechanical system is 14.2 lbs; resulting in a power density of only 286 (in-lbs/sec)/lb for equivalent stroke and similar performance. In addition, the electromechanical actuator is almost two and a half times the cost of the pneumatic cylinder with a high-end solenoid valve. The tradeoff is that electromechanical actuators are very easy to control while the compressibility of the air and the nonlinear flow through the valve system makes precise pneumatic tracking systems difficult, but plausible. Therefore, we can use intelligence in control software design to incorporate a lighter and cheaper system capable of nearly equivalent performance.

To twist the wings, it was necessary to have a small actuator that generated enough torque to deform a semi-rigid wing section under aerodynamic loading. The primary size constraint was that the device had to remain within the wing cross section during actuation, and accomplish all of these tasks in a relatively light package. A small rotary pneumatic actuator was chosen to drive the twist mechanism because it could produce the high torques required at a low overall weight and dimension. A custom device was built to implement the actuator, amplify the output load through a gear train, and provide feedback for closed-loop twist control.

The sweep design requires that the actuator directly support the aerodynamic forces against the wing. A lead screw electromechanical actuator was chosen because it is non-backdrivable under load as opposed to the compressibility in a pneumatic cylinder. The complete internal model and actuator layout is shown in Figure 2-3. The different subsystems include flow controls, the span extension unit, the twist mechanism, the sweep system, tail actuation, and the PC/104 control circuit. Each subsystem will be described in detail in the ensuing sections.

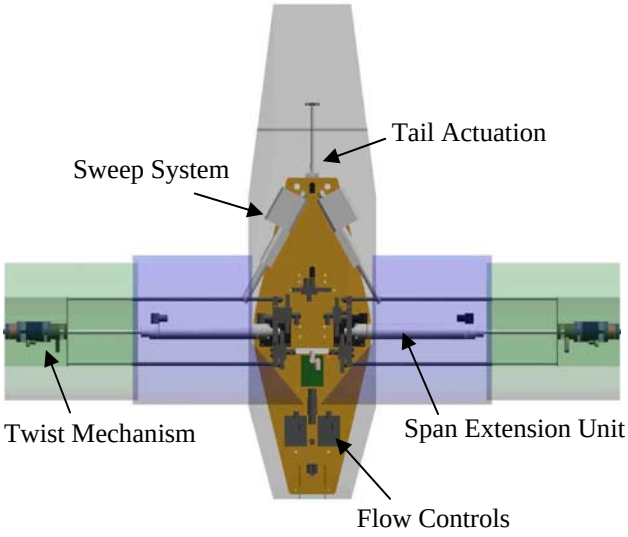

Figure 2-3. Overview of internal vehicle structure. The five primary subsystems in the Phase 1 design are the sweep system, the tail actuation, span extension unit, twist mechanism and flow control devices.

2.4.2 Flow Control Devices

Directional control valves are required to direct airflow to the pneumatic system. Each of the pneumatic mechanisms is double-acting as opposed to spring-return, so each actuator requires two flow inputs. A five-port solenoid valve and its flow path are shown in Figure 2-4. Two microprocessors on each valve provide closed-loop control of the solenoid location using internal pressure feedback. The valves are nominally closed. At one command they connect port A to the air source, and port B to exhaust, at the opposing command the flow paths are switched. A five-port valve is required for a double-acting cylinder so that when the active chamber is connected to the air supply, the compressed air in the passive chamber is ported to exhaust. A limitation with the on/off solenoid valves in the Phase One design is that they only control direction. There is no way to adjust the flow-rate or pressure. Varying the duty cycle proportional to a control signal is the normal solution for generating a control signal with on/off solenoid valves but the response time is approximately 16 ms, which is too slow for duty-cycle control. In addition, operating the valves at high speeds induce excessive system vibration which is problematic considering sensitivity of the wind tunnel balance.

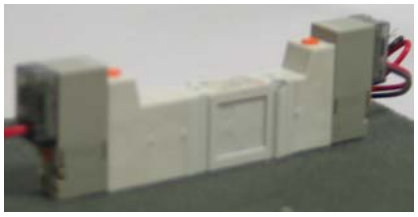

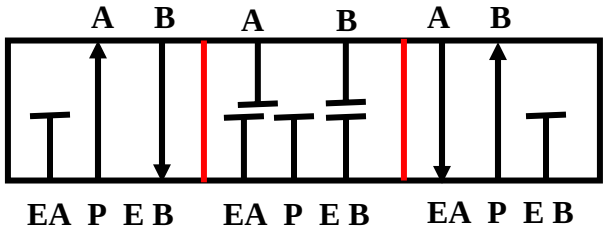

Figure 2-4. Five-port solenoid valve and flow path description. EA is the exhaust port for A, EB is the exhaust port for B and P is the source pressure. This demonstrates a closed-center valve that nominally seals chamber ports.

Electro-pneumatic pressure regulators are included in some of the flow paths to facilitate a proportional control signal. The regulators, pictured in Figure 2-5, are closed-loop devices that generate an output pressure proportional to command signals. The regulators are actually composed of two high bandwidth solenoid valves that are adjusted by the duty-cycle of an internal PWM signal until the commanded output pressure is reached. The regulators have no direction control so they output to a directional valve with the appropriate port determined by the sign of the control signal.

Figure 2-5. Electro-pneumatic pressure regulator. Internal solenoids track a high frequency PWM signal to track a command pressure value.

The pressure regulators do not directly control flow-rate, which is the standard method for pneumatic rate control. Varying the voltage to time-invariant, simple electrical circuits varies the current through the circuit. Similarly, changing the input pressure varied the flow-rate to the actuators so that a pseudo-flow-rate control was

achieved. The regulators are limited in their maximum flow rate to 1.2 standard cubic-feet per minute (scfm) which is too low to actuate the span cylinders effectively because of the larger bore size. They are effective in controlling the wing twist orientation and the tail extension.

2.4.3 Span Extension Unit

Off-the-shelf pneumatic actuators were used to extend and contract the wing. The cylinder body is a thin-walled stainless steel while the rod is a hard, chrome-plated, carbon steel. The actuators form the main structural member for the wing, effectively serving as an active wing spar. They have an 8-inch stroke and a 1.5-inch bore. Each actuator has an internal linear resistive transducer (LRT) for position feedback.

The span unit is required to support the twist mechanism, extend and contract at high rates, and resist aerodynamic loads. To provide structural support, a 3-bar linear thruster was formed that was driven by the pneumatic actuator as seen in Figure 2-6. Two telescoping aluminum rods extend with the actuator rod to sustain lift and moment loads as the span is extended. The thruster is formed by joining the rods and the actuator at three points: at the base with a lexan mount that also houses flow controls for the wing, 6-inches out from the base with acrylic airfoils mounted inside the hollow wing, and at the end of the extending rod with an aluminum plate that connects to the twist mechanism. The span extension unit drives the twist mechanism and the compliant outer-wing seated inside of the hollow structure to form a telescoping wing mechanism.

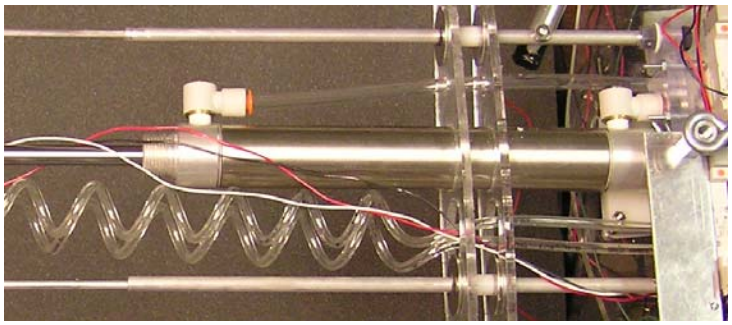

Figure 2-6. Linear span thruster formed from 3-bar segment. The sliding support rods are intended to support torque loads from wing twist and to assist the extending cylinder rod in supporting wing bending loads.

Bang-bang control was used for positioning the span extension. The cylinders are driven directly by the raw air input through the solenoid valves. Figure 2-7 shows the span control circuit. The solenoids limited the extension to accelerate proportional to the source pressure so that constant-rate trajectory control was not possible. Phase One testing only considered static planform responses for which adequate control could be achieved by combining manual flow constriction and on-off solenoid valve commands. Pre-set flow constrictors reduced the input flow rate to the span actuators to slow the acceleration enough that once the stroke was within a specified bandwidth (0.5-percent of stroke) the solenoid valves would stop the motion without overshoot.

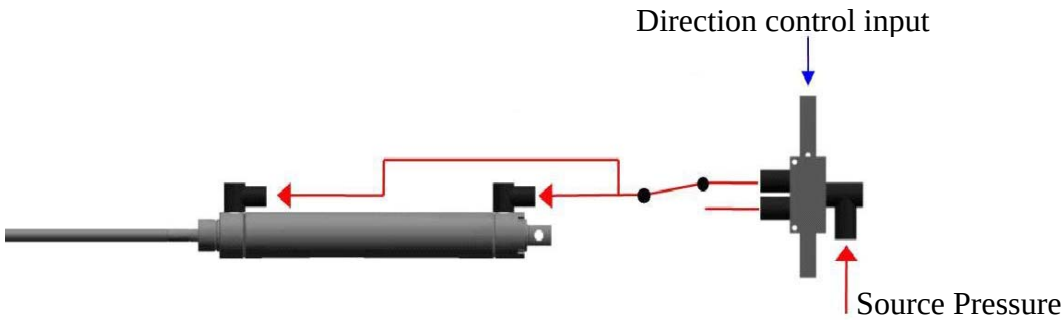

Figure 2-7. Span control circuit demonstrating the solenoid directional flow valve porting to the span actuator chambers. Bang-bang control was used for static positioning because there was no proportional control capability with the solenoid.

2.4.4 Twist Actuation

Figure 2-8 shows internal and external views of the custom mechanism designed to control wing twist. It consists of a 2-inch OD pneumatic rotary actuator driving a gear train to produce the required output torque. The polyurethane mini-coils in Figure 2-6 were used to supply air to the twist actuator. The air-supply coils were very small and compact nominally, but could easily extend with the span as the twist mechanism shifted. A rotary potentiometer indicates the absolute rotation of the actuator for feedback. The vane style actuator is double-acting, permitting rotation in either direction up to 270 degrees. At a line pressure of 70-psi, the actuator generates approximately 16 in-lbs of torque. To increase the output torque, the actuator drives a single-stage planetary gear train with a reduction of 6.67. The total system output is 106.6 in-lbs of

torque and 40.54 degrees of rotation (≈±20 degrees) at 70-psi. The actuator torque output increases linearly with pressure so that at 100-psi operating pressure, the system is capable of over 150 in-lbs of torque. Besides load amplification, the friction in the gear train helps the actuator to maintain constant orientation under load reinforce the compliance of the compressed air supply. The output arm of the planetary set guides a keyed shaft that passes through a rotary bearing and rotates a keyed airfoil section. In the Phase One design, this airfoil was formed from acrylic and bonded to a closed-cell, polyethylene wing section. The compliant wing has a fixed boundary condition where it connects to the rigid hollow wing. When the wing is twisted, the tip orientation decreases linearly to a zero boundary condition at the root.

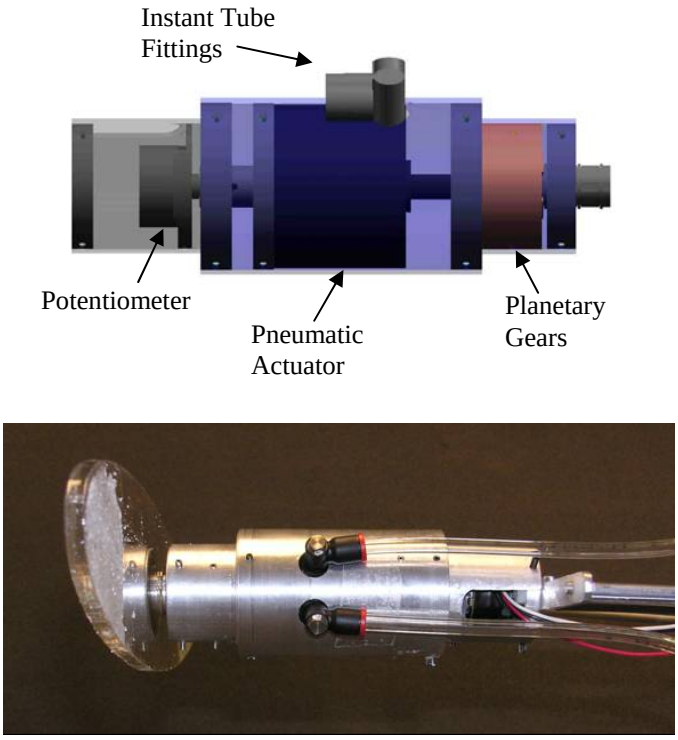

Figure 2-8. Internal and external view of twist mechanism. Significant torque output is produced by the series combination of the pneumatic rotary actuator and the planetary gear set. The gear friction helps the actuator to maintain static positioning.

Twist and span are decoupled mechanically through independent actuation, but the telescopic structure couples the motions aerodynamically. That is, the twist control authority increases with span because the actuated wing area increases along with the moment arm for the twist input. Modeling the twist control authority is therefore a highly nonlinear effect in span increase.

The wing twist must be controlled within very small increments because minor changes generate significant aerodynamic forces. To achieve such precise positioning, the pressure regulators were used to implement a proportional control law. The low flow-rate from the regulators decreased the control torque from the twist mechanism but the compliant wing was still flexible enough to morph. A wing shape was manually cut from a polyethylene foam supply using high-speed cutting and a custom wing guide. The combination of damping from the polyethylene structure and damping from the control algorithm enabled twist orientation control in the lab as shown in Figure 2-9. Wing twist effects were not evaluated in Phase One wind tunnel testing because the compliant surface was found to be incapable of supporting the aerodynamic loads.

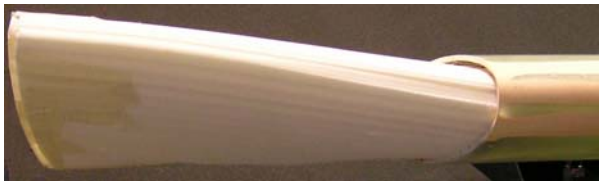

Figure 2-9. Linear twist distribution due to internal actuation. The compliant wing profile was manually cut from a closed-cell polyethylene wing. In addition to a rough exterior surface, the structure was incapable of supporting adequate wing loading.

2.4.5 Sweep Actuation

The wing sweep is controlled by two electromechanical, lead-screw actuators. The actuators are non-backdrivable, and can generate 25-lbs of force, sufficient for varying sweep while under the designed aerodynamic loading. The sweeping motion is actually the output of a 3-bar linkage where the actuator is the driving link. The geometry of the drive system is shown in Figure 2-10. While the design is simple, the model to correlate actuator motion to sweep angle is governed by a nonlinear, transcendental equation describing the linkage motion as a function of the actuator length change. In terms of the actuator length change, δu, and the reference sweep angle change, $\delta\phi$, we obtain the following relationship

$$(\delta u + u_o)^2 = r_{ac}{}^2 + r_{bc}{}^2 + 2r_{ac}r_{bc}\cos((\delta\phi + \phi_o)) \qquad (2.1)$$

for some initial actuator length u_o and some initial reference angle, ϕ_o. Therefore equation 2.1 relates deviations in actuator length to deviations in the sweep angle. In the Phase One model, feedback was taken from a rotary potentiometer mounted at Pivot C to directly monitor the true sweep angle. Direct measurement of the angle, as opposed to the actuator length, facilitated feedback without considering the geometric nonlinearities although equation 2.1 is used in the Phase Two MORPHEUS control design.

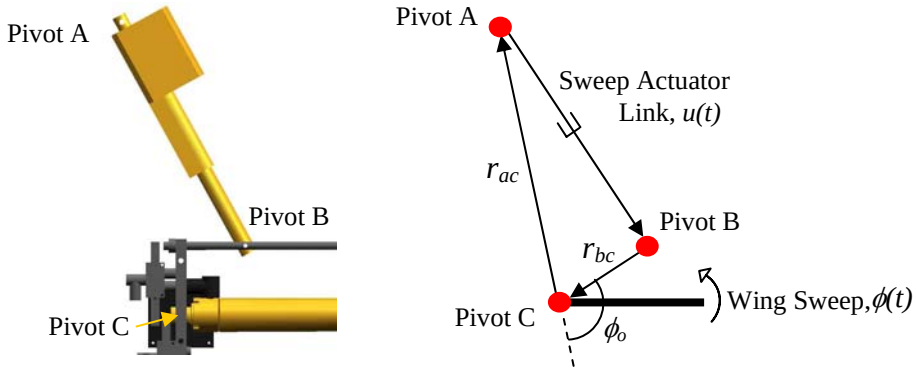

Figure 2-10. Direct-drive sweep geometry. The figure illustrates the actual vehicle system and the corresponding linkage model describing the nonlinear transcendental relationship between linear actuator contraction and wing sweep angle.

The actuators operate at 24V and draw 2.5A each at maximum load. They actuators are limited to a maximum velocity of approximately 2-inches per second which is slow enough for bang-bang control. Because the only concern for testing was static positioning it was not necessary to vary the sweep rate in Phase One. A deadzone corresponding to ±0.3 degrees was established to stop the actuator motion.

2.4.6 Wing Assembly

The effective wing spar is composed of the linear thruster and the twist mechanism. The unit is mounted to a ball-bearing turntable to create a low friction rotation surface for sweep. Steel rods extend from the turntable pivots and are connected by a compact, steel turnbuckle that supports compressive loads as the lift force attempts to raise the wings and tensile loads to support the weight of the wings when unloaded. This setup is displayed in Figure 2-11. The turnbuckle effectively carries whatever load is necessary to maintain a level wing orientation whether loaded or unloaded. This keeps the turntables level so that a low-friction sweep surface is maintained.

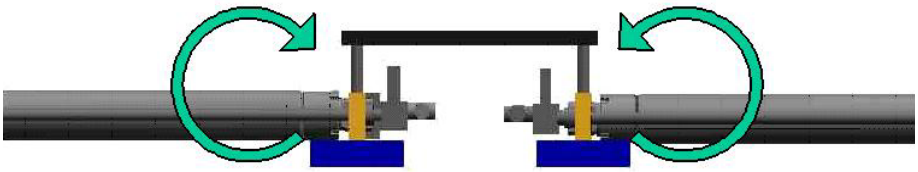

Figure 2-11. Wing assembly demonstrates load transfer to the turnbuckle. The turnbuckle/turntable combination permits low friction wing sweep under aerodynamic loading.

2.4.7 Tail Actuation

The tail extension uses the same style of actuator as the span, with a built-in feedback circuit. The differences are that the tail actuator is 6-inches long and only has a 1-1/16 inch bore. Similar to the twist, precise control is achieved with a proportional control signal sent to via an electro-pneumatic pressure regulator. The regulator outputs to the 3-position solenoid valves discussed previously to control the double-acting cylinder.

2.4.8 Control Circuit

Onboard control and data acquisition is accomplished using PC/104 boards with special software for implementing control algorithms designed in the SIMULINK environment. The PC/104 form-factor consists of individual computer boards, 3.55 x 3.775 inches, with 8-bit and 16-bit data buses that can be connected in stacks to create embedded systems. The stack onboard the Phase One APVE consists of five boards connected to a 16-bit extender that allows horizontal mounting. The stack includes a CPU board with a 233-Mhz processor, a 12-bit 100kHz D/A board for sending analog control signals to the electro-pneumatic pressure regulators, and a 12-bit 500kHz A/D board for measuring potentiometer values on all the internal actuation mechanisms. In addition, there is a 16-channel relay board for automatic switching of the solenoid valves and for powering the sweep actuators. The final board is a power supply that regulates the power input to the CPU (e.g., an external battery).

An overview of the hardware circuit is shown in Figure 2-12. The CPU processes the SIMULINK control structure and communicates with the additional boards in the PC/104 stack. All potentiometer inputs are measured by the A/D board, while the

pressure regulator control signals are output from the D/A board to the twist and tail circuits. The relay board controls all of the solenoid directional valves for the pneumatic actuators and switches/powers sweep actuation.

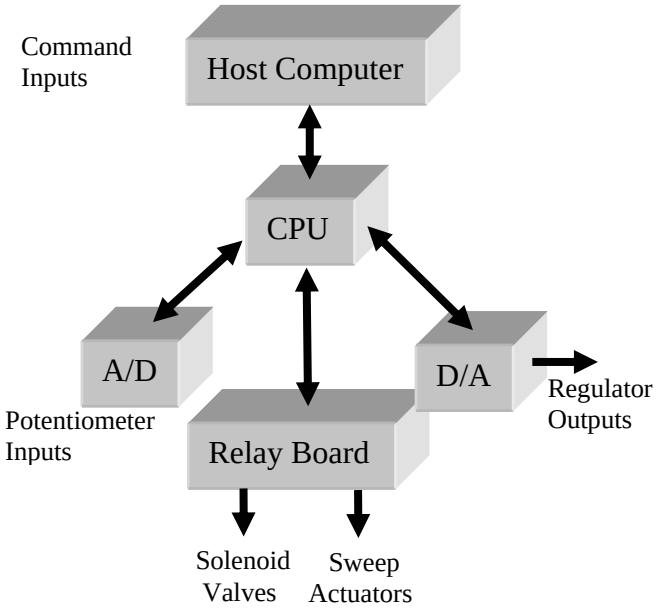

Figure 2-12. Integration of computer hardware into control circuit. The embedded computing stack permits onboard actuator control from a remote unit via a SIMULINK design interface.

The implementation software, XPCTarget uses Real-Time Workshop to directly convert SIMULINK diagrams to C-code and transmits it into the CPU flash memory. There are custom SIMULINK driver blocks to access and control all of the PC/104 boards. This simplifies the implementation of both straightforward and complex control schemes. The SIMULINK model is downloaded to the stack and controlled through the CPU board's Ethernet connection. This allows wireless communication if an Ethernet-to-wireless bridge is connected to the Ethernet port on the CPU. When the SIMULINK model is running on the host computer, any changes made are implemented real-time on the CPU board are real-time data feedback to the host machine is possible based on signal bandwidth.

For static positioning, the control algorithm consists of single feedback loops for each actuator. For the span circuit, the control loops consist of feedback from the LRT probes with a signal sent to the relay board to close the solenoid valve when the position

measurement falls within the established deadzone. A similar control circuit exists for the sweep with the exception that the relay board connects the sweep actuators directly to the system power plant. The tail and twist control circuits consist of true, proportional feedback control. A position error signal is computed and a proportional control signal is generated for the tail control, while a discrete proportional-derivative (PD) compensator is used to prevent overshoot in the twist response. The sign of the control signal is sent to the relay board to switch the solenoid direction while the absolute value is sent to the pressure regulators to output the correct pseudo-control.

The embedded system is compact, lightweight, and powerful in terms of its ability to easily implement complex control algorithms. The true power of the system will manifest itself in later design phases because complex nonlinear or adaptive control designs can be implemented through SIMULINK blocks for autonomous flight control simulation.

2.5 Aerodynamic Performance

Computational methods can be used to estimate the aerodynamic characteristics of a 3-dimensional wing. The lift distribution on an aircraft wing can be represented by a bound vortex system at the ¼-chord (the aerodynamic center for a thin 2-D airfoil). A vortex is a constant strength singularity element with a potential function that satisfies Laplace's equation and induces concentric streamlines of decreasing velocity out from the origin. Hence, a vortex element induces a diminishing tangential velocity at some radius from its origin. By Helmholtz theorems, a vortex element must possess constant circulation strength whereas 3-dimensional flow effects on a wing cause the circulation strength to vary along the span. Therefore the bound vortex system on the wing must be discretized into a number of constant strength elements. Another of the vortex theorems states that a vortex cannot start or end in a fluid, but must form a closed path, end at a boundary, or go to infinity [Katz, 2001]. This implies that boundaries between the constant strength bound vortex segments must be satisfied by vortex legs that extend to infinity. Between two bound vortices, a trailing vortex escapes to infinity to end the previous element while a trailing vortex comes in from infinity to begin the following

element. This can alternatively be represented by a trailing vortex equal to the difference in strength of the two elements escaping to infinity. Since every bound vortex starts at infinity, forms the bound vortex element, and then returns to infinity, the classical 'horseshoe' vortex system is formed.

The normal velocity induced on each bound vortex by the trailing vortices is the wing downwash. Downwash is the 3-dimensional flow effect from pressure equalization at the wing tips. Because of the low pressure flow above the surface and high pressure flow beneath it, a general lateral flow pattern is induced so that flows on the underneath surface tends towards the tips and flows above the surface tend inboard. Overflow onto the upper surface tilts the local velocity direction which creates induced drag and reduces vehicle lift. The horseshoe vortex layout adequately captures the downwash effect and can be used to model the static vehicle response. In general, the circulation strength of the vortices is not known beforehand but the induced normal velocity can be used along with surface boundary conditions to produce a set of linear equations to determine the circulation values. This popular analysis method is termed the Vortex Lattice Method and is presented for predicting the aerodynamics of the APVE planform.

Aerodynamic evaluation requires a combination of experimentation and theory. Experimentation is used to verify new theory, and to obtain data that falls outside of theoretical assumptions. Basic theoretical or computational results are necessary to verify the experimental parameters for simple cases so that researchers have confidence when the testing is extended outside theoretical boundaries. In turn, the experimental data is used to give better estimates to the theoretical analysis and extend the range of application. A custom vortex-lattice code is presented that predicts the 3-dimensional flow over the APVE planform for different configurations. The results are compared to Phase One wind tunnel test results.

2.5.1 Vortex Lattice Aerodynamics

The Vortex Lattice method is a computational technique that forms a system of linear algebraic equations to determine the strength of the bound vortex segments across the span. The planform is divided into a number of panels (lattice) with a bound vortex segment at ¼-chord of the wing camberline and trailing vortices that extend to infinity. A control point is established at ¾-chord of each panel to satisfy the boundary condition

of no flow through the panel surface. This control point location is a result from 2-D airfoil theory of the distance behind the aerodynamic center at which the zero normal flow boundary condition is satisfied. The velocity induced on each panel by each of the horseshoe vortices is computed using Biot-Savart's law.

$$\overrightarrow{dV} = \frac{\Gamma\left(\vec{dl} \times \vec{r}\right)}{4\pi r^3} \tag{2.2}$$

where *dl* is the vortex filament, *r* locates the control point from the filament, and Γ is the circulation strength of the filament [Bertin, 1998].

Discretizing the planform into *n* panels, the total induced velocity at each control point will be the inner product of a *1xn* array of geometric influence coefficients vectors (from the cross product in equation 2.2) and an *nx1* array of unknown circulation strengths. This is repeated for each of the panels and results in a square *nxn* system. The downwash at each control point must balance the normal component of freestream velocity to satisfy the boundary condition. For a planar wing (i.e.. symmetric airfoils and no dihedral), only normal velocities are induced by the vortices, causing the influence coefficient vectors to only have a normal component, C_{ij}. The normal component of freestream velocity, $U_\infty \alpha$, is the same for each panel so that the governing equation becomes

$$\begin{bmatrix} C_{11} & \cdots & C_{1N} \\ \vdots & \ddots & \vdots \\ C_{N1} & C_{N2} & C_{NN} \end{bmatrix} \begin{pmatrix} \Gamma_1 \\ \vdots \\ \Gamma_N \end{pmatrix} = -U_\infty \alpha \begin{pmatrix} 1 \\ \vdots \\ 1 \end{pmatrix} \tag{2.3}$$

Equation (2.3) is solved for the vector of unknown circulation strengths. Applying the Kutta-Joukowski theorem, the total lift for the wing is found from

$$L = \rho_\infty U_\infty \sum_{i=1}^{N} \Gamma_i \Delta y_i \tag{2.4}$$

,where Δy_i is the panel width. The pitching moment is determined from the cross-product of a position vector, r_i, and the bound vortex lift of each panel

$$M = \rho_\infty U_\infty \sum_{i=1}^{N} r_i \times \Gamma_i \Delta y_i \tag{2.5}$$

The root of position vector array is the point about which the moment is calculated.

A custom VLM code was created in Matlab that generated lattice structures for different planform configurations and implemented equations 2.2, 2.3, 2.4, and 2.5. The VLM code is validated against standard planform layouts for which the results are known. The code was tested against two, low aspect ratio configurations of increasing complexity: a rectangular planform, and the Warren 12 planform. Figure 2-13 shows the lattice for the Warren 12 planform which is an especially useful test case because it involves extreme sweep and taper. Table 2-1 compares the current VLM code to established values of $C_{L\alpha}$ and $C_{M\alpha}$ for the two planform configurations [Lan, 1974]. The custom code accurately predicts the aerodynamic characteristics of both planform shapes, so we have confidence in the results when applied to the APVE configuration.

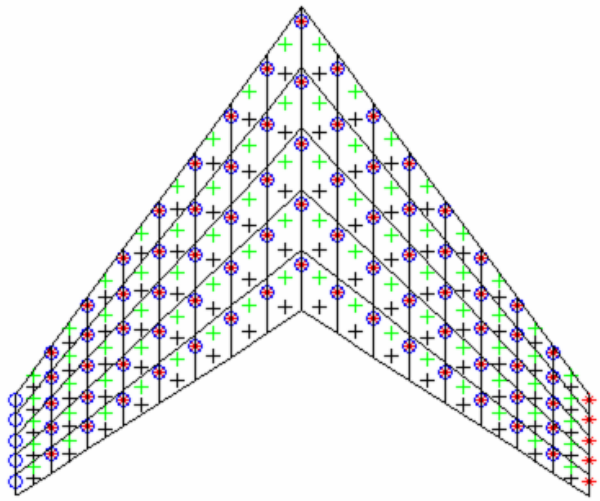

Figure 2-13. Custom vortex lattice structure for Warren 12 planform. o-left vortex boundary, *-right vortex boundary, +-control point, +-vortex lift location

Table 2-2. Validation of Custom VLM Code

	Rectangular, AR=2			**Warren 12, AR=2(2)$^{1/2}$**		
Parameter	**VLM**	**Reference**	**Error**	**VLM**	**Reference**	**Error**
$C_{L\alpha}$ (rad^{-1})	2.574	2.5239	2%	2.8326	2.7944	1.4%
$C_{M\alpha}$ (rad^{-1})	-0.5456	-0.5334	2.3%	-2.99	-3.1775	5.7%

A lattice corresponding to two different APVE planform configurations is displayed in Figure 2-14. The layout indicates the edges of the bound vortices and the control points for each panel. Swing-wing aircraft generally have significant taper so

that alignment of the wing-tip with the freestream direction is not a significant issue. Figure 2-14 shows that as the APVE planform is swept, the leading edge of each panel decreases in angle to ultimately align with the trailing edge angle. The panels also decrease in size out towards the wing tips until they effectively form a point to mimic the actual swept vehicle geometry.

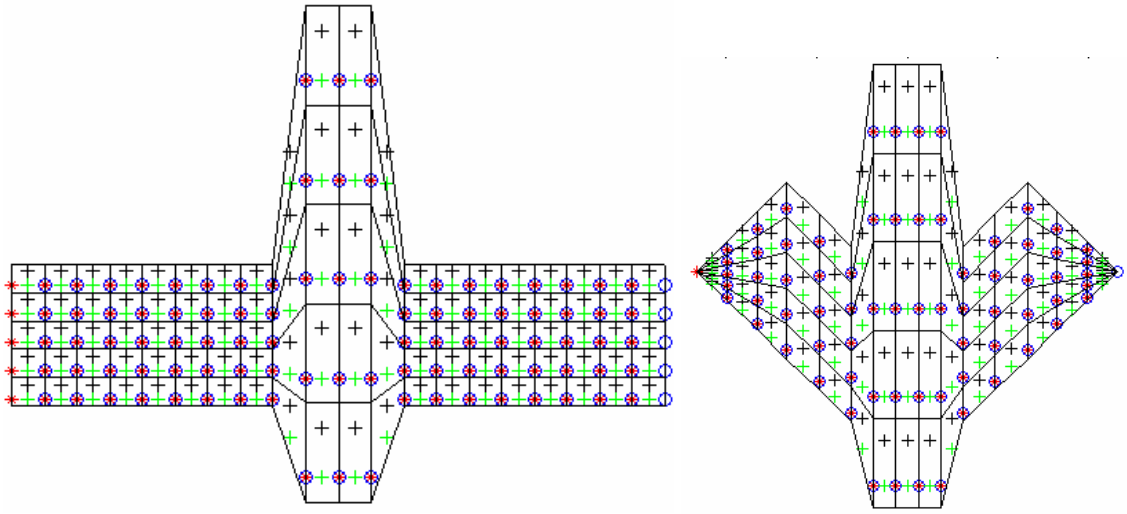

Figure 2-14. Custom vortex lattice structures for two APVE configurations. 1) Fully-extended planform 2) Fully swept, tail and wings contracted

The lift and pitching moment results for the six configurations in Figure 2-1 are displayed in Table 2-3. The aerodynamic center is measured from the fuselage apex. Although the planform area and mean aerodynamic chord vary with the planform changes, the lift and moment forces in Table 2-3 are non-dimensionalized with respect to the constant planform area and reference chord of the unmorphed configuration. Evident from the data is the high sensitivity of aerodynamic response to span and sweep changes, and the low sensitivity to tail extension. In general, $C_{L\alpha}$ increases greatly with wing area, so span increases have a large effect on the lift curve slope. The aerodynamic center, $x_{ac,}$ shifts largely with the sweep angle. The shift becomes even larger when coupled with span changes. Comparing the extended tail configurations to the same configurations without tail extension shows very little change in the aerodynamic response. This is due to a lack of sufficient tail area on the Phase One design.

Table 2-3. Vortex-Lattice results for Aerodynamic Changes with Planform Shape

	Span Extension, Tail Extension, and Wing Sweep (Δb%, Δt%, ΔΛ%)					
	Δb=0 Δt=0 ΔΛ=0	**Δb=100 Δt=0 ΔΛ=0**	**Δb=100 Δt=100 ΔΛ=0**	**Δb=100 Δt=100 ΔΛ=100**	**Δb=0 Δt=0 ΔΛ=100**	**Δb=100 Δt=0 ΔΛ=100**
Parameter						
$C_{L\alpha}$ **(rad^{-1})**	2.671	3.943	3.958	3.538	2.541	3.517
$C_{M\alpha}$ **(rad^{-1})**	-1.535	-2.322	-2.341	-3.271	-2.043	-3.241
x_{ac} **(in)**	12.45	12.77	12.83	20.08	17.46	20.02

2.5.2 Wind Tunnel Test Setup

The APVE model was tested in Virginia Tech's 6x6 ft stability wind tunnel. Figure 2-15 shows the model mounted in the tunnel for testing. The aircraft model is mounted to a rigid strut that is instrumented with strain gauges to measure the forces and moments about the X, Y, and Z inertial axes. Post-processing converts the data to wind axes so the lift and moment data can be analyzed.

Figure 2-15. Experimental model mounted in the Virginia Tech Stability Tunnel for 1st phase static configuration testing. The testing was constrained to angle of attack sweeps for nine different wing configurations.

The test condition and reference parameters used to non-dimensionalize the force and moment coefficients are presented in Table 2-4. The reference area and mean aerodynamic chord (S_{ref} and c_{ref}) correspond to the model with the wings and tail fully retracted and unswept. The length x_{ref} is the distance from the nose of the model to the reference location for the pitching moment computation, as shown in Figure 2-16.

Table 2-4: Test condition and reference parameters

U_∞	73.3 ft/s
S_{ref}	6.81 ft^2
c_{ref}	1.81 ft
x_{ref}	1.37 ft

Figure 2-16 also details the planform variables investigated in this experiment. The Phase One model was physically limited to a half-span range of 6-inches due to sliding surface boundaries as opposed to 8-inches. Wing sweep was tested through its entire range of 0 to 40 degrees. The tail extension range is 0 to 6-inches but the area is so small that there was a negligible effect on the experimental response. Therefore, tunnel data is only presented for the unextended tail case. Testing did not include wing twist because a sufficient wing material had not been identified that could support the appropriate aerodynamic loading while compliant enough for actuation.

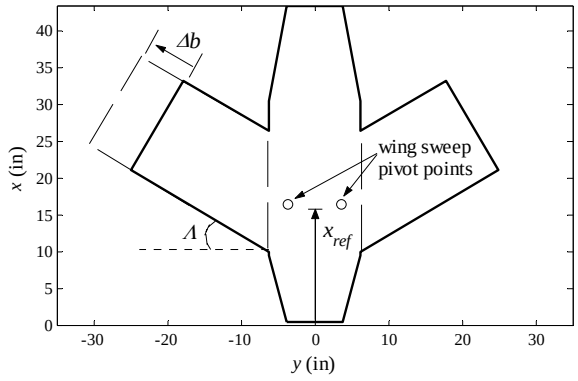

Figure 2-16. Relevant planform parameters to identify iterated wing shape changes.

2.5.3 Wind Tunnel Test Results

Wind tunnel testing was used to determine the sensitivity of aerodynamic characteristics to APVE planform changes. Theory indicates that the induced drag should decrease with span, and the aerodynamic center should shift back with sweep. Experimental testing should confirm these results and allow quantification for general analysis of morphing aircraft.

Figure 2-17 shows the shift in the aerodynamic center location (x_{ac}) with sweep for different values of span extension. In general, the aerodynamic center varies with the area distribution of the planform. Regions with larger planform areas generally carry higher loads, which causes the aerodynamic center to exist closer to these areas. As the wings sweep back, the area distribution moves back and so does the aerodynamic center. As the span increases, and the wings sweep back, there is a larger rearward shift in area distribution which causes larger shift aft in the aerodynamic center. The aerodynamic center shifts 19.5% of c_{ref} for Δb = 0, 22.3% for Δb = 50%, and 25.7% for Δb = 100%. Specific c.g. data is necessary to evaluate the exact stability changes. If the rearward shift in aerodynamic center is greater than the rearward c.g. shift, the aircraft becomes overly stable, which increases trim drag and decreases maneuverability.

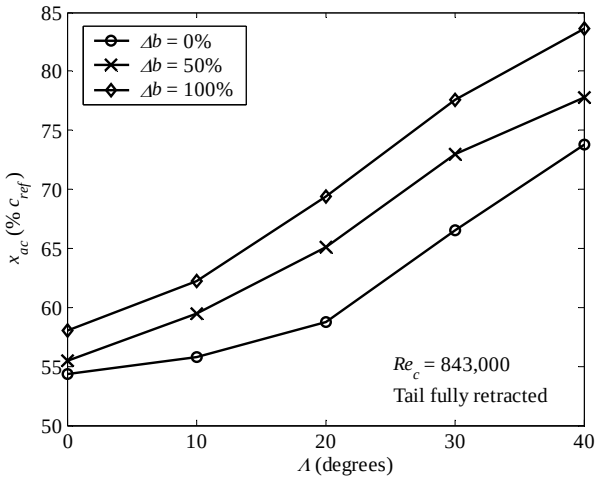

Figure 2-17. The influence of span extension (Δb) and wing sweep (Λ) on the aerodynamic center location. The trends followed expected results with larger aftward area shifts corresponding to larger increases in static margin and trim requirements.

Data on the aerodynamic center was presented as opposed to the pitch stiffness, $C_{M\alpha}$, because of the reference point and c.g. shifts during testing. The wind tunnel measures the pitching moment about the mount point but there are also c.g. shifts during actual testing which varies the pitching moment and clouds the representation. The aerodynamic center location is a linear function of $C_{M\alpha}$, is independent of c.g. locations, and illustrates changes in the planform stability characteristic.

Figure 2-18 shows that $C_{L\alpha}$ decreases with increasing sweep. This reason for this decrease is twofold: 1) there is a reduction in exposed wing area and 2) the effective freestream velocity flowing over the wing is reduced by cosine of the sweep angle. For Δb = 0, $C_{L\alpha}$ changes by 14.2% as Λ changes from 0 to 40 degrees. The percent change for the Δb = 50% and Δb = 100% cases are 15.9% and 14.6%, respectively. This indicates that, as expected, the change in $C_{L\alpha}$ is less sensitive than the aerodynamic center to sweep changes. We also see that although the larger wing area causes the total lift to increase with span, the gradient, $\partial C_{L\alpha} / \partial \Lambda$, is approximately constant with span change.

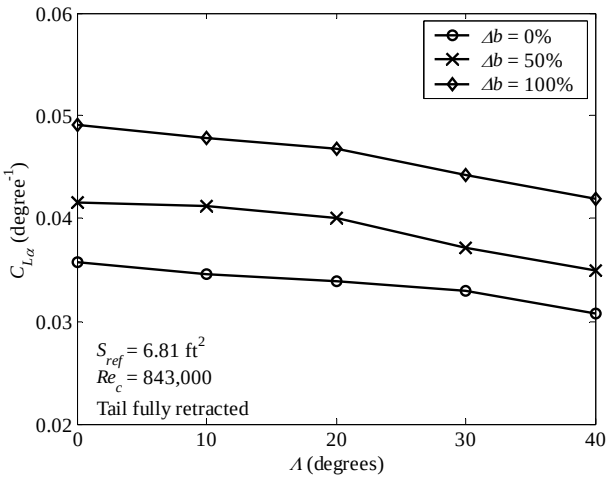

Figure 2-18. The influence of span extension (Δb) and sweep (Λ) on the lift curve slope ($C_{L\alpha}$). Span extension was seen to have little effect on the negative wing sweep gradient although it increased with the absolute lift curve slope.

The lift curve in Figure 2-19 indicates that a swept planform achieves a higher absolute C_L although the lift curve slope is reduced. This comes about because wing sweep delays stall so that a higher angle of attack can be achieved. The delay in stall is caused by the same crossflow effect that reduces the lift curve slope for sweep. The

primary benefit of sweep is the delay in supersonic drag rise by insuring that the leading edge remains within the Mach cone. These supersonic effects were not investigated on the low-speed APVE model.

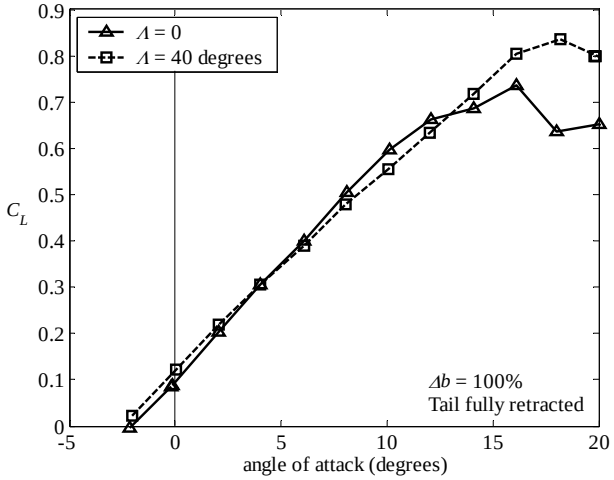

Figure 2-19. Lift-curve for swept and unswept configurations at full span extension. Although the swept configuration had a slightly decreased lift-curve slope, the delayed stall allowed it to achieve a higher total lift value.

The pitching moment curve in Figure 2-20 can be used to determine the relative c.g. location and stability data for a fully extended configuration. When the vehicle is unswept, the pitch stiffness slope is positive which indicates that the aerodynamic center is ahead of the c.g. and the vehicle becomes stable in pitch. As the wings sweep back, the relative redistribution of area is greater than the c.g. shift so that $C_{M\alpha}$ becomes negative and the vehicle obtains pitch stability. In order for the APVE to be fully or marginally stable throughout all planform configurations the nominal c.g. should be shifted forward of the reference point, x_{ref} .

Figure 2-21 validates morphing aircraft in terms of multi-mission performance. It shows that the minimum drag for a given lift coefficient is achieved using different planform shapes. For low lift values the unswept, unextended configuration is optimal. For intermediate lift values, the unswept fully extended configuration is optimal. For high lift, the fully swept, fully extended configuration provides the highest *L/D*. This is due to the high lift capability of the swept wings as seen in Figure 2-20. The drag

response shows that for each planform configuration, *L/D* values vary with flight condition and this can be used to tailor optimal vehicle configurations.

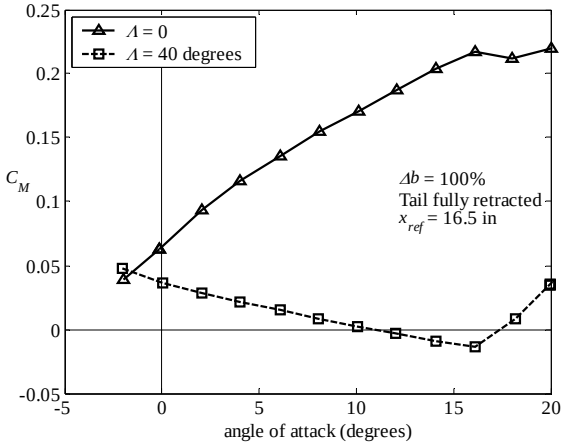

Figure 2-20. Pitching moment response for swept and unswept configurations. The moment response indicates that the unswept configuration is highly unstable about the wind tunnel mount point which can be countered by shifting the nominal c.g. forward.

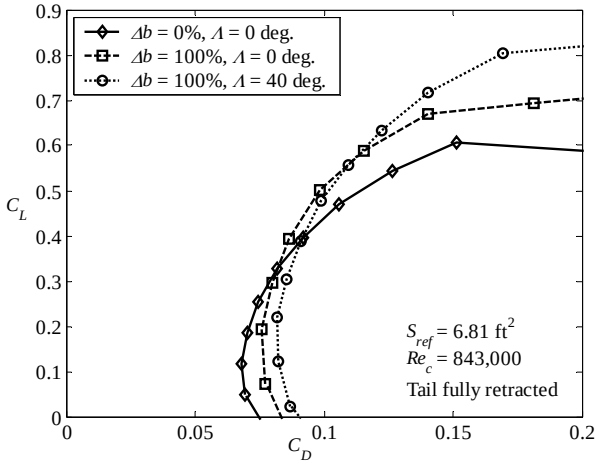

Figure 2-21. Drag reduction for obtaining a given lift coefficient by implementing different planform configurations. The response validates the use of multiple wing configurations to optimize the drag performance during various mission segments.

2.5.4 Experimental Data and Vortex Lattice Predictions

Table 2-5 compares the wind tunnel data and the VLM results for four APVE configurations. The configurations are the four combinations of fully extended span and sweep. All data is presented for a contracted tail.

Table 2-5. Comparison of Vortex Lattice and Experimental Test Results

	Δb=0, ΔΛ=0			Δb=100, ΔΛ=0			Δb=0, ΔΛ=100			Δb=100, ΔΛ=100		
	VLM	**EXP**	**%**	**VLM**	**EXP**	**%**	**VLM**	**EXP**	**%**	**VLM**	**EXP**	**%**
$C_{L\alpha}$	2.67	2.05	30.2	3.62	2.81	28.8	2.54	1.75	45	3.27	2.45	33.5
x_{ac}	12.5	11.7	6.8	12.7	12.6	0.79	17.5	16.1	8.7	19.4	18.2	6.6

The errors between the VLM results and the experimental data are significant but all vary by about the same amount. With the exception of the fully-swept wings contracted case, the difference is approximately 30-percent. Because the percent error is basically constant for three of the four configurations this indicates that the plane demonstrates the same trends as VLM but the data is offset.

A major reason that the experiment had lower lift values is the tail position. When the tail is contracted for the VLM data it is still a continuous surface. When the tail is contracted in the experimental model, a large jump in the profile occurs. The flow separates from the tail and the overall lift decreases. Another cause of decreased wind tunnel lift is suction in the model. The fuselage has significant gaps around the wing which diverts the flow from the surface reducing the total lift. The VLM analysis also assumes ideal conditions and does not account for separation on the fuselage but assumes it is an ideal lifting body. In addition, the proximity of the aircraft to the wall boundary has effects which were not modeled with VLM. The tunnel is six-feet wide and the model at full span extension is 5.38 ft.

The errors in the aerodynamic center location are much less. This is because the same constant source of error in measuring $C_{L\alpha}$ accurately exists when measuring $C_{M\alpha}$. The aerodynamic center is proportional to the ratio of the two values so the source of error cancels and reasonable alignment between data and theory is seen.

Figure 2-22 and 2-23 show the VLM results corresponding to Figures 2-20 and 2-21. They display the relative VLM and experimental results for lift curve slope changes and aerodynamic center shifts. The key result is that the experiment shows the same trends in terms of increasing the aerodynamic center shift with span and sweep and the decrease in the lift curve slope with sweep. The experimental results were valid, it was only model conditions and test parameters that caused a discrepancy in results. Fixing

the model structure to prevent suction, flow profile disruptions and testing at a higher wind speed could help to align experiment and theory in future tests.

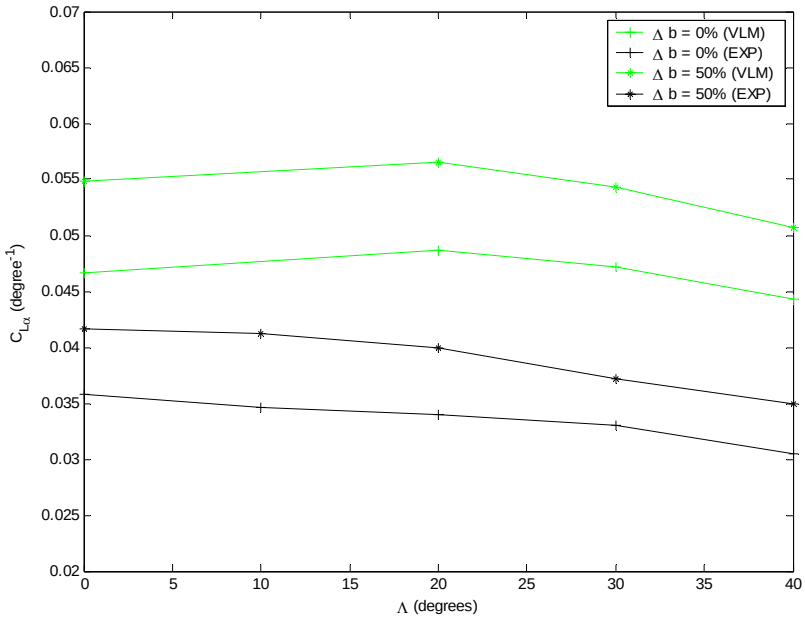

Figure 2-22. Comparison of $C_{L\alpha}$ changes with configuration for VLM and experimental data. The trends are similar although the absolute values are significantly offset.

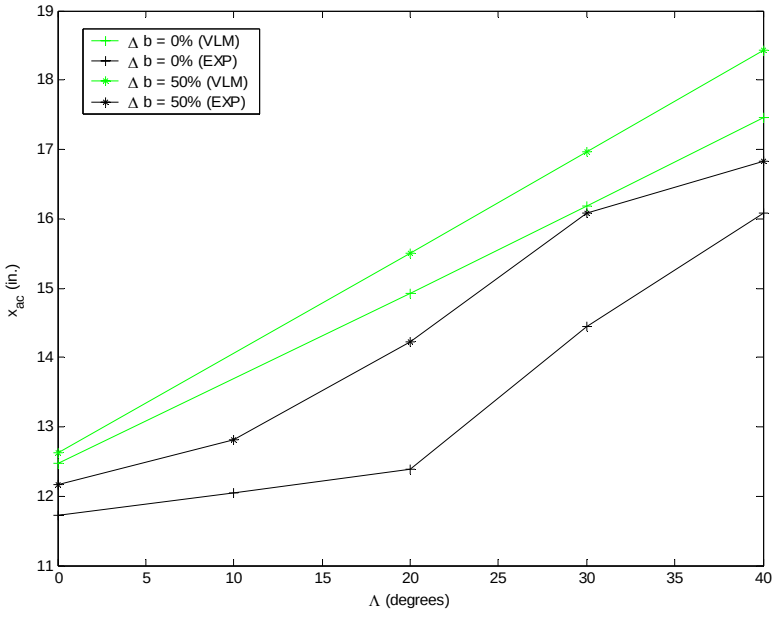

Figure 2-23. Comparison of aerodynamic center changes with configuration for VLM and experimental data. The trends are similar but the absolute values are offset.

2.6 Chapter Summary

The Phase One APVE model is the foundation for the most recent design iteration. The testbed, designed and constructed for large configuration changes, is capable of five independent planform variations along with independent twist control for each wing. The vehicle undergoes a 79% change in half-span, 40 degrees of sweep change, 12% change in chord length and ±20 degrees of wing twist. Wind tunnel results showed that the static aerodynamic characteristics varied significantly with all the morphing degrees of freedom except tail extension.

There were also significant design flaws identified with the Phase One model. The base support for the internal structure was lasercut from ¾-inch acrylic which was light, but could flex easily. The linear thruster for the span extension was too weak to support wing twist actuation. When a large torque was transmitted through the twist mechanism, the support rods for the span actuator failed.

The material for the compliant wing was not strong enough to support the aerodynamic loads, although the wing twisted easily in lab experiments. In addition, there was no way to shape the soft foam except manually on a bandsaw. This resulted in a misshapen airfoil with a rough exterior. In addition, the tail area was too small too significantly alter the aerodynamic center when actuated.

Besides problems with the basic structure there were also performance problems. There were no flowrate control devices to allow direct planform rate control. Planform rate control is necessary for modeling transient aerodynamics and for using planform inputs as general control effectors. The direct feedback of the sweep orientation was inconsistent and bang-bang control did not allow rate variation of the sweep actuators. The electrical circuit design was also unorganized and inconsistent.

Errors in model construction and test parameters resulted in large discrepancies between experimental and test data. The same trends were evident in terms of changes in the aerodynamic characteristics but the large offset is a source of concern for advanced testing. The summation of these issues led to a model redesign and resulted in the Phase Two APVE model: MORPHEUS.

Chapter 3
Phase Two Development: Design and Analysis

3.1 Chapter Overview

Noted deficiencies in the Phase One vehicle design motivated the Phase Two development. The updated model has eight degrees of freedom including wing twist. The main incentive for redesign was that the Phase One model lacked capabilities necessary to meet long-term experimental requirements; specifically a lack of structural strength, no twist function under aerodynamic loading, and the absence of planform rate control. Additional design alterations resulted in a novel morphing architecture capable of distinct configurations, beyond the swing/telescopic-wing approach. The MORPHEUS vehicle combines multiple area shifts and wing sweep to achieve completely separate loiter and attack configurations, but has the potential for infinite symmetric and asymmetric planforms. The Phase Two design is a foundation for future modeling and control experimentation with morphing aircraft.

After an overview of design modifications, the new Phase Two design is presented, in detail. The justification and performance benefit associated with each modification is presented. A majority of the modifications are aimed at increased structural stability, maintaining the stability while morphing under load, or creating dependable subsystem functioning. In addition to modification of Phase One parameters, there are also enhancements presented that increase the vehicle performance and test capacity.

The second part of the chapter covers system level embedded control. The methods and control processes for coordinating the planform motions are presented. In addition, position and trajectory control of the pneumatic and electromechanical systems is presented.

3.2 Morpheus Design Overview

Figures 3-1 and 3-2 depict isometric views of the MORPHEUS internal structure. While the general actuation scheme is maintained from the P1 APVE, the entire internal support system and layout are new. The emphasis in the MORPHEUS design is increased strength and functionality. The base structure was required to support greater aerodynamic loads and the actuation system had to be capable of morphing the wing shape while under load. In contrast to standard aircraft design, the strength designed into the structure had to be maintained dynamically, while the vehicle changed shape. It is shown that many of the new load support elements slide to accommodate this.

In addition to increased aerodynamic loads, the structure had to support the increased internal loads from the addition of various control devices and actuation mechanisms. Therefore, the acrylic base was replaced with a composite structure, created from layers of carbon fiber and aluminum.

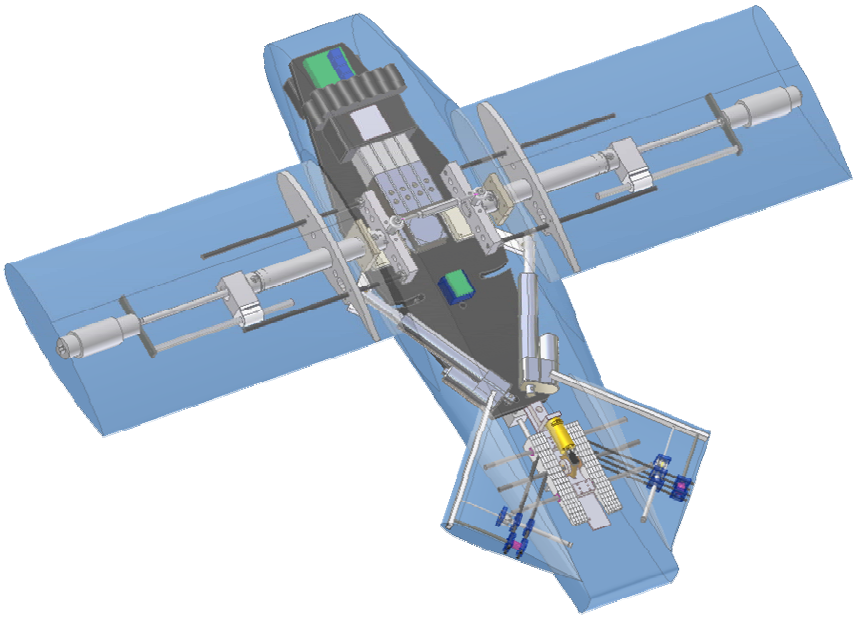

Figure 3-1. Overview of MORPHEUS internal design structure. UPPER VIEW Isometric

The same basic span and sweep actuation is employed, including integration of the twist mechanism with the span extension. The addition of custom-molded compliant wings permits wing twist. Along with load-bearing inserts the material provides the perfect balance of stiffness to support aerodynamic loads and flexibility to permit morphing. Having the wings cast from a specially fabricated mold creates a smooth outer surface and an exact airfoil cross-section. The linear thruster of the span extension unit was replaced with a heavy-duty

sliding constraint to carry increased aerodynamic pitching moment and bending loads while supporting the extending shaft of the pneumatic actuator. The additional support accounts for the inherent compliance in the twisting wing sections.

The new sweep actuators have a higher load capacity and embedded feedback as opposed to the external potentiometer at the wing pivot in Phase One. Removing the potentiometer from the pivot point allowed an additional support turnbuckle underneath the base, effectively doubling the load capacity. The addition of the sliding support helps to transmit wing torque from twist actuation and normal wing loads to the base.

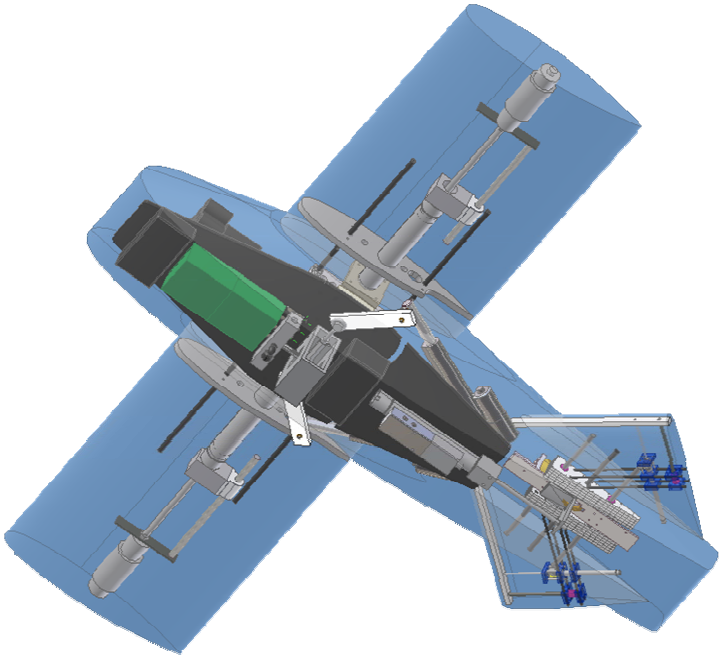

Figure 3-2. Overview of MORPHEUS internal design structure. LOWER VIEW Isometric

The P1 APVE pressure regulators were replaced with compact proportional flow control valves to enable accurate trajectory control of the span extension. Proportional valves allow direct manipulation of flowrate as a control signal for the pneumatic system.

Auxiliary changes included an improved electrical system, an increased power resource, a tri-axial rate/orientation/acceleration sensor, a simplified air delivery system, and a remote control unit. The circuit modifications create reliable and consistent performance while the increased power structure is required to support new devices, and actuators. The new circuit design facilitates rate control of the planform actuators, and precise positioning for the maneuvering actuators. The embedded sensor provides orientation and motion feedback during dynamic testing. In general, the new design is more compact with component locations weighted towards the nose to counter the weight added by the variable geometry tail (VGT).

The VGT is the foremost performance enhancement on MORPHEUS. As opposed to the Phase One arrangement of shifting the rear fuselage and decreasing the chord, the linear tail actuator now controls the longitudinal coordinate of the horizontal tail area, generating a larger shift in the aerodynamic center. The VGT is capable of both longitudinal and lateral planform extensions in addition to a variable incidence angle. The combination of the three motions supports general trim requirements while morphing. The tail contributes to the overall performance in the dash configuration by combining with the then-swept main wing to form a single lifting surface. This allows the overall vehicle planform to approximate a DELTA wing geometry in dash.

The final modification is the new mount structure which slightly projects outside of the fuselage, offsetting the connection from the wind tunnel balance to the main structure. While seemingly trivial, this permits MORPHEUS to be mounted to multiple wind tunnel attachments, including a sting mount which is generally a more accurate testing method than the strut mount used in Phase One testing.

Figure 3-3 illustrates the overall functioning of MORPHEUS and the integration of the different subsystems: control devices, signal conditioning, and actuation. The external system command enters via a hardline or wireless Ethernet connection from the host CPU. The PC-104 processor implements the Simulink-platform control process interfacing with the DAQ system. Analog commands for span, twist, and longitudinal tail extension are transmitted to a circuit which draws power from the battery and sends an excitation signal to the appropriate flow control valve. The valves source air to the target actuator(s) from some external supply through the manifold. Sweep actuation commands are sent from the D/A board to a circuit that generates the appropriate PWM signal for the lead screw actuators to track a command velocity. Commands for lateral tail extension and incidence are sent directly from the serial port on the CPU to the servo-controller. One servo-controller output connects directly to the incidence servo while the other is amplified through an H-bridge to power the lateral tail extension motor. A single unit conditions all feedback signals for transmission to the PC-104 stack.

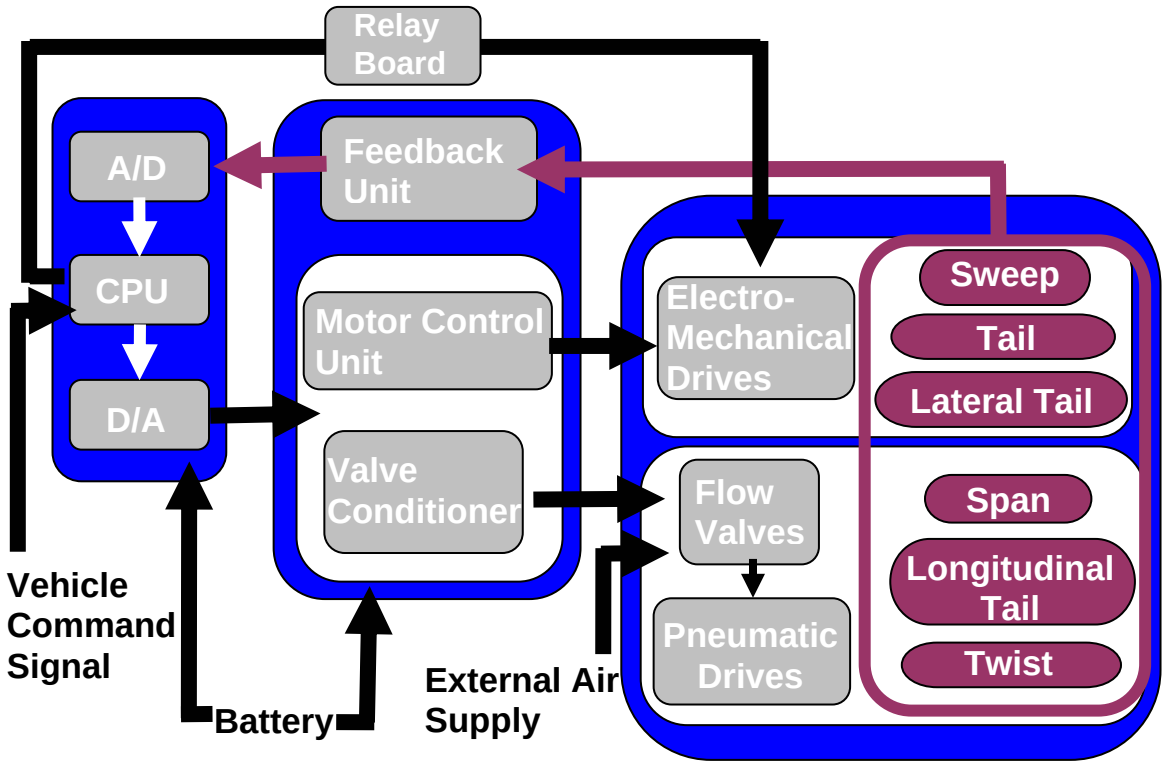

Figure 3-3. Process Diagram illustrating MORPHEUS system organization. Command signals are transmitted through the embedded computer through transducers and out to the pertinent drive systems and actuators.

3.3 Detailed Design and Elementary Strength Analysis

Component design details are presented in addition to an elementary strength analysis of the critical load points. The procedure is to develop an assumed load condition for the vehicle, note the manner in which the loads are transferred to the internal structure, and finally to determine the critical points. Computational methods from traditional mechanics are used supported by ANSYS analysis when necessary. Specifically, we will approximate the load transfer to the base and use ANSYS to compare expected deformation at new load conditions to the previous design structure.

The present analysis will focus on the loiter configuration as that is the most flexible state. Raymer (1999) gives a positive design load factor of six for a general aviation aerobatic vehicle, ranging up to nine for fighters. These numbers obviously consider maneuver loads which become an issue for MORPHEUS during any type of

dynamic testing (e.g. identifying stability derivatives). This would require a dynamic strength analysis using computational tools with assumptions for the unsteady aerodynamics. For static testing, we assume a maximum load of three times the vehicle weight (3W) based on the limits on the wind tunnel balance. We apply a factor of safety of 1.33 to lead to a design load condition of four times the vehicle weight (4W). Aerodynamic analysis reveals a maximum aircraft lift curve slope of 5 rad^{-1} in the loiter state. Based on this value, the reference area and the vehicle weight, the test dynamic pressure of 28 psf generates an aerodynamic load of 3W at 15° angle of attack and 37.7 psf generates 4W at the same angle of attack.

From Figure 3-4 we see that the body-axis loads vary with angle of attack, such that at a given angle, the longitudinal force changes direction and increases with angle of attack because of the lift contribution. Approximations for the drag characteristics of MORPHEUS are presented in Chapter 4 and we can estimate a nominal drag coefficient of 0.153 for the given lift at the design angle of attack. The body axis load coefficient, C_c, is 0.2 and is oriented *into* the flow.

Figure 3-5 shows the assumed load condition for the elementary strength analysis. Wing twist can be used to approximate an elliptic spanload so that the nominal load on each wing (2W) acts at 42-percent of the half-span. The critical points of structural integrity are the extended wings, particularly the extended shaft on the span actuator, the turnbuckles that carry the transmitted wing bending moment, the sweep-wing connection point, and the base which transfers the final load to the wind tunnel mount.

$$C_N = C_L \cos\alpha + C_D \sin\alpha$$
$$C_c = C_L \sin\alpha - C_D \cos\alpha$$
$$C_D = K_{loiter}\left(C_{L\alpha,loiter}\alpha_{design}\right)^2 + C_{Do}$$
$$C_L = C_{L\alpha,loiter}\alpha_{design}$$

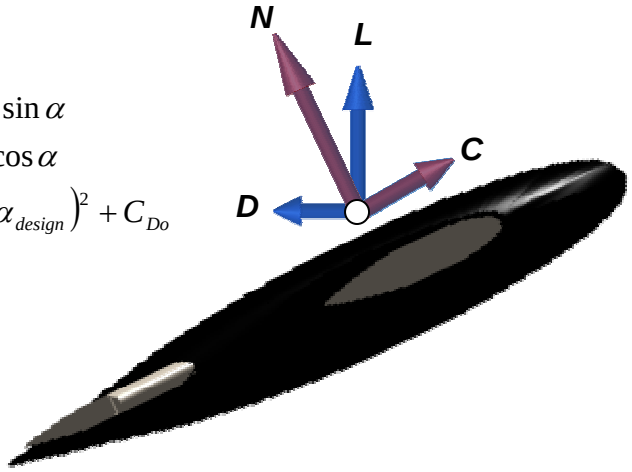

Figure 3-4. Body-axis load distributions

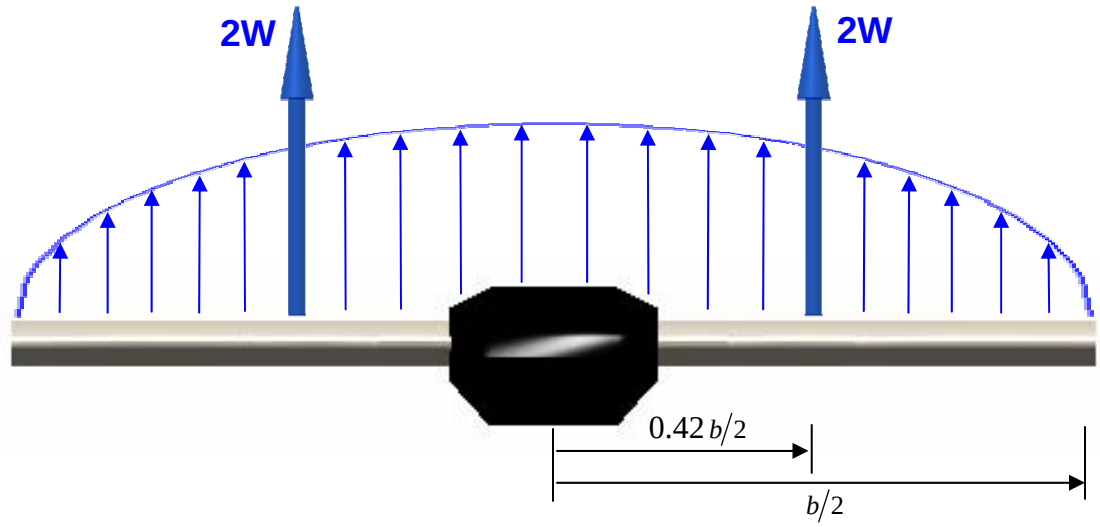

Figure 3-5. Assumed elliptic load distribution for strength analysis and span-wise location of mean load value.

3.3.1 Composite Fuselage Base

The acrylic base was replaced with a carbon-fiber/aluminum hybrid structure to support the additional actuation hardware and to sustain higher transmitted loads from increased test velocity. Significant deflections occurred in the previous design because the actuators would maintain a particular configuration and the external loading would transfer through the actuators, deforming the base. Carbon fiber was chosen as the primary material for its high yield strength to weight ratio. The carbon fiber is a 2x2 twill weave and approximate material properties of a similar composite were taken from [Cruz, 1996]. A single layer of aluminum was added to increase shear load capacity. The base was waterjet machined from two 1/8-inch carbon fiber sheets and a 1/8-inch aluminum sheet. The load potential of the new base will be determined by an ANSYS analysis of the structure. Figure 3-6 illustrates the base layout and assumed load condition. The primary loads are the normal forces at the wing connection point that support wing lift, and the negative tail lift and bending moment. The negative tail lift is a result of trim requirements that will be explored in subsequent chapters. It will be shown later that an antagonistic turnbuckle arrangement carries almost the entire wing bending load so it is not included. The weights of all non-lift generating components are modeled as distributed pressure loads. There is a forward load on the sweep actuators at high angle of attack that reduces the bending moment at the rear of the base. It was not

included in the analysis because it lessened the induced stress of the negative tail lift. There are additional loads in the form of transmitted torques from twist actuation and bending moments from longitudinal forces but these are all relatively small when compared to the applied loading and generally oppose the primary load direction, reducing the stress state.

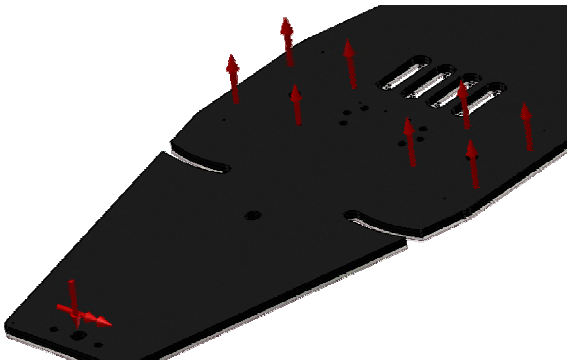

Figure 3-6. Hybrid Fuselage Structure and Assumed Load State for ANSYS analysis. The primary loads are forces and moments from the wing and tail surfaces.

Figures 3-7 shows the resulting deformation of the acrylic base. Figures 3-8 and 3-9 detail the ANSYS analysis for both the acrylic base and the current composite structure. Both supports are 3/8-inch thick but the new base is a full two pounds heavier because of the aluminum plate. The difference in performance of the two structures is obvious in that the acrylic structure deforms approximately 2.4 inches under the maximum load condition while the composite structure deformation is reduced to 0.16 inches. The large deformation of the brittle acrylic structure would most likely result in failure (fracture). While both structures support the normal wing loads well, the greatest effect is from the negative tail lift. The base has to support the entire load and the associated moment with a much longer action arm than for wing lift. It is apparent from Figure 3.7 the significant tail deformation or failure that results.

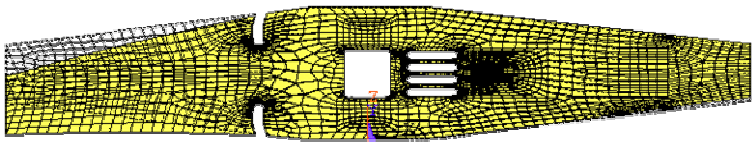

Figure 3-7. Deformation of Acrylic Base Structure. The tail loads are supported directly by the base in induce significant deflection in the acrylic fuselage base design.

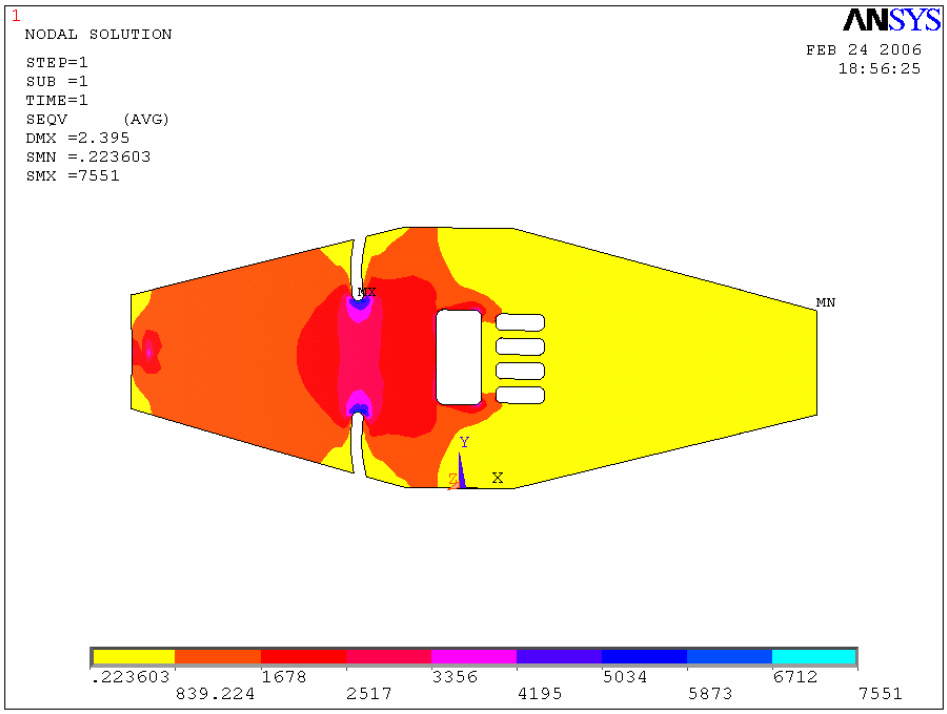

Figure 3-8. Acrlyic Base AnsysAnalysis. There is a maximum deflection of 2.4 inches which would likely cause brittle failure in the structure.

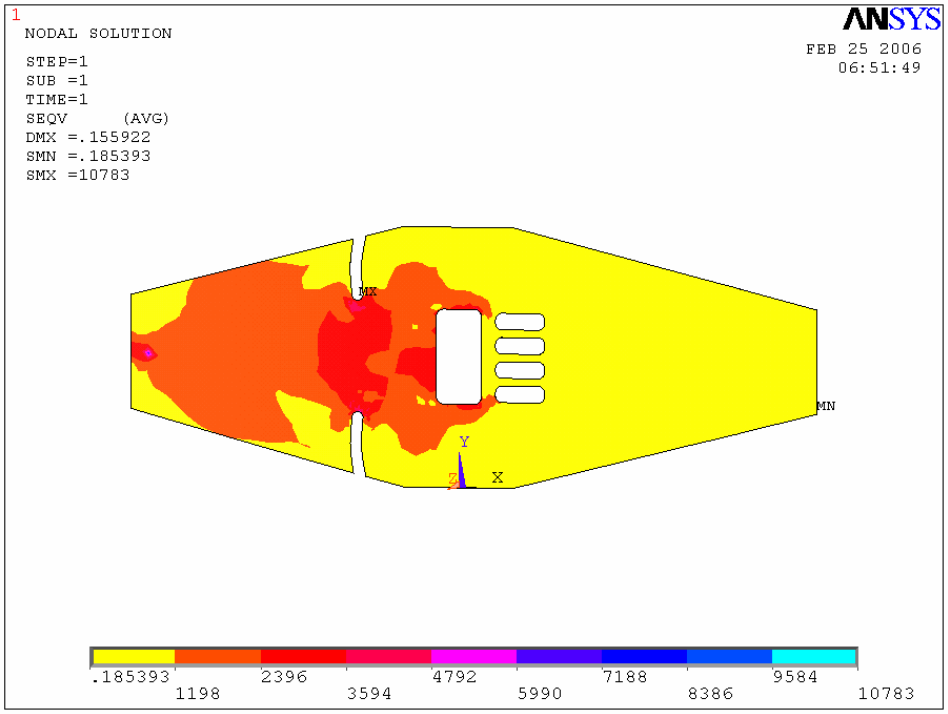

Figure 3-9. Hybrid Composite/Aluminum Base Load Analysis. The maximum deflection is reduced to 0.16 inches. There is a significant reduction in the stress distribution around the sweep paths.

3.3.2 Internal Layout and Function

Figure 3-10 shows the actual internal equipment layout on the upper surface of the fuselage base.

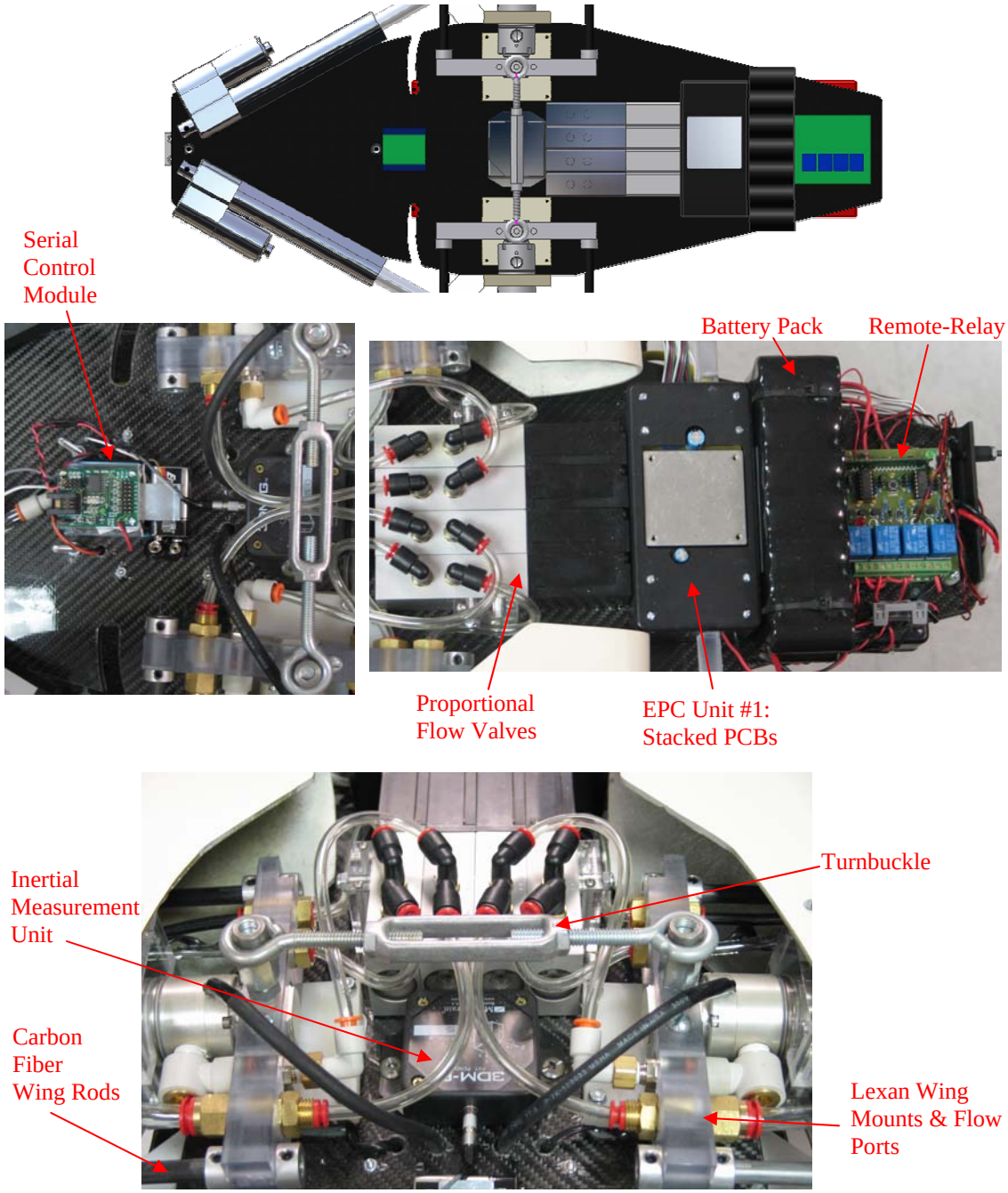

Figure 3-10. Top View of Fuselage Base Layout. The overall component layout is shifted forward to create a weight distribution that assists in stabilizing the vehicle about the mount point.

The remote control unit at the apex of the base consists of relay channels with an onboard receiver. The relay board independently operates each channel to connect power to all the actuation systems. Each relay-channel is connected to an external LED that is mounted on the side of the upper fuselage shell to alert the operator which circuit paths are active. The relay connects each channel to the adjoining battery pack. The 24V, 4500 maH battery is a raw power source for all vehicle sensing and actuation systems.

Behind the battery pack is the first part of the three-component electrical/power/control (EPC) circuit which consists of an enclosure for two, stacked printed circuit boards (PCBs). The boards filter the raw battery input and adjust power/control signals to the neighboring flow control valves.

The directional solenoid valves were replaced with compact proportional flow control valves to permit cylinder velocity control. Planform rate control is critical for developing models of the transient aerodynamics. The flow valves are closed-loop systems that adjust solenoid position in response to an analog command signal thereby providing an approximately proportional flow rate input for the span, twist, and tail actuators. The maximum flowrate of the valves is greater than 12 scfm and they support supply pressures of up to 140 psi. The flowrate is sufficient for driving the large-bore span actuators at their maximum rate (37.5 inches per second) and the pressure capacity is enough to generate significant torque in the twist mechanism (approx. 113 in-lbs at 80 psi). The air supply to the valves is via ports on the underside of the fuselage base that pass through grooves to connect to an air manifold positioned underneath.

Located at the fuselage mount point is an inertial measurement unit (IMU) that measures dynamics for feedback to the PC-104 stack during oscillation tests or wind tunnel control simulation. In addition to dynamics, the IMU computes an orientation vector, offering either Euler angles or quaternion outputs. Three-axis accelerometers measure components of the gravity vector and magnetometers locate the direction of Magnetic North to determine the instantaneous orientation. Rate gyroscopes are used to compensate for drift in accelerating environments. The combination of the three sensor arrays allows static and dynamic orientation to be measured to within +/- 0.5 and +/- 2 degrees, respectively. The raw sensor outputs are also available for angular velocity and acceleration command tracking. The sensors sample at 350 Hz while the orientation

output updates at 100 Hz due to the latency in the microprocessor. The device interfaces with a serial port on the CPU of the PC-104 stack. The data can be fed directly into a SIMULINK control architecture for real-time processing. The serial control module behind the IMU commands a motor control unit for lateral extension of the variable geometry tail.

The IMU is enclosed on either side by the wing sweep/load support assembly pictured in Figure 3-11. The span actuators are mounted above turntables that enable low friction sweep of the wing mechanism. The rods for the upper turnbuckle connection pass straight through the fuselage base and are now connected by a secondary turnbuckle below the wing axis. Although symmetric wing bending loads are distributed to the base through the sweep mechanism and its sliding support, they are primarily supported by the turnbuckle system. Using the design load of 2W in Figure 3-5, the turnbuckles experience symmetric bending moments of 21.5W in-lbs. This requires each turnbuckle to support approximately 322 lbs. The stainless steel turnbuckles each have a listed load capacity of 440 lbs. The corresponding factor of safety is 1.36 for a scenario in which the entire aerodynamic load is supported by the wings alone.

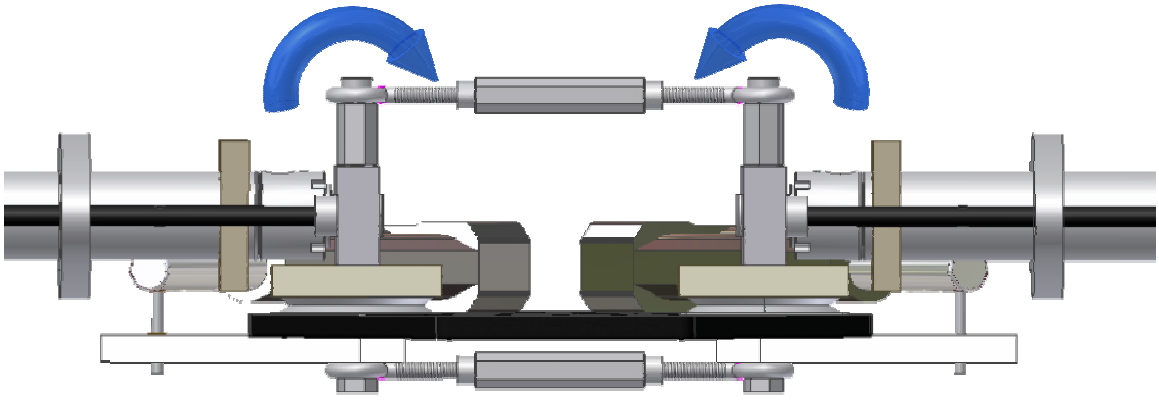

Figure 3-11. Antagonistic turnbuckle arrangement above and below the fuselage base. The turnbuckles support wing bending moments, relieving the base from supporting the additional loads. They also ensure that the wings remain level regardless of loading.

Figure 3-12 shows the sweep-wing connection axis. The sweep actuator drives the wing unit through a stainless steel pin in the rear carbon fiber span rod. The general stability of the pin can be assessed from the longitudinal force. The two critical points are the pin connections to the carbon fiber rod and to the sweep actuator. At a dynamic pressure of 37.7 psf, there is a longitudinal force of 18 lbs on each wing which pulls into

the flow direction due to the vehicle orientation. This load creates both a shear and bending moment between the carbon fiber rod and the span actuator. The pin diameter is only ¼-inch so a maximum normal stress of 16 ksi is generated. Assuming minimum yield strength of 30 ksi for the stainless steel pin, the factor of safety is almost two.

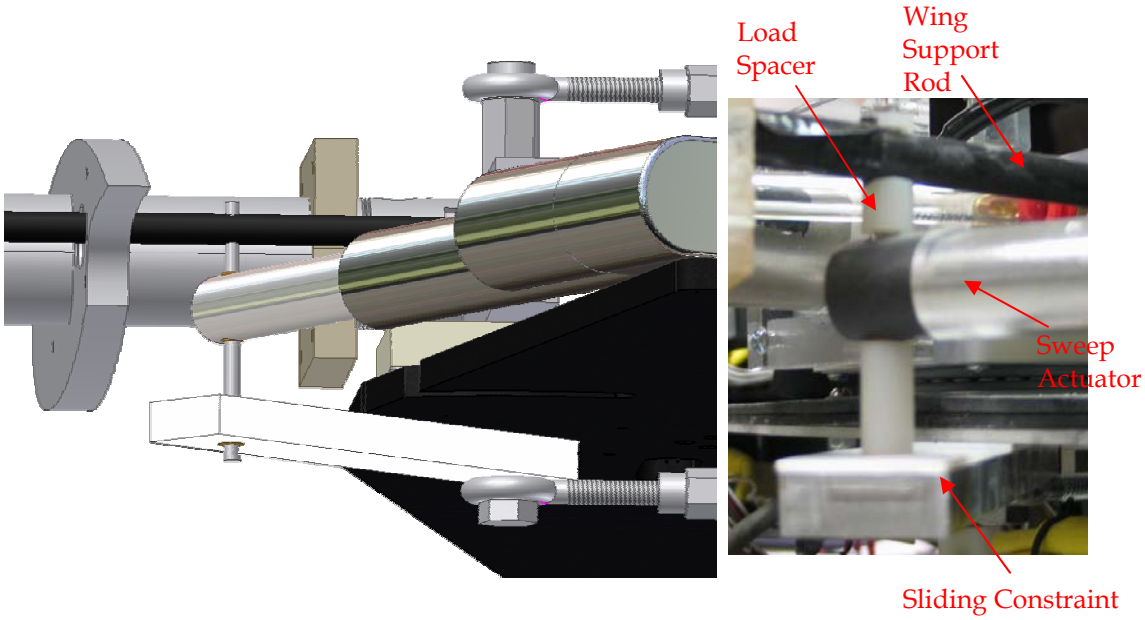

Figure 3-12. Sliding Sweep Constraint. The aluminum bar is coated with a teflon sheet to slide smoothly along the bottom of the base. Pitch moments are transmitted to the base through the sliding block or sweep mechanism depending on the load direction.

Aerodynamic pitching moments and transmitted torque loads from wing twist would cause undesired wing inclination. To maintain level orientation, the wing unit is also attached to a constraint bar that rotates beneath the base. Figure 3-12 shows that the front pivot of the sweep actuator passes straight through the rear rod of the wing system and into a Teflon layered aluminum block that slides along the bottom of the fuselage base. The appropriate grooves are included in the fuselage to maintain the connection for arbitrary sweep angle. A pitching moment or transmitted torque that attempts to pitch the wing forward is resisted by the constraint. Opposing moments are transferred through the upper load spacer, and are ultimately resisted by the sweep actuator which is constrained to the base. The combined system maintains structural integrity while morphing by transferring instantaneous wing forces and moments to the base. We know that the base is well within its load limits and assume that the sliding aluminum

constraint bar and sweep actuator will not fail. The remaining issue is the capacity of the rear carbon fiber rod which must support normal loads from wing twist and shear loads from the pin contact while resisting the longitudinal force.

Assuming a line pressure of 80 psi, the twist mechanism generates almost 113 in-lbs of torque which is transmitted directly to the internal structure. Ultimately, this torque causes a normal load at the root of the carbon fiber rod (the connection to the lexan wing mount in Figure 3-10) and induces a maximum normal stress of 36 ksi. The carbon fiber tubes are standard 33msi carbon with a unidirectional fiber arrangement. The minimum approximate tensile strength is 100 ksi which leads to a factor of safety of approximately 2.75. The shear force from the pin induces an insignificant stress loading relative to the material strength. The analysis indicates significant capacity for supporting aerodynamic pitching moments as well as torque loads from wing twist.

Aerodynamic loads are transferred from the shell to the internal structure at three points. Castigliano's theorem can be applied to determine the reaction at each of the three locations to match the elliptic distribution on the shell. The solution is detailed in the Appendix. The resulting point load application in Figure 3-13 is non-intuitive but is required to balance the pitching moment from the mean load location.

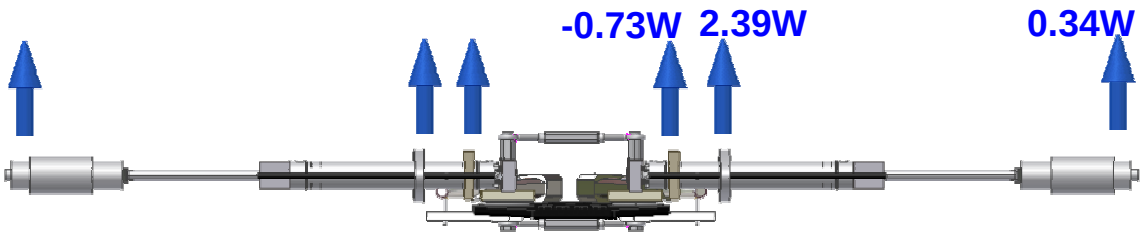

Figure 3-13. Load transfer points to internal structure. The effective point loading is determined from applying Castigliano's theorem to the elliptic load distribution in Figure 3-5.

The end rods on the linear span thruster were too fragile to support the applied torque from twist actuation (the pneumatic shaft does not support a torque load) and offered little assistance for wing bending loads. The small extending rods on the linear thrust mechanism were replaced with a larger steel support rod mounted to the span cylinder through a linear plain bearing. The sliding twist constraint, pictured in Figure 3-14, allows the hardened steel rod to extend parallel to the drive shaft of the pneumatic

actuator. A stainless steel plate connects the shafts and also mates to the twist mechanism. The mechanism supports larger aerodynamic bending loads as the drive rod extends and higher transmitted torques as the wing twists while maintaining a low sliding friction due to the linear bearing.

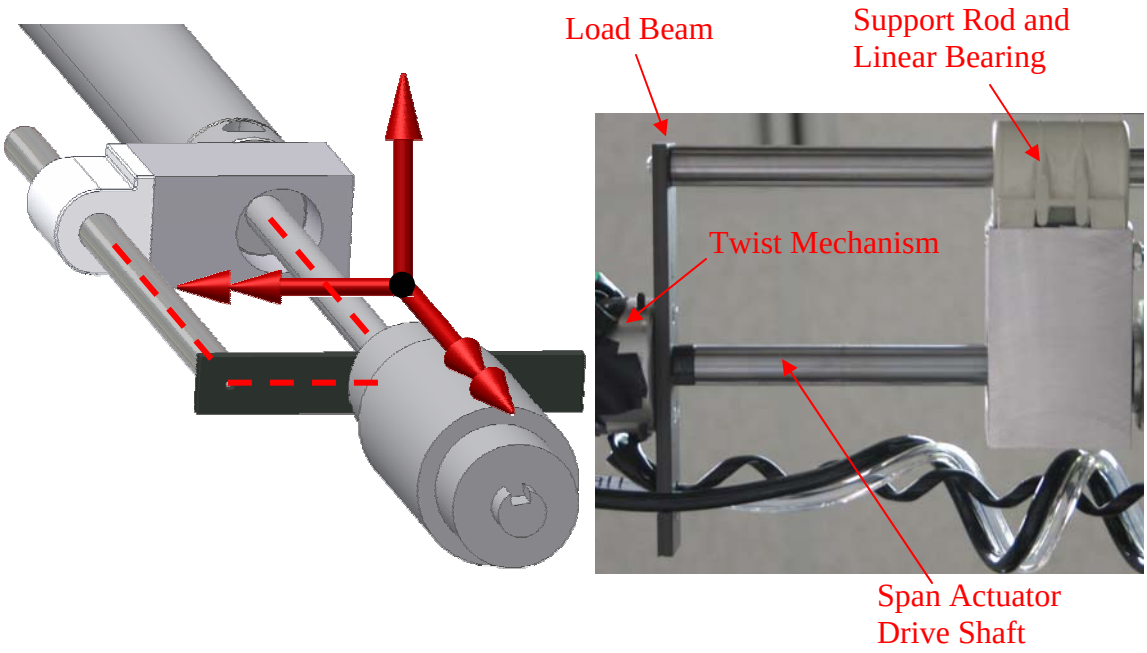

Figure 3-14. Sliding support to maintain wing orientation and support wing bending loads during span extension. A titanium screw joins the load beam to the sliding support rod.

As mentioned previously, at the wing root opposing torques are transmitted to the base either through the sliding sweep constraint or via the sweep mechanism, leaving the sliding twist constraint for analysis. The applied loads are the 113 in-lbs from the twist mechanism, and the effective force/moment transferred from the wingtip force in Figure 3-13. The statically indeterminate support system is easily analyzed by modeling the members as three-dimensional beam elements in ANSYS and assuming a cantilevered boundary condition. The response in Figure 3-15 shows the maximum stress state where torque from positive washout is transmitted through the structure. The maximum stress in the load beam is high enough to validate the stainless steel construction.

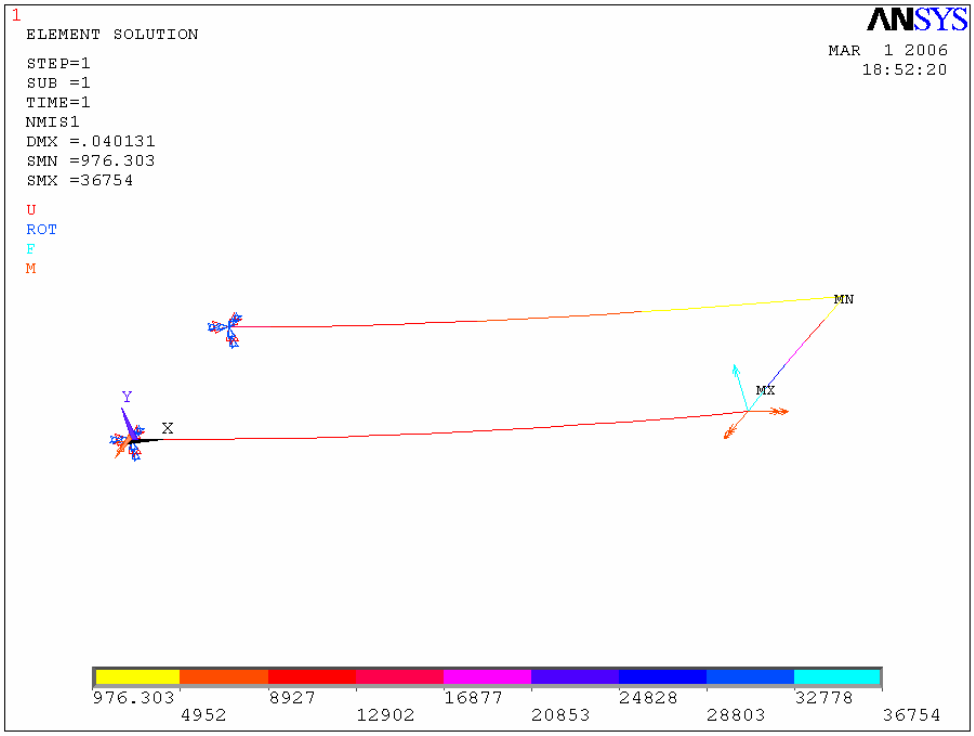

Figure 3-15. Static Response of fully-extended sliding twist constraint. The load condition includes the transmitted wing torque from applied twist and wing bending loads.

Figure 3-16 displays the underside of the fuselage base. Starting at the nose is the second part of the EPC system, an enclosed PCB that has two motor control circuits to govern the linear sweep actuator rate. A 12V battery is also contained within the enclosure to provide nominal power to the relay board on top.

The embedded computing/data acquisition system is positioned aft of the PCB enclosure. The PC-104 stack is maintained as the CPU, the power supply, the D/A, the A/D, and the relay board. The relay board function was reduced to controlling the directional solenoid valve for the false-front tail contraction, and sourcing power to the lateral tail extension.

Behind the PC/104 stack is the air manifold that takes a single input from an external air supply and outputs four vertical flow ports through the fuselage base and into the proportional flow valves above. The manifold also outputs a single horizontal flow port towards the rear that connects to the proportional flow valve for the linear tail actuator.

The vehicle mount is located aft of the air manifold. It ports air and electrical connections to the rear of the plane and attaches the structure to the wind tunnel strut balance or sting mount.

Behind the vehicle mount is the last segment of the EPC system. The enclosure houses a PCB that conditions and reads all analog inputs from the potentiometers. Behind the feedback unit is the linear tail actuator, constrained to the base by flow ports. The corresponding proportional flow valve is mounted beneath the actuator.

The layout demonstrates an efficient use of space for functional enhancements to the vehicle design. All systems are able to coordinate in a well-organized manner to permit reliable and consistent testing at higher loads. Pertinent details for the more significant design enhancements follow.

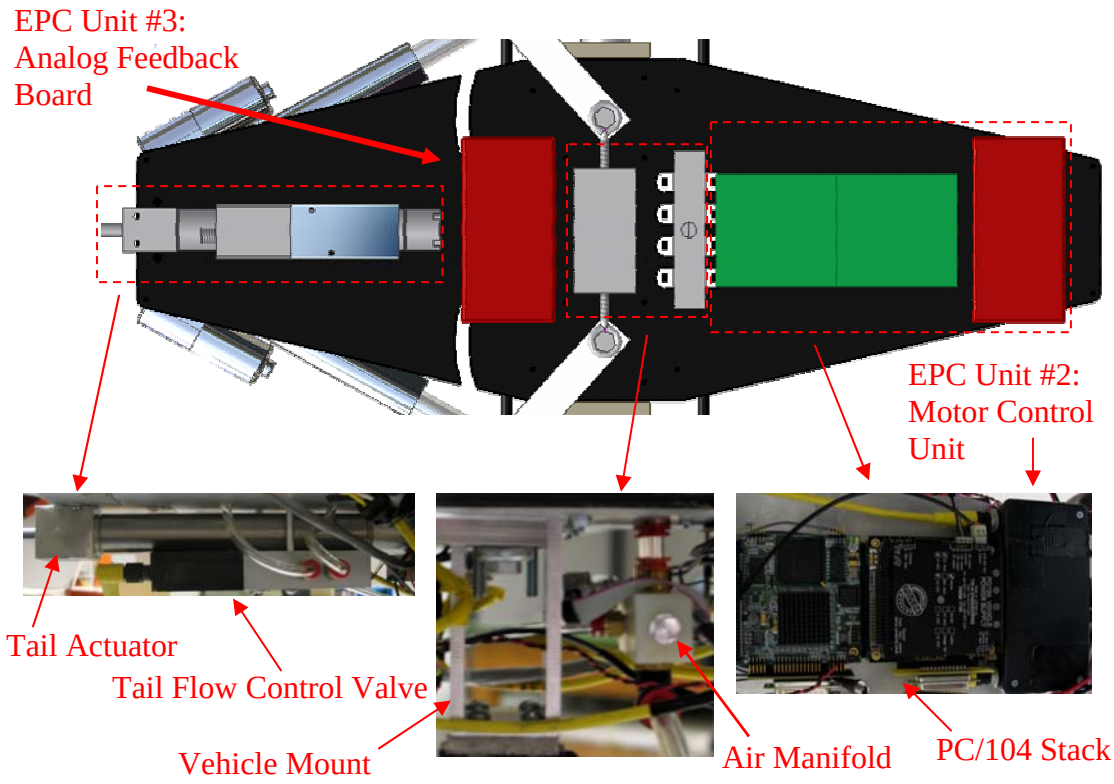

Figure 3-16. Underside of Fuselage Base Detailing Component Arrangement. The design illustrates an efficient use of space permit smooth functioning and integration of all systems.

3.3.3 Variable Geometry Tail Design

The horizontal tail is the main performance addition to the model. It changes the APVE from a variable sweep/variable span planform into a vehicle that completely transforms configurations. The VGT also succeeds as an independent controller for the aerodynamic center location. The fuselage now has a fixed chord length.

The VGT meshes with the swept main wings to create a larger, single wing area and counteracts the aft shift in the aerodynamic center associated with wing sweep. Three planform configurations with various tail orientations and a transparent fuselage shell demonstrates the new loiter-dash transition in Figure 3-17. The tail dimensions and actuation path are set to line up with the outer edge of the main wings when fully morphed. The wings simultaneously contract and sweep back as the tail contracts in the longitudinal axis and extends in the lateral axis. When the main wings sweep back, the two surfaces join together to form a solid wing planform. The result is a transformation from a standard aircraft to a Delta-style planform configuration.

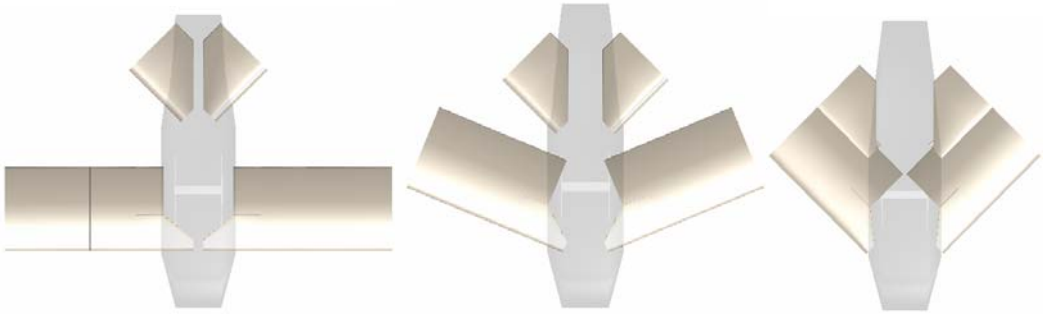

Figure 3-17. Vehicle Planform Transition. The wings sweep back and contract as the tail performs lateral extension and longitudinal contraction. The loiter and dash configuration become completely separate vehicles.

The tail lateral actuation structure pictured in Figure 3-18 is a lead screw device driven by a worm gear and guided by linear bearings. A 24V motor drives a worm gear which rotates a custom formed 3/8-inch lead screw rods with opposing threads. The attachment to right and left-handed nuts mounted inside of the semi-airfoil sections effectively creates dual lead screw drives. The airfoil sections traverse the lead screws guided by 3/8-inch hardened aluminum rods. The rods are mounted to the base tail structure and slide inside of linear plain bearings within the semi-airfoils, mounted parallel to the lead screws.

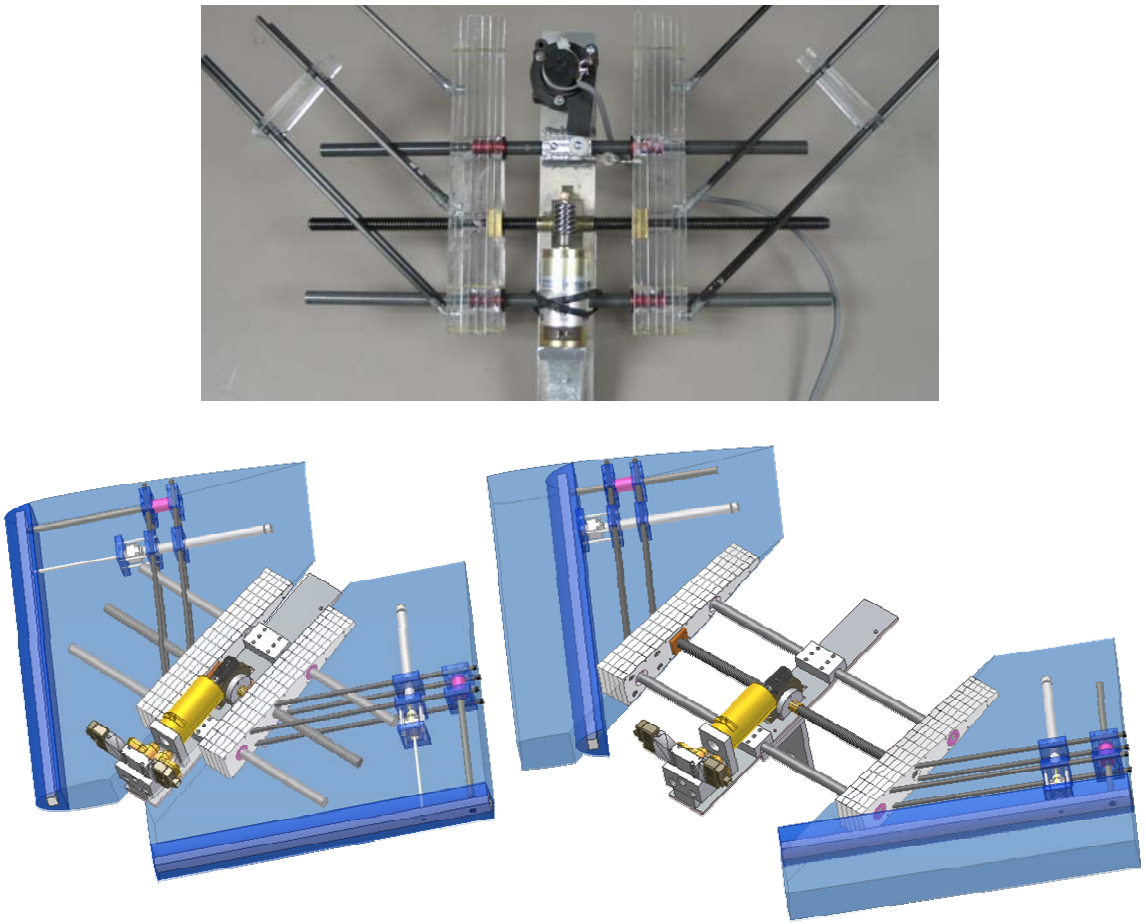

Figure 3-18. Tail Lateral Extension Mechanism and contraction of 'false-front' into wing body. The false-front contraction rate is governed by a manual flow control valve at the input to the solenoid.

The key to meshing the wing and tail surfaces is to somehow remove the nose of the tail when the wings sweep back. This is accomplished by establishing the tail nose as a 'false front' that retracts into the tail body. Similar to the main wings, a modified airfoil is used to shift the thickness distribution to satisfy a morphing function. The tail airfoil was designed as a NACA 0015-62 because shifting the maximum thickness to 20-percent of the wing chord makes it easier for the trailing edge of the main wing to slide inside. The concept of this 'false-front' design is displayed in Figure 3-18. A miniature pneumatic actuator (5/32-inch bore) drives a lexan block mounted inside the nose cavity to a total displacement of 3-inches. A ¼-inch aluminum shaft constrains linear motion and supports lateral forces as it slides through a linear bearing parallel to the drive shaft. The solenoid valve at the front end drives both actuators with the same flow signal.

Geometric constraints limit false-front contraction to points of complete lateral tail extension.

The worm gear drive reduces the 10,000 rpm motor output to 1000 rpm and increases the 2.6 oz-in torque output to 1.6 in-lbs. The lead screws have twelve turns per inch which, combined with the actuation rate, results in a maximum lateral extension rate of 1.4-inches per second. The tail planform was designed to fully mesh with the main wing segment at a linear contraction of six inches and a lateral extension of four inches. At the maximum driving rate, it takes just under three seconds for full lateral extension. Similar to the twist and span coupling, the linear and lateral tail motions are mechanically independent but aerodynamically coupled. As the tail is extended laterally, the effect on the aerodynamic center location depends on its longitudinal reference to the other planform areas which is controlled by the linear extension actuator.

The serial control unit behind the IMU in Figure 3-10 modulates lateral extension of the horizontal tail via the driving motor velocity. The serial unit applies direct motor control using a proportional speed controller that is commanded from the servo-controller mounted above it. H-bridges in the speed controller amplify the servo-controller signal to the high-current PWM required to drive the motor. The servo-controller accepts binary command signals from the PC-104 stack. Feedback is provided from a linear potentiometer attached to an extending semi-airfoil section. The devices are wrapped in a control loop through the on-board CPU to track lateral position.

The addition of the variable geometry tail extends the control and performance capability of MORPHEUS by allowing direct control over the aerodynamic center location. It also increases the possible number of configurations and can be used to vary the stability of each. The most significant benefit is the capability to completely transform the planform geometry through meshing with the main wings in the fully-morphed configuration.

3.3.4 Compliant Twist Wings

The addition of the molded compliant wings facilitated testing wing twist under load. The solution to obtaining a serviceable compliant wing was casting an integral-

skin, flexible polyurethane foam. A special mold was created of the airfoil profile, extruded by 14-inches. The mold included an inset to form a specially shaped void inside the body to avoid the internal wing structure when telescoping. The foam was cast into the mold and cured into the design shape. The integral-skin foam develops a smooth exterior layer of 1/8-inch solid polyurethane rubber on the mold boundaries. The interior foam is 8 lb density and the complete system provides a smooth and compliant body that can be actuated by the twist mechanism and still maintain its smooth exterior form. The wing cross sections displaying the molded insets are displayed in Figure 3-19.

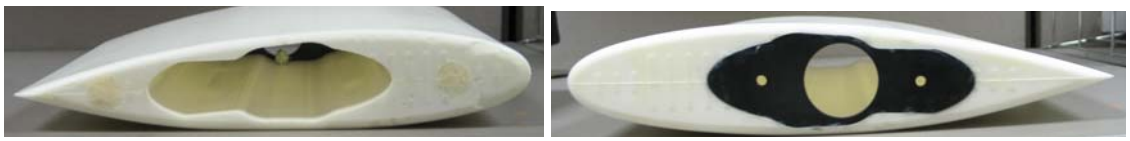

Figure 3-19. Compliant Wing Cross-Section View. The molded inset shape was designed specifically to slide over the internal wing structure during span extension.

The internal cavity consumes a large percentage of the internal wing volume to completely clear the internal structure. Leakage from gaps in the vehicle structure allows air to flow into the wing cavity until a static pressure is formed equal to the dynamic operating pressure. The ANSYS presentation in Figure 3-20 shows that at the design pressure of 37.7 psf, there is significant deflection in the wing form of approximately 1.5-inches

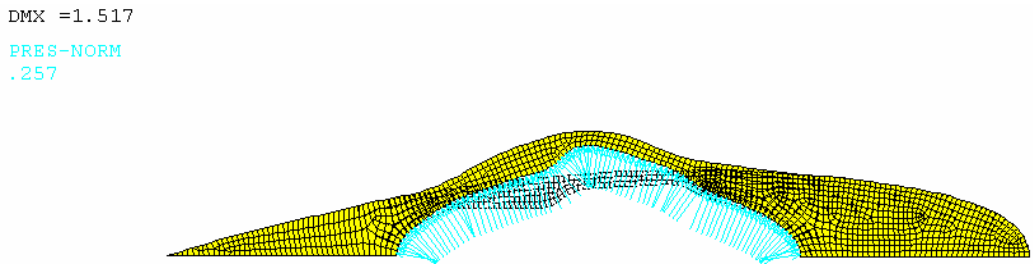

Figure 3-20. Deformation of compliant wing cross-section from pressure loading on the internal cavity. Internal pressure build-up is from flow into fuselage openings. Significant deformation occurs without accounting for the additional external loading.

The ANSYS readout in Figure 3-20 is for an assumed polyurethane modulus of 100 psi and does not take into account the external pressure loading from the aerodynamic forces which would cause further warping.

To prevent the unacceptable deformation, aluminum inserts were designed to provide an internal boundary condition in the cavity. Figure 3-21 shows the layout and function of the additions. Multiple ¼-inch wide (1/16-inch thickness) sections are fixed inside the wing cavity with the purpose of supporting both internal and external pressure loading without impeding the twist capability. The shapes were created by waterjet machining the shapes from a solid aluminum sheet.

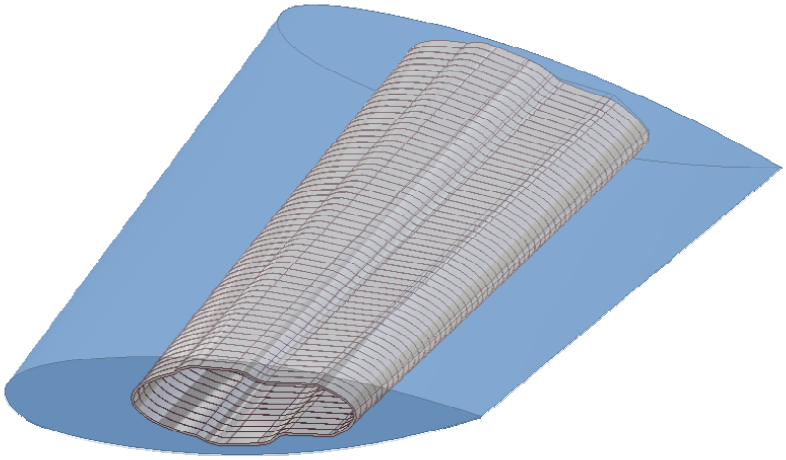

Figure 3-21. Compliant wing with custom aluminum inserts for normal load support. The inserts cause a weight penalty but are required for twist actuation in the wind tunnel.

Figure 3-22 indicates that minimal deflection occurs when the structural analysis is repeated with the internal aluminum sections. External pressure loading is included to simulate actual test conditions. The external pressure distribution was computed from XFOIL using approximately twice the design lift coefficient to account for potentially higher loading with twist actuation. The presentation shows that the maximum deformation under assumed load conditions was reduced to 0.02 inches. The effect of the internal segmentation is precisely what is required for a variable twist wing: a structure that can fully support normal loads, has a smooth exterior surface that is maintained when actuated, but maintains low torsional rigidity for mechanical control. There is just over a one pound increase in the compliant wing weight due to the aluminum sections.

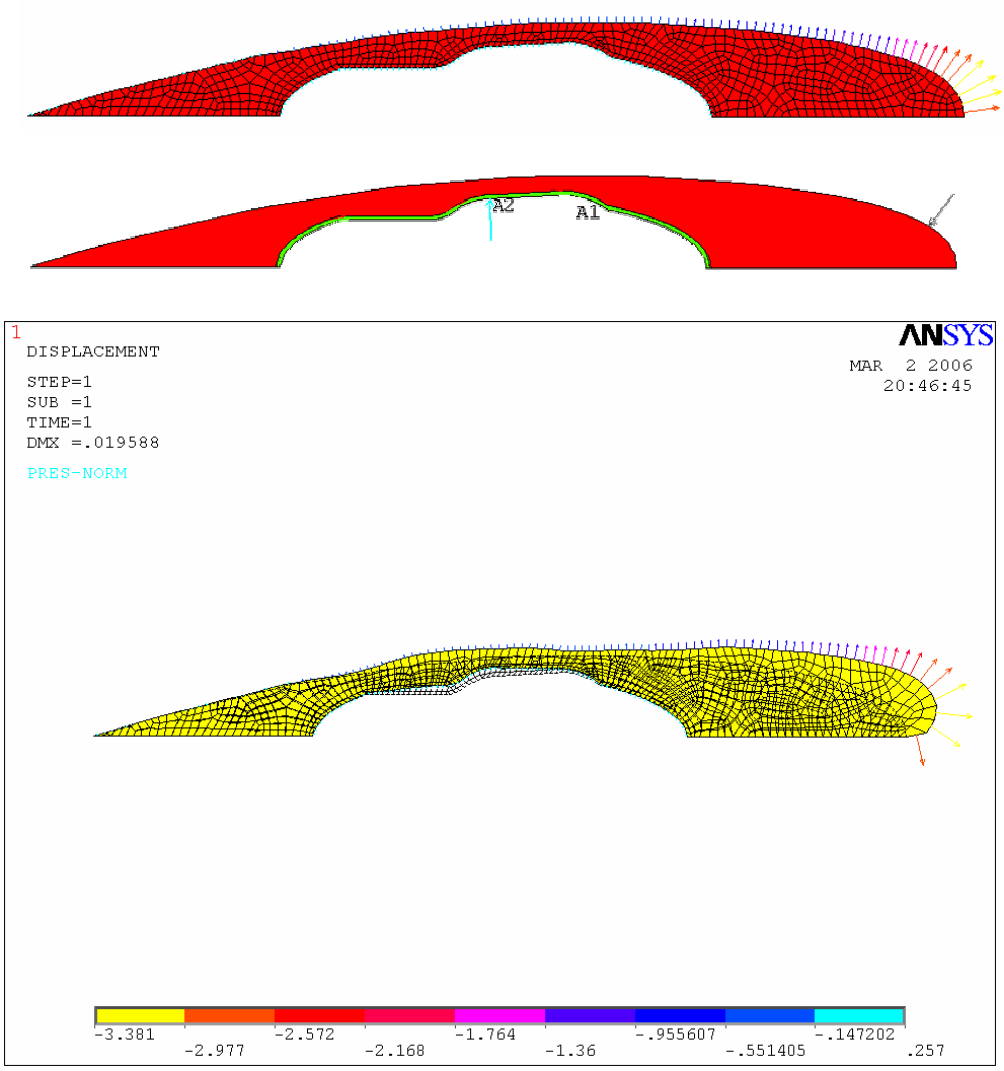

Figure 3-22. Structural analysis of 2D compliant airfoil section with both internal and external pressure loading. The analysis ignores the integral skin structure which would increase structural stiffness.

The wing was actuated by a thermoplastic inset shaped to the void and secured to the outside edge of the body. The second image in Figure 3-19 shows the inset. Wing twist was applied by rotating the inset to twist the compliant wing. The aluminum bar pictured in 3-23 served as the transfer mechanism. The bar was secured to the inset using mount holes and to the twist mechanism via a keyway. As the twist mechanism rotated, the keyway connection forced the aluminum bar to rotate, which caused the

inset to rotate. The inset then twisted the compliant wing. Figure 3-23 shows the compliant wing mounted to the plane and actuated to its limits.

Figure 3-23. Twisting the Compliant Wings. A smooth contour is achieved by combining the internal twist mechanism and the complaint external structure.

3.3.5 EPC Circuit

The previous electrical design for the Phase One model was a single project breadboard that contained a large assortment of wires to connect all the feedback and output units. The design was unreliable, inefficient, and required multiple off-board power supplies to actuate. The current design is comprised of four custom designed printed circuit boards.

The first two boards are pictured in Figure 3-24 and comprise EPC unit one as referenced previously. They work together to provide power and control to the proportional flow valves. The top board consists of a 24V DC-DC switching converter and the required stabilizing circuitry. It takes the raw, power input from the battery and outputs a 'clean' 24V supply while sourcing a maximum of 8.4A. The converter is a switching regulator and uses a transistor to store energy in an inductor and transfers it to a filter capacitor to smooth the output. The switching duty cycle or frequency is

varied through an internal feedback to achieve a set voltage level. The switching process provides protection between the unregulated source and the devices requiring the power input.

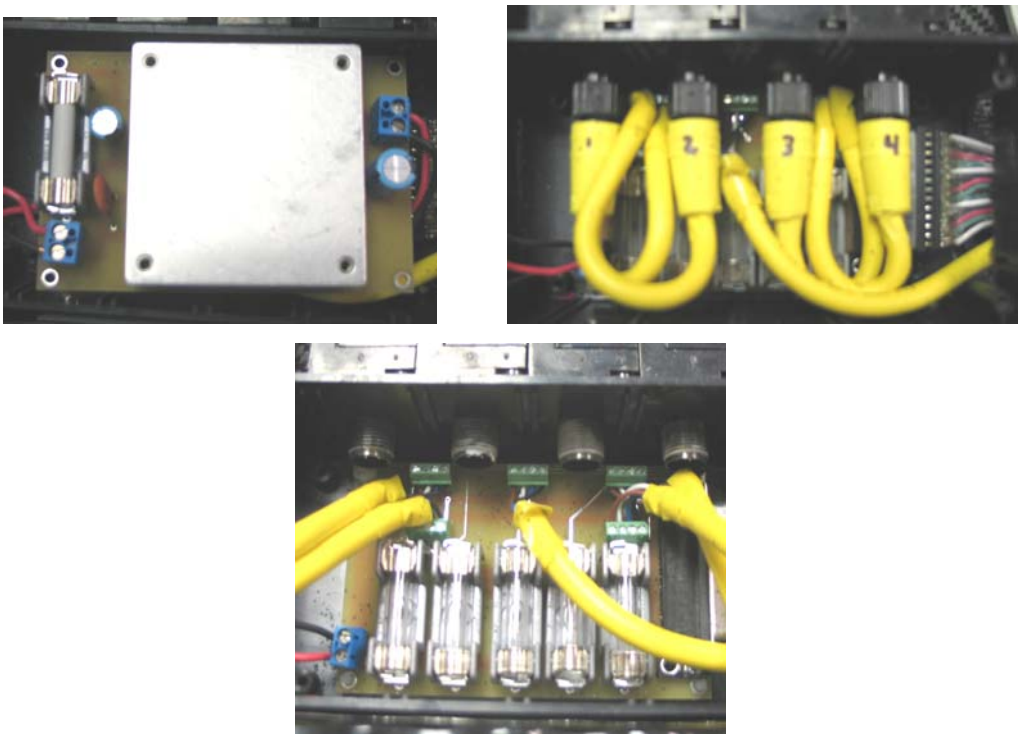

Figure 3-24. EPC Unit One. The top board is a DC/DC converter to clean the source power. Picture B shows the output ports from the valve board connected to the proportional flow valves. Picture C displays the actual valve board which protects and routes data to the valves.

The top board supplies a clean 24V source to the valve conditioner board on bottom. The valve board has a 25-pin serial connection to connect to the D/A board which sends zero to ten-volt command signals from the CPU. The valve board routes the analog command signals and the 24V source to the appropriate flow valve. Each valve draws power from the 24V source (up to 1.1A at maximum solenoid deflection) in response to the analog signal to move the solenoid by the desired amount and generate the commanded flowrate for actuator control.

The second segment of the EPC system is the sweep control unit. Similar to the valve board, it connects to the D/A board over a serial cable to accept both analog and digital command signals. The PCB implements two separate motor control units to manipulate the velocity and direction for each of the sweep actuators. The sweep control

unit is pictured in Figure 3-25. Each motor control circuit consists of an H-bridge motor controller and two high side MOSFETs to control the motor direction. The low side MOSFETs can switch at high frequencies to generate a PWM control signal to the actuators. The H-bridge and high side MOSFETs are integrated in a single primary unit. The primary unit takes direction information from digital I/O pins on the D/A board and a 0-5V analog command signal for the motor rate. The direction input command activates one of two lowside MOSFETs. Rate information controls the duty cycle output from the lowside MOSFET to drive the motor at the desired speed. As a whole, the motor control unit closes a velocity control loop, essentially transforming the sweep actuators into rate-controlled servomotors.

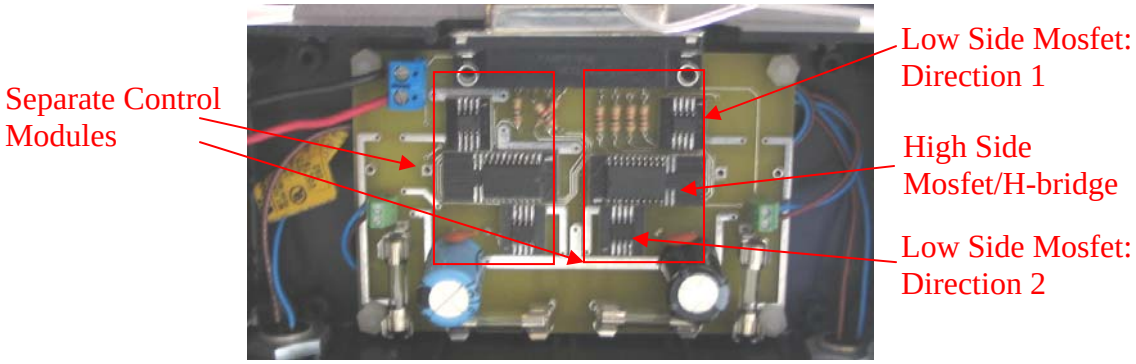

Figure 3-25. EPC Unit Two: Motor Control Unit. Two independent units are combined to independently control each sweep actuator. The unit is designed to control motor velocity in response to an analog command signal.

The final segment of the EPC system is a PCB board that measures data from the potentiometers and transfers it over a serial connection to the A/D board in the PC/104 stack. The board, pictured in Figure 3-26, has a dual op-amp that uses a 12-V supply from the PC/104 boards and amplifies a 5V signal to provide a constant, 10V reference voltage for the potentiometers.

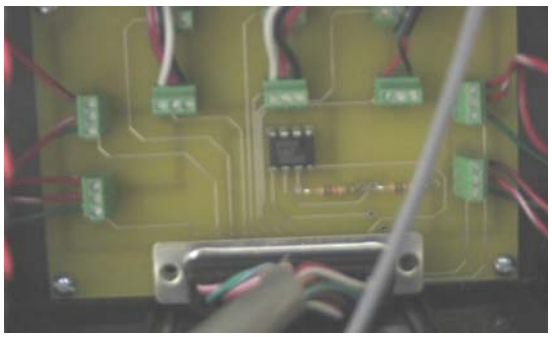

Figure 3-26. EPC Unit Three: Analog Feedback Unit. The appropriate signal conditioning is embedded on the board for all of the analog inputs.

The power schematic, pictured in Figure 3-27 demonstrates how the supply is sourced to the various system subcomponents. The approximate continuous draw of 32.4W means that the 4500 mAH battery can power the aircraft model for 3.5 hours at 24V. Protection hardware is implemented in each power line to permit safe operation.

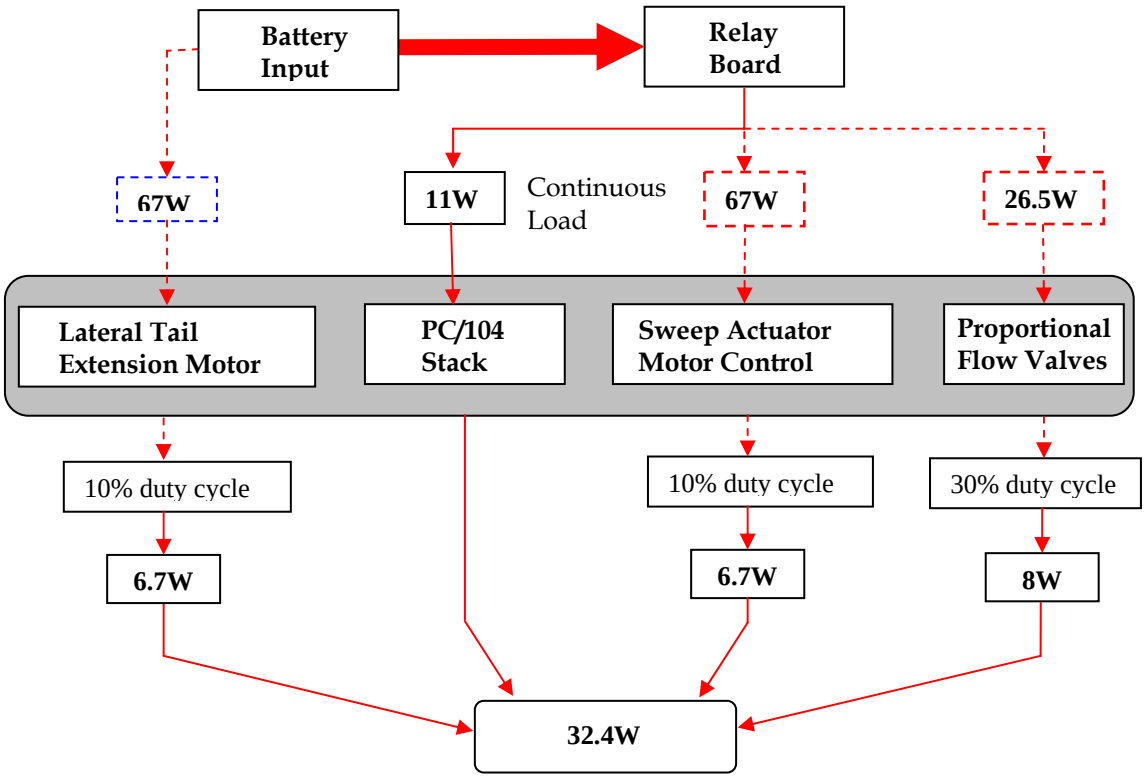

Figure 3-27. System Power Schematic. Dashed lines indicate devices that require intermittent power draw. The continuous load is approximated by the duty cycle of the actuator.

3.4 Embedded Vehicle Control

Subsystem interaction on MORPHEUS requires significant closed-loop manipulation and coordination for the desired vehicle performance. In particular, planform trajectory control is required which requires closed-loop control law construction for the pneumatic actuators beyond simply proportional feedback. Various timing constraints are necessary to effectively control the electromechanical system and specific path commands are required to coordinate the vehicle subsystems.

3.4.1 Pneumatic Control Design

Planform rate control is necessary for modeling the transient aerodynamics during morphing and for any application in which a planform alteration serves as a system control input. Wing twist replaces elevons on the MORPHEUS, requiring precise, high-bandwidth twist control. Span trajectory control is prototyped on a benchtop linear pneumatic cylinder to develop and demonstrate tracking S-curve profiles. Position s-curve profiles correspond to a constant acceleration up to a velocity value that is maintained for some time period and followed by a deceleration of the same magnitude back to zero velocity. It is representative of the desired pneumatic performance to smooth out ramp motions. The benchtop cylinder is connected 'in-the-loop' to the MORPHEUS embedded hardware and data acquisition system to apply control algorithms. Position control for the rotary pneumatic actuators (twist) is developed directly on MORPHEUS testbed.

The dynamics of pneumatic systems are highly nonlinear due to the compressibility of the fluid. The standard actuator model first presented by Shearer (1956) is composed of three parts: the flow valve, cylinder chamber, and load dynamics. The system in Figure 3-28 details the simplified model assumptions in deriving the equations of motion.

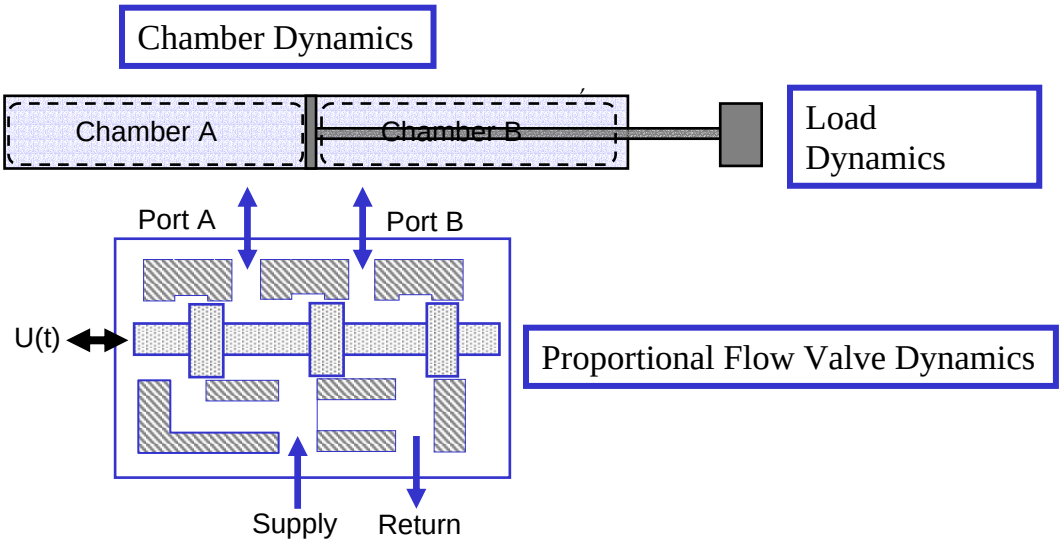

Figure 3-28. Pneumatic Actuation Schematic. The nonlinear dynamics corresponding to each subsystem is presented in Appendix C.

The nonlinear dynamics for figure 3-28 can be found in a majority of pneumatic control literature, all derived from the initial presentation by Shearer (Appendix C). The important result for the current control design is the load dynamics model which is computed from a simple force balance on the piston which requires pressure inputs from the chamber dynamics

$$\ddot{x} = \frac{1}{m}\left(A_a P_a - A_b P_b - \left(A_a - A_b\right)P_{atm} - F_f - b\dot{x}\right) \tag{3.1}$$

The friction term, F_f, is generally modeled as Columb friction and is a major obstacle in accurate trajectory control. The pressure in the cylinder chamber has to reach an adequate level to overcome the static friction and begin motion. This leads to significant delay which is a general characteristic of pneumatic actuation. Figure 3-29 shows force response results from load cell testing of the benchtop cylinder with disconnected airports. This general method of friction identification was used by [Richer, 2000] to identify Columb friction and the viscous damping coefficient. A load cell was attached to the cylinder and it was manually actuated. Peaks in the force response correspond to the static friction load required to initiate motion. An approximately constant value of 1.3 lbs was determined for the unloaded cylinder.

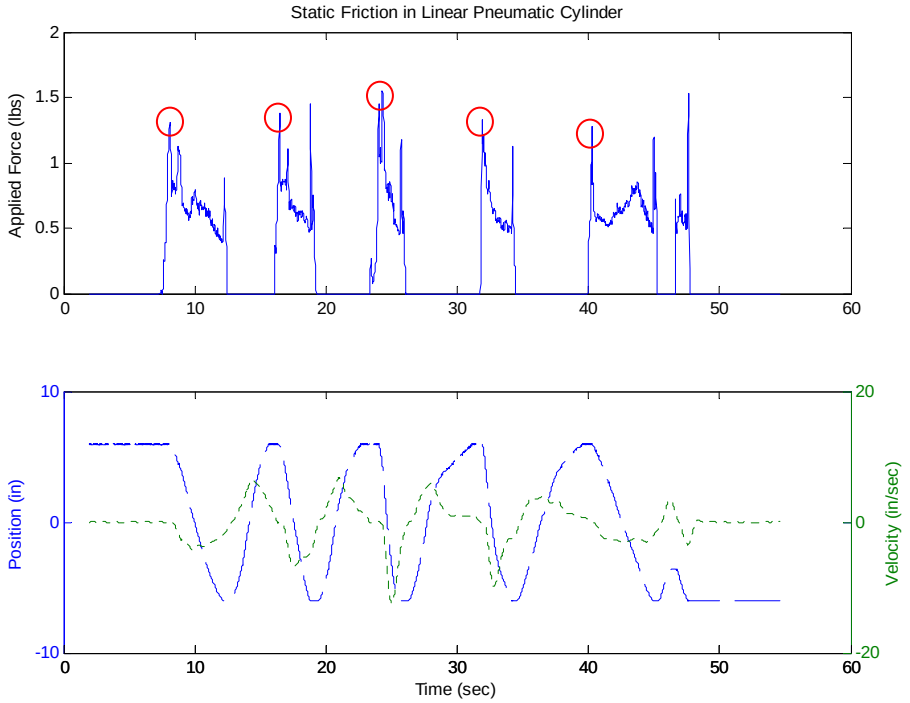

Figure 3-29. Friction Response of pneumatic cylinder. Highlighted peaks correspond to initiation of motion and static friction value. A pressure differential has to generate approximately 1.4 lbs of force before the unloaded cylinder rod moves.

The complete equations of the cascaded system are highly nonlinear and researchers have applied a host of linear, intelligent, adaptive, and nonlinear control methods with varying levels of success [Linnet, 1989; Lai, 1990; Wang, 2001; Bobrow, 1991; Varseveld, 1997; Pu, 1991a]. In general, model based control techniques require detailed system identification of flow parameters which are difficult to obtain. The current control method consists of combined proportional control with feedforward position command signals. Initially the proportional gain was maximized which generated an accurate, but oscillatory tracking response. Figures 3.30 and 3.31 illustrate the tradeoff in accurate tracking versus smooth motion with increasing proportional gain. Note that the figures on the right illustrate the velocity command and tracking corresponding to the s-curve trajectory on the left. Figures 3.30 corresponds to a high gain response and 3.31 to low gain response for tracking a 10 inch-per-second ramp command. There is significant delay in starting the motion because the error has to build up to overcome the static friction. Once the cylinder starts moving, the high proportional gain generates a control effort that causes the cylinder rod to move faster than the reference signal. As the cylinder position approaches the instantaneous command value, the control effort falls off to zero and the error has to build up enough to overcome friction and continue the motion. The result is a 'stair-stepping' position response and a marginally stable velocity response although the general command signal is tracked.

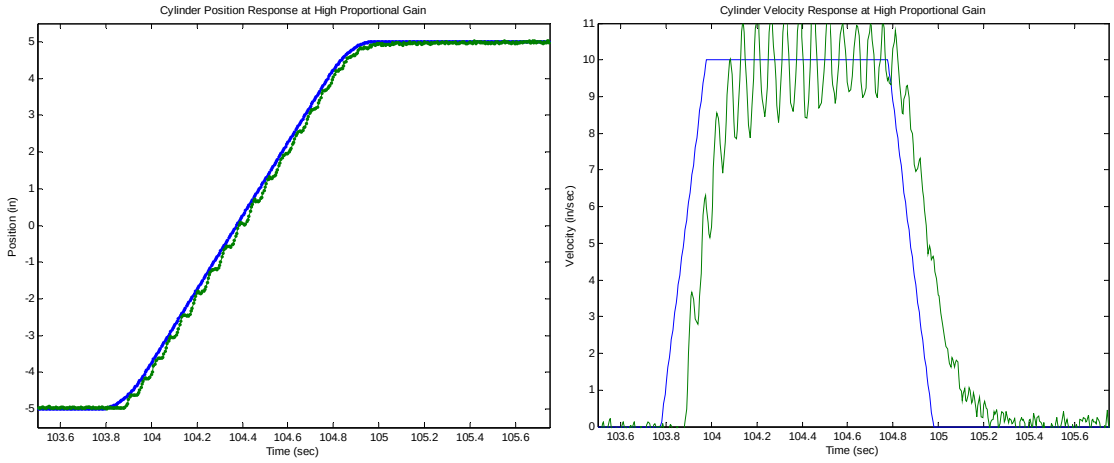

Figure 3-30. Controlled pneumatic response to proportional gain. High gain values cause 'stair-step' position tracking with an oscillatory velocity response.

With low proportional gain, there is a much larger response delay and the signal is always chasing the reference because the gain is not high enough to yield an accelerated response to catch it. The result is a smooth motion but the cylinder rod does not approach the reference trajectory.

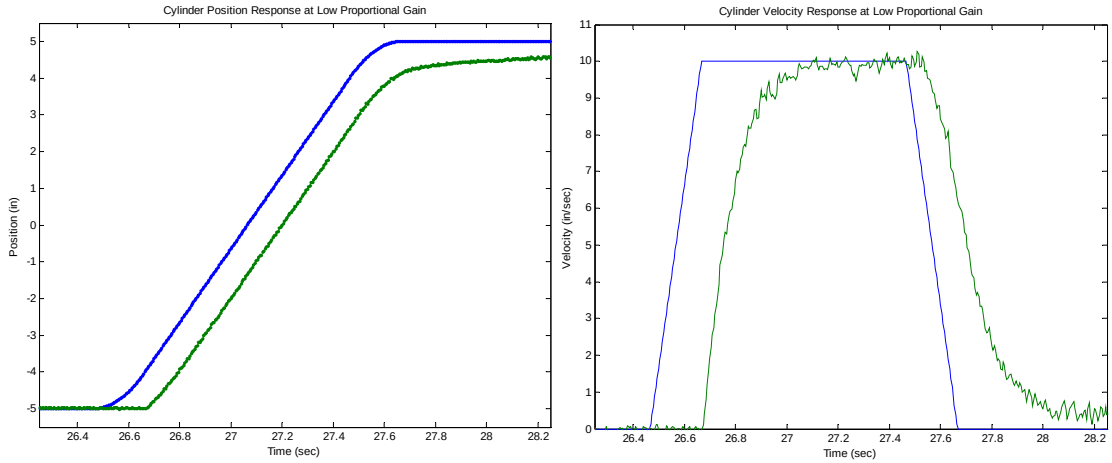

Figure 3-31. Controlled pneumatic response to proportional gain. Low gain values experience a smooth motion but a significant response delay.

Figure 3.32 amplifies the position tracking response for the high proportional gain, illustrating the acceleration of the cylinder rod between 'stair-steps'. We see that the gain still is not high enough to overcome friction in reaching the trajectory. The tracking requirement is to increase the proportional gain value to for error attenuation but to avoid the oscillatory velocity response that will increase with the system gain.

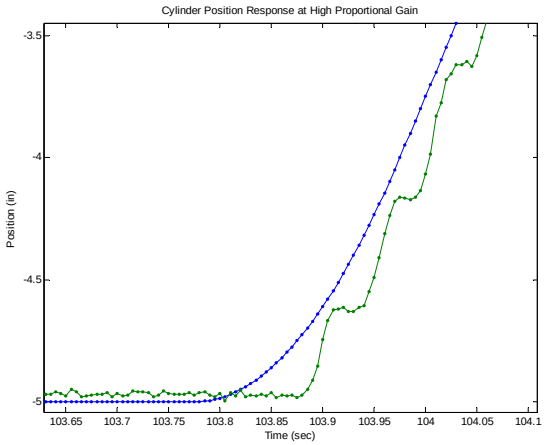

Figure 3-32. Illustration of stair-step position tracking. In between steps the cylinder velocity stops until enough pressure builds up to overcome the static friction. Note that the command signal still is not achieved so the control gain is not large enough.

We see from Figure 3-31 that the solution to achieving smooth ramp tracking is for the cylinder to never stop moving, so that friction only needs to be overcome at the initial motion. By reducing the proportional gain the cylinder does not initially jump up to the command signal so a constant error signal is maintained with the command signal and the appropriate velocity signal is tracked smoothly. The two drawbacks to the low gain method are pictured in Figure 3-31: 1) there is a constant delay in the tracking response that increases with the command signal and 2) the final position value is not achieved because of the low proportional gain. Both problems can be alleviated through feedforward control of some number of samples of the reference signal. The correct number of feedforward samples is scheduled a priori and decreases with the command rate. The drawback of the method is that it lacks robustness with respect to the predetermined feedforward samples for tracking. In future application, adaptive neurocontrol methods will be implemented to control the nonlinear dynamics in (3.1)-(3.3) with uncertain parameters. Figure 3-33 demonstrates accurate tracking with a moderate control gain and position feedforward. This is an initial design attempt and robust tracking improvement is possible by combining higher proportional gains with acceleration feedback to stabilize the motion. Pu (1991) and Wang (1999) found acceleration feedback to be useful for stabilizing the velocity response at higher proportional gains by emulating inner loop pressure feedback to the load dynamics in (3.1).

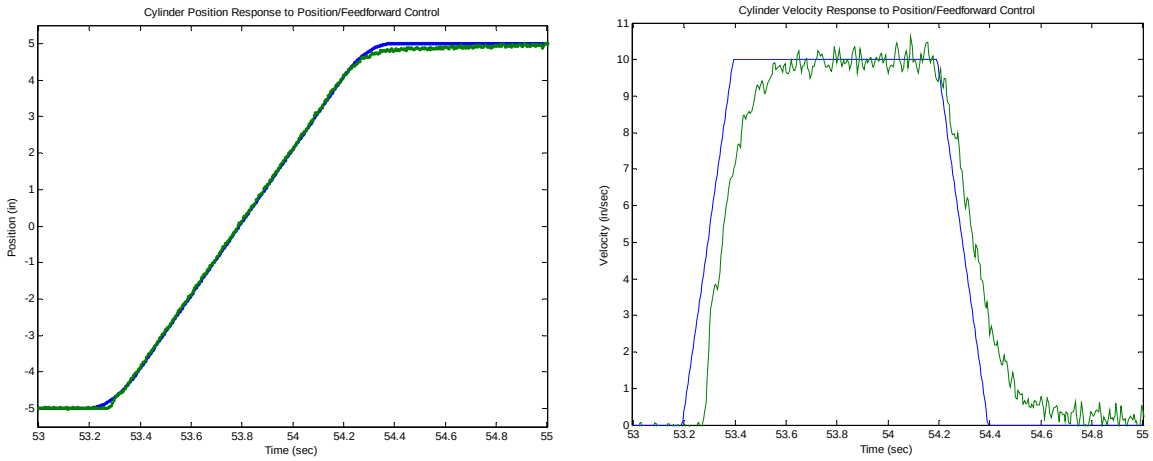

Figure 3-33. Position and velocity tracking with tuned control law. Feedforward control allows almost perfect tracking but is not robust. Note that the delay in the velocity response is due in part to lag produced by the applied noise filter.

3.4.2 Electromechanical Control Methods

The major electromechanical devices are the two lead-screw actuators for wing sweep and the worm gear drive for lateral extension of the horizontal tail. The motor control unit and servocontrol unit both simplify the control task because they output an open-loop current command to correspond to some motor velocity.

For tracking reference trajectories the motor control unit acts as an inner-loop velocity controller that responds to a command input from the position loop proportional gain. This is a standard method for position control of motor driven systems in which the outer loop gain on the position error acts as a velocity command input to the motor control unit. The control procedure is split so that the magnitude of the control effort is sent to the D/A driver block and the direction sends the appropriate vector to the digital I/O driver to change which low-side MOSFET the control signal is actuating. The control effort is set to zero within a desired deadband of the final value. In addition, a reset vector is sent through the digital block to clear the unit and permit further actuation. The key to the design is ensuring that the actuator has enough authority to reach the deadband to reset the motor control unit. Proportional control alone is insufficient because as the error decreases or for small commands there is not enough control effort to overcome friction in the system and the control position might not reach the deadband. Bounded integral control was added to reduce the steady-state error and ensure that the actuator position reached the deadband even for small command inputs. The bounded integrator only sums errors within a set boundary of the command value with a relatively high gain to quickly move within the desired range. Once the deadband is reached, an external signal resets the integrator and a switch supplies a null error signal so that overshoot does not occur when the bounded integration is reactivated.

An added issue with the sweep control is generating the appropriate command signal for the linear actuator. The feedback and control is applied to the linear actuator which drives the three-bar linkage discussed in Chapter Two to control the sweep. The nonlinear relationship between variation in sweep angle and actuator length is repeated here from equation (2.1) along with the sweep linkage image in Figure 3.34.

$$(\delta u + u_o)^2 = r_{ac}{}^2 + r_{bc}{}^2 + 2 r_{ac} r_{bc} \cos((\delta\phi + \phi_o)) \tag{3.2}$$

Equation (3.5) is evaluated at zero sweep orientation to determine u_o from computation of ϕ_o, and the link lengths, r_i. Simplifying in terms of the initial conditions and link lengths yields the required transformation from a desired sweep trajectory to a corresponding actuator command

$$u(t) = \sqrt{A + B\cos(\phi(t) + \phi_o)} - u_o \tag{3.3}$$

where A and B are constant functions of the link lengths. Equation (3.6) is implemented in the SIMULINK sweep system to transform S-curve commands in sweep trajectory to reference commands for actuator length. Differentiating (3.6) reveals the corresponding bound on sweep rate as a function of sweep orientation using known information on the maximum extension speed of the linear actuator

$$\dot{\phi} = \frac{-2\dot{u}\sqrt{A + B\cos(\phi(t) + \phi_o)}}{B\sin(\phi(t) + \phi_o)} \tag{3.4}$$

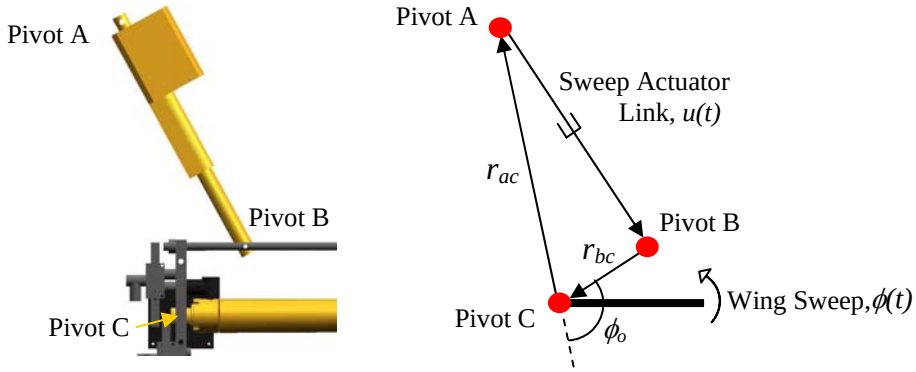

Figure 3-34. Direct-drive sweep geometry. The figure illustrates the actual vehicle system and the corresponding linkage model describing the nonlinear transcendental relationship between linear actuator contraction and wing sweep angle.

Figure 3-35 shows the sweep rate as a function of sweep angle for various actuator speeds. Intuitively, the wing sweep increases sensitivity to linear contraction as the sweep orientation increases and the potential sweep rate increases near the end of the motion. At working conditions the linear actuator contract rate is approximately 2.4 inches per second, resulting in a maximum sustained sweep rate of 30 degrees per second. This value bounds the sweep ramp amplitude and constrains the maximum vehicle transition rate to at least 1.5 seconds to accomplish a 45-degree sweep change.

The general bounds on sweep rate as indicated in Figure 3-35 are 25 to 40 degrees per second based on operating load.

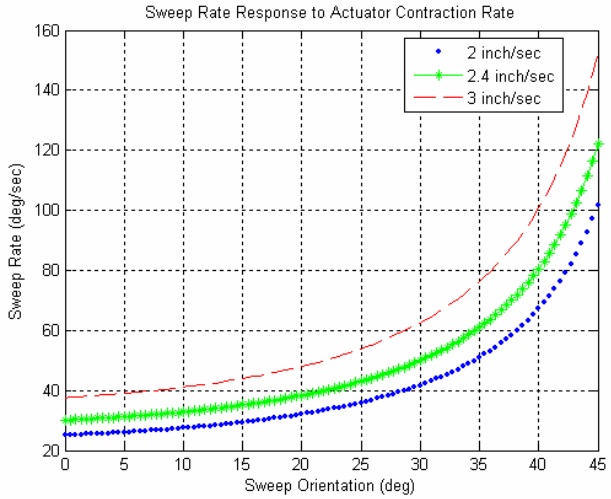

Figure 3-35. Relation between linear velocity of extension actuator and resulting sweep rate. The minimum value indicates the maximum constant-rate input signal.

Figure 3-36 details the reference linear extension command corresponding to the nominal sweep rate limit of 30 degrees per second. Tracking a constant velocity sweep input requires tracking a decelerating linear contraction. This indicates that near perfect tracking of the deceleration signal is necessary because small errors in the linear extension correlate to larger sweep errors at greater orientations.

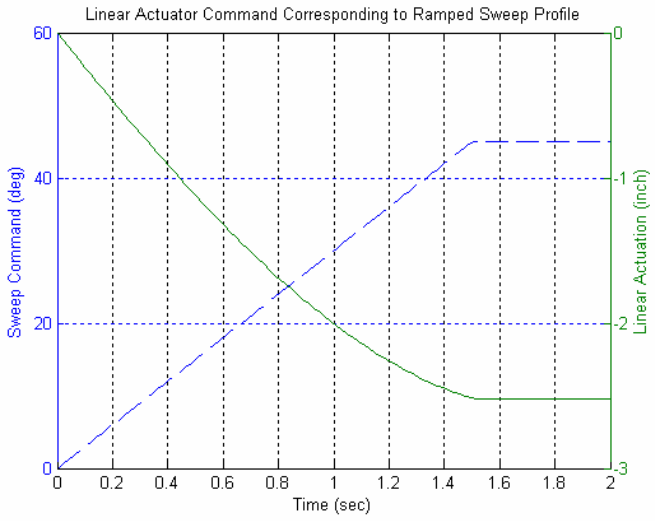

Figure 3-36. Resulting linear extension command signal for constant rate sweep increase. Precise tracking of the deceleration signal is required because of the sensitivity of the sweep response at significant orientation.

Figure 3-37 demonstrates experimental position tracking of a ramped sweep command. The response show sufficient accuracy for tracking the decelerating command signal.

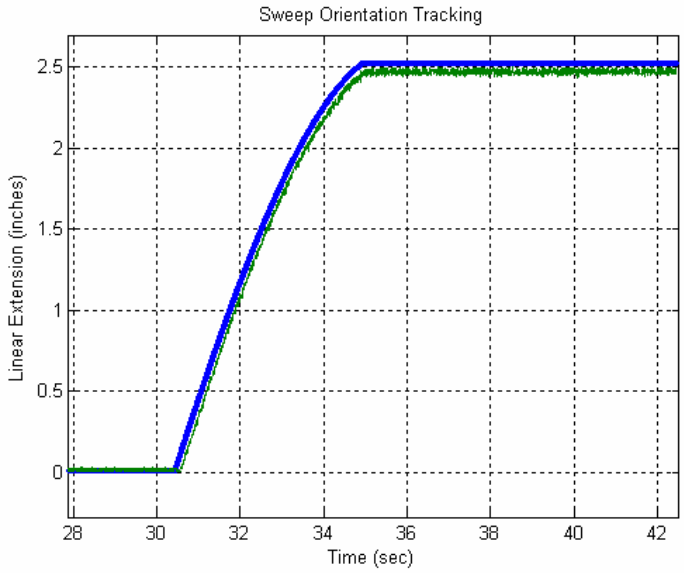

Figure 3-37. Tracking of ramped sweep reference signal. The bounded integrator ensures precise tracking of the decelerating linear extension command.

The lateral tail extension unit implements a similar control structure. Due to the bearing supports friction is less of a concern and simple proportional gain is adequate for tracking command positions. The linear potentiometer directly measures the lateral extension for feedback to the position control loop which generates a command sent to the motor controller. The servo controller basically converts a binary rate command from the position control loop to a duty cycle output to the motor controller which draws from the battery to generate an amplified control signal for the drive motor.

MORPHEUS is designed to operate in two modes. The first mode has each planform state as an independent control input for aerodynamic modeling or planform control implementation. The second mode is coordinated transition motion to study the associated dynamics when converting from loiter to dash states. It is necessary to automate the individual command signals to operate from a single source that can regulate the total vehicle transition rate.

For state transition, MORPHEUS is characterized by symmetric planform commands in span extension, $u_s(t)$, wing sweep, $\Lambda(t)$, and a combined tail motion, $u_{ta}(t)$. The vehicle command signal, $r(t)$, is a bounded ramp input with a slope equal to the reciprocal of the desired transition time, τ_f. The time constant is bounded by the minimum actuator control rate. Coordinating commands for the span, sweep, and generalized tail control is simply accomplished by

$$
\begin{aligned}
u_s(t) &= \frac{\left|u_s^*\right|t}{\tau_f}\left|r^*\right|\mathrm{sgn}(r)\left(1-\Phi\left(t-\tau_f\right)\right) \\
\Lambda(t) &= \frac{\left|\Lambda^*\right|t}{\tau_f}\left|r^*\right|\mathrm{sgn}(r)\left(1-\Phi\left(t-\tau_f\right)\right) \\
u_{ta}(t) &= \frac{\left|u_{ta}^*\right|t}{\tau_f}\left|r^*\right|\mathrm{sgn}(r)\left(1-\Phi\left(t-\tau_f\right)\right)
\end{aligned}
\tag{3.5}
$$

where $|x^*|$ is the actuation range amplitude and $sgn(r)$ changes the path direction based on the terminal transition state. Although equation (3.5) specifies ramp commands, the actual inputs for span and sweep motions are s-curves with short acceleration and deceleration phases to reduce vehicle vibration to the instantaneous impulse at the start or end of a ramp motion. For span and sweep motions, equation (3.5) is sufficient but tail control requires further coordination of the lateral and longitudinal elements to correspond to the generalized tail input $u_{ta}(t)$ which is detailed in Appendix B.

3.5 Chapter Summary

The MORPHEUS redesign has addressed all of the drawbacks of the Phase One APVE model. The basic structure has been greatly enhanced and is capable of supporting significantly higher aerodynamic loads. Functional twist actuation is enabled via the new compliant wing structure and planform rate control will permit transient aerodynamic modeling and dynamic planform maneuver control. Besides increasing the function of the Phase One design, MORPHEUS also implements the variable geometry tail to create completely different vehicles in loiter and dash states. The tail also serves as an independent

control on angle of attack which can be used to reduce static margin and hence trim drag. The following chapter presents a theoretical comparison of the aerodynamic performance of the Phase One APVE, MORPHEUS, and an industry morphing vehicle and demonstrates the effectiveness of the horizontal tail addition.

Chapter 4
Elementary Aerodynamic Analysis

4.1 Chapter Overview

The APVE vehicles were not developed using standard aircraft design techniques. In standard airframe design, the mission parameters are defined first and then the airfoil and wing are shaped to satisfy constraints. The APVE models were designed around mechanical requirements to achieve a set of desired morphing parameters, corresponding to the DARPA initiative. The initial sizing was performed to satisfy the large geometry changes and smoothly integrate all actuation systems as opposed to optimizing for specific mission parameters. The working assumption was that achieving the large geometry changes would facilitate optimization for specific missions. The design constraints were the size of the wind tunnel test section, the required geometry changes issued by DARPA, and the space requirements to include all of the necessary actuation systems.

The chapter consists of a geometric and aerodynamic comparison of the P1-APVE model, the Phase Two model (MORPHEUS), and the NextGen N-MAS configuration based on vortex lattice analysis. It was shown in Chapter Two that VLM is useful for identifying parameter trends during morphing, including the changes in stability from neutral point shifts. In this respect, lattice analysis can be used to perform quick comparisons between the general aerodynamic characteristics of different vehicles, or a single vehicle in different morphed configurations.

4.2 Comparison of APVE and NMAS Configurations

A general aerodynamic and geometric comparison of the Phase One model, MORPHEUS, and a single degree of freedom N-MAS prototype is presented. The

aerodynamic coefficients are approximated using VLM analysis supported by empirical results where necessary. Empirical methods like those presented in Raymer are simple, first-cut design techniques and can be used with primarily planform and airfoil data, allowing the methods to be extended to the limited configuration data available for the N-MAS configuration. In particular, results for profile drag, which is not available from VLM analysis, will be derived using empirical techniques.

Comparisons are limited to loiter and dash configurations based on the available geometries of the NMAS prototype. Throughout the analysis, the NMAS vehicle is considered ideal and it is illustrated how the Phase One and Two APVE models compare. In particular, MORPHEUS demonstrates significant improvement in stability characteristics at the expense of a slight drag penalty when compared to the P1 APVE.

Comparing the aerodynamic performance of different morphing air vehicles is dependent on the reference geometry definition because the standard parameters change with the planform state. Traditional reference geometry definitions are suitable for comparison of separate vehicles, but comparative analysis of the different configurations of a single morphing vehicle should be conducted with constant reference parameters. The effectiveness of morphing in adjusting the vehicle performance is not just aerodynamic, but also in geometry changes. With constant reference geometry, the benefits due to geometry changes are effectively captured in the aerodynamic coefficients. To summarize, traditional reference geometry will be used to compare different vehicles (N-MAS to MORPHEUS, etc) but constant parameters when comparing different configurations of a single vehicle.

4.2.1 *Loiter-Dash* Geometry Comparisons

The reference parameters for normalizing aerodynamic functions are a reference area, S_{ref}, a reference span length, b_{ref}, and the mean aerodynamic chord, $\bar{c}$. Computing the reference area and mean aerodynamic chord for MORPHEUS is nontrivial because the tail merges with the main wing as the vehicle transitions to dash. As illustrated by the tail coordination functions in the Appendix, the mission actuation commands for the tail are piecewise smooth. The tail and main wing mesh once the tail alignment time is reached. Further merging of the tail into the main wing becomes a single degree of

freedom control. Therefore the reference area, mean aerodynamic chord, and effective span length are piecewise continuous, transitioning at the tail alignment time. This discontinuity in reference parameters is further evidence of the need to use constant reference geometry for normalizing coefficients.

Figure 4-1 shows the characteristic planform view of each vehicle in loiter-dash transition. Of note from Figure 4.1 is the fact that the N-MAS prototype consists of a morphing *wing* while MORPHEUS is a morphing *vehicle* that incorporates the tail in the transformation. In the dash configuration, MORPHEUS approximates a delta planform.

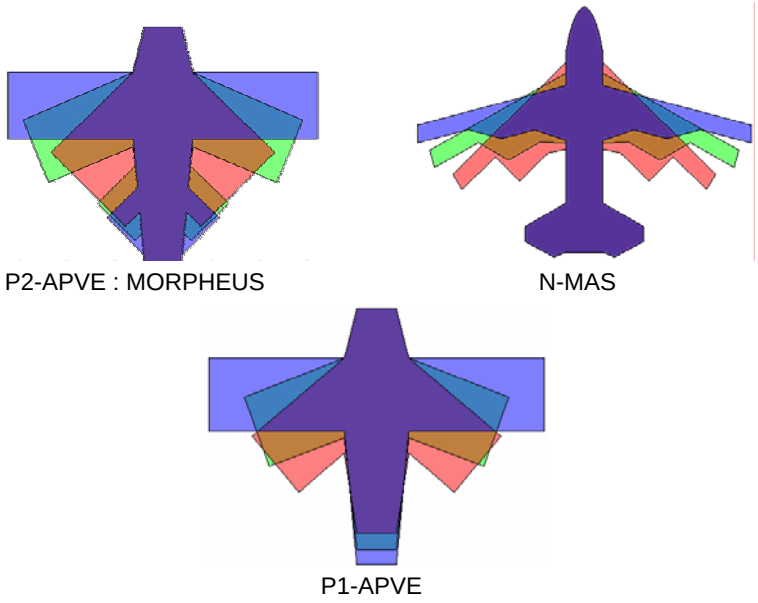

Figure 4.1. The three morphing aircraft in loiter-dash transition illustrating the qualitative differences in the geometry variations.

Key geometric features of the three configurations are detailed in Table 4.1. Because the Phase One and Two vehicles each have the same loiter configuration, it is a convenient reference point for scaling. The N-MAS planform geometry is scaled to the APVE span length in loiter for direct comparison.

Although DARPA mandated percentage changes in aspect ratio and wing area, the total change is not as significant as in what mission phase that change occurs. The goal of vehicle transition is opposing changes in area and span to achieve larger changes in aspect ratio which directly affects the vehicle lift and drag. The Phase One APVE increases area with span during transition to loiter due to the extending wing area. The N-MAS plane actually decreases reference area during dash→loiter transition for a

greater aspect ratio increase. MORPHEUS still has the telescoping wing issues of the Phase One design but in Table 4.1 it appears that it decreases reference area as well during loiter transition. This is due to the merged wing state in the dash configuration which causes an increase in apparent reference area. The result is slightly deceptive because the drag reference area includes the merged tail surface. This indicates the need for a better analysis constraint than solely aspect ratio change.

The true key to multi-mission optimization is large changes in *wetted* aspect ratio. The wetted aspect ratio is computed using the entire exposed surface area, S_{wet}. Parasite drag is proportional to wetted area and induced drag is inversely related to span length. Therefore, a higher wetted aspect ratio directly indicates a higher maximum lift to drag ratio $(L/D)_{max}$ [Raymer, 2004]. The N-MAS vehicle is aerodynamically efficient because it simultaneously decreases wetted area and increases span while transitioning to the loiter configuration. Meanwhile, the telescoping span extension of the APVE models increases wetted area during the same transition. Nonetheless, because of the significant span and sweep changes of the APVE models, the planform geometry change overcomes the surface area increase to cause significant change in wetted aspect ratio, indicating a drag benefit.

Table 4.1. Loiter-Dash geometry comparison of APVE Models and N-MAS prototype.

	Loiter			Dash			Percent Change (D→L)		
Parameter	**P1**	**P2**	**N-Mas**	**P1**	**P2**	**N-Mas**	**P1**	**P2**	**N-Mas**
Wing Area (ft^2)	6.27	6.27	2.89	4.9	6.54	3.84	28.0	-4.1	-24.7
Wing Span (ft)	5.37	5.37	5.37	3.98	3.86	4.08	34.9	39.1	31.6
Aspect Ratio	4.6	4.6	9.95	3.23	2.28	4.34	42.4	101.8	129.5
$Area_{wet}$ (ft^2)	21.5	23	12.7	17.6	18.6	14.0	22.2	23.7	-9.3
$Aspect\ Ratio_{wet}$	1.34	1.25	2.27	0.90	0.80	1.19	48.9	56.3	90.7
MAC (ft)	1.17	1.17	0.64	1.37	2.11	1.14			
LE Sweep (°)	0	0	15	40	45	45			

The wetted area of the APVE models was determined using three-dimensional CAD models. Figure 4.2 shows the custom models created for the surface area computation. Because only 2-dimensional layouts were available for the N-MAS vehicle, classical approximations were used from Raymer for the fuselage and wing wetted areas.

$$\text{wing surfaces:}\quad S_{wet} = A_{\exp osed}\left[1.977 + 0.52(t/c)\right] \tag{4.1}$$

The wing area is a function of the airfoil thickness and the true exposed planform area as opposed to the reference wing area which extends to the fuselage centerline. The N-MAS fuselage wetted area is determined from computing the area under the fuselage perimeter versus chord chart in Figure 4.3.

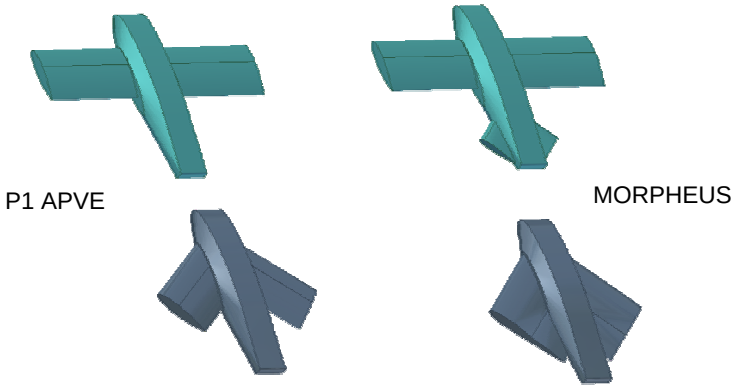

Figure 4.2. Three-dimensional solid models for computing wetted area of P1 and P2 APVE models. The addition of the tail structure causes an wetted area penalty on MORPHEUS which will increase profile drag.

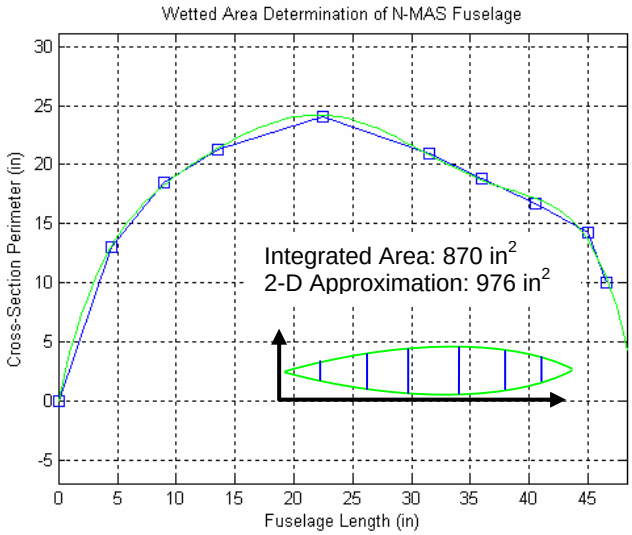

Figure 4.3. N-MAS fuselage perimeter plot and polynomial-fit integrated to approximate the wetted area. The integrated value yields a lower result than the 2-D approximation presented by Raymer that only considers profile views.

The standard definition of the mean aerodynamic chord requires integrating the squared chord function over a half-span. For multiple trapezoidal wing sections, the function is the summation of linear chord segments

$$\bar{c} = \frac{2}{S}\int_0^{b/2} c(y)^2\,dy = \frac{2}{S}\left[\sum_{i=1}^{n}\int_0^{d_i} c_i(y)^2\,dy\right] \tag{4.2}$$

based on the wing definitions in Figure 4.4. The location of the mean aerodynamic chord behind the reference wing apex is computed in a similar expansion of the standard integral

$$x_{mac} = \frac{2}{S}\int_0^{b/2} x(y)c(y)dy = \frac{2}{S}\left[\sum_{i=1}^{n}\int_0^{d_i} x_i(y)c_i(y)dy\right] \tag{4.3}$$

These parameters are used to reference the pitching moment to determine the aerodynamic center and particularly to note the *change* in aerodynamic center

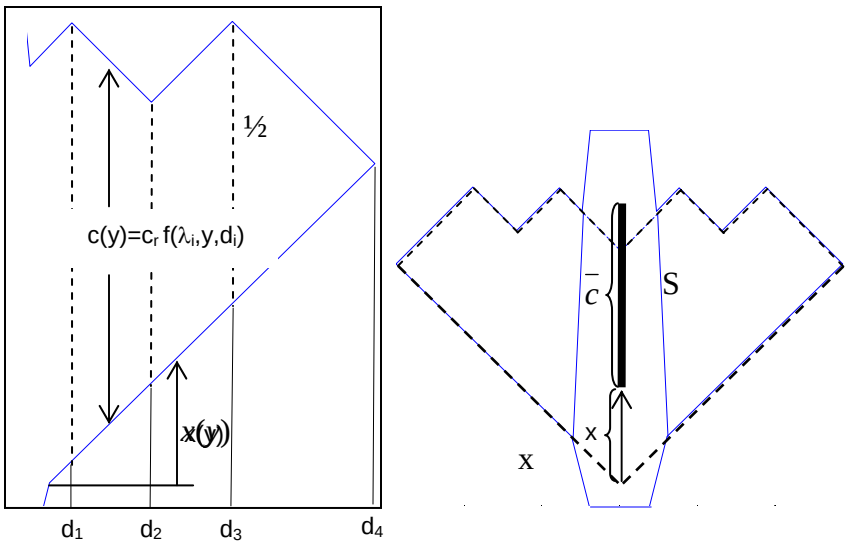

Figure 4.4. Half-span and full planform views of a wing planform demonstrating geometric reference parameters for multi-segmented vehicles. Computing parameters for segmented planforms requires repeated application of the integrals in (4.2) and (4.3)

4.2.2 MORPHEUS Airfoil Analysis

There are general theoretical and empirical guidelines for determining the wing parameters best suited for different flight segments. For loiter and cruise segments, maximizing L/D is the driving factor, which indicates the obvious need to decrease drag for a given lift. Total drag is a summation of parasite drag, a function of surface area and airfoil geometry, and induced drag (drag-due-to-lift), which is a function of planform geometry (wing span in particular).

Parasite drag has three contributing factors: skin friction drag, viscous separation

drag, and wave drag. For subsonic flight, profile drag (skin friction + viscous separation) dominates. Skin friction drag is a result of boundary layer growth and viscous form drag arises from pressure difference between attached and detached flow at the airfoil separation point [Bertin, 1998]. For supersonic flight, wave drag is generated due to the pressure differences across shock waves. We will only analyze parasite drag contributions from profile effects throughout this document.

Elementary aerodynamic analysis texts indicate how airfoil thickness, thickness location, and surface roughness control the profile drag [Bertin, 2004]. Thick airfoils create a larger flow path which accelerates the flow, decreases the surface pressure, and creates greater lift for a cambered airfoil (or a symmetric wing at some angle of attack). The increased flow velocity creates a greater adverse pressure gradient from the point of maximum thickness to the trailing edge which decelerates the flow. This has a dual effect on drag; it causes laminar to turbulent transition earlier which increases skin friction drag but the energy in the turbulent flow delays separation, decreasing viscous drag [Bertin, 1998]. Therefore, there is a limit on increasing wing thickness for maximum lift because of subsonic drag penalties. For a 'fat' airfoil like the APVE models, the primary drag contribution is from viscous separation because there is a lower ratio of flow path to maximum flow velocity. It is better for such airfoils to have turbulent flow to overcome the large adverse pressure gradient and remain attached as long as possible. As noted in Chapter 2, to permit internal actuators, the maximum wing thickness was shifted aft to 40-percent of the chord. This shifts the start of the adverse pressure gradient farther aft, delaying separation. Therefore in the APVE models the increased separation from the extremely 'fat' airfoil is somewhat countered by shifting the maximum thickness aft.

A freeware software package for viscous analysis of two-dimensional airfoil shapes (XFOIL) can be used to analyze the characteristics of both the wing and fuselage airfoil sections. Figure 4.5 details XFOIL results for three symmetric airfoil sections, a 0020-64 APVE wing airfoil, a 0020 airfoil without the modification in thickness location, and a standard 0012 airfoil section. The viscous analysis indicates that using a thicker airfoil did not significantly affect the wing characteristics, but shifting the maximum thickness back did. Comparing the two thick airfoils, there is a 17-percent reduction in

the lift curve slope from 1.92π to 1.59π. Stall is delayed with the airfoil modification from 19 to 20.6 degrees such that the maximum lift coefficient for the modified airfoil is only 4-percent less than the NACA 0020 and 7-percent less than the 0012. This loss of lift is due to increased separation from the modified airfoil as can be seen from the significant drag penalty for higher C_l values. The 0020-64 modified airfoil is by no means optimal but permits morphing functions while still achieving reasonable performance, particularly at higher angle of attack values.

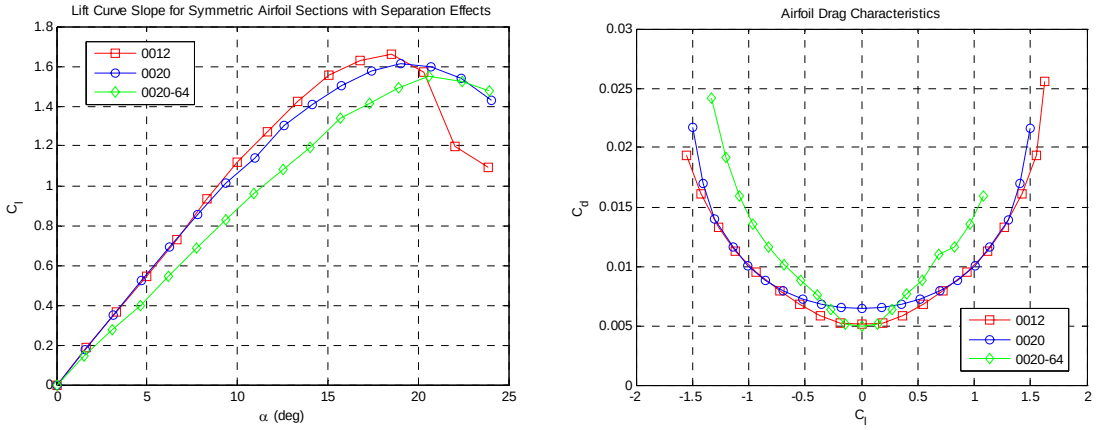

Figure 4.5. Two-dimensional Airfoil Drag Characteristics for APVE modified airfoil and conventional airfoil sections. The wing thickness modification reduced the lift curve slope but increased the stall angle to permit similar maximum lift values.

4.2.3 *Loiter-Dash* Drag Response

The TORNADO program is a MATLAB based vortex-lattice analysis package that permits multiple vehicles to be analyzed quickly [Melin, 2000]. TORNADO geometry functions make it especially easy to add multiple lifting surfaces such as the horizontal tail for the MORPHEUS and unconventional planform arrangements like the N-MAS. Initially, the full TORNADO algorithm will be used to establish general comparisons in the three-dimensional planform effects of the three vehicles. The unconventional horseshoe vortex, wake arrangement, and post-processing in TORNADO extend beyond planar geometry assumptions and account for nonlinear flow boundary conditions. In the following chapter on *Continuous Aerodynamic Modeling*, TORNADO geometry subfunctions will be extracted and combined with the author's VLM code presented in Chapter 2 (based on results from [Bertin, 1998]) for a linear

vehicle analysis.

The vortex-lattice method only computes drag due to lift, so to find the maximum (L/D) we have to use an empirical formulation by Raymer to compute the subsonic parasite drag.

$$C_{D_0} = \left(\frac{\sum C_{f_i} FF_i Q_i S_{wet_i}}{S_{ref}} \right)_{profile} + C_{D_{misc}} + C_{D_{L\&P}} \tag{4.4}$$

The parasite drag equation is based on a summation of three separate parameters: profile drag, miscellaneous drag, and leakage/protuberance drag. The profile drag is a build-up of skin friction, form-factor, and interference drag that is summed for every exposed aircraft segment (wings, fuselage, etc.). The skin friction and form-factor contributions have been discussed previously, the interference factor, *Q*, scales the profile drag based on external components like stores in close proximity to the wings and the overall wing orientation relative to the fuselage. The weighted average of the drag contributors relative to the reference area result in the total profile drag. The miscellaneous drag factors are for external components like landing gear and additional surfaces not accounted for in the profile drag like wing flaps and external stores. The last component of parasite drag is a leakage and protuberance drag coefficient ($C_{D_{L\&P}}$) due to high pressure air flows into structural gaps decreasing the flow energy and inducing separation.

The skin friction drag coefficient is a function of Mach number for high speed flight and the local Reynolds number. Assuming completely turbulent flow gives a worst case estimate for the drag. Raymer gives the following expression which simplifies at low Mach numbers

$$C_f = \frac{0.455}{\left(\log_{10} R\right)^{2.58} \left(1 + 0.144 M^2\right)^{0.65}} \approx \frac{0.455}{\left(\log_{10} R\right)^{2.58}} \tag{4.5}$$

Tables 4.2 and 4.3 detail the characteristic length for each component on all three vehicles, the local Reynolds number, and the resulting friction coefficient for the respective loiter and dash configurations. The assumed test velocity is 220 *ft/sec* (M ≅ 0.2) and sea level conditions are assumed.

Table 4.2. Skin Friction Drag Computations for Loiter Configuration

	ℓ (ft)			R (E6)			C_f (E-3)		
Loiter	***fuse***	***wing***	***tail***	***fuse***	***wing***	***tail***	***fuse***	***wing***	***tail***
N-MAS	4.0	0.64	0.70	2.17	0.347	0.380	3.88	5.49	5.39
P1 APVE	4.1	1.17		2.22	0.635		3.87	4.87	
MORPHEUS	4.1	1.17	1.06	2.22	0.635	0.575	3.87	4.87	4.97

Table 4.3. Skin Friction Drag Computations for Dash Configuration

	ℓ (ft)			R (E6)			C_f (E-3)		
Dash	***fuse***	***wing***	***tail***	***fuse***	***wing***	***tail***	***fuse***	***wing***	***tail***
N-MAS	4.0	1.14	0.70	2.17	0.619	0.380	3.88	4.90	5.39
P1 APVE	4.1	1.37		2.22	0.743		3.87	4.73	
MORPHEUS	4.1	2.11		2.22	1.145		3.87	4.36	

In particular we note from Table 4.2 the skin friction drag penalty caused on the APVE design by implementing the variable geometry tail.

The form-factor drag for wing and tail surfaces presented in Raymer is given by

$$FF = \left[1 + \frac{0.6}{(x/c)_m}\left(\frac{t}{c}\right) + 100\left(\frac{t}{c}\right)^4\right]\left[1.34M^{0.18}(\cos\Lambda_m)^{0.28}\right] \qquad (4.6)$$

where (x/c) and (t/c) are the location and value of maximum thickness, and Λ_m is the maximum thickness sweep line. For the fuselage, the form factor coefficient is

$$FF = \left(1 + \frac{60}{f^3} + \frac{f}{400}\right), \qquad \text{where } f = \frac{l}{\sqrt{(4/\pi)A_{\max}}} \qquad (4.7)$$

where f is the ratio of the characteristic length to the equivalent circle diameter of the maximum cross-sectional area. This 'fineness' parameter will be used in the DATCOM expressions in the following chapter.

For the APVE configurations, the fuselage is a blended airfoil profile, so equation 4.6 is used to compute its form factor drag. This requires an equivalent airfoil thickness and maximum thickness location. Both values are obtained for the outer fuselage segment (interpolation of two airfoils) by integrating the linear distributions over the partition defined by d_1 and d_2 as shown in Figure 4.6. The area weighted value with the d_0 – d_1 partition is then computed.

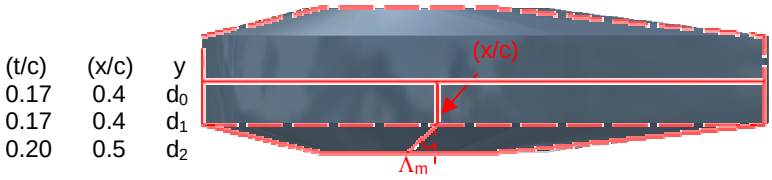

Figure 4.6. Interpolating APVE fuselage for equivalent airfoil parameters

An equivalent maximum sweep angle (area-weighted) was computed for the cranked wing sections of the N-MAS vehicle along with the APVE fuselage. Because the wings of the APVE models pivot, the maximum sweep line is equivalent to the leading edge sweep angle. In addition, the APVE pivot causes the streamwise airfoil thickness to reduce by the cosine of the leading edge sweep angle due to an increase in the effective chord length. Tables 4.4 and 4.5 present values for the vehicle components in both loiter and dash configurations.

Table 4.4. Viscous Drag Computations for Loiter Configuration

	(t/c) %			*(x/c) %*			*Λ_m (°)*			*FF*		
Loiter	***F***	***W***	***T***	***F***	***W***	***T***	***F***	***W***	***T***	***F***	***W***	***T***
N-MAS		12	12		30	30		9	23.6	1.22	1.26	1.23
P1 APVE	17.4	20		41.4	40		-15	0		1.33	1.46	
MORPHEUS	17.4	20	11	41.4	40	28	-15	0	45	1.33	1.46	1.13

Table 4.4 shows a significant decrease in the viscous drag contribution for the N-MAS vehicle. Equation 4.7 does not account for Reynolds number but with turbulent flow the separation of the 'fat' wing airfoils of the APVE could be less, decreasing the form factor contribution. Although the APVE fuselage is an aerodynamic shape, it is also larger percentage of the total vehicle volume when compared to the N-MAS fuselage. It is reasonable to assume a higher form-factor contribution.

To demonstrate the effects of wing pivot on airfoil chord, the tip and stream-aligned MORPHEUS dash airfoil sections are displayed in Figure 4.7. The actual dash airfoil is the stream-aligned airfoil section which has chord length increased by over 40% due to the wing pivot. The effective thickness of the combined wing is 13% but for the stream-aligned section it is reduced to 9% which creates benefits for high-speed subsonic flight.

Figure 4.7. Tip-aligned and Stream-aligned airfoil sections for MORPHEUS dash. Wing sweep causes in increase in the effective chord which decreases the thickness ratio, creating a more efficient wing profile for dash.

Thinner wings decrease the wave drag component for high-speed flight and take fuller advantage of vortex lift which induces nonlinear increases in the lift curve slope and delays separation. The viscous characteristics of the dash-slice wing in Figure 4.8 indicate that the flow begins to separate off the back-half of the airfoil at only 11° angle of attack but three-dimensional flow effects counter this and permit MORPHEUS to take advantage of the increased effective chord. Thinner wings have lower wave drag, permitting higher angles of attack and generating greater lift. All of these features help to create a better dash vehicle. The thickness decrease is not an apparent effect like the reference area increase because the airfoil change directly affects the streamwise flow characteristics. In addition, the tail is no longer enveloped in wing downwash so contributes more to the lifting capacity.

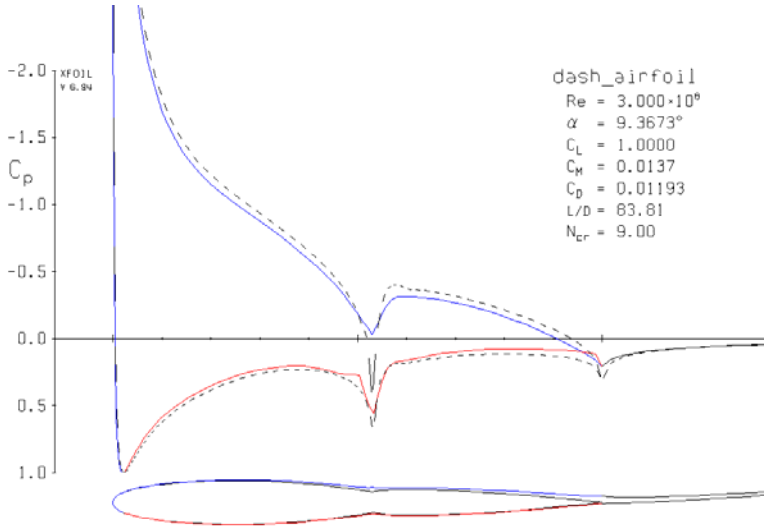

Figure 4.8. XFOIL output of Viscous Flow Characteristics of Dash airfoil section. The thinner effective wing profile has an improved drag characteristic. The solid and dashed lines represent the viscous and inviscid solutions respectively

The form-factor drag expression in (4.6) requires a single set of airfoil characteristics so an equivalent airfoil was created for the MORPHEUS dash

configuration to account for the segmented combination of the wing and tail surfaces. The maximum thickness and location of modified NACA airfoil sections were analyzed in XFOIL until similar viscous flow characteristics were obtained. Figure 4.9 shows that, over the operating range of lift coefficients, the combined dash airfoil has a similar drag profile to a NACA 0016-64. The first figure shows the lift response of the true drag airfoil shape implemented in XFOIL. There is a significant improvement in the lift-curve slope because the reduction in effective airfoil thickness helps to keep the flow attached. The second figure compares the drag response of the actual dash airfoil and the equivalent NACA section. The drag profile is an improvement on the NACA 0020-64 wing alone, although still not quite as efficient as the NACA 0012. XFOIL would not converge above 14° angle-of-attack for the dash airfoil. The NACA 0016-64 airfoil parameters are used in (4.7) to define the form-factor drag. Table 4.5 indicates a noticeable reduction in the form-factor contribution for the MORPHEUS wings as expected from 2-D analysis.

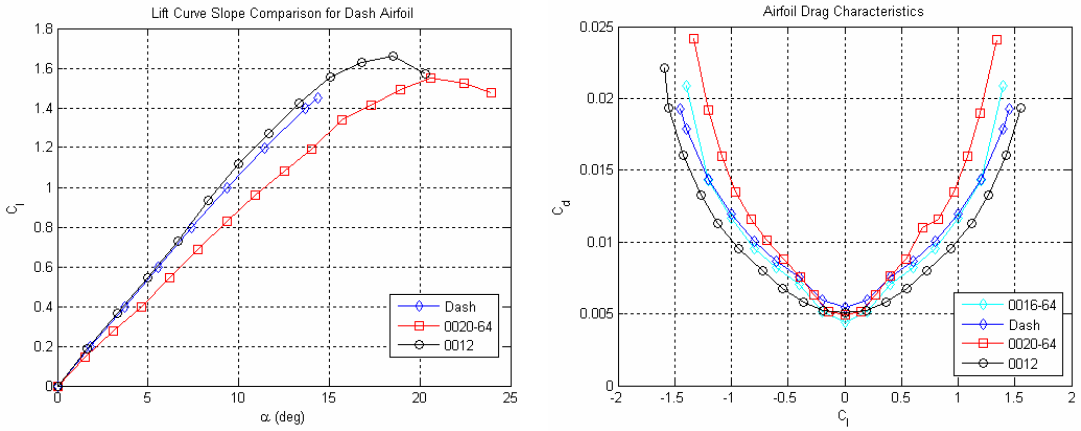

Figure 4.9. Viscous Flow Characteristics of Dash airfoil section comparing lift and drag to a standard NACA 0012 airfoil, the NACA 0020-64 airfoil of MORPHEUS-loiter, and an equivalent NACA 0016-64 airfoil.

Table 4.5. Viscous Drag Computations for Dash Configuration

	(t/c) %			*(x/c) %*			Λ_m (°)			*FF*		
Loiter	***F***	***W***	***T***	***F***	***W***	***T***	***F***	***W***	***T***	***F***	***W***	***T***
N-MAS		12	12		30	30		37.4	23.6	1.22	1.19	1.23
P1 APVE	17.4	15.3		41.4	30.6		-15	40		1.33	1.26	
MORPHEUS	17.4	16		41.4	40		-15	45		1.33	1.19	

It is assumed that external stores, engine intake, etc are similar for both vehicles so that the only interference drag is from wing alignment relative to the fuselage. The

APVE configurations have a high wing set and the N-MAS model a mid-wing set which both indicate interference factors of 1.0 [Raymer, 2004]. Miscellaneous drags are assumed to be the same for each vehicle but because of the multiple shifting surfaces, and it is assumed that the leakage drag $(LP)_n$ is a constant 15-percent for all airframes in both configurations. Substituting results from Tables 4.2, 4.3, 4.4, and 4.5 into the equation (4.8) yields total parasite drag values for the three vehicles in loiter and dash configurations which are presented in Tables 4.6 and 4.7.

$$C_{D_0} = \left(\frac{\sum C_{f_i} FF_i Q_i S_{wet_i}}{S_{ref}} \right)_{pro} + (LP)_n C_{D_0} \rightarrow C_{D_0} = \frac{1}{1-(LP)_n} \left(\frac{\sum C_{f_i} FF_i Q_i S_{wet_i}}{S_{ref}} \right)_{pro} \quad (4.8)$$

Table 4.6. Parasite Drag Computations for Loiter Configuration

	S_{wet} (ft^2)			$C_{Do\ profile}$ (e-3)				C_{Do}
Loiter	***fuse***	***wing***	***tail***	***fuse***	***wing***	***tail***	Σ	
N-MAS	6.05	4.74	1.944	28.6	32.8	12.89	74.29	.0302
P1 APVE	9.72	11.78		50.0	83.8		133.8	.0251
MORPHEUS	9.72	11.78	1.496	50.0	83.8	8.38	142.2	.0267

Table 4.7. Parasite Drag Computations for Dash Configuration

	S_{wet} (ft^2)			$C_{Do\ profile}$ (e-3)				C_{Do}
Dash	***fuse***	***wing***	***tail***	***fuse***	***wing***	***tail***	Σ	
N-MAS	6.05	6.02	1.944	28.6	35.1	12.89	76.6	.0235
P1 APVE	9.72	7.89		50.0	47.0		97.0	.0233
MORPHEUS	9.72	8.92		50.0	46.3		96.3	.0173

The summation column (Σ) represents the profile drag accumulation before normalizing by the reference area and is a good representation of the absolute values for comparison. The effect of the APVE telescoping span extension is clearly evident because the wetted area increase causes a much larger drag accumulation in loiter than in dash. Conversely, the N-MAS decreases drag accumulation from dash to loiter. The form-factor and skin friction contributions for the N-MAS and APVE configurations were similar but the wetted area increase dominated the absolute drag values. Normalizing with standard reference parameter definitions shows increased parasite drag efficiency of the APVE models over the N-MAS. This is especially evident in the

MORPHEUS dash configuration because it maintains a low drag accumulation at a much larger reference area. The low drag accumulation is due to both the low skin friction contribution, and the decrease in wetted area that accompanies the tail merge. We conclude that although the total APVE drag forces are higher than the N-MAS design, per unit planform area they are still efficient vehicles.

The complete subsonic drag characteristic has a term proportional to the squared lift coefficient. Because the drag polar is an offset parabolic function, the maximum curvature yields the maximum (L/D) [Raymer, 2004]. This corresponds to the intersection of a line from the origin and the parabola. For a symmetric airfoil this intersection occurs when

$$\varepsilon C_L = C_{D_0} + K C_L{}^2 \quad \rightarrow \quad C_L = (2K)^{-1}\left(\varepsilon \pm \sqrt{\varepsilon^2 - 4KC_{D_0}}\right) \tag{4.9}$$

which yields a single solution if

$$\varepsilon = 2\sqrt{KC_{D_0}} \quad \rightarrow \quad C_L{}^* = \varepsilon(2K)^{-1} = \sqrt{C_{D_0}/K} \quad \rightarrow \quad C_D{}^* = C_{D_0} + K\left(C_L{}^*\right)^2 = 2C_{D_0}$$

the maximum (L/D) presented is therefore

$$\left(L/D\right)_{\max} = C_L{}^* / C_D{}^* = \varepsilon^{-1} = \left(2\sqrt{KC_{D_0}}\right)^{-1} \tag{4.10}$$

The result in (4.10) can be found in any low-speed aerodynamics text. The drag-due-to-lift factor, *K*, is computed from the TORNADO vortex-lattice results. Figure 4.10 displays drag polars for each of the three vehicles in both loiter and dash configurations. Each curve is obtained by operating TORNADO for a particular vehicle configuration over a range of angle-of-attack values and computing the resultant lift and drag coefficients. The N-MAS vehicle has a lower drag-due-to-lift factor in both cases. The two APVE vehicles are similar in the loiter configuration, although the addition of the horizontal tail on MORPHEUS induces a slight penalty. MORPHEUS takes a significant hit in vortex drag for the dash configuration but accounts for it with a low parasite drag value.

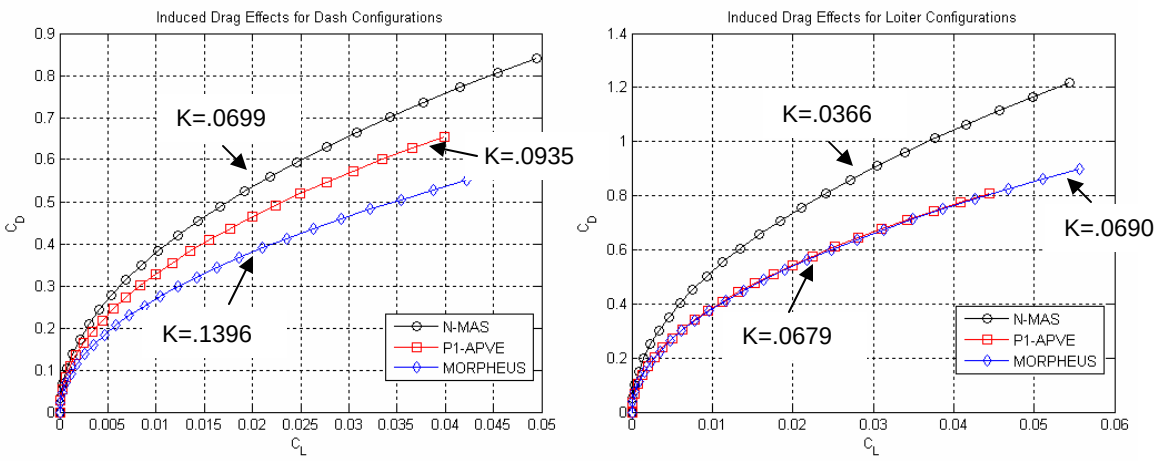

Figure 4.10. Induced Drag and 'drag-due-to-lift' factor computed with TORNADO for dash and loiter configurations. The reduced span of the MORPHEUS dash configuration causes a significant increase in the induced drag factor.

Including the parasite drag results, the maximum *(L/D)* for each vehicle in each configuration is presented in Table 4.8. The N-MAS design has an increase in lift-to-drag ratio of 22%. The value at the loiter configuration is representative of a commercial transport and the dash value is characteristic of a high-end supersonic fighter [Bertin, 1998]. The P1-APVE has an *(L/D)* increase of just 13% with morphing. The vehicle design goal was large changes in performance and MORPHEUS has a maximum *(L/D)* increase of 14%. The percentage change from loiter to dash for each vehicle correlates well with what is expected based on the wetted aspect ratio changes in Table 4.1. MORPHEUS has slightly reduced loiter efficiency in exchange for improved stability characteristics. Wing twist can be used to achieve very slight increases in *(L/D)* but the primary benefit of variable wing twist is reducing drag for 'off-design' conditions. The main conclusion from Table 4.8 is that the aerodynamic efficiency is greatly reduced in the APVE loiter configurations due to the telescoping area increase. Decreasing wing thickness and/or slight increases in aspect ratio would have significant results on increasing the vehicle efficiency.

Table 4.8. Maximum Lift to Drag Ratio for all vehicles and configurations

	Loiter	Dash
N-MAS	15.0	12.3
P1-APVE	12.1	10.7
MORPHEUS	11.7	10.2

4.2.4 *Loiter-Dash Planform Characteristics*

From the (L/D) results we know that increased aerodynamic efficiency is possible with the P1 APVE. The advantage of the MORPHEUS concept is preferred static stability characteristics for various planform states by exploiting the variable geometry tail. Qualitatively, the presence of the horizontal tail increases loiter stability by shifting the neutral point back and providing trim control through variable incidence. For the Phase 1 APVE and N-MAS, wing sweep causes a large aftward shift in the aerodynamic center which reduces maneuverability in the dash configuration and increases trim drag due to higher deflections to balance the pitching moment. The forward tail shift by MORPHEUS reduces the neutral point shift, creating a more favorable condition in dash.

The lift-curve slope and pitch stiffness ($C_{L\alpha}$ and -$C_{m\alpha}$) are computed from TORNADO and are used to locate the vehicle aerodynamic center (neutral point). The neutral point can be found from the load location that results in zero pitch stiffness about the center of gravity [Etkin, 1996]. The actual location of the aerodynamic center can be found from measurements of the static margin

$$-C_{m_\alpha} = C_{L_\alpha}\left(h_n - h\right) \qquad \rightarrow \qquad x_{ac} = x_{cg} - \bar{c}\left(C_{m_\alpha} / C_{L_\alpha}\right) \tag{4.11}$$

where h and h_n represent the respective vehicle aerodynamic center and c.g. locations, normalized by the mean aerodynamic chord. In theory, the designer can place the vehicle c.g. anywhere so equation (4.11) indicates that any fixed point, h (or x_i), that the pitching moment is computed about will mark the reference point for the resulting aerodynamic center location. The leading edge of the MAC for the N-MAS and APVE configurations is chosen as the reference point for the pitching moment calculation. The reference points and their location relative to the rest of the aircraft must be tracked carefully for the different morphing configurations.

The normalizing reference geometry for the APVE vehicles and the N-MAS configurations are the highlighted wing outlines in Figure 4.11. Each wing is in its intermediate morphing configuration. The perforated line on the APVE model indicates the difference between the Phase One and Phase Two geometries although only the primary wing is used for reference.

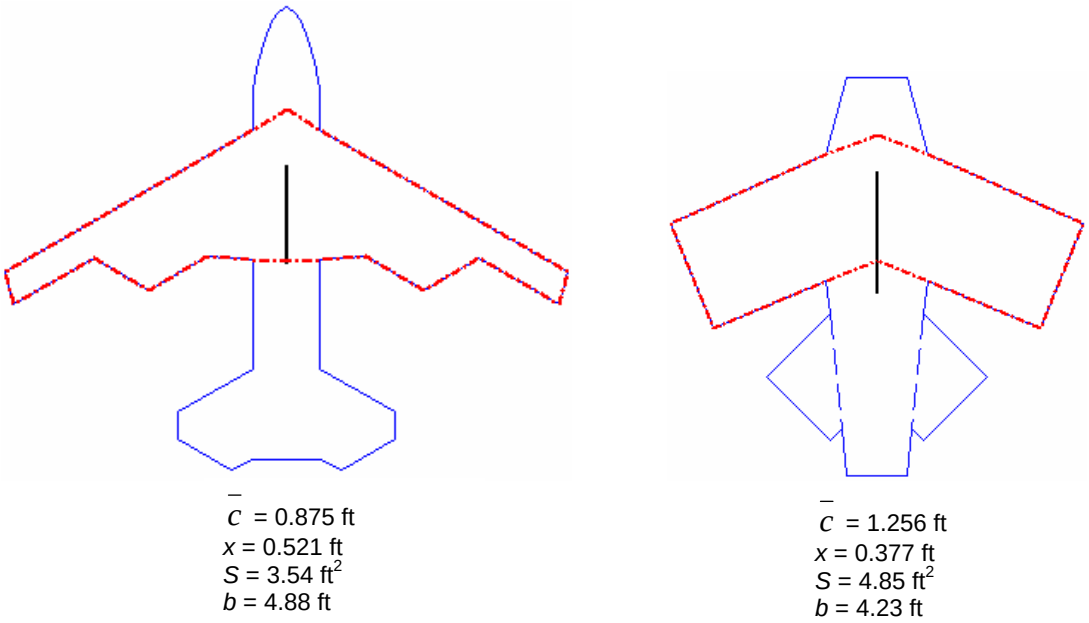

Figure 4.11. Nominal reference geometries used to normalize aerodynamic forces and moments to a constant planform for various morphing conditions.

The resultant VLM aerodynamic coefficients and stability results are detailed in Tables 4.9, 4.10, and 4.11 along with the roll damping parameters. Rolling motion is simulated in TORNADO by rotating the trailing vortices far downstream by an angle proportional to the ratio of normal velocity from the rolling motion and longitudinal velocity from the freestream [Melin, 2000]. The VLM boundary condition is modified to account for the effective angle of attack change for the same linearly decreasing angle.

Two related stability parameters are included, the static margin and the aerodynamic center location. Classically, the static margin, K_n, is a measure of how stable the vehicle is because it is the distance between the center of gravity and the aerodynamic center. Because the pitching moment is referenced to a designated coordinate other than the center of gravity, the margin will be used here to give qualitative estimates of the required trim amplitudes. The true value of the aerodynamic center is computed from 4.11 and is presented relative to the nose of the aircraft, not to the apex of the reference geometry. This gives a grounded reference for computing the percentage shift aft when converting to the dash configurations.

Considering each vehicle as a separate entity, the aerodynamic values computed with true reference parameters are used first to compare the overall airframe

effectiveness. The N-MAS vehicle has a very efficient loiter configuration. The high lift curve slope allows it to cruise at a lower angle of attack, and still support the aircraft weight. This results in decreased pitching moment and lower required trim deflections and resultant drag. The loiter configuration of the P1-APVE model generates less lift but also has lower pitch stiffness. Therefore for equal weight, it must fly at a higher angle of attack but the pitch stiffness is low enough to reduce the trim deflections. Positive washout (negative twist angle) is required to trim because of the lack of a horizontal tail or an elevator control surface. Positive washout creates a nose-up pitching moment by reducing lift at the aerodynamic center which is aft of the reference point. The small associated reduction in lift requires a higher angle of attack and an even greater washout angle. It will be shown in the following chapter that washout increases the aerodynamic efficiency by reducing tip loading but too much will adversely affect parasite drag with separation.

The MORPHEUS loiter configuration is an improvement on the P1-APVE design because it maintains the low static margin which suggests smaller trim deflections but has a horizontal tail like the N-MAS that can be used to trim as opposed to wing twist. Supplementing tail incidence with wing washout creates a configuration with lower trim deflections and increased aerodynamic efficiency. The relative values of the required trim amplitudes of the N-MAS and MORPHEUS can be seen clearly through the static margin parameter. The MORPHEUS margin is approximately one-half that of the N-MAS indicating significantly lower trim deflections. In addition, the control power of the MORPHEUS tail is approximately 13-percent greater because of the larger tail planform area that overcomes the slightly smaller moment arm to the reference point. Distributing trim requirements to wing twist can then be used to further reduce control deflections. The higher static margin of the N-MAS loiter configuration is attributed to an increased percentage of total planform area behind the reference point due to the initial wing sweep.

Comparison of the dashed and loiter configurations indicate the absolute stability change for each airframe. The aerodynamic center of the N-MAS shifts back by 79-percent compared to 113 and 110-percent for the P1-APVE and MORPHEUS models. This indicates the necessity of the horizontal tail shift because MORPHEUS sweeps back

an additional 5-degrees compared to the P1-APVE but still has less shift in the aerodynamic center. The results are skewed because the N-MAS loiter configuration has an initial sweep of 15-degrees so the total sweep change is only 30-degrees compared to 45-degrees for MORPHEUS. In general, the large shift in aerodynamic center makes the vehicles too stable and difficult to trim. The static margin results in the dash configurations indicate further benefit of the MORPHEUS tail shift. Its static margin is significantly less than that for the P1-APPVE and N-MAS configuration. The reduction in pitching moment from the forward tail shift exceeds the decrease in lift that accompanies the span reduction, in turn making it easier to trim MORPHEUS relative to the other vehicles. This is accomplished in spite of a greater absolute sweep change than both of the other models.

The nominal values are useful for comparing the change in configurations because the effect of the geometry change is included in the coefficient. Due to the constant reference, percentage changes in the nominal values reveal the change in effectiveness of a vehicle in different planform states as opposed to the previous analysis which assumed that the six planform arrangements were completely separate aircraft. In particular we see that normalizing for geometry effects, the N-MAS only has a 22-percent increase in the lift-curve slope compared to approximately 60-percent increases for the APVE models. In addition we see much larger decreases in the roll damping of over 70-percent in loiter-dash transition of the APVE models compared to 30-percent for the N-MAS. The results indicate that the method of APVE vehicle actuation is superior to the N-MAS scheme, although in terms of absolute parameters, the N-MAS is aerodynamically superior.

The initial design assumption was that zero wing sweep yields the most favorable APVE loiter condition because it maximizes the aspect ratio. The location of the wing pivot point indicates that if the span measurement is taken with respect to the vehicle extremes, the maximum span actually occurs at a sweep angle of approximately 15 degrees. VLM analysis shows that the small aspect ratio increase reduces the MORPHEUS induced drag coefficient from 0.069 to 0.0648. This is accompanied by a reduction in the form factor parasite drag due to the decrease in apparent streamwise thickness with wing sweep. The resultant parasite drag coefficient reduces from 0.0267

to 0.0262 and the combined effects are an increase in $(L/D)_{max}$ from 11.65 to 12.13. Table 4.12 summarizes the results for the modified loiter configuration.

The aerodynamic center position is slightly farther aft compared to the other loiter configurations which makes trim more difficult as evidenced by the increased reference margin. The change in the aerodynamic center is reduced to approximately 60% due to the initial sweep (compared to 79-percent for the same sweep variation in the N-MAS design). Compared to the unswept MORPHEUS configuration, the modified loiter arrangement has higher lifting capacity because of the increased span but intermediate stability performance due to the pre-swept configuration. The variable geometry tail can be shifted forward to counter the pre-swept condition and recover a more favorable trim state while retaining the aerodynamic efficiency. This slightly reduces the tail moment arm but the decrease in control effectiveness is overshadowed by the reduction in static margin. In addition, washout is more effective in trimming a swept configuration because the aerodynamic center is farther aft of the reference point. It is obvious that with the numerous degrees of planform freedom, analytical methods can be devised to morph into optimal configurations. Implementing such techniques requires continuous, differentiable representations of the aerodynamics as a function of planform state which will be covered in the following chapter.

Table 4.9. N-MAS Aerodynamic Coefficients and Stability Parameters

	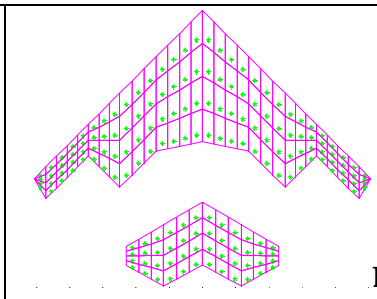 **Dash**		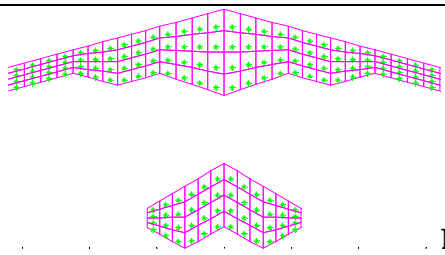 **Loiter**	
	True	**Nominal**	**True**	**Nominal**
$C_{L\alpha}$	3.67	3.98	5.93	4.85
$C_{M\alpha}$	-5.536	-7.79	-4.36	-2.52
K_n	1.508		0.735	
x_{ac}	34.0		19.0	
C_{lp}	-0.410	-0.310	-0.461	-0.455

Table 4.10. P1-APVE Aerodynamic Coefficients and Stability Parameters

	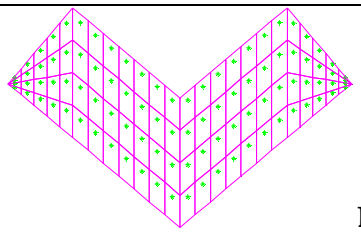 Dash		 Loiter	
	True	**Nominal**	**True**	**Nominal**
$C_{L\alpha}$	3.13	3.16	3.91	5.05
$C_{M\alpha}$	-3.48	-3.84	-0.924	-1.109
K_n	1.111		0.236	
x_{ac}	28.3		13.3	
C_{lp}	-0.263	-0.236	-0.392	-0.815

Table 4.11. MORPHEUS Aerodynamic Coefficients and Stability Parameters

	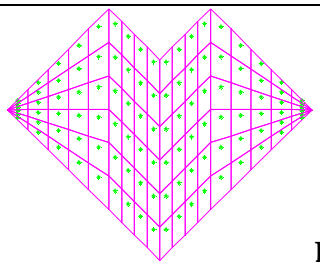 Dash		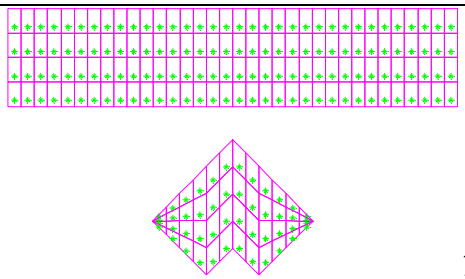 Loiter	
	True	**Nominal**	**True**	**Nominal**
$C_{L\alpha}$	2.62	3.54	4.29	5.54
$C_{M\alpha}$	-2.26	-5.13	-1.549	-1.859
K_n	0.863		0.361	
x_{ac}	31.8		15.1	
C_{lp}	-0.200	-0.224	-0.393	-0.818

Table 4.12. Modified MORPHEUS Aerodynamic Coefficients and Stability Parameters

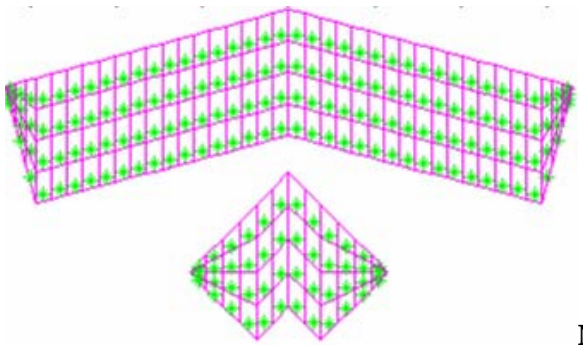

Modified Loiter

S (ft^2)	b (ft)	AR	MAC	$C_{L\alpha}$	$C_{M\alpha}$	K_n	x_{ac}	$(L/D)_{max}$
6.29	5.51	4.83	1.185	4.37	-3.25	0.744	20.6	12.13

4.3 Chapter Summary

The elementary aerodynamic analysis presented showed that the alterations for the MORPHEUS vehicle improved the APVE stability characteristics. These results came at the expense of slightly degraded aerodynamic efficiency. Although the APVE models do not match up to the absolute performance of the N-MAS design, analysis of the static margin predicts superior trim characteristics and roll maneuverability for MORPHEUS. In addition we have demonstrated increased transition efficiency. One major problem with the analysis is the blunt edge for swept APVE configurations. The VLM analysis does not account for the explicitly thick trailing edge out towards the wing tips when the vehicles are swept which could reduce some of the computed effectiveness with span increase.

Detailed analysis of MORPHEUS requires a more thorough treatment than basic VLM computations. Standard applications of VLM do not specifically include fuselage effects which will improve the usefulness of the aerodynamic coefficients in control applications. Advanced modeling techniques that implement higher-fidelty analysis methods are necessary for performance optimization and stability analysis of morphing

vehicles. The MORPHEUS design could then be actuated to sub-optimal configurations for different segments of the morphing flight mission.

Chapter 5
Continuous Aerodynamic Modeling

5.1 Chapter Overview

Qualitative trim analysis in Chapter Four indicated that the planform and control degrees of freedom associated with MORPHEUS enables vehicle optimization while satisfying aerodynamic constraints. We will examine a limited view of vehicle optimization with respect to wing twist commands. Qualitatively, it is apparent how to vary the twist distribution with the planform state to relieve trim deflections and reduce drag. We will develop a quantitative method of producing the optimal twist distribution as a function of wing morphing for the MORPHEUS design.

As noted in Phase One wind tunnel analysis, the usefulness of VLM is limited when correlating to actual experimental data, and higher fidelity analysis methods are required. This is, in part, due to the lack of fuselage interference effects in VLM analysis. Therefore, a hybrid modeling method is presented that integrates a linear VLM expansion with DATCOM expressions for an improved aerodynamic model. This hybrid model is used with the optimal wing twist results for minimum drag trim analysis. The result of the analysis is that while we can optimize aerodynamic efficiency while trimming MORPHEUS, the control deflections indicate that a softer cost function should be implemented for basic trim analysis. This conclusion is based on the assumption of accurate trim effectiveness results from Vortex Lattice analysis.

5.2 A Note on Computational Tools

USAF DATCOM is a standard tool for stability and control analysis [Hoak, 1978]. DATCOM accepts unconventional planform shapes, creates an 'equivalent', tapered wing section and then applies a host of empirical functions to compute the stability and

control parameters. The empirical methods are not designed to capture odd configuration like an asymmetric planform state or the unconventional twist variation with wing sweep in MORPHEUS. The result is that while DATCOM is extremely useful for standard configurations, enhancements are necessary for morphing airframes. The hybrid modeling presented here is an improvement on DATCOM methods alone because there is no need to try and apply the limited empirical functions to odd configurations and deflections that can be captured fairly accurately with VLM analysis.

While TORNADO was the VLM tool for the analysis in Chapter Four, all of the development of the optimal twist distribution and the hybrid modeling technique is performed with an updated VLM code. The updated code combines geometry subfunctions from TORNADO with the author's VLM code presented in Chapter Two for a linear vehicle analysis. The TORNADO geometry functions simplify development of an interface that automates geometry formation for planform iteration. The TORNADO software cannot be used exclusively because the unconventional vortex structure, wake arrangement, and post-processing methods go beyond the linear flow and planar geometry assumptions. In addition, the unconventional variation in MORPHEUS twist distribution with wing sweep requires a custom treatment of the flow boundary conditions. Therefore, wing shapes commands are sent through a transformation routine to extract an initial lattice arrangement from TORNADO. The lattice is adapted for panel realignment, and transformed boundary conditions from the wing twist distribution are applied. Finally, a custom post-processing for a planar wing configuration is implemented to obtain ideal linear coefficients.

5.3 Washout Optimization for Continuous Planform States

We know from lifting-line theory that the minimum induced drag is achieved from an elliptic wing planform which generates an elliptic load distribution. For non-elliptic wings, Oswald's efficiency factor, e, relates how close a planform comes to achieving the ideal elliptic spanload distribution. In general, the achievable drag-due-to-lift factor is

$$K = \left(\pi A e\right)^{-1} \tag{5.1}$$

where e is one for an elliptic spanload and generally varies between 0.6 and 0.95 for non-elliptic spanloads [Bertin, 1998]. Equation (5.1) results from integrating an elliptic circulation distribution over a wing planform and computing the ratio of lift to drag coefficients. We see that using morphing to maximize aspect ratio is not enough for an ideal loiter configuration because the efficiency factor is also a function of morphing. Empirical values for e in equations (5.2) and (5.3) demonstrate that efficiency is inversely related to aspect ratio so some balance is necessary in optimizing vehicle performance. To enhance aerodynamic efficiency, aspect ratio should be increased while maintaining an elliptic spanload distribution. For respective straight and swept wings Raymer (2001) details

$$e = 1.78\left(1 - 0.045A^{0.68}\right) - 0.64 \tag{5.2}$$

$$e = 4.61\left(1 - 0.045A^{0.68}\right)\left(\cos\Lambda_{LE}\right)^{0.15} - 3.1 \tag{5.3}$$

Variable wing twist can be used on the APVE models for a slight increase in absolute loiter efficiency but it will be shown that twist control is most useful for maintaining a close-to-optimal load distribution for varying flight conditions.

Classically, washout is designed into an aircraft wing to optimize a cruise flight condition based on a set planform configuration. An elliptic chord distribution induces the optimal elliptic spanload but has unfavorable stall characteristics and is difficult to physically realize. Comparatively, a wing of constant chord has relatively excessive area at the tips and generates too much outboard lift to approximate an elliptic distribution [Raymer, 2004]. Setting the tip airfoil at a negative angle-of-attack reduces tip loading to approximate an elliptic spanload distribution for various planform arrangements.

Washout creates even greater benefits for swept wings. Sweep diverts the air towards the tips increasing the tip loading and requires even less lift at the tips in order to minimize induced drag. Hence, equation (5.3) indicates that a swept planform has a much lower efficiency than an unswept model of equivalent aspect ratio. When moderate sweep is required (e.g. the modified MORPHEUS-loiter configuration), variable washout can be used to reduce the additional tip-loading for efficient performance. Taper ratio can be used to cause the same lift reduction at the wing tips but variable taper is more difficult to implement and it lacks the maneuvering potential of twist control. Lifting-line theory can be used to generate closed-form solutions that

relate induced drag to wing twist and angle-of-attack to determine optimal relationships for the APVE models [Phillips, 2004].

5.3.1 Washout Optimization from Lifting-Line Theory

Prandtl's lifting-line theory relates the spanwise lift coefficient to local 2-D airfoil characteristics evaluated at the vehicle angle of attack reduced by the local downwash angle [Katz, 2001]. The downwash and spanwise lift distributions are computed from a Fourier sine-series approximation of the general circulation distribution.

$$\Gamma(\phi) = 2bU_{\infty}\sum_{1}^{N} A_n \sin n\phi \tag{5.4}$$

where ϕ is found from a coordinate transformation of the span coordinate, y. The lifting-line method expands the solution for the spanwise downwash to compute the coefficients of the circulation distribution. The governing formula is the classic *monoplane* equation

$$\begin{gathered}\mu(\phi)\theta(\phi)\sin(\phi) = \sum A_n \sin n\phi(\mu n + \sin\phi) \\ \mu(\phi) = \frac{c(\phi)a_o(\phi)}{4b}\end{gathered} \tag{5.5}$$

Equation (5.5) is obtained by assuming a distribution of 2D airfoil shapes with a local angle of attack reduced by the spanwise downwash distribution. The resultant circulation values are equated to (5.4) to produce a set of linear equations to determine the series coefficients. We see that the solution allows for spanwise variation in the 2D lift curve slope, a_o, the orientation relative to the freestream, θ, and the chord length, c. Only odd terms are retained in the summation because of the assumed symmetric load distributions. Integrating the series circulation expression in (5.4) results in the following expressions for the lift and induced drag coefficients [Bertin, 1998]

$$\begin{gathered}C_L = A_1\pi \cdot A \\ C_{Dv} = \frac{{C_L}^2}{\pi \cdot A}\left(1 + \sum_{n=1}^{N}(2n+1)\left(\frac{A_{2n+1}}{A_1}\right)^2\right)\end{gathered} \tag{5.6}$$

We can see that the maximum lift to drag ratio occurs when the amplitude of the additional series contributions is zero, leaving only the first coefficient in the drag response which represents the elliptic distribution. Relating (5.6) to (5.1) we can relate

lifting-line theory to Oswald's efficiency factor

$$e^{-1} = \left(1 + \sum_{n=1}^{N} (2n+1)\left(\frac{A_{2n+1}}{A_1}\right)^2\right) = (1+\delta) \tag{5.7}$$

,where δ will be referred to as the drag addition and is zero for the elliptic distribution.

Equation (5.5) has been evaluated to develop closed-form solutions for twisted elliptic wing planforms and Phillips (2004) showed that a washout angle exists that induces an elliptic load distribution for arbitrary rectangular planforms [Filotas, 1971]. Washout is accounted for in the monoplane equation by modeling the spanwise angle-of-attack as a linear function of the washout angle. The resulting circulation distribution is a nonlinear function of angle-of-attack and wing twist, indicating that the optimum washout varies with flight condition and suggesting variable twist as a worthwhile morphing function. A custom solution is required for MORPHEUS because the span is segmented with a discontinuous break between the rigid and compliant wing sections. We begin the analysis with the zero sweep loiter configuration. If the start of the compliant wing is at $y = b^*$, then the corresponding angular breakpoint can be found from the simple transformation

$$y = -b/2\cos\phi \rightarrow \phi^* = \cos^{-1}(2b^*/b) \tag{5.8}$$

Using the heaviside function for the discontinuity, the angle-of-attack distribution becomes

$$\theta(\phi) = \alpha + \varphi(\phi) \tag{5.9a}$$

$$\varphi(\phi) = \varphi^* \cos\left(\frac{\phi\pi}{2\phi^*}\right)\left[1 - \Phi(\phi - \phi^*)\right] \tag{5.9b}$$

where α is the vehicle angle-of-attack and φ^* is the command twist angle which changes the local geometric angle of attack. Equation (5.9) simply offsets the start point of the the linear twist distribution to the angular breakpoint. The heaviside function produces zero twist from ϕ^* to $\pi/2$. The monoplane equation for the MORPHEUS loiter configuration becomes

$$\begin{aligned} \phi \le \phi^* \qquad & \mu\left[\alpha + \varphi^* \cos\left(\frac{\phi\pi}{2\phi^*}\right)\right]\sin(\phi) = \sum A_n \sin n\phi(\mu n + \sin\phi) \\ \phi > \phi^* \qquad & \mu\alpha\sin(\phi) = \sum A_n \sin n\phi(\mu n + \sin\phi) \end{aligned} \tag{5.10}$$

$$\mu = 0.0864\pi \qquad \phi^* = 0.3116\pi$$

where the 2D viscous lift curve slope determined from XFOIL is used in computing μ. Numerical evaluation of (5.10) for span coordinates from *0* to $\pi/2$ in *m* increments produces *m* linear equations and Fourier coefficients. For five span increments the governing equations are

$$\begin{bmatrix} 0.838e-1\alpha + 0.734e-1\varphi^* \\ 0.1595\alpha + 0.851e-1\varphi^* \\ 0.2195\alpha + 0.1287e-1\varphi^* \\ 0.2580\alpha \\ 0.2713\alpha \end{bmatrix} = \begin{bmatrix} 0.1793 & 0.909 & 1.666 & 1.786 & 0.850 \\ 0.505 & 1.333 & 0 & -2.37 & -1.781 \\ 0.874 & 0.502 & -2.17 & 0.837 & 2.63 \\ 1.163 & -1.037 & 0 & 1.675 & -3.23 \\ 1.271 & -1.814 & 2.36 & -2.90 & 3.44 \end{bmatrix} \begin{bmatrix} A_1 \\ A_3 \\ A_5 \\ A_7 \\ A_9 \end{bmatrix} \tag{5.11a}$$

$$\begin{bmatrix} A_1 \\ A_3 \\ A_5 \\ A_7 \\ A_9 \end{bmatrix} = \begin{bmatrix} 0.247\alpha + 0.369e-1\varphi^* \\ 0.293e-1\alpha + 0.458e-1\varphi^* \\ 0.599e-2\alpha + 0.1699e-1\varphi^* \\ 0.1533e-2\alpha - 0.860e-3\varphi^* \\ 0.313e-3\alpha - 0.1862e-2\varphi^* \end{bmatrix} \tag{5.11b}$$

From (5.11b) we see that, in general, the relative influence of twist increases for the additional Fourier terms. We can maximize aerodynamic efficiency by choosing an angle-of-attack and twist command to minimize δ which will in turn maximize *e*

$$\begin{aligned} \delta(\alpha,\varphi^*) = {} & 3\left(\frac{0.293e-1\alpha + 0.458e-1\varphi^*}{0.247\alpha + 0.369e-1\varphi^*}\right)^2 + 5\left(\frac{0.599e-2\alpha + 0.1699e-1\varphi^*}{0.247\alpha + 0.369e-1\varphi^*}\right)^2 \\ & + 7\left(\frac{0.1533e-2\alpha - 0.860e-3\varphi^*}{0.247\alpha + 0.369e-1\varphi^*}\right)^2 + 9\left(\frac{0.313e-3\alpha - 0.1862e-2\varphi^*}{0.247\alpha + 0.369e-1\varphi^*}\right)^2 \end{aligned} \tag{5.12}$$

Equation (5.12) can be used the determine the globally optimal flight condition by computing the combination of twist and angle-of-attack that minimizes δ. It can also be used to compute an optimal twist input for a given angle-of-attack to determine the

most favorable washout variation with flight condition, exploiting the mission-optimization benefit of variable twist.

Applying the *fmincon* constrained minimization algorithm in MATLAB to (5.12) evaluated for 15 coefficients yields the optimal flight condition with segmented wing twist.

$$\begin{array}{cccc} \alpha = 8.603° & \varphi^* = -5.03° & \delta = 0.0023 & e = 0.9977 \\ & \varphi^* = 0° & \delta = 0.0462 & e = 0.9558 \end{array} \tag{5.13}$$

We see from (5.13) that the combination of wing twist and angle of attack reduces the drag addition, δ, by more than 95-percent. For the zero twist case, the amplitude of each term in the Fourier series is a linear function of angle-of-attack, yielding the same δ value regardless of angle-of-attack. Based on the vehicle aspect ratio and zero lift-drag coefficient the resulting decrease in induced drag factor and increase in aerodynamic efficiency is

$$\begin{array}{ccc} K_{rect} = 0.0723 & K_{twist} = 0.0693 & \Delta = -4.20\% \\ \left(L/D\right)_{\max} = 11.73 & \left(L/D\right)_{\max} = 11.99 & \Delta = +2.14\% \end{array} \tag{5.14}$$

Therefore wing-twist creates small changes in the absolute lift-to-drag ratio but can emulate this improvement in 'off-design' conditions. For example, if we examine the drag polar for the optimal twist angle in Figure 5.1, we see that the washout value does create an optimal condition at that angle-of-attack with the consequence of sub-optimal performance at other flight conditions. Using basic calculus to solve equation (5.12) for the optimal δ assuming a fixed angle of attack yields the optimal variation of segmented wing-twist with flight condition

$$\varphi^* = -0.579\alpha \tag{5.15}$$

Substituting this optimal ratio into (5.12) and comparing to a zero-twist condition reveals an approximately 94-percent reduction in drag addition for each flight condition and the improved drag polar demonstrated in Figure 5.1. The variable twist schedule is seen to maximize the aerodynamic performance along the entire range of flight conditions.

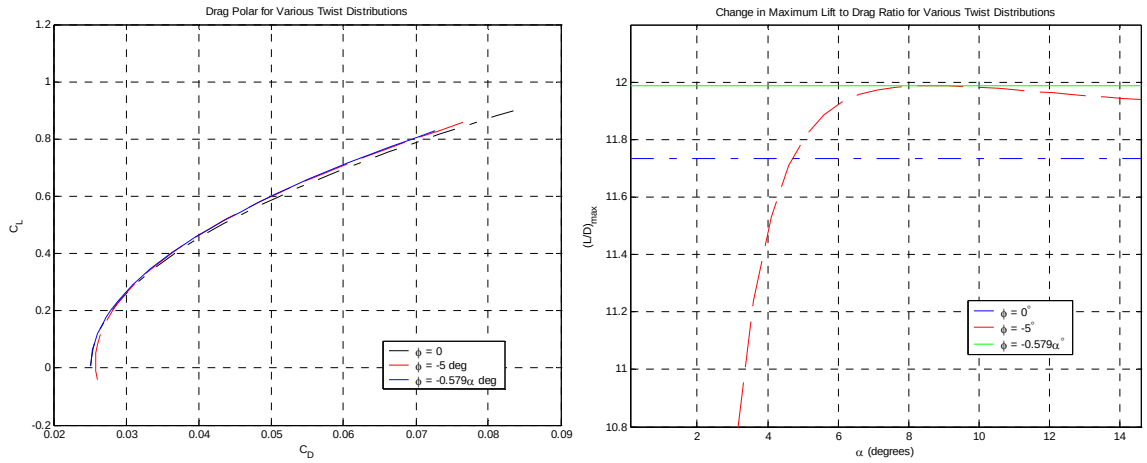

Figure 5.1. Induced Drag and Aerodynamic Efficiency of APVE P1 loiter model for various washout values. With the optimal twist distribution the minimum drag is maintained over all flight conditions.

5.3.2 Extension of Washout Optimization to Arbitrary Planforms

It would be useful to extend lifting-line analysis of the segmented-twist APVE models to various morphed configurations (variable span and sweep) to approximate performance improvements with variable wing twist. Lifting-line theory is an idealized method that produces reasonable results for unswept, high aspect ratio (> 5) planforms. A linear vortex-lattice model provides a fairly accurate circulation result for arbitrary planforms and was previously applied to determine the induced drag factor for various airframes. The VLM method is used here to extrapolate results obtained from lifting-line theory to a morphing planform configuration.

A reasonable solution seems to be possible by correlating the circulation distribution obtained from VLM with the closed-form drag and lift coefficient values derived from a Fourier sine-series representation of the circulation distribution in (5.4). The complete method consists of evaluating the custom vortex-lattice solution for the spanwise circulation distribution in terms of twist and angle of attack variables. Then a fit-algorithm is applied in MATLAB for a sine-series equation of the form in (5.4). The resulting coefficients are applied to (5.6) in the same manner as the results from lifting-line theory. The Oswald efficiency factor, and consequently the induced drag coefficient, then result from equation (5.7). This is a fairly accurate method of computing the aerodynamic characteristics of a single lifting surface because VLM does not depend on

the restrictive assumptions of lifting-line theory and the post-processing results for the generalized series circulation distribution are exact solutions with no assumptions. In particular, the true downwash velocity on the wing is obtained by integrating the gradient of the trailing vortex system as opposed to the approximate downwash velocity computed from standard VLM processing. The VLM lift coefficient serves as a check on the sine-series fit solution.

Aerodynamic coefficients and optimal twist results are now computed using the custom aerodynamic code that is a hybrid of TORNADO geometry functions and linear post-processing functions. We can compute closed-form solutions for the drag addition, δ, by taking advantage of linear theory in the VLM model (assuming small aerodynamic and deflection angles) to derive an optimal twist schedule. The vortex-lattice governing equation for a planar wing with wing twist and linear flow assumptions simplifies to

$$[C]\underline{\Gamma} = -U_\infty \left[\underline{\alpha} - \underline{\Theta}\varphi^*\right] \tag{5.16}$$

where $\underline{\Theta}$ is a vector that represents the twist distribution across the wing. For the segmented wing, $\underline{\Theta}$ maps the input command to zero and begins a linear distribution after the wing transition point. As mentioned previously, the twist distribution requires a custom treatment because the axis rotates with sweep and the boundary condition must realign on the new panel arrangement.

For each configuration the panels are arranged such that the trailing vortices are parallel to the freestream velocity. Figure 5.2 illustrates the method. An inverse mapping is applied to each new collocation point to determine where its effective unswept coordinate, so that the appropriate twist value is assigned. Given the current collocation points, $\underline{P}$, and the wing pivot point, $\underline{O}$, we have

$$\underline{P}_i = \left[x_i + j(y_i)\right] \qquad \underline{O} = \left[ox + j(oy)\right] \tag{5.17a}$$

$$\underline{R}_i = \underline{P}_i - \underline{O} \quad \rightarrow \quad \underline{p}_i = \underline{R}_i e^{-i\Lambda} + \underline{O} \tag{5.17b}$$

where Λ is the sweep angle and $\underline{p}_i$ are the swept collocation points rotated to their unswept span location. The twist allocation ($0 \rightarrow 1$) is the ratio of differences between the y-location of the transformed collocation point and the wing segment boundary

$$\underline{\Theta} = \frac{\mathrm{Re}\left(\underline{p}_i\right) - y^*}{b/2 - y^*} \tag{5.18}$$

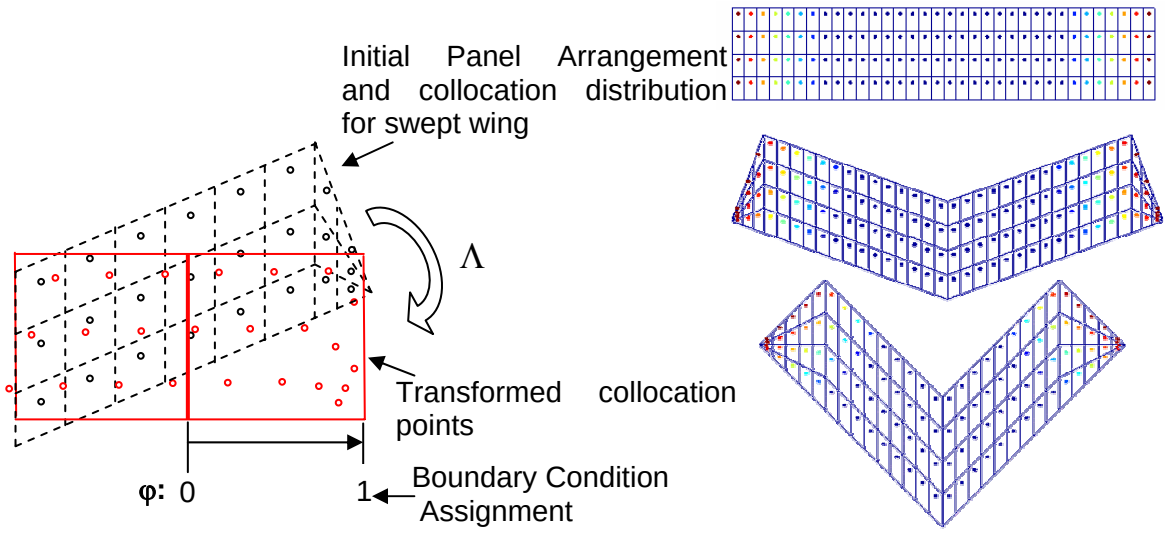

Figure 5.2. Boundary Condition Assignment for VLM Collocation Points when combining variable twist with wing pivot. The image on the right shows the reassignment from equations (5.17)-(5.18) applied to enforce the correct boundary slope.

At an instantaneous planform state with planar assumptions, the influence coefficient matrix, *C*, is constant and the circulation is proportional to the local angle of attack (total vehicle orientation minus local twist deflection). Because the aerodynamic forces are proportional to the circulation distribution, the linear static coefficients and control derivatives as a function of planform state (Δp) can be formed from (5.19), and Joukowski's theorem

$$C_{L\alpha} = -\frac{2}{S}\sum\left[C(\Delta p)\right]^{-1}\left[\underline{1}\right]\Delta y_i \tag{5.19a}$$

$$C_{L\varphi} = -\frac{2}{S}\sum\left[C(\Delta p)\right]^{-1}\left[\underline{\Theta}\right]\Delta y_i \tag{5.19b}$$

In the *Continuous Aerodynamic Modeling* section, these functions will be evaluated and fit to polynomial expressions. Johnston used this approach for a single-degree of freedom folding wing to determine a polynomial expression for the aerodynamic coefficients [Neal, 2004]. Currently, we will take the linear circulation contributions of (5.19) and create a separate sine-series fit of each contribution to the total circulation value

$$\gamma_\alpha = -C^{-1}\left[\underline{1}\right](2b)^{-1}\alpha = \left[A_{\alpha 1}\sin(\phi) + A_{\alpha 3}\sin(3\phi) + \ldots + A_{\alpha n}\sin(n\phi)\right]\alpha \tag{5.20a}$$

$$= \alpha\left[A_{\alpha i}\right]^T\left[\sin(i\phi)\right] \qquad i = 1,3,\ldots n$$

$$\gamma_\varphi = C^{-1}\left[\underline{\Theta}\right](2b)^{-1}\varphi = \left[A_{\varphi 1}\sin(\phi) + A_{\varphi 3}\sin(3\phi) + \ldots + A_{\varphi n}\sin(n\phi)\right]\varphi$$

$$= \varphi\left[A_{\varphi i}\right]^T\left[\sin(i\phi)\right] \qquad i = 1,3,\ldots n \tag{5.20b}$$

where the nondimensional VLM circulation distributions, γ, have coefficients $\alpha A_{\alpha i}$ and $\varphi A_{\varphi i}$ respectively. Summing the distributions and applying equation (5.7) yields the drag addition value

$$\delta = \frac{\left[A_{\alpha i}\sqrt{i}\right]^T\left[A_{\alpha i}\sqrt{i}\right]\alpha^2 + 2\left[A_{\alpha i}\sqrt{i}\right]^T\left[A_{\varphi i}\sqrt{i}\right]\alpha\varphi + \left[A_{\varphi i}\sqrt{i}\right]^T\left[A_{\varphi i}\sqrt{i}\right]\varphi^2}{{a_{\alpha 1}}^2\alpha^2 + 2a_{\alpha 1}a_{\varphi 1}\alpha\varphi + {a_{\varphi 1}}^2\varphi^2} \tag{5.21}$$

where i = 3, 5, …n. Equation (5.21) can be expressed as

$$\delta = \frac{\beta_1(\Delta p)\alpha^2 + 2\beta_2(\Delta p)\alpha\varphi + \beta_3(\Delta p)\varphi^2}{\beta_4(\Delta p)\alpha^2 + 2\beta_5(\Delta p)\alpha\varphi + \beta_6(\Delta p)\varphi^2} \tag{5.22}$$

where the six β_i coefficients are nonlinear functions of the planform state, Δp. This delta parameter can be used as a standalone function to optimize twist at a particular angle of attack but this will change the trim condition so in general it should be used as a cost function in some type of trim algorithm. Because δ has been formed as a quadratic cost in the state, α, and control input, φ, it can be manipulated into a standard quadratic regulator control problem. For example, if it was desired to track a flight path and maximize aerodynamic efficiency then we could use the augmented system cost

$$J_{aug} = x^T Q x + u^T R u + J_\delta \tag{5.23a}$$

$$J_\delta = \begin{bmatrix}\alpha & \varphi\end{bmatrix}\begin{bmatrix}\beta_1 & \beta_2 \\ \beta_2 & \beta_3\end{bmatrix}\begin{bmatrix}\alpha \\ \varphi\end{bmatrix} \tag{5.23b}$$

Although the augmented cost only minimizes the numerator of (5.22), this is not limiting because the entire goal of variable wing twist is to reduce the amplitude of the non-elliptic sine-series contributions to zero. The denominator of (5.22) is the elliptic contribution to the Fourier sine series and is directly dependent on the lift coefficient which will be set by trim constraints in the augmented cost. The numerator of (5.22) is the additional circulation contributions for the remaining sine terms which should be reduced as small as possible. Therefore, the augmented cost seeks to maximize aerodynamic efficiency at a given lift coefficient. For an n-dimensional state vector, x,

and *m*-dimensional control input, *u*, the augmented weighting matrices for a standard LQR cost function become

$$J_{aug} = \begin{bmatrix} x^T & u^T \end{bmatrix} \left(\begin{bmatrix} Q & 0 \\ 0 & R \end{bmatrix} + \begin{bmatrix} \mathrm{B}_1 & \mathrm{B}_2 \\ \mathrm{B}_2{}^T & \mathrm{B}_3 \end{bmatrix} \right) \begin{bmatrix} x \\ u \end{bmatrix} \tag{5.24}$$
$$= x^T (Q + \mathrm{B}_1) x + 2 x^T \mathrm{B}_2 u + u^T (R + \mathrm{B}_3) u$$

where α and φ are respectively located at the i*th*, and j*th* locations in the state and control vectors

$$x^T = \begin{bmatrix} x_1 & \dots & x_i & \dots & x_n \end{bmatrix} \qquad u^T = \begin{bmatrix} u_1 & \dots & u_j & \dots & u_m \end{bmatrix} \tag{5.25}$$

Each element of the matrix B_k is zero with the exception of the listed parameter located at the x-y coordinate

$$\mathrm{B}_1 = \left[\beta_1\right]_{ii} \in \Re^{nxn} \qquad \mathrm{B}_2 = \left[\beta_2\right]_{ij} \in \Re^{nxm} \qquad \mathrm{B}_3 = \left[\beta_3\right]_{jj} \in \Re^{mxm} \tag{5.26}$$

Upon iterating the VLM function, the β_i parameters can be computed as functions of wing sweep and span extension. Fitting the resulting surface plots to a polynomial expression yields an analytic representation of (5.24)-(5.26) that can be used for control implementation. Like the static coefficients in (5.19) the δ coefficients will be explored in the continuous modeling section.

The previous analysis extended the results from lifting line theory to arbitrary wing planforms by exploiting the vortex lattice method. The power of the method lies in the ability of VLM to compute circulation distributions for arbitrary planform arrangements and multiple lifting surfaces. The technique is derived for a single wing planform but if additional surfaces are present, such as the variable geometry tail for MORPHEUS, the Fourier series should be computed for the wing circulation resulting from the interference caused by the additional surfaces in VLM. The result will no longer predict the true vehicle drag coefficient but can still be used to minimize the drag on the main wing.

5.4 Continuous Modeling of Aerodynamic Coefficients

Empirical functions from USAF DATCOM will be combined with VLM analysis to approximate a limited set of continuous aerodynamic functions for MORPHEUS. These functions will lay the framework for future stability analysis and control design. The planform set is limited to symmetric configurations and the combined longitudinal/lateral tail shift is ignored in favor of variable incidence for trim control. Specifically, the model will comprise of a fixed tail location with a main wing that varies in sweep, span extension, and wing twist. In this initial development, only longitudinal aerodynamic models and stability equations are computed.

DATCOM applies empirical functions to classical stability equations in a built-up formulation that assumes independent lifting surfaces [Hoak, 1978]. The approach used for MORPHEUS is to apply linear VLM results in place of all empirical functions relating to the lifting capacity of a wing surface and to use the empirical functions of DATCOM to amplify for fuselage effects while establishing a set of linear aerodynamic expressions. The model is formulated within the framework of classical stability expressions from Etkin. It was necessary to compare DATCOM expressions with classic stability equations to understand where to make the appropriate modifications for variable wing geometry and where VLM analysis could be applied in identifying stability parameters.

A general expansion is presented to show the need for smooth aerodynamic functions for an adaptive planform. A linear VLM expansion follows to show how the local aerodynamic functions are obtained followed by integration with DATCOM to compute aerodynamic coefficients for the entire vehicle. Surface responses of these aerodynamic coefficients are presented as a function of the morphing parameters. The responses are fit to 3D polynomial functions in span and sweep changes that can be applied in both stability analysis and control design. Elementary trim analysis with the previously derived minimum drag washout constraint concludes the section. Throughout the derivation, nominal parameters from the reference geometry in Figure 4.11 are used to nondimensionalize the coefficients.

5.4.1 Aerodynamic Expansions for a Dynamic Planform

First-order panel methods lend themselves to developing state-dependent aerodynamic forces. A relatively simple method for deriving analytical functions is blended modeling that incorporates empirical functions from DATCOM and circulation distributions from computational algorithms like vortex-lattice or vortex-ring methods. Iteration through the planform trajectory results in smooth aerodynamic functions that can be exploited for first-cut stability analysis and control design. In general, we can develop a set of quasi-steady aerodynamic functions, *N(p(t),w(t))*, that are implicit functions of time through the planform (*p*) and aerodynamic (*w*) states. A Taylor expansion about an equilibrium point is used to obtain standard aerodynamic coefficients but because of the relatively large planform motions, the expansion must be performed about a nominal planform *trajectory* for morphing analysis

$$N(p(t),w(t)) \cong N_o\big|_{c_o} + N_p\big|_{c_o}\,\tilde{p}(t) + N_w\big|_{c_o}\,\tilde{w}(t) \tag{5.27}$$

where $c_o = \begin{bmatrix} p_o(t) & w_o \end{bmatrix}$. We assume a quasi-steady dependence of the aerodynamic forces on the planform state so the coefficients continually update with the instantaneous planform value. For small perturbations in the aerodynamic state, we can represent the general aerodynamic stability derivatives as a summation of the zero-state response and linear coefficients of fast and slow aerodynamic states. Slow states are defined as those states with a nonzero trim point.

$$N(p(t),w(t)) = N_0\big(p(t)\big) + N_{ws}(p(t))w_s(t) + N_{wf}(p(t))w_f(t) \tag{5.28}$$

Note that 5.28 is *not* an expansion, but rather is obtained by assuming linear coefficients for small state values. Hence, the true aerodynamic states, w_s and w_f, are used and not state deviations from an equilibrium point. Expansion of (5.28) about the equilibrium trajectory c_o results in

$$N\big(p(t),w(t)\big) \approx N_o\big|_{c_o} + \left(\frac{\partial N_o}{\partial p} + \frac{\partial N_{ws}}{\partial p}w_{so}\right)_{p_o(t)} \tilde{p}(t) + N_w\big|_{c_o}\,\tilde{w}(t) \tag{5.29}$$

where the fast and slow aerodynamic states have been joined in the final expansion. We see from the planform (morphing) derivative that the coefficients of slow aerodynamic states with a nonzero trim point must be differentiable functions of the planform state. As it stands, equation (5.29) is a simple way of integrating quasi-steady aerodynamic

functions into the flight equations for a dynamic planform. As an example, the pitching moment coefficient for a nominal span trajectory, $r(t)$ would be

$$C_M(p,\alpha,q,t) \approx C_{Mo}\big|_{r(t)} + \left[\frac{\partial C_{Mo}}{\partial b} + \alpha_o \frac{\partial C_{M\alpha}}{\partial b}\right]\Bigg|_{r(t)} \tilde{b}(t) + C_{M\alpha}\big|_{r(t)} \tilde{\alpha}(t) + C_{Mq}\big|_{r(t)} q(t) \quad (5.30)$$

The present analysis is concerned with static trim so the planform derivatives are not required but the expansion illustrates the need for aerodynamic coefficients as smooth functions of the planform parameters.

5.4.2 Implementing the VLM Solution into DATCOM Stability Equations

The linear VLM expansion presented will be referred to through the derivation of the linear coefficients. The basic expansion presented in equation (5.19) did not separate the effects of a wing and a tail included in the panel geometry and was not extended to compute downwash results. If we denote the negated inverse of the influence coefficient matrix in (5.19) as a partitioned matrix ($[G]=-[C(\Delta p)]^{-1}$), we obtain the following wing and tail circulation distributions for small angles

$$\frac{1}{U_\infty}\begin{Bmatrix}\underline{\Gamma}_W\\ \underline{\Gamma}_T\end{Bmatrix} = \begin{bmatrix}G_W\\ G_T\end{bmatrix}\begin{Bmatrix}\underline{1}\\ \underline{1}\end{Bmatrix}\alpha + \begin{bmatrix}G_W\\ G_T\end{bmatrix}\begin{Bmatrix}\underline{\Theta}\\ \underline{0}\end{Bmatrix}\varphi \quad \Rightarrow \quad \begin{matrix}\underline{\gamma}_{W\alpha} = G_W \underline{\mathrm{I}} & \underline{\gamma}_{W\varphi} = G_W \underline{\Psi}\\ \underline{\gamma}_{T\alpha} = G_T \underline{\mathrm{I}} & \underline{\gamma}_{T\varphi} = G_T \underline{\Psi}\end{matrix} \quad (5.31)$$

$$\mathrm{I} = \begin{bmatrix}\underline{1} & \underline{1}\end{bmatrix}^T \qquad \Psi = \begin{bmatrix}\underline{\Theta} & \underline{0}\end{bmatrix}^T$$

$$G_W \in \Re^{n\times(n+m)} \qquad G_T \in \Re^{m\times(n+m)} \qquad \mathrm{I}, \Psi \in \Re^{(n+m)\times 1}$$

where $\underline{\mathrm{I}}$ and $\underline{\Psi}$ are the respective coefficient vectors of α and φ and the γ-vectors are the nondimensional circulation distributions along the span. The partition for [G] is for the separate angle of attack and twist influence on the wing and tail where *n* and *m* are the respective number of panels. Equation (5.31) demonstrates the power of VLM by illustrating the effect of cross-coupling on the aerodynamic forces. For example, although the twist input is solely on the wing, we see that the tail circulation is effected through $[G_T]\underline{\Theta}$. The straightforward empirical functions from DATCOM would never capture this effect, so we see that judicious implementation of the VLM solution allows more accurate modeling results. With the nondimensional circulation values we can

compute the explicit *local* aerodynamic coefficients as

$$C_{L\alpha W} = -\frac{2}{S}\sum \gamma_{W\alpha i}\Delta y_{Wi} \qquad C_{M\alpha W} = -\frac{2}{S\bar{c}}\sum r_i \cdot \gamma_{W\alpha i}\Delta y_{Wi} \tag{5.32a}$$

$$C_{L\varphi W} = -\frac{2}{S}\sum \gamma_{W\varphi_i}\Delta y_{Wi} \qquad C_{M\varphi W} = -\frac{2}{S\bar{c}}\sum r_i \cdot \gamma_{W\varphi_i}\Delta y_{Wi} \tag{5.32b}$$

$$C_{L\alpha T} = -\frac{2}{S_T}\sum \gamma_{T\alpha i}\Delta y_{Ti} \qquad C_{M\alpha T} = -\frac{2}{S_T\bar{c}}\sum r_i \cdot \gamma_{T\alpha i}\Delta y_{Ti} \tag{5.32c}$$

$$C_{L\varphi T} = -\frac{2}{S_T}\sum \gamma_{T\varphi_i}\Delta y_{Ti} \qquad C_{M\varphi T} = -\frac{2}{S_T\bar{c}}\sum r_i \cdot \gamma_{T\varphi_i}\Delta y_{Ti} \tag{5.32d}$$

where the tail area, S_T is used to temporarily normalize the appropriate local coefficients.

There is further cross-coupling evidenced in the induced velocity results. In conventional VLM post-processing, the induced drag is computed from the velocity induced by the trailing vortices [Katz, 2001]. The influence of the trailing vortices on one another is formed as a separate influence coefficient matrix, [V] (the influence of the bound vortices is removed) and the induced velocity at the collocation points is found via [V]$\underline{\Gamma}$. In general this is not correct because the true induced velocity is computed by integrating the gradient of the circulation distribution across the wing but it suffices for the present analysis. Carrying through the expansion, we obtain the following result for the velocity induced at the collocation point of each panel, w

$$\begin{Bmatrix} \underline{w}_W \\ \underline{w}_T \end{Bmatrix} = U_\infty \begin{bmatrix} V_{Ww} & V_{Wt} \\ V_{Tw} & V_{Tt} \end{bmatrix} \begin{Bmatrix} \underline{\gamma}_W \\ \underline{\gamma}_T \end{Bmatrix} = U_\infty \begin{bmatrix} V_{Ww}G_W + V_{Wt}G_T & V_{Ww}G_W + V_{Wt}G_T \\ V_{Tw}G_W + V_{Tt}G_T & V_{Tw}G_W + V_{Tt}G_T \end{bmatrix} \begin{Bmatrix} \underline{\mathrm{I}} \\ \underline{\Psi} \end{Bmatrix} \tag{5.33}$$

where the first subscript denotes the lifting surface upon which circulation of the second subscript acts (e.g. V_{Tw} is velocity induced on the tail collocation points by the trailing vortices from the wing). Noting that for small angles, the downwash angle can be computed as the ratio of the induced velocity to freestream velocity, we can define the tail downwash angle as $\varepsilon = w_T/U_\infty$ which is proportional to angle-of-attack and twist commands

$$\varepsilon_\alpha = -\sum \left[V_{Tw}G_W + V_{Tt}G_T\right]\underline{\mathrm{I}} \qquad \varepsilon_\varphi = -\sum \left[V_{Tw}G_W + V_{Tt}G_T\right]\underline{\Psi} \tag{5.34}$$

The summation in (5.34) results in a spanwise distribution of the downwash angle gradient with respect to angle of attack and twist inputs across the tail. In a general derivation of the stability equations, the total downwash angle at the tail adjusts the

local angle of attack. The derivation of the influence coefficients for the VLM model is based on satisfying a boundary condition for induced velocity due to the trailing and bound vortices. Therefore, the VLM circulation solution at the tail already accounts for the effective angle of attack reduction from the trailing vortices. Hence, the downwash computed in (5.34) will only be used in approximating fuselage effects from DATCOM.

Figure 5.3 displays the general configuration and coordinates used in deriving the longitudinal stability equations. The figure is slightly modified from the presentation in [Etkin, 1996] to include the wing apex reference position. The relevant aerodynamic forces are a lift force and a pitching moment located at the aerodynamic center of the main wing and tail. Each lifting surface is represented by its mean aerodynamic chord which is globally referenced to x, the location of the nominal wing mean aerodynamic chord behind the nominal apex.

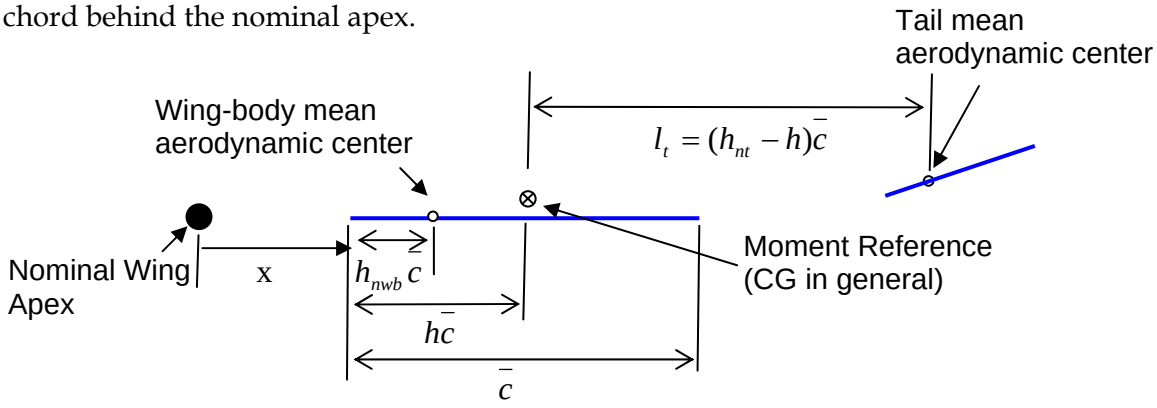

Figure 5.3. Parameter definitions for the classic stability equations presented by Etkin. All parameters are globally referenced to the nominal wing apex and are nondimensionalized by the reference mean aerodynamic chord.

The total aircraft lift coefficient presented in [Etkin] is

$$C_L = C_{Lwb} + \frac{S_t}{S} C_{Lt} = C_{L\alpha}\alpha_{wb} + C_{Lo} \tag{5.35a}$$

$$C_{L\alpha} = C_{L\alpha wb} + \frac{S_t}{S} C_{Lt}\left(1 - \frac{d\varepsilon}{d\alpha}\right) \tag{5.35b}$$

$$C_{Lo} = C_{Lowb} + C_{L\alpha t}\frac{S_t}{S}\left(i_t + \varepsilon_o\right) \tag{5.35c}$$

The zero-lift response will obviously become a function of the washout command due to variable wing twist. Hence the zero angle of attack wing lift coefficient, C_{Lowb}, is

computed as a term proportional to wing twist using $C_{L\varphi W}$.

Due to interference from the wing and fuselage, the dynamic pressure at the tail is reduced by η and downwash from the wing reduces the local angle of attack. The downwash angle at the tail, ε, is generally approximated by the sum of a constant component due to built-in geometric twist (ε_o) and a component due to the trailing wing vortices that varies linearly with alpha ($d\varepsilon/d\alpha$) [Etkin, 1996]. Separating the tail downwash angle into components is necessary when the aerodynamic parameters of the wing and tail are computed as two independent surfaces. As mentioned previously, the combined VLM analysis removes the need to include these effects. The influence of the twist-induced downwash on the tail is captured in $C_{L\varphi T}$ and the lift-induced downwash by $C_{L\alpha T}$.

We also assume direct control of the tail orientation through the incidence angle. Including these specific variations we can manipulate the standard equations to represent the lift coefficient as three separate components proportional to angle of attack, wing twist, and tail incidence.

$$C_L = \left[K_{wf} C_{L\alpha w} + C_{L\alpha t}\eta\frac{S_t}{S}\right]\alpha_{wb} + \left[K_{wf} C_{L\varphi w} + C_{L\varphi t}\eta\frac{S_t}{S}\right]\varphi + \left[-C_{L\alpha t}\eta\frac{S_t}{S}\right]i_t \quad (5.36)$$

DATCOM results have been included to account for fuselage effects on the wing lift-curve slope and zero-lift response. The fuselage interference factor, K_{wf}, is computed from DATCOM as a nonlinear function of the ratio of the maximum equivalent fuselage diameter and the wing span. Equation (5.36) combines local VLM results, classical stability expressions, and DATCOM parameters to determine the linear lift coefficient for the entire aircraft. It is the first of two fundamental trim equations. Balancing the pitching moment is the second.

The pitching moment result presented by Etkin (with amplification for the wing-body lift coefficient at zero angle of attack) is

$$C_m = C_{m\alpha}\alpha + \overline{C}_{mo} \quad (5.37a)$$

$$C_{m\alpha} = \left[C_{L\alpha wb}\left(h - h_{nwb}\right) - V_H C_{L\alpha t}\left(1 - d\varepsilon/d\alpha\right)\right] \quad (5.37b)$$

$$\overline{C}_{mo} = \left[C_{Macwb} + V_H C_{L\alpha t}\left(i_t + \varepsilon_o\right) + C_{Lowb}\left(h - h_{nwb}\right)\right] \quad (5.37c)$$

where the horizontal tail volume ratio can be represented in terms of Figure 5.3 as

$$V_H = \frac{l_t S_t}{\bar{c} S} = (h_{nt} - h)\frac{S_t}{S} \tag{5.38}$$

The major effects that must be included from DATCOM are the zero-lift pitching moment due to the fuselage and the shift in the wing aerodynamic center due to the fuselage. We again manipulate the standard equations to include DATCOM approximations and VLM results where applicable, yielding the fundamental linear pitching moment expression

$$\begin{aligned} C_M = C_{Mof} &+ \left[K_{wf} C_{L\alpha w} \left(h - \left(h_{nw} + dh_{nf}\right)\right) + C_{L\alpha t}\eta\left(h - h_{nt}\right)\frac{S_t}{S} \right]\alpha_{wb} \\ &+ \left[K_{wf} C_{L\varphi w} \left(h - \left(h_{nw} + dh_{nf}\right)\right) + C_{L\varphi t}\eta\left(h - h_{nt}\right)\frac{S_t}{S} \right]\varphi + \left[C_{L\alpha t}\eta\left(h - h_{nt}\right)\frac{S_t}{S} \right] i_t \end{aligned} \tag{5.39}$$

where all appropriate VLM parameters have been defined previously with the exception of the fuselage zero-lift pitching moment coefficient, C_{Mof}, and the shift in the wing aerodynamic center due to the fuselage, dh_{nf}. The former is computed using DATCOM approximations and the method to determine the latter was reported in [Roskam, 1979].

In Figure 5.3, h represents the normalized distance of the c.g. behind the apex of the mean aerodynamic chord but it can also be a random reference point for the moment computation. In this analysis it is chosen to be the mount point of the MORPHEUS wind tunnel model. The aerodynamic center of the wing and tail are located at h_{nw} and h_{nt}, which can be computed using the local VLM coefficients for each lifting surface

$$h_{nw} = h - \frac{C_{M\alpha w}}{C_{L\alpha w}} \qquad h_{nt} = h - \frac{C_{M\alpha t}}{C_{L\alpha t}} \tag{5.40}$$

We note that by using the VLM coefficients, the local aerodynamic center of each lifting surface is computed with consideration of flow interaction with the other.

The fuselage zero lift pitching moment is found from the following DATCOM expression which segments the fuselage and computes the weighted incidence angle using the mean segment width

$$C_{mof} = \frac{k_2 - k_1}{36.5 S \bar{c}} \sum_{i=1}^{13} {w_{fi}}^2 \left(i_f - i_w + \alpha_{olw}\right)\Delta x_i \tag{5.41}$$

where (k_2 - k_1) is an empirical DATCOM function based on the fineness parameter and the fuselage and wing incidence angles are i_f and i_w respectively. The summation to determine the mean fuselage width can be replaced with three integral expressions

corresponding to the piecewise continuous fuselage segments in Figure 5.4. Equation (5.41) simplifies for MORPHEUS because of the zero-camber fuselage line and the lack of wing incidence. Because, the zero-lift angle of attack (α_{olw}) varies with wing twist and there is no camber contribution, we can use the chain rule to derive the following simplified result, incorporating the VLM solution

$$\alpha_{olw} = \frac{\partial \alpha_w}{\partial \varphi}\varphi = \frac{\partial \alpha_w}{\partial C_{Lw}}\frac{\partial C_{Lw}}{\partial \varphi}\varphi = \frac{C_{L\varphi w}}{C_{L\alpha w}}\varphi \quad \Rightarrow \quad C_{mof} = \frac{k_2 - k_1}{36.5\bar{S}\bar{c}}\frac{C_{L\varphi w}}{C_{L\alpha w}}\varphi\int_0^L w^2(x)dx \quad (5.42)$$

The expansion provides another term in the fundamental pitching moment equation (5.39) that is proportional to wing twist.

The wing aerodynamic center shift, dh_{nf}, is found from [Roskam, 1979] as

$$dh_{nf} = -\frac{1}{2.92\bar{S}\bar{c}}\sum_{i=1}^{13} w_{fi}{}^2\left(d\bar{\varepsilon}/d\alpha\right)_i \Delta x_i \quad (5.43)$$

While the fuselage segmentation can be simplified to a sum of several integrals, the value of the flow angle gradient $(d\bar{\varepsilon}/d\alpha)_i$ changes as we proceed towards the tail. Analytical flow assumptions are used to compute the gradient value at fuselage segments ahead of the primary wing corresponding to the upwash. The solution for the aft segments assumes a linear increase in the fuselage downwash based on the tail downwash gradient ($d\varepsilon/d\alpha$) which we compute from VLM. To apply the hybrid modeling method to (5.43) we separate the integral into fore and aft wing sections that implement either the empirical upwash function or the VLM downwash solution

$$dh_{nf} = -\frac{1}{2.92\bar{S}\bar{c}}\left[\int_0^{L_1} w^2(x)\frac{d\bar{\varepsilon}}{d\alpha}(x)dx + \frac{\left(1-\varepsilon_\alpha\right)}{x_h}\int_{L_1}^{L}\left(x-L_1\right)w^2(x)dx\right] \quad (5.44)$$

In (5.44) L_1 locates the x-coordinate of the wing-fuselage intersection and x_h is the distance of the tail mean aerodynamic center behind L_1 which changes with morphing inputs. The downwash ε_α in the second term is the previously derived VLM result. Data points approximated from a graph of the wing upwash in [Roskam, 1979] corresponds fairly well to a sum of exponential functions so that the upwash function can be approximated by

$$\frac{d\bar{\varepsilon}}{d\alpha}(x) = 0.7168e^{-2.058x} + 1.096e^{-0.0256x} \qquad 0 \le x \le L_1 \quad (5.45)$$

where the coefficients are computed using *MATLAB* software.

The fuselage segments and dimensions are displayed in Figure 5.4. The results in the figure are sufficient for computing a closed-form expression for C_{M0f} but the aerodynamic center shift, dh_{nf}, must be computed as a function of morphing due to the VLM solution in the second term. The general result is an aftward shift of the wing aerodynamic center due to the fuselage.

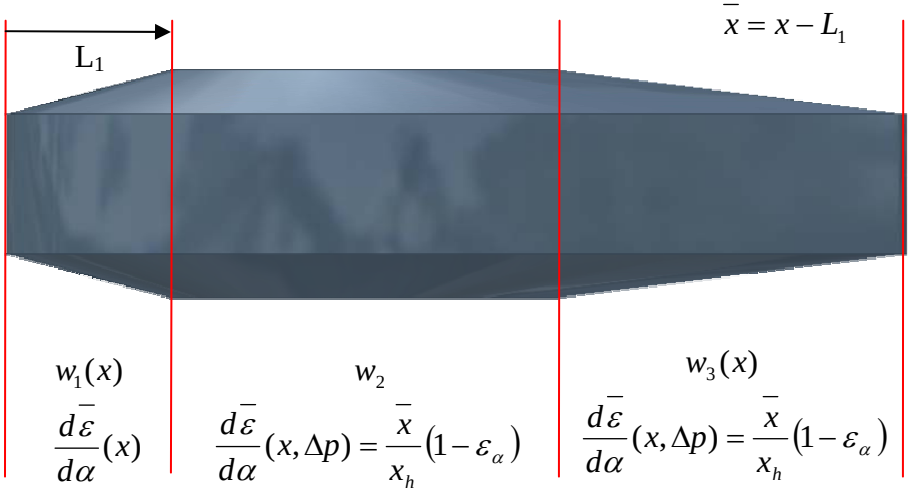

Figure 5.4. Fuselage segmentation for computing pitching moment parameters. The first segment consists of upwash from (5.45). The intermediate and final segments are a linear function of the VLM derived downwash value.

Equations (5.36) and (5.39) define the coefficients for the static aircraft lift and pitching moment equations as a function of morphing using the hybrid modeling method. For trim analysis the equations can be simplified to

$$C_L = C_{L\alpha}(\Delta p)\alpha_{wb} + C_{L\varphi}(\Delta p)\varphi + C_{Lit}(\Delta p)i_t \tag{5.46a}$$

$$C_M = C_{M\alpha}(\Delta p)\alpha_{wb} + C_{M\varphi}(\Delta p)\varphi + C_{Mit}(\Delta p)i_t \tag{5.46b}$$

5.4.3 Minimum Drag Trim Analysis

The VLM expansion has already been detailed and the lift and moment coefficients have been specified. Elementary trim analysis requires that lift support the weight while enforcing zero pitching moment. Using equation (5.46), and expanding Etkin's basic trim solution to include variable tail incidence we obtain

$$\begin{bmatrix} C_{L\alpha} & C_{L\varphi} & C_{Lit} \\ C_{M\alpha} & C_{M\varphi} & C_{Mit} \end{bmatrix} \begin{Bmatrix} \alpha_{wb} \\ \varphi \\ i_t \end{Bmatrix} = \begin{bmatrix} W / \bar{q} S \\ 0 \end{bmatrix} \tag{5.47}$$

Equation (5.47) can be solved as an optimization problem in minimizing the weighted deflections or by constraining a degree of freedom. For instance, if we solve for the optimal twist schedule based on minimizing the drag addition, δ, we obtain

$$\varphi = \Omega(\Delta p)\alpha_{wb} \tag{5.48}$$

as a function of the morphing inputs based on the β_i parameters in equation (5.22). The Fourier sine-series fit is produced of the wing circulation values *with the tail included in the model*. Constraining the degree of freedom simplifies the trim equations to the square system

$$\begin{bmatrix} C_{L\alpha} + \Omega C_{L\varphi} & C_{Lit} \\ C_{M\alpha} + \Omega C_{M\varphi} & C_{Mit} \end{bmatrix} \begin{Bmatrix} \alpha_{wb} \\ i_t \end{Bmatrix} = \begin{bmatrix} W / \bar{q} S \\ 0 \end{bmatrix} \tag{5.49}$$

yielding the minimum drag trim conditions

$$\begin{Bmatrix} \alpha_{wb} \\ i_t \end{Bmatrix} = \frac{W}{\Delta \bar{q} S} \begin{bmatrix} C_{Mit} \\ -C_{M\alpha} - \Omega C_{M\varphi} \end{bmatrix} \tag{5.50a}$$

$$\Delta = C_{Mit}\left(C_{L\alpha} + \Omega C_{L\varphi}\right) - C_{Lit}\left(C_{M\alpha} + \Omega C_{M\varphi}\right) \tag{5.50b}$$

The custom VLM code is used to compute the two governing trim coefficients as a function of wing sweep and span

$$C_1(\Lambda, \Delta b) = \frac{C_{Mit}}{\Delta} \qquad C_2(\Lambda, \Delta b) = \frac{-C_{M\alpha} - \Omega C_{M\varphi}}{\Delta} \tag{5.51}$$

The post-processing implements the following procedure. First, the six β_I parameters are identified from the Fourier sine-series fit and used to form the optimal twist ratio, Ω(Δp). This value can be determined for an instantaneous span and sweep configuration by applying elementary calculus to equation (5.22) yielding

$$\Omega(\Delta p) = \frac{-\left(\beta_3\beta_4 - \beta_1\beta_6\right) + \sqrt{\left(\beta_3\beta_4 - \beta_1\beta_6\right)^2 + 4\left(\beta_2\beta_4 - \beta_1\beta_5\right)\left(\beta_2\beta_6 - \beta_3\beta_5\right)}}{2\left(\beta_3\beta_5 - \beta_2\beta_6\right)} \tag{5.52}$$

The six lift and moment coefficients are then computed where the final coefficients from equations (5.46) are

$$C_{L\alpha}(\Delta p) = \left[K_{wf} C_{L\alpha w} + C_{L\alpha t} \eta \frac{S_t}{S} \right] \tag{5.53a}$$

$$C_{L\varphi}(\Delta p) = \left[K_{wf} C_{L\varphi w} + C_{L\varphi t} \eta \frac{S_t}{S} \right] \tag{5.53b}$$

$$C_{Lit}(\Delta p) = \left[- C_{L\alpha t} \eta \frac{S_t}{S} \right] \tag{5.53c}$$

$$C_{M\alpha}(\Delta p) = \left[K_{wf} C_{L\alpha w} \left(h - \left(h_{nw} + dh_{nf} \right) \right) + C_{L\alpha t} \eta \left(h - h_{nt} \right) \frac{S_t}{S} \right] \tag{5.53d}$$

$$C_{M\varphi}(\Delta p) = \left[K_{wf} C_{L\varphi w} \left(h - \left(h_{nw} + dh_{nf} \right) \right) + C_{L\varphi t} \eta \left(h - h_{nt} \right) \frac{S_t}{S} + \mathrm{X} \frac{C_{L\varphi w}}{C_{L\alpha w}} \right] \tag{5.53e}$$

$$C_{Mit}(\Delta p) = \left[- C_{L\alpha t} \eta \left(h - h_{nt} \right) \frac{S_t}{S} \right] \tag{5.53f}$$

In (5.53e) the fuselage zero-lift pitching moment (C_{M0f}) expansion has been integrated into the twist coefficient so that:

$$X = \frac{k_2 - k_1}{36.5 S \bar{c}} \int_0^L w^2(x) dx \tag{5.54}$$

Finally, the coefficients C_1 and C_2 are computed and multiplied by the nominal wing loading to obtain a solution that scales with the inverse of dynamic pressure.

5.4.4 VLM Surface Plot Solutions

Iteration of the VLM code through multiple wing geometries is nontrivial because of the changing panel arrangement with wing geometry. With multiple lifting surfaces, singularities can arise if the trailing vortices from one surface intersect or approach the collocation points on a surface behind it [Mason, 1995]. Because the TORNADO panel arrangement varies with span and sweep there are many configurations in which the wing vortices intersect the tail collocation points and incorrect results are obtained. A dynamic panel re-alignment was performed for each lattice structure generated by the TORNADO subfunction such that the trailing vortices of the interior wing panels align in the span coordinate with those of the tail for each configuration. The remaining panels are redistributed across the wing to maintain a constant number of panels on each surface for smooth parameter variation.

Chosen aerodynamic coefficients from equation (5.53) are presented for a qualitative analysis of the variation in aerodynamic characteristics with planform state. Although it would be instructive to see how local coefficients vary with morphing, for the sake of brevity only the total vehicle coefficients are presented. Surface responses of the aircraft lift curve slope, aerodynamic center and twist sensitivities as a function of wing sweep and span are displayed and fit to polynomial expressions. The vehicle aerodynamic center is computed in the same manner as the local aerodynamic centers by exchanging the local lift curve slope and pitch stiffness in (5.40) with absolute values for the entire aircraft. The variation in the optimal twist distribution with sweep and span changes, $\Omega(\Delta p)$, is also presented.

The following array definitions are used to simplify the polynomial representations

$$v_i = \begin{bmatrix} 1 & \Lambda & \Lambda^2 & \dots & \Lambda^{i-1} \end{bmatrix} \cdot \frac{\pi}{180} \qquad u_i = \begin{bmatrix} 1 & \hat{b} & \hat{b}^2 & \dots & \hat{b}^{i-1} \end{bmatrix}^T \tag{5.55}$$

where $\hat{b}$ is the nondimensional span extension, $\delta b/\Delta B$ and Λ is the wing sweep. The arrays bound a constant matrix of coefficients with the appropriate dimensions. Using the array definitions in (5.55) simplifies the differentiation required for the morphing stability derivatives. The first derivative of an aerodynamic parameter corresponds to a single order reduction in the array and multiplication by a diagonal matrix so that

$$\frac{\partial v_i}{\partial \Lambda} = \begin{bmatrix} 0 & v_{i-1} \end{bmatrix} diag\{0 \quad 1 \quad 2 \quad \cdots \quad i-1\} \quad \frac{\partial u_i}{\partial b} = diag\{0 \quad 1 \quad 2 \quad \cdots \quad i-1\} \begin{bmatrix} 0 & u_{i-1} \end{bmatrix}^T \tag{5.56}$$

The simplified representations of (5.55) and (5.56) are useful for representing the aerodynamics as an explicit nonlinear function of the planform state in the equations of motion.

The aircraft lift curve slope in Figure 5.5 follows the expected trends. It is approximately linear in span extension and quadratic in sweep. It increases initially because of the initial increase in effective span due to the pivot location but decreases beyond this point. The aerodynamic center shifts further back as a greater percentage of wing area is moved aft. The reference point for the moment calculation is at h =0.3026 so Figure 5.6 indicates that MORPHEUS is longitudinally stable about the wind tunnel mount point for sweep angles above approximately 10-degrees.

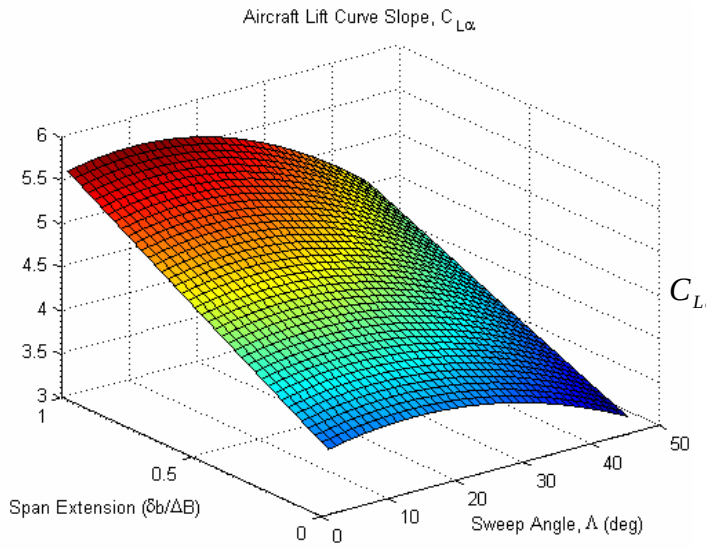

$$C_{L\alpha} = v_3^{\,T} \begin{bmatrix} 3.73 & 1.785 & 0.043 \\ 1.022 & 0.0254 & -0.0044 \\ -2.15 & -0.807 & -0.0218 \end{bmatrix} u_3$$

Figure 5.5. Aircraft Lift Curve Slope Variation with Planform State

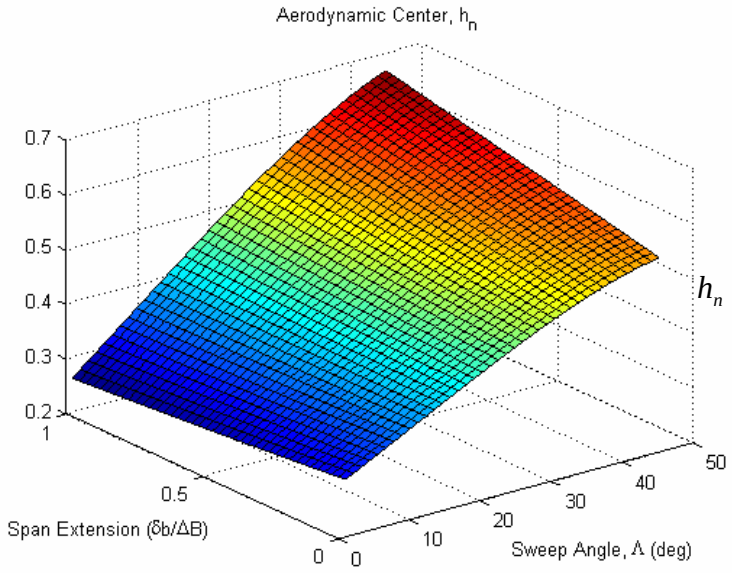

$$h_n = v_3^{\,T} \begin{bmatrix} -0.225 & -0.598 & -0.191 \\ -1.13 & 0.419 & 0.382 \\ 0.870 & -0.634 & 0.652 \end{bmatrix} u_3$$

Figure 5.6. Aircraft Aerodynamic Center Shift with Planform State

We see from Figures 5.7 and 5.8 that we not only maintain control authority with twist but actually increase authority with greater sweep angles up to approximately 30-degrees. This is an unintuitive result but is most likely due to the increase in circulation strength from the decreasing distance between the twisting section and all other collocation points. Using the standard coordinate system, positive washout generates negative lift. Therefore, when trying to minimize drag in flight, it will be necessary to fly at a higher angle of attack to account for the loss of lift. Comparing Figure 5.7 with the magnitude of the lift curve slope we see that approximately five times as much twist would be required to cancel the lift from angle of attack. We can be confident in exploiting the favorable pitch response to variable twist for satisfying trim requirements.

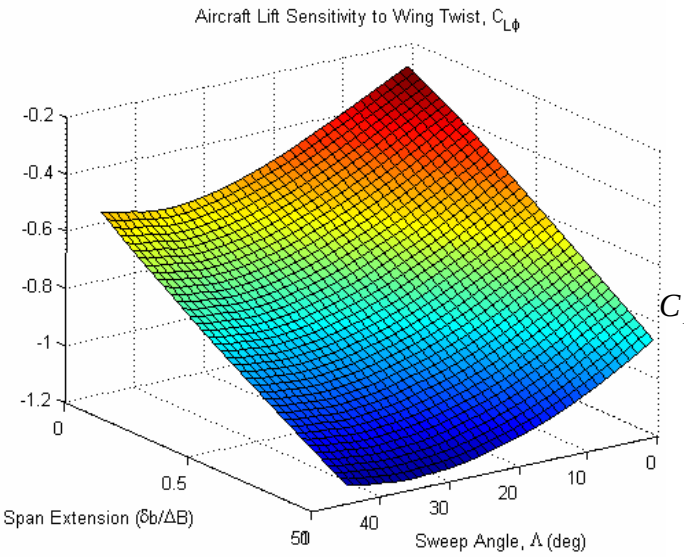

$$C_{L\varphi} = v_4^{\,T} \begin{bmatrix} -0.258 & -0.515 & -0.0618 \\ -0.749 & -0.202 & -0.0513 \\ -0.189 & 0.657 & 0.245 \\ 0.829 & -0.804 & 0.0774 \end{bmatrix} u_3$$

Figure 5.7. Variation in Aircraft Lift Sensitivity to Twist with Planform State

The pitch sensitivity to wing twist is essentially the weighted sum of the momen ts induced by wing and tail lift forces about the reference point at zero angle of attack. In terms of standard stability coefficients this is the sensitivity of C_{mo} to wing twist. At positive washout decreases the lift here which in turn reduces the nose-down pitching moment. The overall result is that washout establishes a positive C_{mo} value that increases with the percentage of swept wing area. Alone, this coefficient change would require a

higher trim angle of attack but the same planform motions counter the increase in C_{mo} by inducing greater absolute pitch stiffness. Dependence on the percentage of active wing area aft of the reference point is why the pitch sensitivity to twist generally follows the aerodynamic center results in Figure 5.6, increasing with sweep and span. The difference is that at zero sweep there is essentially no change or a slightly nose down pitch effect because the wing aerodynamic center is ahead of the reference point.

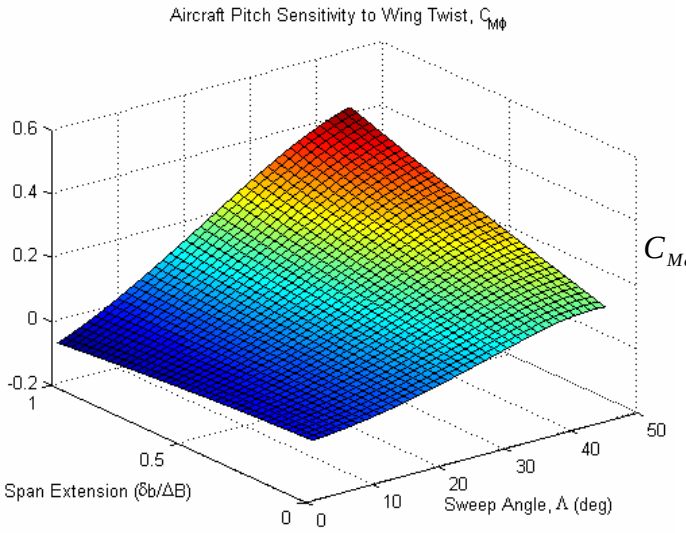

$$C_{M\varphi} = v_5^{\,T} \begin{bmatrix} -0.0141 & -0.0397 & -0.030 \\ 0.125 & 0.159 & 0.193 \\ 0.033 & 0.730 & -0.134 \\ 0.851 & -1.502 & 0.317 \\ -0.932 & 1.109 & -0.441 \end{bmatrix} u_3$$

Figure 5.8. Variation in Aircraft Pitch Sensitivity to Twist with Planform State

The optimal twist distribution in Figure 5.9 has strong nonlinearity in both span and sweep. For large span extensions the optimal washout begins at approximately -0.8α and decreases with sweep. This is due to the increase in twist effectiveness which was seen in Figure 5.7. Lower washout values are required to decrease the lift at the tips in trying to approximate an elliptic wing loading when the lift gradient to twist is higher. The planar VLM analysis does not capture the lateral flow behavior on the wing which would suggest greater washout with wing sweep. Because trim requirements are shared between a positive tail incidence and washout, lower washout angles with sweep will shift more of the stabilizing burden onto the tail. Therefore, we expect higher trim deflections with sweep angle.

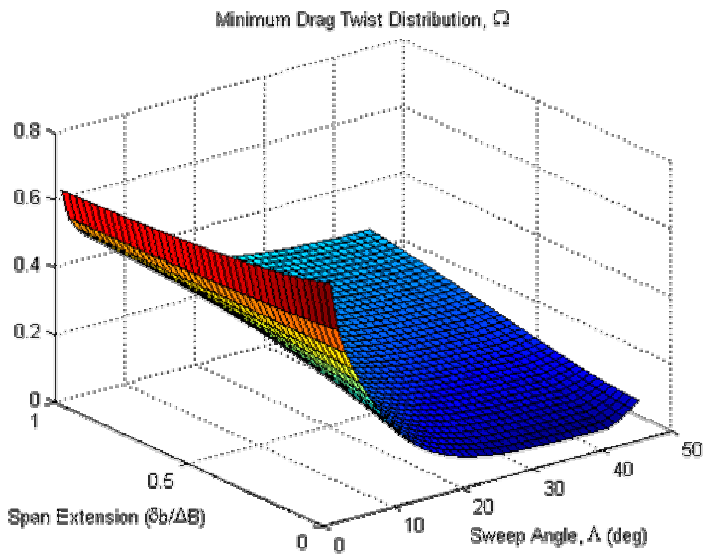

$$\Omega = v_5{}^T \begin{bmatrix} 0.748 & -0.141 & 0 \\ -4.73 & 3.55 & -0.733 \\ 12.89 & -10.15 & 1.973 \\ -16.2 & 12.7 & -2.28 \\ 7.84 & -6.27 & 1.20 \end{bmatrix} u_3$$

Figure 5.9. Variation in Optimal Twist Distribution with Planform State

The minimum drag trim results in Figures 5.10 and 5.11 indicate that reasonable displacements are required even in the face of stringent trim constraints. Obviously, higher angles of attack are necessary for less planform area and swept configurations which have smaller lift curve slope. The tail incidence to balance the pitching moment increases to almost 14-degrees at high sweep angles because the wing twist decreases as indicated by the minimum drag twist distribution. As mentioned in Chapter Four, positive washout and tail incidence work together to share longitudinal trim requirements. Because the twist effectiveness increases with sweep, the optimal twist distribution decreases with sweep, increasing the requirements on the tail to balance the pitching moment. Enforcing the minimum drag twist constraint requires too much tail incidence so a softer constraint could be used. Also, if longitudinal tail shift was implemented this could reduce the deflections by lowering the pitch stiffness amplitude at high sweep angles.

These expressions are simply approximations to begin control design and simulation. Further wind tunnel testing is necessary to tune the parameters to include influences like wall effects that change with the planform shape. This is especially important because the results are so dependent on the change in twist effectiveness with sweep which must be verified experimentally.

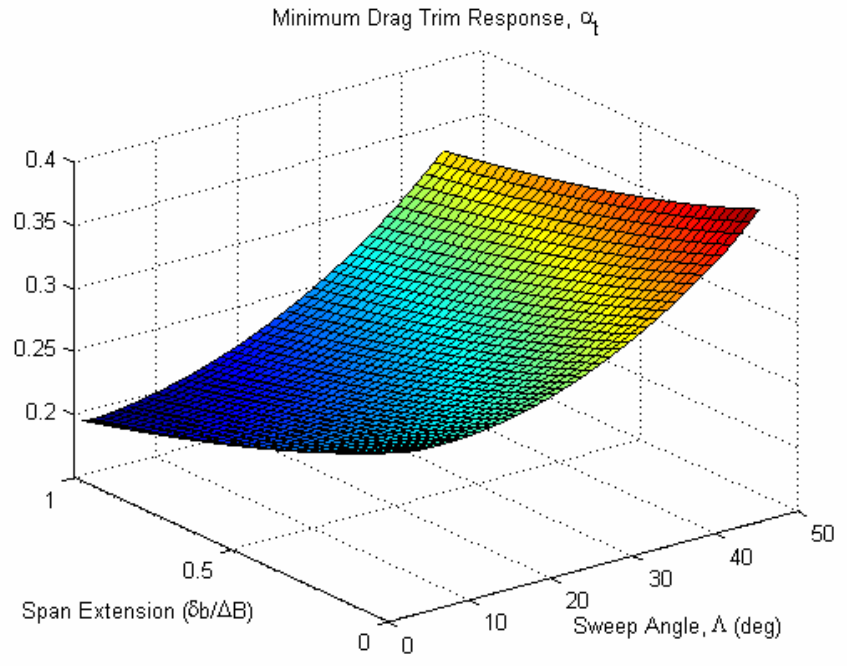

Figure 5.10. Minimum Drag Angle-of-Attack Trim Response

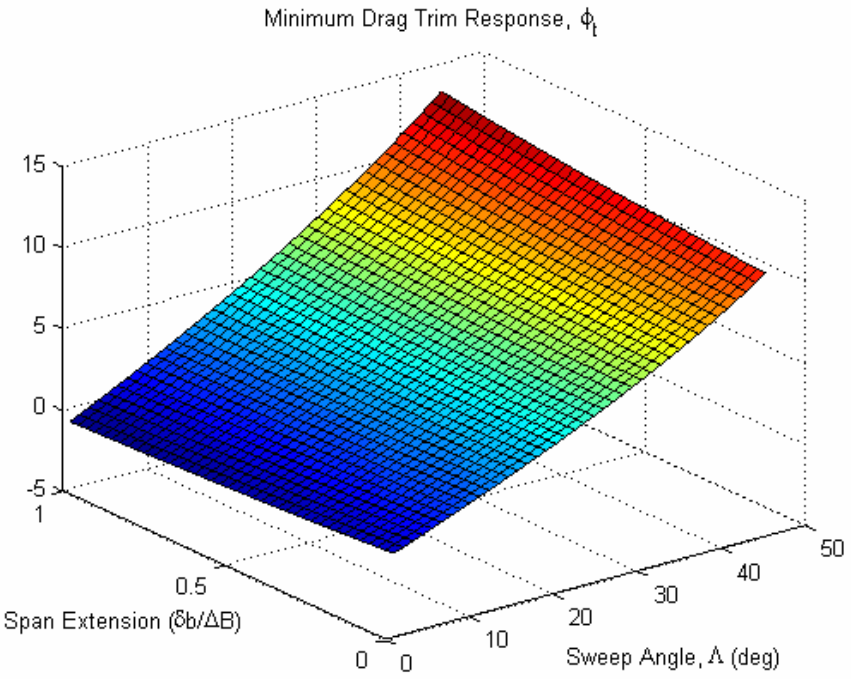

Figure 5.11. Minimum Drag Trimming Tail Incidence

5.5 Chapter Summary

Analysis showed that by fitting a Fourier sine-series to a VLM circulation distribution, an analytical function for the optimal twist schedule could be derived. The power of the sine-series method is in deriving washout functions for off-design conditions and the general quadratic expressions can be formulated into a cost function as a minimum drag constraint in real-time flight control. The minimum drag constraint was combined with the hybrid longitudinal aerodynamics model to obtain an efficient trim schedule for a morphing aircraft with that should match well with wind tunnel experiments.

With the augmented LQR cost function and the polynomial expressions for the planform-dependent aerodynamic coefficients we have set the framework for dynamic longitudinal control. This static analysis could be extended to include the actual dash transition of MORPHEUS which would require the effect of tail motion to be included. This would require true planform optimization which was not investigated in this work. The current analysis applies wing twist and tail incidence to achieve efficient trim at each planform state but does not compute which planform states should be used in a particular flight condition. While planform shapes can be scheduled a priori, some researchers have suggested an intelligent planform optimization as a need for future work [Seigler, 2005].

At first glance it is not obvious why analytical trim results are necessary when a simple tracking control law can be implemented to trim automatically. When deriving a time-varying model of the morphing system, it is convenient to linearize about constant velocity planform trajectories. Linearization about a trajectory requires a solution for the control inputs, states and the corresponding derivatives. The trim solutions will serve as an approximate equilibrium trajectory for deriving a Jacobian matrix while achieving well-behaved state derivatives. Finally, the VLM expansion can be extended and combined with other stability derivatives from DATCOM like pitch and roll damping to create improved models for general flight control derivations.

Chapter 6
Conclusions

This work has documented the design and development of two adaptive vehicle prototypes. An overview of the results for each design is presented including the advantages of the Phase Two development. Theoretical analysis results for optimizing the Phase Two configuration and developing general stability and control expressions are reviewed. Finally, recommendations for future research opportunities with the MORPHEUS design are presented.

6.1 Contributions

The Phase One design considered a morphing planform with freedom in span, sweep, and a slight modification in fuselage boom length. The vehicle used a combination of pneumatic and electromechanical actuators to achieve position control. Trajectory control was not possible because discrete solenoid valves were used as actuation drives for the pneumatic system. The Phase One model was wind tunnel tested at various configurations and the drag response illustrated the effectiveness of an adjustable planform shape for flight control missions. The aerodynamic coefficient variation with planform command followed the trends estimated from a first cut vortex lattice analysis. Design deficiencies motivated the Phase Two MORPHEUS development.

The advantages of MORPHEUS beyond the Phase One model include a higher load capacity through an increase in fundamental strength, a controllable planform *trajectory*, adaptive twist capability, and a variable geometry tail. Redesign of the primary structural components was used to increase the load capacity to more than four times the vehicle weight. Proportional solenoid valves enabled rate control as opposed to solely position control of the planform shape. A compliant wing fabrication including

a segmented internal structure facilitated wing twist under load. Structural analysis in ANSYS was used to confirm the load capacity of the new design. The distinctive capability of MORPHEUS is the ability to morph into a completely separate vehicle configuration in which the tail merges with the main wing structure to approximate a delta-wing planform. Both vehicles use an embedded PC/104 stack to implement control structures derived in the SIMULINK design environment.

Vortex lattice analysis using commercial software was used to compare the Phase One design, MORPHEUS, and an industry morphing concept, the N-MAS. Aerodynamic efficiency results indicated that the presence of the tail on MORPHEUS created a slight drag penalty in the loiter configuration as compared to the Phase One model. A slight modification in the initial sweep value of the loiter configuration can be used to achieve a reasonable lift-to-drag ratio in spite of span limitations due to the wind tunnel test section capacity. The wing-tail merge resulted in a MORPHEUS dash configuration with low parasite drag that helps offset the large reduction in lift. In spite of the slightly diminished aerodynamic efficiency, trim analysis of the VLM static margin results showed that favorable trim characteristics were achievable by exploiting variable washout control and longitudinal shifting of the variable geometry tail.

Detailed analysis using a custom VLM construction was used to develop a quantified method for determining the optimal washout command for MORPHEUS and how it varies with planform state. A Fourier sine-series fit of the general circulation results from vortex lattice analysis was used to derive a minimum drag washout constraint as a function of angle of attack. The constraint was expanded into a general quadratic cost function that could be used in dynamic flight control applications. An important contribution was demonstrating that low-order analysis methods like VLM could be used in developing cost functions for morphing aircraft.

Linear VLM analysis was combined with DATCOM expressions to formulate classic stability expressions for an adaptive planform vehicle. Specifically, DATCOM was used to augment VLM results to include fuselage effects. The stability and control expressions were iterated using the custom VLM construction to generate surface responses of the aerodynamic coefficients with a limited set of planform variations, namely sweep and span changes. The resulting functions were combined with the

minimum drag twist constraint and used for analysis of minimum drag trim control for MORPHEUS. The results indicated that including variable tail incidence allowed MORPHEUS to be trimmed while optimizing aerodynamic efficiency. Unintuitive results for the variation in twist effectiveness with sweep forced large tail incidence but including tail geometry in the optimization could be used to reduce the required trim displacement.

6.2 Future Work Recommendations

There are several avenues for future work in the MORPHEUS research project. The most immediate issue is conducting an extensive wind tunnel test of the Phase Two design. Even with the DATCOM approximations, vortex lattice is still a very limiting analysis tool and many of the results derived, particularly the twist response, require experimental verification.

The second avenue for future work is repeating the trim and stability analysis using vortex ring elements. Vortex ring elements satisfy flow boundary conditions on the vehicle surface as opposed to on the camberline and are a higher fidelity analysis tool. The vortex ring method still implements Biot-Savart's law to compute induced velocities at collocation points. The result is still a set of spanwise circulation values so the linear expansion can still be applied. Using vortex ring elements on the vehicle surface permits inclusion of wall effects to better simulate test conditions and expansion to unsteady analysis for identification of the transient aerodynamic response.

Transient aerodynamics is the yet unidentified result for morphing aircraft. Unsteady effects are important because the planform changes occur in such a constrained time-frame that the steady-state values can be temporarily exceeded, affecting vehicle stability and performance. There has been significant research into modeling unsteady aerodynamics, particularly for variable incidence flow. It is necessary to expand current results for variable planform motion so as to include first order transient effects into the system model. Analytical derivations can be verified with wind tunnel analysis of MORPHEUS. Combining the complete aerodynamic model and

the rigid-body dynamics permits analysis of system stability during configuration changes.

A final suggestion for future work is dynamic planform optimization of MORPHEUS. The planform optimization concept has been suggested by previous researchers as an optimization problem as opposed to viewing the aircraft as a dynamic system and trying to frame it as a nonlinear control problem. Modeling the vehicle, system to include control commands, the planform state and the resulting aerodynamic coefficients (steady-state and transient) allows well-developed tools of control theory to be applied in optimizing the configuration with definable stability results.

Bibliography

Abdulrahim, M., et al, "Flight Testing a Micro Air Vehicle Using Morphing for Aeroservoelastic Control", 45th AIAA/ASME/ASCE/AHS/ASC Structures, Structural Dynamics, and Materials Conference, 19-22 April 2004, Palm Springs, CA.

Amprikidis, M., et al, "On the Use of Adaptive Internal Structures for Wing Shape Control", 45th AIAA/ASME/ASCE/AHS/ASC Structures, Structural Dynamics, and Materials Conference, 19-22 April 2004, Palm Springs, CA.

Bae, J., Seigler, T., Inman, D., "Aerodynamic and Static Aeroelastic Characteristics of a Variable-Span Morphing Wing", Journal of Aircraft, Vol. 42, March-April 2005

Bartley-Cho, J.D., et al, "Development, Control, and Test Results of High-Rate, Hingeless Trailing Edge Control Surface for the Smart Wing Phase 2 Wind Tunnel Model," SPIE Symposium on Smart Structures and Materials, San Diego, CA, March 2002

Bertin, J., Smith M., *Aerodynamics for Engineers*, 3rd edition, Prentice Hall, Upper Saddle River, NJ 1998

Blondeau, J., et al. "Design, development and testing of a morphing aspect ratio wing using an inflatable telescopic span", 44th AIAA/ASME/ASCE/AHS/ASC Structures, Structural Dynamics, and Materials Conference, 7-10 April 2003, Norfolk, VA.

Blondeau, J., Pines, D.J., "Wind Tunnel Testing of a Morphing Aspect Ratio Wing Using an Pneumatic Telescopic Spar", 2nd AIAA "Unmanned Unlimited" Systems, Technologies, and Operations-Aerospace, Land, and Sea Conference and Workshop & Exhibit, San Diego, CA, September, 2003

Blondeau, J., Pines, D.J. "Pneumatic Morphing Aspect Ratio Wing", 45th AIAA/ASME/ASCE/AHS/ASC Structures, Structural Dynamics, and Materials Conference, 19-22 April 2004, Palm Springs, CA.

Bobrow, J.E., Jabbari, F., "Adaptive Pneumatic Force Actuation and Position Control", Journal of Dynamic Systems, Measurement, and Control, Vol. 113, June 1991.

Boothe, K., Fitzpatrick, K., Lind, R., "Controllers for Disturbance Rejection for a Linear Input-Varying Class of Morphing Aircraft", 46th AIAA/ASME/ASCE/AHS/ASC Structures, Structural Dynamics, and Materials Conference, 18-21 April 2005, Austin, TX

Cadogan, D., "Morphing Inflatable Wing Development for Compact Package Unmanned Aerial Vehicles", 45th AIAA/ASME/ASCE/AHS/ASC Structures, Structural Dynamics, and Materials Conference, 19-22 April 2004, Palm Springs, CA.

Cruz, J.R., et al, "Properities of Two Carbon Composite Materials using LTM25 Epoxy Resin", NASA TM-110286, November 1996

Curry, Marty, "NASA AFTI/F-111 MAW Fact Sheet" NASA Dryden Flight Research Center, http://www.dfrc.nasa.gov/Gallery/Photo/F-111 AFTI/HTML/EC88-0052-4.html, Dec. 2004

Curry, Marty, "NASA AAW Fact Sheet, FS-061-DFRC" NASA Dryden Flight Research Center, http://www.dfrc.nasa.gov/centers/dryden/news/FactSheets/FS-061-DFRC.html, Feb. 2005

Davidson, J. et al, "Flight Dynamic Simulation Assessment of a Morphable Hyper-Elliptic Cambered Span Winged Configuration", AIAA Atmospheric Flight Mechanics Conference and Exhibit, 11-14 August 2003, Austin, TX

Etkin, B., Reid, L.D., *Dynamics of Flight: Stability and Control*, John Wiley & Sons Inc., 3rd edition, 1996

Filotas, L.T. "Solution of Lifting-Line Equation for Twisted Elliptic Wings", Journal of Aircraft Vol. 8, No. 10, October 1971

Frommer, J.B., Crossley, W.A., "Enabling Continuous Optimization for Sizing Morphing Aircraft Concepts", 43rd AIAA Aerospace Sciences Meeting and Exhibit, 10-13 January 2005, Reno, NV

Gern, F., et al, "Structural and Aeroelastic Modeling of General Planform Wings with Morphing Airfoils", AIAA Journal, Vol. 40 No. 4, April 2002

Gern, F., et al, "Computation of Actuation Power Requirements for Smart Wings with Morphing Airfoils", 43rd AIAA/ASME/ASCE/AHS/ASC Structures, Structural Dynamics, and Materials Conference, 22-25 April 2002, Denver, CO

Guiler, R., Huebsch, W., "Wind Tunnel Analysis of a Morphing Swept Wing Tailless Aircraft", 23rd AIAA Applied Aerodynamics Conference, 6-9 June 2005, Toronto, Ontario, Canada

Hallenberg, Jonathan, "The Wright Brothers, the Invention of the Aerial Age", National Air and Space Museum Smithsonian, http://nasm.si.edu, 2004.

Hoak, D.E., et al, *USAF Stability and Control DATCOM*, Flight Control Division, Air Force Flight Dynamics Laboratory, WPAFB, Ohio 1978

Johnston, C.O., et al, "A Model to Compare the Flight Control Energy Requirements of Morphing and Conventionally Actuated Wings", 44th AIAA/ASME/ASCE/AHS/ASC Structures, Structural Dynamics, and Materials Conference, 7-10 April 2003, Norfolk, VA.

Johnston, C.O., et al, "Actuator-Work Concepts Applied to Unconventional Aerodynamic Control Devices", 10th AIAA/ISSMO Multidisciplinary Analysis and Optimization Conference, 30 August-1 September 2004, Albany, NY

Katz J., Plotkin, A., *Low-Speed Aerodynamics*, 2nd edition, Cambridge University Press, 2001. Cambridge CB2 2RU, UK

Kudva, J.N., et al, "Overview of the DARPA/AFRL/NASA Smart Wing Program," SPIE Symposium on Smart Structures and Materials, San Diego, CA, March 2002

Lai, J., et al, "Accurate Position Control of a Pneumatic Actuator", Journal of Dynamic Systems, Measurement, and Control, Vol. 112, December 1990

Lan, C.E., "A Quasi-Vortex-Lattice Method in Thin Wing Theory," Journal of Aircraft, Vol. 11, No. 9, September, 1974

Linnett, J.A., Smith, M.C., "An Accurate Low-Friction Pneumatic Position Control System", Proceedings of the Institute of Mechanical Engineers, Vol. 203, May 1989

Love, M.H., et al., "Impact of Actuation Concepts on Morphing Aircraft Structures", 45th AIAA/ASME/ASCE/AHS/ASC Structures, Structural Dynamics, and Materials Conference, 19-22 April 2004, Palm Springs, CA.

Marmier, P., Werely, N., "Morphing Wings of a Small Scale UAV Using Inflatable Actuators for Sweep Control", 44th AIAA/ASME/ASCE/AHS/ASC Structures, Structural Dynamics, and Materials Conference, 7-10 April 2003, Norfolk, VA.

Martin, Christopher, et al, "Design, Fabrication, and Testing of a Scaled Wind Tunnel Model for the Smart Wing Project", Journal of Intelligent Material Systems and Structures, Vol. 15-April 2004

Mason, W.H., *Applied Computational Aerodynamics Online Text, Ch. 6: Aerodynamics of 3D Lifting Surfaces through Vortex Lattice Methods*, 1995
http://www.aoe.vt.edu/~mason/Mason_f/CAtxtTop.html

Melin.T, "Tornado, a vortex lattice MATLAB implementation for Linear Aerodynamic Wing applications", Masters Thesis, Royal Institute of Technology (KTH), Sweden, December 2000.

Neal, D.A., Akle, B.A., Hesse, T., "Optimal Flight Control of an Adaptive Aircraft Wing Modeled by NeuroFuzzy Techniques," Proceedings. of. the. 2003 IEEE. International Symposium. on. Intelligent Control. Houston, Texas October. 5-8, 2003

Neal, D.A., Johnston, C.O., "Dynamic Stabilization of a Folding Aircraft Wing", Design Report, 2004

Pettit, G., et al, "A Model to Evaluate the Aerodynamic Energy Requirements of Active Materials in Morphing Wings", Proceedings of DETC'01 2001 ASME Design Engineering Technical Conferences, September 2001

Phillips, W.F., "Lifting-Line Analysis for Twisted Wings and Washout-Optimized Wings", Journal of Aircraft, Vol. 41, No. 1, January-February 2004

Pu, J., et al, "Digital Motion Control and Profile Planning for Pneumatic Servos", Journal of Dynamic Systems, Measurement, and Control Vol. 114, December 1992

Pu. J., et al "Digital Servo Motion Control of Air Motors,", International Journal of Production Research., Vol. 29 No. 3, 1991

Ramrkahyani, D., et al, "Aircraft Structural Morphing Using Tendon Actuated Compliant Cellular Trusses", 45th AIAA/ASME/ASCE/AHS/ASC Structures, Structural Dynamics, and Materials Conference, 19-22 April 2004, Palm Springs, CA.

Raymer, D., *Aircraft Design: A Conceptual Approach*, AIAA Education Series, American Institute of Aeronautics and Astronautics, Reston, VA 3rd edition, 1999

Raymer, D., "Vehicle Scaling Laws for Multidisciplinary Optimization," 39th Aerospace Sciences Meeting, Reno, NV, Jan. 2001

Richer, E., Hurmuzlu, Y., "A High Performance Pneumatic Force Actuator System: Part I—Nonlinear Mathematical Model", Journal of Dynamic Systems, Measurement, and Control, Vol. 122, Sept. 2000

Roskam, J., *Airplane Design: Part VI Preliminary Calculation of Aerodynamic, Thrust, and Power Characteristics*, Design Analysis and Research corporation, Lawrence, KS 2004

Roth, B., et al, "Aircraft Sizing with Morphing as an Independent Variable: Motivation, Strategies, and Investigations", AIAA's Aircraft Technology, Integration, and Operations 2002 Technical, 1-3 October 2002, Los Angeles, CA

Seigler, T., Bae, J., Inman, D., "Flight Control of a Variable Span Cruise Missle", Proceedings of IMECE'04 Anahein, CA Nov. 13-20, 2004

Seigler, T.M., “Dynamics and Control of Morphing Aircraft”, PhD Dissertation, Virginia Polytechnic Institute and State University, Blacksburg, VA August, 2005

Seigler, T.M., et al, “Modeling and Flight Control of Large-Scale Morphing Aircraft”, submitted to Journal of Aircraft, 2005

Shearer, J.E., “Study of Pneumatic Process in the Continuous Control of Motion with Compressed Air-I, II”, Transactions of the ASME, Feb. 1956

Thornborough, Tony, *F-111 AARDVARK - USAF's ultimate strike aircraft*, OSPREY Aerospace Ltd 1993

Valasek, J., Tandale, M., Rong, J., “A Reinforcement Learning – Adaptive Control Architecture for Morphing”, AIAA 1st Intelligent Systems Technical Conference, 20-22 September 2004, Chicago, IL

Varseveld, R.B., Bone, G.M., “Accurate Position Control of a Pneumatic Actuator using On/Off Solenoid Valves”, IEEE/ASME Transactions on Mechatronics, Vol. 2, No. 3, Sept. 1997

Wang, J., et al, “A Practical Control Strategy for Servo-pneumatic Actuator Systems”, Control Engineering Practice, No. 7 1999

Wang, J., et. al, “Modelling Study, Analysis and Robust Servocontrol of Pneumatic Cylinder Actuator Systems”, IEEE Proceedings of Control Theory Applications, Vol. 148 No. 1, January 2001

Wiggins, et al, “A Design and Analysis of Morphing Hyper-Elliptic Cambered Span (HECS) Wing”, 45th AIAA/ASME/ASCE/AHS/ASC Structures, Structural Dynamics, and Materials Conference, 19-22 April 2004, Palm Springs, CA.

Wlezien, R.W., et al, “The Aircraft Morphing Program”, 39th AIAA/ASME/ASCE/ASC Structures, Structural Dynamics, and Materials Conference, April 1998, Long Beach, CA

Appendix A

Castigliano's Solution for Point-Load Transfer to Internal Wing Structure

The aircraft wing is subjected to an elliptic lift distribution on the wing surface. However, to evaluate the structural response of the internal structure, it is necessary to compute the equivalent loads at the three transfer points illustrated in Figure A.1. The equivalent force diagram is presented in Figure A.2.

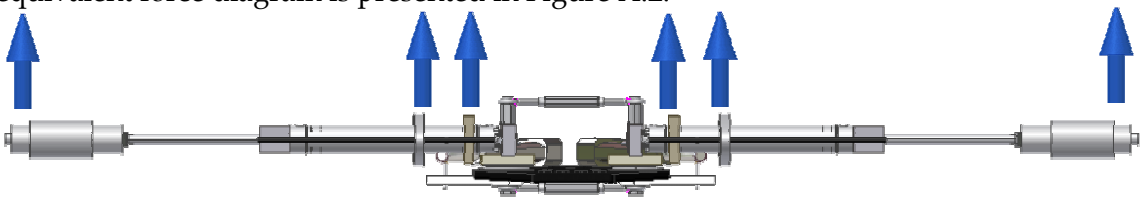

Figure A.1. Load transfer points to internal structure. The effective point loading is determined from applying Castigliano's theorem to an elliptic load distribution.

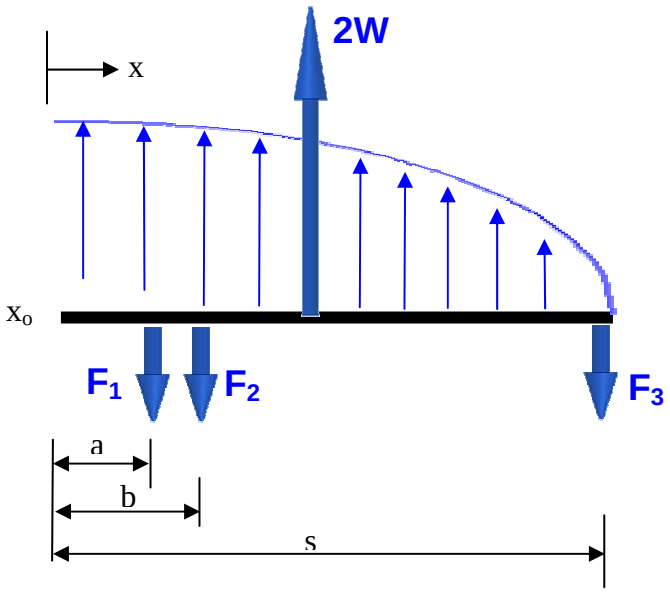

Figure A.2. Force diagram for load transfer to internal structure. X_o is the distance from the fuselage centerline to the wing pivot point where all other distances are referenced to.

Because there are more than two transfer points, Castigliano's theorem is used to provide an additional boundary condition to the standard equilibrium summations. We assume that the three transfer points are rigid so that no deformation occurs there. The initial task is to model the load density of the elliptic distribution and the corresponding bending moment from the origin.

The elliptic load shape is

$$w(\gamma) = \alpha\sqrt{1-\left(\frac{\gamma}{s}\right)^2} \tag{A.1}$$

where γ is a length parameter, s is the half-span of the wing (the entire coordinate axis in Figure A.2), and α is a normalizing coefficient to be determined. The positive bending moment due to the elliptic distribution at some point x from the origin can be computed from simple calculus via

$$M_o(x) = \int_0^x \gamma\, w(\gamma)\, d\gamma = \alpha\int_0^x \gamma\sqrt{1-\left(\frac{\gamma}{s}\right)^2}\, d\gamma = \frac{-\alpha s^3}{3}\left[\left(1-\left(\frac{x}{s}\right)^2\right)^{3/2} - 1\right] \tag{A.2}$$

Because the design load condition is four times the vehicle weight the elliptic lift distribution over the half span is half twice the vehicle weight. Hence, integrating the load density over the half-span yields a solution for the normalizing coefficient, α.

$$\begin{gathered}\int_0^s w(x)dx = 2W \\ \int_0^s \alpha\sqrt{1-\left(\frac{x}{s}\right)^2}\, dx = \frac{\alpha\pi s}{4} = 2W \\ \alpha = \frac{8W}{\pi s}\end{gathered} \tag{A.3}$$

Summing the forces and moments in Figure A.2 yields the two of the three required relationships

$$\sum F_y = F_1 + F_2 + F_3 = 2W \tag{A.4a}$$

$$\sum M = F_1\left(d-\left(x_o+a\right)\right) + F_2\left(d-\left(x_o+b\right)\right) = F_3\left(\left(x_o+c\right)-d\right) \tag{A.4b}$$

which can be simply presented as

$$\begin{bmatrix} 1 & 1 \\ \left(d-\left(x_o+a\right)\right) & \left(d-\left(x_o+b\right)\right) \end{bmatrix}\begin{Bmatrix} F_1 \\ F_2 \end{Bmatrix} = \begin{bmatrix} 2W-F_3 \\ \left(\left(x_o+c\right)-d\right)F_3 \end{bmatrix} \tag{A.5a}$$

$$\begin{bmatrix} 1 & 1 \\ \mathrm{X} & \mathrm{Y} \end{bmatrix} \begin{Bmatrix} F_1 \\ F_2 \end{Bmatrix} = \begin{bmatrix} 2W - F_3 \\ F_3 Z \end{bmatrix} \Rightarrow \begin{Bmatrix} F_1 \\ F_2 \end{Bmatrix} = \frac{1}{\mathrm{Y} - \mathrm{X}} \begin{bmatrix} 2W\mathrm{Y} - F_3\mathrm{Y} - F_3 Z \\ F_3\mathrm{X} - 2W\mathrm{X} + F_3 Z \end{bmatrix} \quad \text{(A.5b)}$$

As an additional equation we use Castiglianos theorem which basically relates the force gradient of internal energy at a point to the deformation due to the force at that point. Assuming the wing shell is a beam that undergoes pure bending and computing the internal energy as a function of the squared bending moment distribution, the integral equation is

$$\int_0^a M(x) \frac{\partial M(x)}{\partial F} dx = \delta y(a) \quad \text{(A.6)}$$

Zero deformation at the tip shell is the boundary point so that the bending moment expression for the wing must be expanded between the force singularities

$$M_1(x) = M_o(x) \quad \text{(A.7a)}$$

$$M_2(x) = M_o(x) - F_1\left(x - \left(x_o + a\right)\right) \quad \text{(A.7b)}$$

$$M_3(x) = M_o(x) - F_1\left(x - \left(x_o + a\right)\right) - F_2\left(x - \left(x_o + b\right)\right) \quad \text{(A.7c)}$$

and the final boundary equation becomes

$$\int_0^{x_o+a} M_1(x) \frac{\partial M_1(x)}{\partial F_3} dx + \int_{x_o+a}^{x_o+b} M_2(x) \frac{\partial M_2(x)}{\partial F_3} dx + \int_{x_o+b}^{x_o+c} M_3(x) \frac{\partial M_3(x)}{\partial F_3} dx = 0 \quad \text{(A.8)}$$

where the first term goes to zero because of no dependence on F_3. The force enters (A.7b) and (A.7c) through the force and moment summation in (A.5b).

Equation A.8 was integrated in Mathematic to yield the following results:

```
w = α * Sqrt[1 - (γ/s)^2];
d = Integrate[γ * w, {γ, 0, s}] / Chop[Integrate[w, {γ, 0, s}]];

X = (d - (xo + a));
Y = (d - (xo + b));
Z = (s - d);

F1 = 1/(Y - X) * (Y * Fr - Y * F3 - Z * F3);
F2 = 1/(Y - X) * (X * F3 - X * Fr + Z * F3);

Mo = Simplify[Integrate[γ * w, {γ, 0, x}, Assumptions → {x > 0, x ≤ s, s > 0, x ∈ Reals, s ∈ Reals}]];
M2 = Mo - F1 * (x - (xo + a));
M3 = Mo - F1 * (x - (xo + a)) - F2 * (x - (xo + b));

xo = 3.6;
a = 2.174; b = 5.013;
s = 32.22;
d;
α = 4 * Fr / (π * s)

Fr = 2 W;
Simplify[F1]
Simplify[F2]

F = Simplify[Solve[Integrate[M2 * D[M2, F3], {x, xo + a, xo + b}]
      + Integrate[M3 * D[M3, F3], {x, xo + b, s}] == 0, F3]]
F1 = Simplify[1/(Y - X) * (Y * Fr - Y * F3 - Z * F3) /. F]
F2 = Simplify[1/(Y - X) * (X * F3 - X * Fr + Z * F3) /. F]
```

```
F1=-0.73W
F2=2.39W
F3=0.34W
```

Appendix B
Variable Geometry Tail Time-Varying Transformations

Besides having multiple control inputs, the tail merges into the main wing which creates coordination problems in describing a continuous vehicle motion.

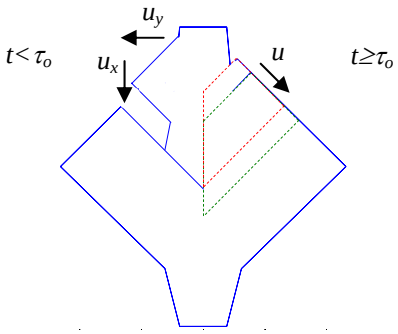

Figure B.1. Partitioned view of dash configuration before and after the tail has merged with the main wing. Before τ_o the tail has two independent degrees of freedom. After the alignment time the motions are coordinated.

The tail alignment time, τ_o, denotes when the lateral and longitudinal tail extensions align so that they can be controlled by a single control input. By necessity this time is less than the total vehicle transition time. Prior to τ_o the motions can still be coordinated in terms of the single control input. The dynamic equations for the lateral and longitudinal tail extensions, $u_{yta}(t)$ and $u_{xta}(t)$, can be coordinated into a single degree of freedom driven by $u_{ta}(t)$

$$\begin{aligned} u_{nta}(t) &= \left(c_{n1} + c_{n2}\left(\frac{\tau_f}{\tau_o} - \frac{\tau_f}{t}\right)\Phi(t-\tau_o) + c_{n2}\left(\frac{\tau_f}{t} - 1\right)\Phi(t-\tau_f)\right) u_{ta}(t) \\ &= N(t)u_{ta}(t) \end{aligned} \tag{B.1}$$

where the constants c_{ni} are defined as

$$c_{n1} = \frac{u_{nta_1}{}^{*}\tau_f}{u_{ta}{}^{*}\tau_o} \qquad c_{n2} = \frac{u_{nta_2}{}^{*}\tau_o - u_{nta_1}{}^{*}\tau_f}{u_{ta}{}^{*}(\tau_f - \tau_o)} \tag{B.2}$$

and the driving input $u_{ta}(t)$ is

$$u_{ta}(t) = u_{ta}^{*}\left(t/\tau_f + \left(1 - t/\tau_f\right)\Phi\left(t - \tau_f\right)\right) \tag{B.3}$$

The motions are related in terms of the desired *n* coordinate at the transition time, $u_{nta_1}^{*}$ at τ_o, and the ultimate coordinate value at the final transition time $u_{nta_2}^{*}$ at τ_f. The last constant is the (arbitrary) final value of the generalized tail input, u_{ta}^{*}. Equation B.1 represents a time-varying transformation between the driving input and the corresponding lateral and longitudinal extensions. The concept is presented graphically in Figure 3.x2. The general tail input ramps up at some constant rate and the transformations are piecewise continuous at the transition time so that the correct longitudinal and lateral tail outputs can be mapped from the single input. For MORPHEUS the transformation constants are $u_{xta_1}^{*}$=3.75, u_{xta2}^{*}=6, $u_{yta_1}^{*}$=1.75, and u_{yta2}^{*}=4 (inches).

To extract a static relationship over the range of the general tail control, input-output ratios are determined piecewise in the alignment time. From (B.3) $t = \tau_f u_{ta}(t)/u_{ta}^{*}$ Therefore the transition point can be converted to a spatial coordinate, $t < \tau_o \Rightarrow u_{ta} < \tau_o u_{ta}^{*}/\tau_f$. The static relationships between the generalized tail input and the longitudinal and lateral extensions become

$$u_{ta} < \tau_o u_{ta}^{*}/\tau_f \qquad\qquad u_{nta} = c_{n1}u_{ta} \tag{B.4}$$

and

$$\tau_o u_{ta}^{*}/\tau_f \le u_{ta} \le u_{ta}^{*} \qquad\qquad u_{nta} = \left(c_{n1} + c_{n2}\left(\frac{\tau_f}{\tau_o} - \frac{u_{ta}^{*}}{u_{ta}} \right)\right)u_{ta} \tag{B.5}$$

For a maximum general input command of five, the simple static mapping for the variable geometry tail is

$$U_T < 1.25 \qquad u_{xta} = 3U_T \qquad u_{yta} = 1.4U_T \tag{B.6}$$

$$1.25 \le U_T \le 5 \qquad u_{xta} = 0.6U_T + 3 \qquad u_{yta} = 0.6U_T + 1 \tag{B.7}$$

The time-varying transformations in equation 3.9 will be used as reference inputs for the longitudinal and lateral tail command signals.

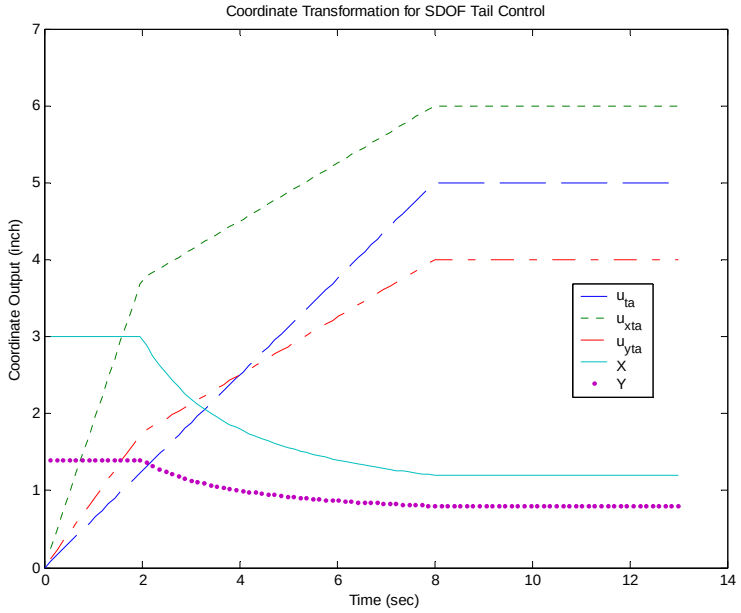

Figure B.2 Coordinate transformations to unify horizontal tail control

Appendix C

Nonlinear Equations of Motion for Pneumatic Cylinder System

The dynamics of pneumatic systems are highly nonlinear due to the compressibility of the fluid. The standard actuator model first presented by Shearer is composed of three parts: the flow valve, cylinder chamber, and load dynamics (Shearer, 1956). The system in Figure C-1 details the simplified model assumptions in deriving the equations of motion.

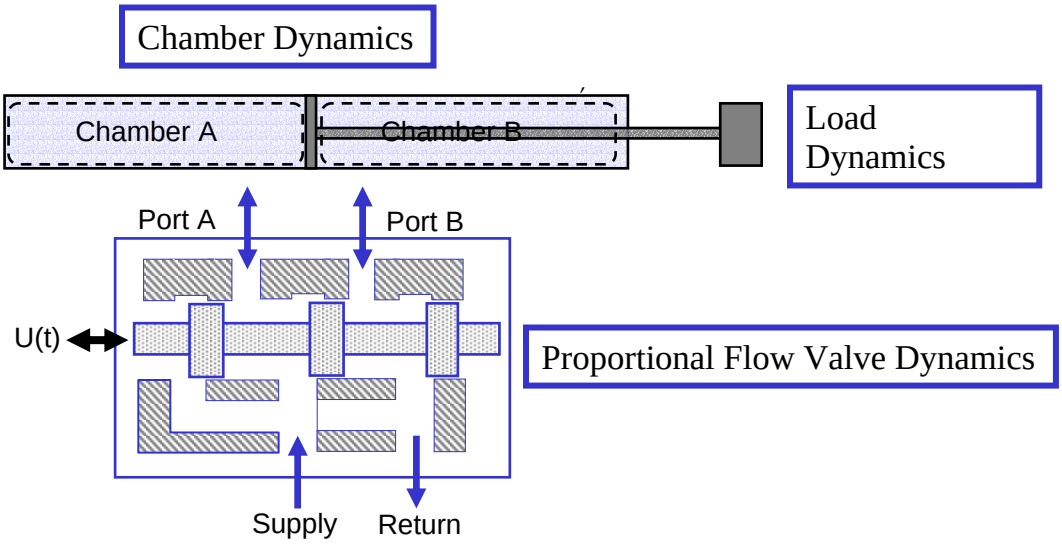

Figure C-1. Pneumatic Actuation Schematic denoting the three primary subsystems: nonlinear flow valve dynamics, chamber dynamics, and load dynamics

The flow valves are modeled as an orifice with upstream stagnation conditions and downstream variable pressure. From compressible flow dynamics we know that as the downstream pressure decreases the output flow velocity and mass flowrate increases until a critical value is reached and the flow chokes. This result can be generalized to the pressure ratio across the orifice. Starting from the energy equation

and assuming isentropic flow the result is a flow condition that switches based on the pressure ratio

$$\dot{m} = C_d C_f(\beta) A_e \, P_u \Big/ \sqrt{T} \, \mathrm{sgn}(u), \quad C_f = \begin{cases} C_1 & \frac{P_{atm}}{P_u} < \beta \le C_r \\ C_2 \left(\beta^{\frac{2}{\gamma}} - \beta^{\frac{\gamma+1}{\gamma}} \right)^{1/2} & C_r < \beta < 1 \end{cases} \tag{C.1}$$

where β is the pressure ratio and the flow constants, C_i, are nonlinear functions of the specific heat ratio and the gas constant. The orifice area, A_e, is approximately proportional to the control input, u. On the drive side of the cylinder, equation C.1 is applied with the supply as the upstream pressure and the active cylinder chamber as the downstream pressure. On the passive side the chamber is the upstream pressure and the atmosphere is the downstream pressure.

The chamber dynamics are derived by applying the First Law of Thermodynamics to a control volume around the chamber and assuming adiabatic flow. The two sides of the cylinder vary in which control volume is doing positive work from moving the piston or negative work from volume contraction. For each chamber the flow energy has opposing signs due to mass flowrate into a drive chamber or out of the passive chamber

$$\begin{gathered} \dot{m}h - P\dot{V} = \dot{U} = C_v \, d \Big/ dt \left(\rho V T \right) \\ \dot{m} = \frac{1}{RT} \left(P\dot{V} + \frac{1}{\gamma} \dot{P} V \right) \rightarrow \dot{P} = \frac{\dot{m} \gamma R T}{V} - \frac{\gamma P \dot{V}}{V} \end{gathered} \tag{C.2}$$

Equation (C.2) is a state equation in pressure with a mass flowrate input from the solenoid valve equations. The load dynamics are computed from a simple force balance on the piston which requires pressure inputs from the chamber dynamics (C.2)

$$\ddot{x} = \frac{1}{m} \left(A_a P_a - A_b P_b - (A_a - A_b) P_{atm} - F_f - b\dot{x} \right) \tag{C.3}$$

The friction term, F_f, is generally modeled as Columb friction and is a major obstacle in accurate trajectory control. The pressure in the cylinder chamber has to reach an adequate level to overcome the static friction and begin motion. This leads to significant delay which is a general characteristic of pneumatic actuation.

Appendix D

Custom Vortex Lattice Code

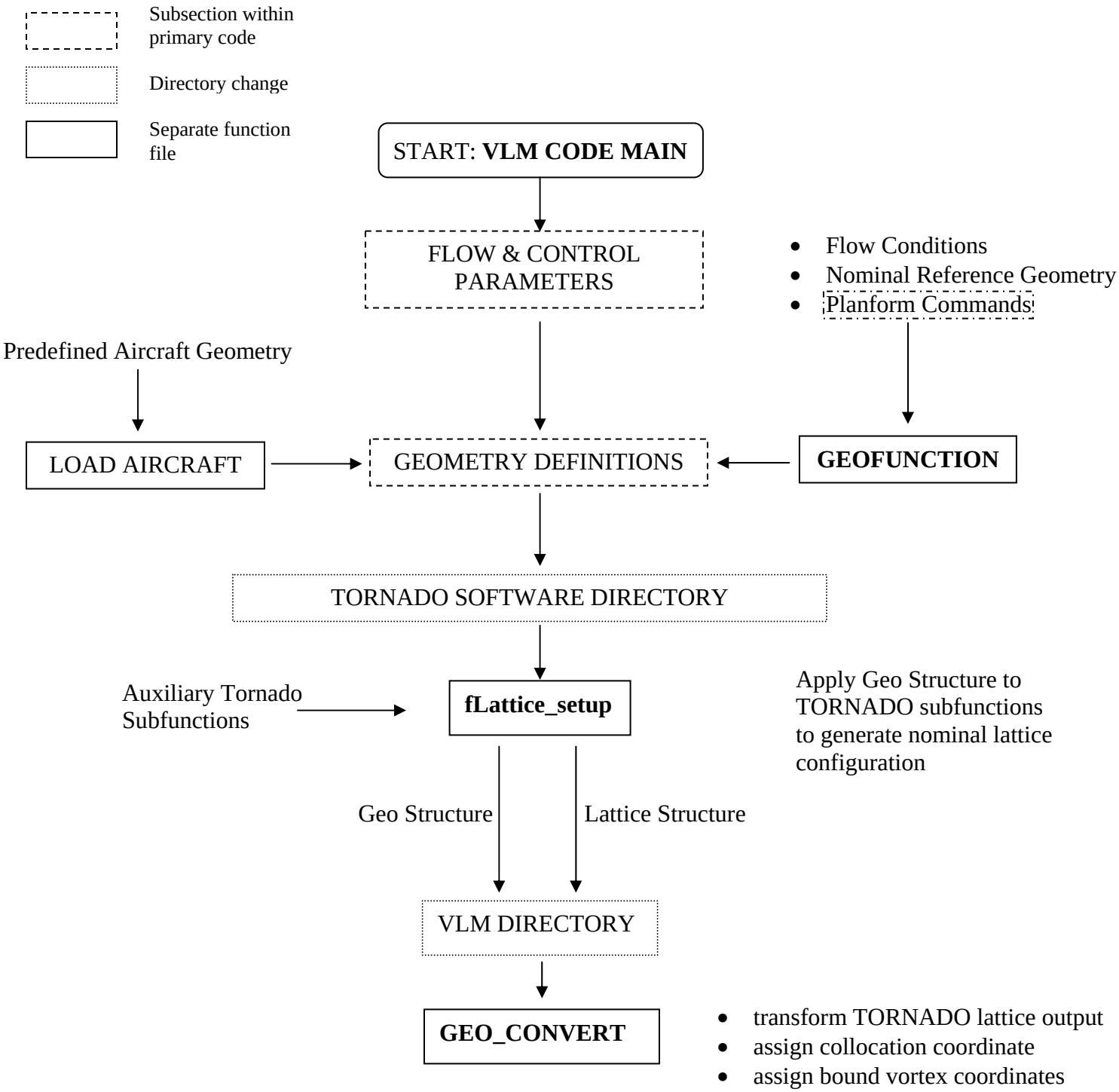

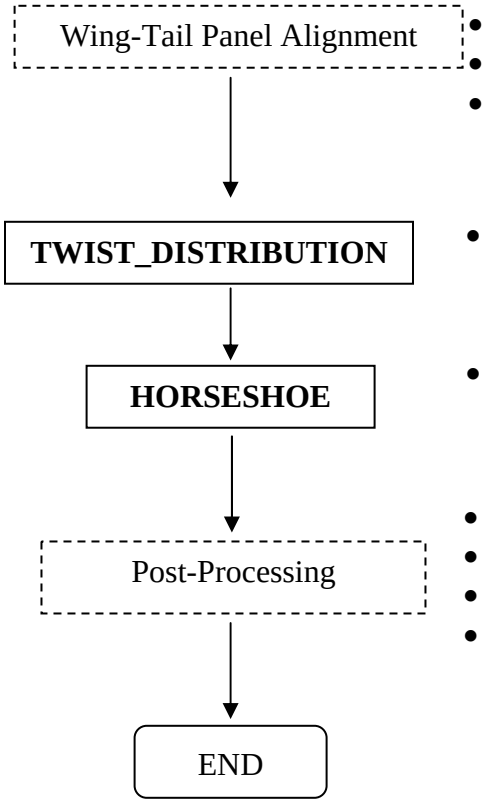

- Reassign wing lattice to align with tail
- Reassign collocation coordinate
- Reassign bound vortex coordinates

- Apply coordinate transformation for slope at swept collocation points

- Planar application of Biot-Savart's law to compute influence coefficents

- Compute nondimensional circulations
- Integrate hybrid DATCOM solutions
- Sine-series circulation data fits
- Application of minimum drag solution

VLM CODE (MAIN)

```
function [output]=vlm_code(span,sweep)%input,aircraft,area,span,AR)
%span=8;sweep=0;
%*********************************************************************
****
%FLOW AND CONTROL PARAMETERS
%twist is in radians and is positive down (conventional)
%tail incidence is in radians and is positive down (conventional)
%alpha is in radians and is positive up (conventional)
%*********************************************************************
****
U_fs=220*12; %in/sec
rho=2.38e-3*12^(-3); %slug/ft^3
alpha=9*pi/180;%value(1);%8.603*pi/180; %radian
Sn=698.567; %in^2 nominal value
cn=15.072; %in nominal value
Bo=24.2277;
St=285.421; %in^2, tail area

tw=0;%input(2);%1*pi/180;%value(2);%0*pi/180; %twist command
dB=span; %0-8 inches (span command)
B=2*(dB+Bo); %inches (unswept span length)
SWEEP=sweep; %0-45 deg
tail=0; %0-5 inches (coordinated motion)
trig=1; %1=tail, 0=no tail
ro=4.561; %reference at wing mount relative to leading edge of nominal
MAC

%*********************************************************************
****
%GEOMETRY DEFINITIONS
%*********************************************************************
****
[geo]=geo_function(dB,SWEEP,tail,trig);
%cd c:\Matlab6p5\work\Tornado\aircraft
%load(aircraft)
%save('p2_loiter_new','geo')

cd c:\Matlab6p5\work\Tornado\data
load expansion
cd ..
[lattice,ref]=fLattice_setup(geo,state);
cd c:\Matlab6p5\work\aerocodes

nwings=length(geo.nelem);
parts=2*geo.nelem;
reshpan=geo.ny.*geo.nx;
reshpane=reshape(reshpan',1,[]);
nblocks=reshape([reshpane;reshpane],1,[]);
sp_panels=sum(geo.ny,2);
ch_panels=geo.nx(:,1);
panels=2*sp_panels.*ch_panels;%*[1;0];
bounds=(ch_panels+1).*(2*sp_panels+1);
```

```
area=geo.area; %overwrite nominal value
sb=sum(geo.b,2);
span=2*sb(1); %true swept span value
AR=span^2/area; %true reference aspect ratio
span_panels=geo.ny(1);

%CUSTOM CONVERSION CODE FOR TORNADO GEOMETRY SUBFUNCTIONS, + VORTEX
ARRANGEMENT
[WING_X,WING_Y,COLLOC_X,COLLOC_Y,NY_C,NY_D,NX_C,NX_D]=geo_convert(latti
ce,ref,geo);

%DYNAMIC PANEL ALIGNMENT
wingx=reshape(WING_X(1:bounds(1)),geo.nx(1,1)+1,[]);
wingy=reshape(WING_Y(1:bounds(1)),geo.nx(1,1)+1,[]);
tailx=reshape(WING_X(bounds(1)+1:end),geo.nx(2,1)+1,[]);
taily=reshape(WING_Y(bounds(1)+1:end),geo.nx(2,1)+1,[]);
wcolloc_x=reshape(COLLOC_X(1:panels(1)),geo.nx(1,1),[]);
wcolloc_y=reshape(COLLOC_Y(1:panels(1)),geo.nx(1,1),[]);
tcolloc_x=reshape(COLLOC_X(panels(1)+1:end),geo.nx(2,1),[]);
tcolloc_y=reshape(COLLOC_Y(panels(1)+1:end),geo.nx(2,1),[]);
wy_c=reshape(NY_C(1:panels(1)),geo.nx(1,1),[]);
wx_c=reshape(NX_C(1:panels(1)),geo.nx(1,1),[]);
wy_d=reshape(NY_D(1:panels(1)),geo.nx(1,1),[]);
wx_d=reshape(NX_D(1:panels(1)),geo.nx(1,1),[]);

%boundaries to align with tail vortex boundaries
a=max(find(wingy(1,:)<taily(1,1)));
b=max(find(wingy(1,:)<taily(1,end)));

aa=find(abs(abs(wingx(end,:))-max(wingx(end,:)))<0.01);
out=wingy(1,aa(end));
in=taily(1,end);

%setup linear wing distribution outside of tail vortex boundaries
%vary panels on swept segment with sweep angle
if SWEEP==0
    pan=12;
    wingy_align=[in:(out-in)/pan:out];
    nwingy=ones(geo.nx(1,1)+1,1)*[-fliplr(wingy_align),taily(1,2:end-
1),wingy_align];
else
    %pan=8-ceil(SWEEP/10);
    pan=8;%-ceil(SWEEP/10);
    wingy_align=[in:(out-in)/pan:out];
    tipout=wingy(1,end);
    tipin=wingy_align(end);
    %wingy_tip=[tipin:(tipout-tipin)/ceil(SWEEP/10):tipout];
    wingy_tip=[tipin:(tipout-tipin)/4:tipout];
    nwingy=ones(geo.nx(1,1)+1,1)*[-fliplr(wingy_tip(2:end)),-
fliplr(wingy_align),taily(1,2:end-1),wingy_align,wingy_tip(2:end)];
end
nwcolloc_y=nwingy(1:4,1:end-1)+0.5*diff(nwingy(1:4,:),1,2);
nwy_c=nwingy(1:end-1,1:end-1);
nwy_d=nwingy(1:end-1,2:end);

for ii=1:geo.nx(1,1)+1
```

```
    nwingx(ii,:)=interp1(wingy(1,:),wingx(ii,:),nwingy(1,:));
end
for ii=1:geo.nx(1,1)

nwcolloc_x(ii,:)=interp1(wcolloc_y(1,:),wcolloc_x(ii,:),nwcolloc_y(1,:)
,'linear','extrap');

nwx_c(ii,:)=interp1(wy_c(1,:),wx_c(ii,:),nwy_c(1,:),'linear','extrap');

nwx_d(ii,:)=interp1(wy_d(1,:),wx_d(ii,:),nwy_d(1,:),'linear','extrap');
end

COLLOC_X(1:panels(1))=reshape(nwcolloc_x,1,[]);
COLLOC_Y(1:panels(1))=reshape(nwcolloc_y,1,[]);
WING_X(1:bounds(1))=reshape(nwingx,1,[]);
WING_Y(1:bounds(1))=reshape(nwingy,1,[]);
NY_C(1:panels(1))=reshape(nwy_c,1,[]);
NY_D(1:panels(1))=reshape(nwy_d,1,[]);
NX_C(1:panels(1))=reshape(nwx_c,1,[]);
NX_D(1:panels(1))=reshape(nwx_d,1,[]);

[TWIST]=twist_distribution(COLLOC_X(1:panels(1)),COLLOC_Y(1:panels(1)),
SWEEP,B);

%**************************************************************************
****
%COMPUTING INFLUENCE COEFFICIENTS
%**************************************************************************
****
%RESHAPING STRUCTURES FOR LOOP
x_cp=COLLOC_X;
y_cp=COLLOC_Y;
tw_cp=-TWIST';%reshape(tw_cp,prod(size(tw_cp)),1);

x_C=NX_C;
y_C=NY_C;
x_D=NX_D;
y_D=NY_D;

NN=sum(panels);
%Matrix of influence coefficients
for mc=1:NN %control panel
    for n=1:NN %horseshoe vortex

[w(n),v(n)]=horseshoe(x_cp(mc),y_cp(mc),x_C(n),x_D(n),y_C(n),y_D(n));
    end
    Cc(mc,:)=w/(4*pi);
    Cv(mc,:)=v/(4*pi);
end

%**************************************************************************
****
%POST-PROCESSING:WING
%**************************************************************************
****
```

```
I=ones(panels(1)+panels(2),1);
PSI=[tw_cp;zeros(panels(2),1)];

G=-inv(Cc);
Gw=G(1:panels(1),:);
Gt=G(panels(1)+1:end,:);

wspan_loc1=reshape(WING_Y(1:bounds(1)),geo.nx(1,1)+1,[]);
wspan_loc2=reshape(WING_Y(bounds(1)+1:end),geo.nx(2,1)+1,[]);

%locating midpoint of bound vortices for wing and tail
wcirc_loc1=reshape(COLLOC_Y(1:panels(1)),geo.nx(1,1),[]);
wspan_locx1=reshape(WING_X(1:bounds(1)),geo.nx(1,1)+1,[]);
w_locx1=wspan_locx1(1:end-1,:)+.25*diff(wspan_locx1,1);
for ii=1:geo.nx(1,1)

wvort_locx1(ii,:)=interp1(wspan_loc1(ii,:),w_locx1(ii,:),wcirc_loc1(ii,
:));
end
rw=17-wvort_locx1;

wcirc_loc2=reshape(COLLOC_Y(panels(1)+1:end),geo.nx(2,1),[]);
wspan_locx2=reshape(WING_X(bounds(1)+1:end),geo.nx(2,1)+1,[]);
w_locx2=wspan_locx2(1:end-1,:)+.25*diff(wspan_locx2,1);
for ii=1:geo.nx(2,1)

wvort_locx2(ii,:)=interp1(wspan_loc2(ii,:),w_locx2(ii,:),wcirc_loc2(ii,
:));
end
rt=17-wvort_locx2;
h=ro/cn; %nondimensionalized reference point relative to leading edge
of nominal MAC

CLa_w=2/Sn*sum(sum(reshape(Gw*I,geo.nx(1,1),[]),1).*diff(wspan_loc1(1,:
)));
CLphi_w=2/Sn*sum(sum(reshape(Gw*PSI,geo.nx(1,1),[]),1).*diff(wspan_loc1
(1,:)));
CMa_w=2/(Sn*cn)*sum(sum(rw.*reshape(Gw*I,geo.nx(1,1),[]),1).*diff(wspan
_loc1(1,:)));
CMphi_w=2/Sn*sum(sum(rw.*reshape(Gw*PSI,geo.nx(1,1),[]),1).*diff(wspan_
loc1(1,:)));
hnw=h-CMa_w/CLa_w;
ac_w=hnw*cn+4.509+7.93; %global ac location of wing

CLa_t=2/St*sum(sum(reshape(Gt*I,geo.nx(2,1),[]),1).*diff(wspan_loc2(1,:
)));
CLphi_t=2/St*sum(sum(reshape(Gt*PSI,geo.nx(2,1),[]),1).*diff(wspan_loc2
(1,:)));
CMa_t=2/(St*cn)*sum(sum(rt.*reshape(Gt*I,geo.nx(2,1),[]),1).*diff(wspan
_loc2(1,:)));
CMphi_t=2/St*sum(sum(rt.*reshape(Gt*PSI,geo.nx(2,1),[]),1).*diff(wspan_
loc2(1,:)));
hnt=h-CMa_t/CLa_t;
ac_t=hnt*cn+4.509+7.93; %global ac location of tail
```

```
V=Cv;
Vw_w=V(1:panels(1),1:panels(1));
Vw_t=V(1:panels(1),panels(1)+1:end);
Vt_w=V(panels(1)+1:end,1:panels(1));
Vt_t=V(panels(1)+1:end,panels(1)+1:end);

epsilon_ta=sum(reshape([Vt_w*Gw+Vt_t*Gt]*I,geo.nx(2,1),[]),1);
epsilon_tphi=sum(reshape([Vt_w*Gw+Vt_t*Gt]*PSI,geo.nx(2,1),[]),1);

Kwf=1+.025*(10.65/(span))-0.25*(10.65/(span^2));
eta=0.9;
de_da=-mean(epsilon_ta);
de_dphi=-mean(epsilon_tphi);

CLa=Kwf*CLa_w+eta*CLa_t*St/Sn;%*(1-de_da);
%CLphi=Kwf*CLphi_w-eta*CLa_t*St/Sn*de_dphi;
CLphi=Kwf*CLphi_w+eta*CLphi_t*St/Sn;
CLi=-CLa_t*eta*St/Sn;

X=129.16/(Sn*cn);
xh=ac_t-10;
dhnf=-(851.42+15068.5*(1-de_da)/xh+64178.6*(1-de_da)/xh)/(2.92*Sn*cn);

CMa=Kwf*CLa_w*(h-(hnw+dhnf))+CLa_t*eta*(h-hnt)*St/Sn;%*(1-de_da);
%CMphi=Kwf*CLphi_w*((hnw+dhnf)-h)-CLa_t*eta*(hnt-
h)*St/Sn*de_dphi+X*CLphi_w/CLa_w;
CMphi=Kwf*CLphi_w*(h-(hnw+dhnf))+CLphi_t*eta*(h-
hnt)*St/Sn+X*CLphi_w/CLa_w;
CMi=-CLa_t*eta*(h-hnt)*St/Sn;

hn=h-CMa/CLa;
AC=hn*cn+4.509+7.93;

%Minimum Drag Response
y_s=wcirc_loc1(1,:)/(span/2); %nondimensional span coordinate at mean
location of circulation distribution
gamma_nd_alpha=sum(reshape(Gw*I,geo.nx(1,1),[]),1)/(2*span);
%nondimensional circulation distribution due to angle of attack
gamma_nd_twist=sum(reshape(Gw*PSI,geo.nx(1,1),[]),1)/(2*span);
%nondimensional circulation distribution due to twist input
phi=acos(-y_s); %coordinate transformation of span dimension to polar
dimension

%ALPHA SINE-SERIES FIT OF CIRCULATION DISTRIBUTION
N=6;
for i=1:N
    n=2*(i-1)+1;
    if i==1
        sine_series=['a' num2str(n) '*sin(phi)'];
    else
        sine_series=[num2str(sine_series) '+' num2str(['a' num2str(n)
'*sin(' num2str(n) '*phi)'])];
    end
end
```

```
ftype=fittype(num2str(sine_series),'ind','phi');

[fresult,g,out]=fit(phi',gamma_nd_alpha',ftype,'StartPoint',zeros(1,N))
;
RMSEalpha=g.rmse;

for i=1:N
    n=2*(i-1)+1;
    an_alpha(i)=sqrt(n)*eval(['fresult.a' num2str(n)]);
    a_alpha(i)=eval(['fresult.a' num2str(n)]);
end

%TWIST SINE-SERIES FIT OF CIRCULATION DISTRIBUTION
N=6;
for i=1:N
    n=2*(i-1)+1;
    if i==1
        sine_series=['a' num2str(n) '*sin(phi)'];
    else
        sine_series=[num2str(sine_series) '+' num2str(['a' num2str(n)
'*sin(' num2str(n) '*phi)'])];
    end
end

ftype=fittype(num2str(sine_series),'ind','phi');

[fresult,g,out]=fit(phi',gamma_nd_twist',ftype,'StartPoint',zeros(1,N))
;
RMSEtwist=g.rmse;

for i=1:N
    n=2*(i-1)+1;
    an_twist(i)=sqrt(n)*eval(['fresult.a' num2str(n)]);
    a_twist(i)=eval(['fresult.a' num2str(n)]);
end

coeff_nalpha=an_alpha;
coeff_ntwist=an_twist;

%**************************************************************************
****
%OUTPUTS
%**************************************************************************
****
%Coefficients of drag addition
%output=zeros(12,1);
beta(1)=coeff_nalpha(2:end)*coeff_nalpha(2:end)';
beta(2)=coeff_nalpha(2:end)*coeff_ntwist(2:end)';
beta(3)=coeff_ntwist(2:end)*coeff_ntwist(2:end)';
beta(4)=coeff_nalpha(1)^2;
beta(5)=coeff_nalpha(1)*coeff_ntwist(1);
beta(6)=coeff_ntwist(1)^2;

omg1=beta(3)*beta(4)-beta(1)*beta(6);
```

```
omg2=beta(2)*beta(4)-beta(1)*beta(5);
omg3=beta(2)*beta(6)-beta(3)*beta(5);
omg4=beta(3)*beta(5)-beta(2)*beta(6);

OMEGA=(-omg1+sqrt(omg1^2+4*omg2*omg3))/(2*omg4);

%Relevant Aircraft coefficients
output(1)=OMEGA;
output(2)=CLa;
output(3)=hn;
output(4)=CLphi;
output(5)=CMphi;
output(6)=CMi;


%Trim Deflections
DELTA=CMi*(CLa+OMEGA*CLphi)-CLi*(CMa+OMEGA*CMphi);

output(7)=CMi/DELTA;
output(8)=-(CMa+OMEGA*CMphi)/DELTA;
```

GEOFUNCTION

```
function [geo]=geo_function(span,sweep,tail,trig)

uspan=span;%[0 1.6 3.2 4.8 6.4 8];
usweep=sweep*pi/180;%[0 9 18 27 36 45]*pi/180;
utail=tail;%[0 1 2 3 4 5];
%trig=1;

%CONSTANTS
gam_o=18.6934*pi/180;
cw=14;
bo=24.2277;
bto=3.7367;
bt1=7.7782;
usp=uspan;
usw=usweep;
bref=(bo+usp)*cos(usw);
p1=bref-cw/2*sin(usw);
p2=bref+cw/2*sin(usw);
yo_w=(17.021-tan(usw)*3.6025)+21.774*(sin(usw+.32626)-
tan(usw)*cos(usw+.3263));
ut=utail;

%implement trigger on tail
if trig==1
    %set constraint on tail-wing interference condition; constraint
    %piecewise in tail transition point
    if ut>=1.25
        z=(14.6139-1.2*ut-23.8728*sin(gam_o+usw)+(-2.17672-
0.11568*ut+23.8728*cos(gam_o+usw))*tan(usw))/(tan(usw)-1);
        if z>=0
            constraint=1;
        else
            constraint=0;
        end
        ux=0.6*ut+3;
        uy=0.6*ut+1;
        xs=(7.7411-1.2*ut-
21.7738*sin(.3263+usw)+(3.6025+21.7738*cos(.3263+usw))*tan(usw))/(tan(u
sw)-1);
        x3=(-6.87275+2.099*sin(.3263+usw)+(5.7792+.11568*ut-
2.099*cos(.3263+usw))*tan(usw))/(tan(usw)-1);
        y_xs=xs-1.2*ut+24.7625;
        yb_xs=xs-1.2*ut+24.7625+11*sqrt(2);
        yo_t=-1.2*ut+24.7625;
        yb_t=-1.2*ut+24.7625+11*sqrt(2);
    elseif ut<1.25
        z=(18.6139-4.4*ut-23.8728*sin(gam_o+usw)+(-1.79112-
0.424162*ut+23.8728*cos(gam_o+usw))*tan(usw))/(tan(usw)-1);
        if z>=0
            constraint=1;
        else
            constraint=0;
        end
        ux=3*ut;
```

```
        uy=1.4*ut;
        xs=(11.7411-4.4*ut-
21.7738*sin(.3263+usw)+(3.6025+21.7738*cos(.3263+usw))*tan(usw))/(tan(u
sw)-1);
        x3=(-6.87275+2.099*sin(.3263+usw)+(5.39362+.424162*ut-
2.099*cos(.3263+usw))*tan(usw))/(tan(usw)-1);
        y_xs=xs-4.4*ut+28.7625;
        yb_xs=xs-4.4*ut+28.7625+11*sqrt(2);
        yo_t=-4.4*ut+28.7625;
        yb_t=-4.4*ut+28.7625+11*sqrt(2);
    end
    %if no interference define a geometry
    if constraint==0
        d1=yo_w-yo_t;
        d2=y_xs-yo_t;
        %define tail geometry with and without reference area merge
        if d1>=0
            ct=11*sqrt(2)-abs(d1);
            bt=xs;
            ct_o=11*sqrt(2);
            p=3;
            t_lam(1:p)=[ct_o/(ct_o-abs(d1)) 1 0];
            t_span(1:p)=[xs bto+uy-xs bt1];
            t_sweep(1:p)=[atan2(xs*tan(usw)+1/4*abs(d1),xs)*180/pi 45
27]*pi/180;
            t_cr=ct_o-abs(d1);
            t_apex=yo_w;
            %                   w_apex=yo_w-cw/cos(usw);
        else
            ct=11*sqrt(2);
            bt=0;
            ct_o=11*sqrt(2);
            p=2;
            t_lam(1:p)=[1 0];
            t_span(1:p)=[bto+uy bt1];
            t_sweep(1:p)=[45 27]*pi/180;
            t_cr=ct_o;
            t_apex=yo_t;
        end
        %define wing geometry with and without sweep
        geo.c=[cw/cos(usw)];                    %Root chord (2d array)
        if usw==0
            a=1;
            geo.nelem=[a p];                %number of partitions on
each wing (1d array)
            geo.T=[1 zeros(1,p-a);t_lam];                   %Taper
ratio (2d array)
            geo.SW=[0 zeros(1,p-a);t_sweep];                    %Sweep
(2d array)
            geo.b=[bref zeros(1,p-a);t_span];%span(distance root->tip
chord) (2d array)
            geo.area=2*[geo.b(1)*geo.c];
            geo.ny=[18 zeros(1,p-a);2 4];%2 4
        else
            a=2;
            geo.nelem=[a p];
```

```
            geo.T=[1 0 zeros(1,p-a);t_lam];                 %Taper
ratio (2d array)
            geo.SW=[usw atan2((p2-p1)*tan(usw)-
.25*cw/cos(usw),cw*sin(usw)) zeros(1,p-a);t_sweep];
%Sweep (2d array)
            geo.b=[p1 p2-p1 zeros(1,p-a);t_span];%span(distance root-
>tip chord) (2d array)
            geo.area=2*[geo.b(1)*geo.c+geo.c*geo.b(2)/2];
            geo.ny=[14 4;2 4];
        end

        geo.fnx=zeros(2,p);                 %number of panels on flap
chords (2d array)
        %geo.ny=ceil(1/2*geo.b);                    %number of panels
in span (2d array)
        geo.nx=[4*[ones(1,a),zeros(1,p-a)];4*ones(1,p)];
%number of panels on chord (2d array)
        geo.fsym=zeros(2,p);                %flap deflection symmetry
boolean bit  (2d array)
        geo.fc=zeros(2,p);                  %flap chord in percent of
wingchord (2d array)
        geo.flapped=zeros(2,p);             %flapped partition(wing
part) boolean bit (2d array)
        geo.TW(:,:,1)=zeros(2,p);           %partition twist (3d
array)<1 inboard, 2 outboard>
        geo.TW(:,:,2)=zeros(2,p);
        geo.foil(:,:,1)=[20*[ones(1,a),zeros(1,p-a)];12*ones(1,p)];
%Partition airfoils (3d array)
        geo.foil(:,:,2)=[20*[ones(1,a),zeros(1,p-a)];12*ones(1,p)];
%1 inboard, 2 outboard
        geo.c=[cw/cos(usw) t_cr];                   %Root chord (2d
array)
        geo.dihed=zeros(2,p);               %Dihedral (2d array)
        geo.symetric=[1 1];             %Wing symmetry boolean bit (2d
array)
        geo.startx=[yo_w-cw/cos(usw) t_apex];               %Partition
starting coordinate (2d array)
        geo.starty=[0 0];               % ---"----
        geo.startz=[0 0];               % ---"----
        geo.nwing=2;                %number of wings (scalar)
        geo.morph=[usp usw ut];
        geo.flap_vector=zeros(2,p);          %Flap deflection vector
        geo.ref_point=[11.6503 0 0];      %System reference point at
start of MAC of int. wing config
    end
elseif trig==0
    %define wing geometry with and without sweep
     geo.c=[cw/cos(usw)];                   %Root chord (2d array)
    if usw==0
        a=1;
        geo.nelem=[a];              %number of partitions on each wing
(1d array)
        geo.T=[1];                  %Taper ratio (2d array)
        geo.SW=[0];                 %Sweep (2d array)
        geo.b=[bref];%span(distance root->tip chord) (2d array)
        geo.area=2*[geo.b*geo.c];
        geo.ny=[13];
```

```
    else
        a=2;
        geo.nelem=[a];
        geo.T=[1 0];                    %Taper ratio (2d array)
        geo.SW=[usw atan2((p2-p1)*tan(usw)-
.25*cw/cos(usw),cw*sin(usw))];                   %Sweep (2d array)
        geo.b=[p1 p2-p1];%span(distance root->tip chord) (2d array)
        geo.area=2*[geo.b(1)*geo.c+geo.c*geo.b(2)/2];
        geo.ny=[10 3];
    end
    geo.fnx=zeros(1,a);                 %number of panels on flap
chords (2d array)
    %geo.ny=ceil(1/2*geo.b);                    %number of panels in
span (2d array)
    geo.nx=[4*ones(1,a)];                   %number of panels on chord
(2d array)
    geo.fsym=zeros(1,a);                %flap deflection symmetry
boolean bit  (2d array)
    geo.fc=zeros(1,a);                  %flap chord in percent of
wingchord (2d array)
    geo.flapped=zeros(1,a);             %flapped partition(wing part)
boolean bit (2d array)
    geo.TW(:,:,1)=zeros(1,a);           %partition twist (3d array)<1
inboard, 2 outboard>
    geo.TW(:,:,2)=zeros(1,a);
    geo.foil(:,:,1)=[20*ones(1,a)];         %Partition airfoils (3d
array)
    geo.foil(:,:,2)=[20*ones(1,a)];         %1 inboard, 2 outboard
    geo.dihed=zeros(1,a);               %Dihedral (2d array)
    geo.symetric=[1];               %Wing symmetry boolean bit (2d
array)
    geo.startx=[yo_w-cw/cos(usw)];              %Partition starting
coordinate (2d array)
    geo.starty=[0];             % ---"----
    geo.startz=[0];             % ---"----
    geo.nwing=1;                %number of wings (scalar)
    geo.morph=[usp usw ut];
    geo.flap_vector=zeros(1,a);          %Flap deflection vector
    geo.ref_point=[11.6503 0 0];      %System reference point at start
of MAC of int. wing config
end
```

GEOCONVERT

```
function
[WING_X,WING_Y,COLLOC_X,COLLOC_Y,Y_C,Y_D,X_C,X_D]=geo_convert(lattice,r
ef,geo)

nwings=length(geo.nelem);
parts=2*geo.nelem;
reshpan=geo.ny.*geo.nx;
reshpane=reshape(reshpan',1,[]);
nblocks=reshape([reshpane;reshpane],1,[]);
sp_panels=2*sum(geo.ny,2);
ch_panels=geo.nx(:,1);
panels=sp_panels.*ch_panels;

wing=lattice.XYZ;
vxy=lattice.COLLOC;

for j=1:size(wing,2)
    for i=1:length(nblocks)
        if i==1
            partwing(j,i)={wing(1:nblocks(i),j,:)}; %change 1 to j when
iterating for various columns
            partvort(i)={vxy(1:nblocks(i),:)};
        else
            partwing(j,i)={wing(sum(nblocks(1:i-
1))+1:sum(nblocks(1:i)),j,:)};
            partvort(i)={vxy(sum(nblocks(1:i-
1))+1:sum(nblocks(1:i)),:)};
        end
    end
    %create reshaping & dimension flip vectors
    clear pv flip
    for i=0:parts(1)-1
        if 2*i<parts(1)
            pv(i+1)=parts(1)-2*i;
            flip(i+1)=pv(i+1);
        else
            pv(i+1)=abs(parts(1)-(2*i+1));
            flip(i+1)=0;
        end
    end
    jj=length(flip);
    if length(parts)>1
        padd=parts(1)+diff(parts)*heaviside(diff(parts),0);
        for i=0:parts(2)-1
            if 2*i<parts(2)
                pv(parts(1)+i+1)=padd+parts(2)-2*i;
                flip(jj+i+1)=pv(parts(1)+i+1);
            else
                pv(parts(1)+i+1)=padd+abs(parts(2)-(2*i+1));
                flip(jj+i+1)=0;
            end
        end
    end
    %apply reshaping vector & flipping appropriate dimension
```

```
    for i=1:length(pv)
        if flip(i)~=0
            if i==1

Wing(1:nblocks(pv(i)),j,:)=flipud(squeeze(partwing{j,pv(i)}));

Vort(1:nblocks(pv(i)),:)=flipud(squeeze(partvort{pv(i)}));
            else
                Wing(sum(nblocks(pv(1:i-
1)))+1:sum(nblocks(pv(1:i))),j,:)=flipud(squeeze(partwing{j,pv(i)}));
                Vort(sum(nblocks(pv(1:i-
1)))+1:sum(nblocks(pv(1:i))),:)=flipud(squeeze(partvort{pv(i)}));
            end
        else
            if i==1
                Wing(1:nblocks(pv(i)),j,:)=squeeze(partwing{j,pv(i)});
                Vort(1:nblocks(pv(i)),:)=squeeze(partvort{pv(i)});
            else
                Wing(sum(nblocks(pv(1:i-
1)))+1:sum(nblocks(pv(1:i))),j,:)=squeeze(partwing{j,pv(i)});
                Vort(sum(nblocks(pv(1:i-
1)))+1:sum(nblocks(pv(1:i))),:)=squeeze(partvort{pv(i)});
            end
        end
    end
    Wing_x=Wing(:,j,1);
    Wing_y=Wing(:,j,2);
    Vort_x=Vort(:,1);
    Vort_y=Vort(:,2);

    Wing_xw=reshape(Wing_x(1:panels(1)),max(geo.nx(1,:)),[]);
    Wing_XW(:,:,j)=[flipud(Wing_xw(:,1:end/2)),Wing_xw(:,end/2+1:end)];
    Wing_YW(:,:,j)=reshape(Wing_y(1:panels(1)),max(geo.nx(1,:)),[]);

    Vort_xw=reshape(Vort_x(1:panels(1)),max(geo.nx(1,:)),[]);
    Vort_XW=[flipud(Vort_xw(:,1:end/2)),Vort_xw(:,end/2+1:end)];
    Vort_YW=reshape(Vort_y(1:panels(1)),max(geo.nx(1,:)),[]);

    if length(parts)>1
        Wing_xt=reshape(Wing_x(panels(1)+1:end),max(geo.nx(2,:)),[]);

Wing_XT(:,:,j)=[flipud(Wing_xt(:,1:end/2)),Wing_xt(:,end/2+1:end)];

Wing_YT(:,:,j)=reshape(Wing_y(panels(1)+1:end),max(geo.nx(2,:)),[]);

        Vort_xt=reshape(Vort_x(panels(1)+1:end),max(geo.nx(2,:)),[]);
        Vort_XT=[flipud(Vort_xt(:,1:end/2)),Vort_xt(:,end/2+1:end)];
        Vort_YT=reshape(Vort_y(panels(1)+1:end),max(geo.nx(2,:)),[]);
    end
end

WING_xw=[Wing_XW(:,:,1);Wing_XW(end,:,4)];
WING_XW=[WING_xw,WING_xw(:,1)];

WING_yw=[Wing_YW(:,:,1),Wing_YW(:,end,2)];
WING_YW=[WING_yw;WING_yw(end,:)];
```

```
ny_Cw=WING_YW(1:geo.nx(1,1),1:end-1);
ny_Dw=WING_YW(1:geo.nx(1,1),2:end);

nwing_xCDw=WING_XW(1:end-1,:)+0.25*diff(WING_XW,1);
nx_Cw=nwing_xCDw(:,1:end-1);
nx_Dw=nwing_xCDw(:,2:end);

if length(parts)>1
    WING_xt=[Wing_XT(:,:,1);Wing_XT(end,:,4)];
    WING_XT=[WING_xt,WING_xt(:,1)];

    WING_yt=[Wing_YT(:,:,1),Wing_YT(:,end,2)];
    WING_YT=[WING_yt;WING_yt(end,:)];

    ny_Ct=WING_YT(1:geo.nx(2,1),1:end-1);
    ny_Dt=WING_YT(1:geo.nx(2,1),2:end);

    nwing_xCDt=WING_XT(1:end-1,:)+0.25*diff(WING_XT,1);
    nx_Ct=nwing_xCDt(:,1:end-1);
    nx_Dt=nwing_xCDt(:,2:end);

    WING_X=[reshape(WING_XW,[],1);reshape(WING_XT,[],1)];
    WING_Y=[reshape(WING_YW,[],1);reshape(WING_YT,[],1)];
    COLLOC_X=[reshape(Vort_XW,[],1);reshape(Vort_XT,[],1)];
    COLLOC_Y=[reshape(Vort_YW,[],1);reshape(Vort_YT,[],1)];

    Y_C=[reshape(ny_Cw,[],1);reshape(ny_Ct,[],1)];
    Y_D=[reshape(ny_Dw,[],1);reshape(ny_Dt,[],1)];

    X_C=[reshape(nx_Cw,[],1);reshape(nx_Ct,[],1)];
    X_D=[reshape(nx_Dw,[],1);reshape(nx_Dt,[],1)];
else
    WING_X=reshape(WING_XW,[],1);
    WING_Y=reshape(WING_YW,[],1);

    COLLOC_X=reshape(Vort_XW,[],1);
    COLLOC_Y=reshape(Vort_YW,[],1);

    Y_C=reshape(ny_Cw,[],1);
    Y_D=reshape(ny_Dw,[],1);

    X_C=reshape(nx_Cw,[],1);
    X_D=reshape(nx_Dw,[],1);
end
```

TWIST DISTRIBUTION

```
function [TWIST] = twist_distribution(COLLOC_X,COLLOC_Y,SWEEP,B);

P = COLLOC_Y+i*COLLOC_X;

O = 17*i+3.6025;
On = 17*i-3.6025;
TWo=17.9775;

for jj=1:length(COLLOC_Y)
    if COLLOC_Y(jj)>0
        R=P(jj)-O;
        p(jj)=R.*exp(-i*SWEEP*pi/180)+O;
    else
        R=P(jj)-On;
        p(jj)=R.*exp(i*SWEEP*pi/180)+On;
    end
end

for jj=1:length(p)
    if real(p(jj))>TWo
        TWIST(jj)=(real(p(jj))-TWo)/(B/2-TWo);
    elseif real(p(jj))<-TWo
        TWIST(jj)=(abs(real(p(jj)))-TWo)/(B/2-TWo);
    else
        TWIST(jj)=0;
    end
end
```

HORSESHOE

```
function [W,V]=horseshoe(xm,ym,x1n,x2n,y1n,y2n);

a=xm-x1n;
b=xm-x2n;
c=ym-y1n;
d=ym-y2n;
e=x2n-x1n;
f=y2n-y1n;

P1=1/(a*d-b*c);
P2=[(e*a+f*c)/sqrt(a^2+c^2)]-[(e*b+f*d)/sqrt(b^2+d^2)];
P3=-1/c*[1+a/sqrt(a^2+c^2)]+1/d*[1+b/sqrt(b^2+d^2)];

W=P1*P2+P3;

V=P3;
```